University of Bergen
Department of Physics and Technology

Master in Particle Physics

Study on viability of Gain Stabilization of SiPMs and determination of b-quark fragmentation fraction ratio f_c/f_u in pp collisions at $\sqrt{s} = 13$ TeV with the ATLAS detector

Author:
Are Træet

Supervisor:
Prof Gerald Eigen

August 4, 2017

Abstract

Gain Stabilization of SiPMs through the usage of an external board to regulate bias voltage based on temperature yields a variation in gain of less than 0.5 % using a system of four SiPMs with temperature readout in close vicinity. A proper system test should still be explored, although these preliminary tests show promising results.

The estimation of B_c^+ mass and the fragmentation ratio f_c/f_u using 2015 and 2016 ATLAS data at $\sqrt{s} = 13$ TeV yields $M_{B_c^+} = 6268.32 \pm 4.77(\text{stat}) \pm 3.78(\text{syst})$ MeV c^{-2} and $f_c/fu = 3.06 \pm 0.51_{\text{stat}} \pm 2.72_{\text{syst}} \times 10^{-4}$. The fragmentation ratio of f_c/f_u is determined through the relative efficiency-corrected yields of $B_c^+ \to J/\psi\pi^+$ over $B_u^+ \to J/\psi K^+$ and the branching fraction ratio $\mathcal{B}\left(B^\pm \to J/\psi K^\pm\right)/\mathcal{B}\left(B_c^\pm \to J/\psi\pi^\pm\right)$.

Contents

List of Figures

List of Tables

Glossary

ADA Board

a power supply where the voltage can be automatically adjusted based on a measured temperature. This is done through a programmable voltage versus temperature function. 6, 36, 49

ATLAS

. 51–57, 75, 77, 82, 91, 93, 94, 97, 103, 104

CERN

. 51

CKM

. 66, 67

climate chamber

a chamber in which one can control and monitor the ambient temperature, through both manual and automatic operation via a built in touchscreen. 3–5, 29, 36, 37

DAQ

the process of measuring an electrical or physical phenomenon such as voltage, current, temperature, pressure, or sound with a computer. A DAQ system consists of sensors, DAQ measurement hardware, and a computer with programmable software. 3, 5, 6, 49

dG/dT

determines the gradient of the temperature dependence of the gain. 2, 24, 25, 31, 33, 35

dG/dV

determines the gradient of the voltage dependence of the gain. 2, 24, 25, 31, 33, 35

dV/dT

determines the gradient of the temperature dependence of the voltage. 2, 6, 24, 29, 32, 34, 36–40, 46, 49, 50

ECAL

. 53, 57

EW

. 60, 64–66

HCAL

. 53, 57

ID

. 54, 55

Keithley 2100 6 1/2 digit multimeter

an apparatus that is used to measure voltage, current and resistance in electrical circuits or components. 26

LeCryo Model 6104 12bit ADC 2.5GS/s

the oscilloscope which was used to do all of the waveform recording. 7

LHC

. 51, 53, 69

MC

. 75, 77–80, 83, 88–96, 99–101, 103

MS

. 53, 54

MSME

Mean Start Mean End integration window. 17, 19, 20, 39–45, 47

MSVE

Mean Start Variable End integration window. 18, 19, 43, 45, 47

Parasitic Pickup Signal

A signal which distorted the waveforms recorded by the oscilloscope. 13, 14, 16–20, 43–45

PDF

. 21, 78, 88, 89, 93, 94, 104

p.e. peak

photoelectron peak(s) which arises from integration over several waveforms from the detectors. 6, 19–24, 32, 38, 43, 44, 47

Pedestal Contributions

Contributions that add up to the pedestal in a photoelectron spectrum. 13, 14, 20

PT1000

PT1000 temperature sensors which were used for all temperature measurements in study. 3, 5, 36

QCD

. 60, 64

QED

. 60, 63, 65

QFT

. 52, 62, 63, 65

QRLED

a signal generator which generates a 3.4 ns wide sinusoidal shape above a fixed threshold, the amplitude and rate of the generated signal is adjustable, and rate has a range of up to 100 kHz. 5–7, 13, 23

SiPM

a type of device that consists of many n-p junction semiconductors that function as an array of avalanche photodiodes. 1–3, 6–11, 23, 29

SM

. 59, 60, 62–64, 69, 103

VSME

Variable Start Mean End integration window. 18, 47

VSVE

Variable Start Variable End integration window. 18, 47

Chapter 1

Motivation

> *"It doesn't matter how beautiful your theory is, it doesn't matter how smart you are. If it disagrees with experiment, it's wrong."*
>
> — Richard Feynman

This will be a two-fold thesis. The motivation will cover both topics, while they will be presented separately following this chapter. The first part of this thesis, chapter 2 and onwards to chapter 6, will encapsulate the work done in relation to a study done on SiPM gain stabilization, while the remainder of this thesis will be covering the analysis of the fragmentation ratio f_c/f_u using ATLAS data from 2015 and 2016 at $\sqrt{s} = 13$ TeV.

All the analysis parts of this thesis have been carried out through use of the ROOT library classes for the programming languages C++ and Python [1]. Specifically we have used the RooFit library for all the fitting routines [2], [3], and the TSpectrum class [4] for the spectra analysis of the SiPMs. There were also many other tools, programs, and programming languages which were used to simplify different tasks where those previously discussed were not optimal.

1.1 Gain Stabilization

In a modern detector setup, whether it's in a scientific laboratory deep underground or located in an examination room at a hospital, one has a temperature variance. In a scientific experiment such as for instance ATLAS, this is something that can be corrected offline for the whole system if the temperature variance at each point in time and its gain vs temperature dependence is known. While in other cases this is added as a possible source of error or, as in most hospital settings, simply neglected altogether. Correcting for these effects offline is a resource and time consuming process which should in all likelihood be replaced by an online system. The main motivation behind the study carried out in thesis is to check whether such a system is a viable solution.

The impact of the temperature variance on modern detectors depends on what their purpose is and what technology is applied, i.e. a smoke detector is not as influenced as a scientific laboratory detector. The main focus of the study carried out and explained within this thesis is to achieve a stable gain from Silicon Photo-Multiplier (SiPM) over normal operational conditions. One of the main features of a solid state detector is that the gain is dependent on an applied bias voltage, which is further dependent on the temperature of the sensor. As such, local temperature fluctuation due to normal operating conditions of a sensor might result in a different energy measurement from two identical particles with the same momentum. For a clinical setting this may result in an image taken during winter might show differences compared to that taken during a summer, due to effects being masked by the gain differences.

In order to correct the applied bias voltage to reach a constant gain for a detector, one needs knowledge of its innate voltage-versus-temperature (dV/dT). This parameter can be extracted from measurements of the gain-versus-bias voltage (dG/dV) and gain-versus-temperature (dG/dT) for a specific model or sensor. Knowledge of this parameter enables one to continuously adjust the applied bias voltage as the temperature of the sensor changes. This further results in uniform gain during the data-taking period. The goal of this analysis was to achieve a gain non-uniformity within 1 % in the temperature range of 20–30 °C.

To this end we tested a total of 30 different SiPM from the manufacturers of Hamamatsu, Ketek and CPTA. The objective was to show that one can viably correct for the temperature induced gain fluctuations and achieve a gain stability of less than 1% within the range of 1 to 50 ℃. We have tested each detector individually and in a small setup where we had four detectors connected to a common power source. This was done to further check the impact of having a larger system of these detectors, since in a real life HEP environment the number of detectors within a subsystem is in the order of 10^6.

1.2 ATLAS Analysis

The Standard Model is the theory we use in particle physics to explain all known subatomic particles and their interactions with each other. It currently consists of 19 definite particles and explains electroweak and strong interactions within certain thresholds. Though there are several parameters in this theory that remain unmeasured to this date, amongst these is the fragmentation probability of f_c. Within this thesis we aim to successfully measure the fragmentation probability ratio of f_c/f_u. Since f_u has been very precisely measured in the past, one can then determine the value of f_c. The knowledge of this fragmentation probability is necessary in order to gauge a better understanding of doubly heavy quark hadrons like the B_c meson. Through this latter part of the thesis from Chapter 7 onwards to Chapter 12 we will refer to the $B_u^{\pm}$ simply as B^+ or $B^{\pm}$. We will be using natural units, although masses and momenta will in most cases be given with the corresponding number of c.

Chapter 2

Experimental Setup

2.1 Black Box

The black box consists of an aluminum outer shell which was completely sealed during Data Acquisition (DAQ), this to remove any outside light source. Inside of this box we had four sockets in which to attach the SiPMs to the preamplifiers. There were also four adjustable lanes where we could insert optical fibers - this was made so we could secure the fibers and precisely set the distance between the fiber opening and the detector's surface. The box has several connectors attached to supply the bias voltage of the different detectors and the several temperature sensors inside. The opening that had to be kept for the insertion of the optical fibers was shielded from the compartment where the detectors were mounted.

2.2 Temperature Measurements

The temperature measurements were carried out using seven PT1000 Temperature Sensors (PT1000); where we had one sensor near each of the SiPMs, a fifth one along the inner wall of the black box, sixth one was fixed to measure the ambient temperature inside of the black box and lastly a seventh was located outside the black box which was used to get a more accurate ambient temperature measurement inside the Spirale 3 Climats. One can see an example of the recorded temperature measurements in Figure 2.2. Non of the temperature profiles went below 1 °C as we did not have any way to mitigate the humidity in the system nor any method in which we could prevent rime buildup, where any subsequent melting would most likely damage the equipment.

The sensors were attached to a control board made by MPI of Physics München, while a ROOT script was used as an interface to read this data out to a text file. The temperature was recorded roughly every ten seconds from each sensor. This took continuous measurements throughout almost the whole DAQ period, the only downtime was when the system had to be shut down for technical purposes.

2.3 Climate Chamber

We were using a Spirale3 climate chamber built by Climats, which could be operated by a built in touchscreen, which included both manual and automatic operation methods. Using the touchscreen one could program a temperature versus time function which, when activated, the climate chamber would automatically follow. This is something which we utilized fully to take data overnight, a plot showing the temperature measurements for one of these overnight runs can be seen in Figure 2.2.

Figure 2.1: Here we see the internal layout of the black boxed used in the analysis. The four pre-amplifiers can be seen with their own SiPM mounted in the socket. The small white chip seen near the detectors is the PT1000 temperature monitors. The cable ties seen on the right hand side in the picture are there to securely fasten the mounting for the optical fibers.

Once the climate chamber was set to a certain temperature it took a while before it reached its equilibrium, showing only a fluctuation of $\approx \pm 0.2\,°\mathrm{C}$ within the target temperature. While the climate chamber we used had its own temperature sensors to monitor the internal conditions, our own measurements suggests that the actual temperature inside the chamber was consistently $\approx 0.4\,°\mathrm{C}$ above what the chamber reported, and therefore the target temperature. Both these two factors have been taken into considerations when we developed the software for this analysis.

The front door of the climate chamber features an open window which was promptly concealed through securely taping a cutout cardboard piece over it. This was to further minimize any chance of light throughput influencing the data. All cables which were needed for the operation within the climate chamber were inserted through an open hole on the side. This hole had its own plug to securely seal it after the necessary wires were stretched through.

2.4 Quasi Resonant LED Driver

All of the detectors were tested by simultaneously illuminating them using a UV light source located on the outside of the climate chamber. It was placed here to minimize the chances of inducing noise. The light was guided from the light source using several optical fibers. Inside of the black box we had channels where the fibers were inserted and securely mounted where one could adjust the distance between the fiber openings and the detector surface through the use of thumbscrews.

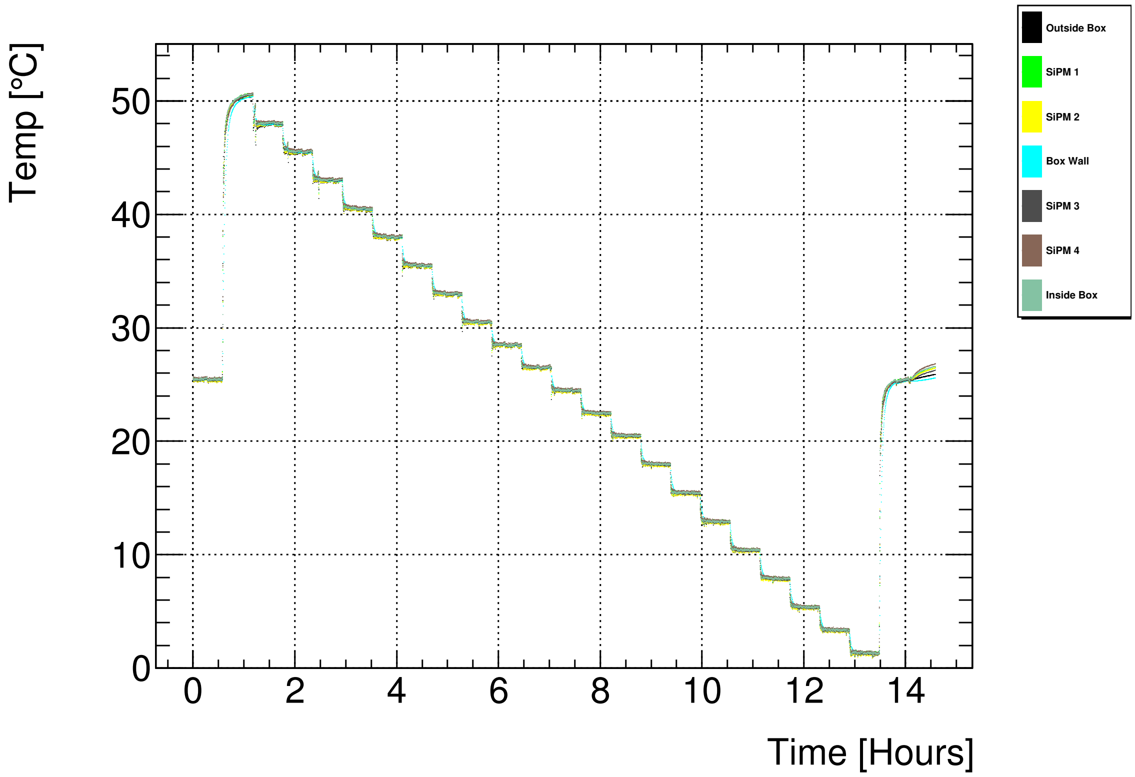

Figure 2.2: Can in this plot observe the temperature data recorded by the different PT1000. The temperature profile shown here is what were used for the overnight stabilization run of the S13360 detectors. It was programmed through the touchscreen interface of the climate chamber.

Using this we manually adjusted the fibers until each detector had the same surface illumination and the recorded waveforms had similar shapes and pulse heights.

The light source used consists of a Quasi Resonant LED driver (QRLED) developed by members of the Czech Collaborators. It was controlled with a CAN bus interface and was used as the trigger for the DAQ. The QRLED generates a 3.4 ns wide sinusoidal shaped pulse, where both repetition rate and light intensity is adjustable [5]. The repetition rate is adjustable up to 100 kHz while the light intensity is adjustable through the applied current. Throughout all analysis covered in this thesis the repetition rate was set to 10 kHz, though some special runs were carried out where we varied both the light rate and intensity.

2.5 Data Recording Equipment

All of the data were recorded directly using a digital oscilloscope made by LeCroy. The oscilloscope in question was model 6104 with 12 bit ADC at 2.5 GS/s which had 4 channels [6]. The control of the experiments was done via a LabView routine we specifically made for this setup. Through this we could adjust the recording parameters of the oscilloscope, i.e. recording window in nanoseconds, voltage threshold, voltage offset, sampling rate, number of waveforms of the oscilloscope. We could also change the light intensity and rate of the QRLED, as well as control the bias power supply. The voltage controller for the preamplifiers was controlled manually, and the recording of the temperature data was done through the use of a temperature sensor board developed by MPI of Physics München with readout done with a ROOT based script.

Utilizing this oscilloscope we could record 50 000 waveforms from each of the detectors simultaneously, this was achieved through the use of its Sequence Sampling Mode Acquisition [7], which minimizes dead time by allocating several different memory segments and storing each individually triggered waveform in these segments. This allows for very high rates of DAQ where it typically took less than a second to record all two hundred thousand waveforms, while processing and transferring of the data took little over half a minute. Through this oscilloscope we could visually inspect any number of waveforms or integrate over the a selected number of waveforms or time period in order to determine how the photoelectron spectrum of these waveforms looked like. Through this we could perform on the fly adjustments of the different parameters of the DAQ based on the results observed. These visual inspecting features slowed down the whole DAQ process while activated. Hence they were only used during setup of each detector to determine their response to the QRLED intensities and bias voltage. Since it had to be disabled while we were taking data this means that some features that could indicate issues were not discovered before the analysis stage.

Its 12 bit ADC gave us superior ability to see smaller details in the data recorded which allowed for more precise knowledge of how the system behaved. Though due to the amount of data a 12 bit system records, it resulted in us having storage issues, and having to resort to several different ways to mitigate this. One of which was limiting the DAQ window, another was to shift from storing data in comma separated values, to doubles stored as binary, then finally to a modified version using shorts and conversion factors. These conversion factors were necessary to convert the shorts back to doubles and was stored in a file containing the metadata for each 50 000 waveform. This file also contained the bias voltage measured as well as other detector relevant information. In order to get as much detail as possible out of the 12 bit system, we had to manually adjust the voltage window to what values we assumed we'd get - as the bin size is determined by the voltage range - as such there was cases where the waveforms with the highest amplitudes were not fully recorded and instead ended up clipped. Though these facts should not impact any of the results, as we do not use more than the three first p.e. peaks and the waveforms contributing to these peaks were always contained in the data taking window.

2.6 Adaptive Power Supply Board

In order to keep the gain stable throughout operation one needs a voltage source that automatically adjusts itself with temperature. For this purpose an Adaptive Power Supply Board (ADA Board) had been constructed by the Institute of Physics of the Czech Academy of Sciences. This ADA Board provides a stable regulated DC voltage in the range of 15–90 V, where the stability achieved is less than 5 mV and has a temperature influenced stability of less than $1\,\mathrm{mV\,^{\circ}C^{-1}}$ in the entirety of the voltage range. It has an adjustable dV/dT function in the range of 10–$100\,\mathrm{mV\,^{\circ}C^{-1}}$ where it slowly ramps the voltage up and down to its set parameters [8].

As such we needed to determine this voltage-versus-temperature (dV/dT) correction factor and the nominal operational bias voltage for each detector, as these were both needed as input parameters of the ADA Board.

2.7 Detectors

For the tests we had a total of 30 different SiPM from three separate manufacturer, Hamamatsu [9][10], KETEK [11] and CPTA. This was to be able to show that

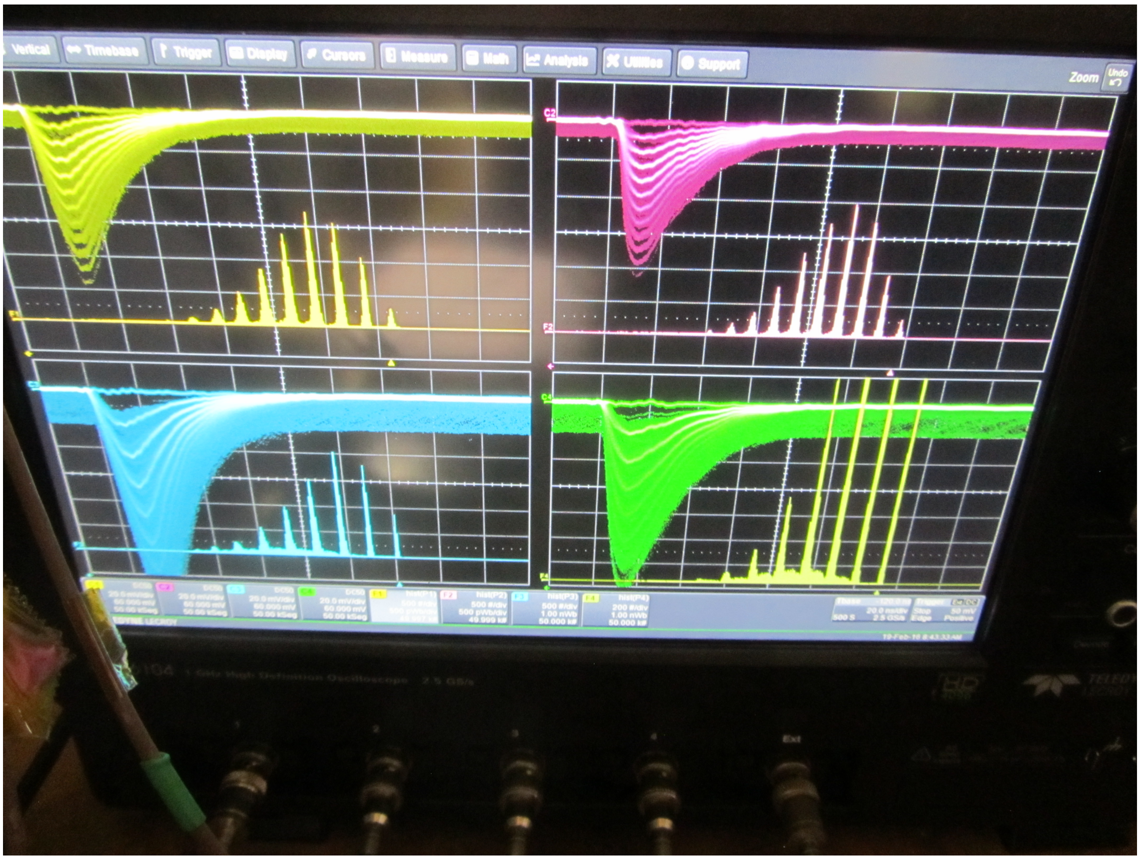

Figure 2.3: Here we can see the waveform segmentation and online integration capabilities of the LeCryo Model 6104 12bit ADC 2.5GS/s oscilloscope which was used in this analysis.

the system we used to stabilize the gain is independent of the SiPM used. The different detectors that we used in these tests can be seen in Table 2.1. While some of these models were prototypes which had no producer data sheet available that we could refer to, most of them had their gain, recommended operational bias voltage, and breakdown voltage on a sticker. The rest were either determined through measurements, or as one can seen from the missing values in the table, not estimated at all.

We had a total of 18 detectors from Hamamatsu, where six of these had trenches to reduce optical crosstalk and is supposed to have a much lower dark rate count, that will be the LCT and S13360 detectors. From KETEK we had a total of eight different detectors where the two W12 detectors were prototypes. The four detectors from CPTA had a scintillation tile and a wavelength shifter glued to them and since we did not want to damage the detectors by removing these, they were left on during all data taking that we've done. As such when viewing any results from these detectors one should also take into account that these two objects are attached, while all other detectors are directly illuminated by the QRLED.

Table 2.1: Information on the 30 SiPM used in this test. Most detectors had their serial number specific values on a sticker on their accompanying box. However, this information was sometimes incomplete. The prototypes had their own specific information listed on the packaging they came in, and nothing else is known about them. All others values are taken from either the product sheets from the manufacturer website, or the serial number specific information sticker. For both the Hamamatsu and KETEK SiPMs the listed specifications are for 25 °C while for CPTA they are for 22 °C.

Type	**Model**	**Serial#**	**Pixel Pitch** [μm]	**Active Area** [mm^2]	**#Pixels**	**Nominal** $V_{bias}[V]$	**Breakdown** $V_{bias}[V]$	**Gain** [10^6]
Hamamatsu Prototypes								
A	1		15	1.0 × 1.0	4400	67.22	-	0.2
A	1		20	1.0 × 1.0	2500	66.73	-	0.23
A	2		15	1.0 × 1.0	4400	67.15	-	0.2
A	2		20	1.0 × 1.0	2500	66.7	-	0.23
B	1		15	1.0 × 1.0	4400	74.16	-	0.2
B	1		20	1.0 × 1.0	2500	73.33	-	0.23
B	2		15	1.0 × 1.0	4400	73.99	-	0.2
B	2		20	1.0 × 1.0	2500	73.39	-	0.23
LCT	4	6	50	1.0 × 1.0	400	53.81	50.81	1.6
LCT	4	9	50	1.0 × 1.0	400	53.98	50.93	1.6
Hamamatsu								
S12571	010C	271	10	1.0 × 1.0	10000	69.83	-	0.135
S12571	010C	272	10	1.0 × 1.0	10000	69.87	-	0.135
S12571	015C	136	15	1.0 × 1.0	4489	68.08	-	0.229
S12571	015C	137	15	1.0 × 1.0	4489	68.03	-	0.230
S13360	1325CS	10143	25	1.3 × 1.3	2668	57.18	52.18	0.7
S13360	1325CS	10144	25	1.3 × 1.3	2668	57.11	52.11	0.7
S13360	3025CS	10103	25	3.0 × 3.0	14400	57.66	52.66	1.7
S13360	3025CS	10104	25	3.0 × 3.0	14400	56.97	51.97	1.7
KETEK Prototypes								
W12	A		20	3.0 × 3.0	12100	28	25	0.54
W12	B		20	3.0 × 3.0	12100	28	25	0.54
KETEK								
PM33	50	1	50	3.0 × 3.0	3472	32.4	-	2
PM33	50	2	50	3.0 × 3.0	3472	32.4	-	2
PM33	50	5	50	3.0 × 3.0	3472	32.4	-	2
PM33	50	6	50	3.0 × 3.0	3472	32.4	-	2
PM33	50	7	50	3.0 × 3.0	3472	32.4	-	2
PM33	50	8	50	3.0 × 3.0	3472	32.4	-	2
CPTA Prototypes								
		857	40	1.0 × 1.0	796	33.4	31.9	0.71
		922	40	1.0 × 1.0	796	33.1	31.6	0.63
		972	40	1.0 × 1.0	796	33.3	31.8	0.63
		1065	40	1.0 × 1.0	796	33.1	31.6	0.70

Chapter 3

Introduction to Silicon Photomultiplier

3.1 Breakdown voltage

The breakdown voltage V_{break} is the bias point at which, when above this, the electric field strength generated in the depletion region of the detectors is sufficient to create a Geiger discharge. The V_{break} point can most easily be identified on a current versus voltage plot by the sudden increase in current. The dependence is typically linear before this point occurs.

3.2 Overvoltage

Overvoltage is one of the most important aspects affecting the operation of a SiPM, since it directly influence the gain attained by the detector, as well as the dark count rate, optical crosstalk and indirectly the amount of afterpulses. It is defined as the difference in the applied bias voltage and the current breakdown voltage of the SiPM, as seen in Eq. 3.1.

$$\Delta V = V_{bias} - V_{break} \tag{3.1}$$

3.3 Gain

The gain of a SiPM sensor is defined as the amount of charge created for each detected particle, and it depends on the pixel size and the overvoltage applied to it. Each pixel in a SiPM generates highly uniform and quantized amount of charge by each avalanche which is initiated by a particle being absorbed, or a charged particle transversing its active volume. The gain of a single pixel, and hence also the whole sensor, is defined as the ratio between the charge from an activated pixel over the charge of a single electron. The gain for a SiPM can therefore be calculated using the ΔV, the pixel capacitance C, and the charge of an electron e, as seen in Eq. 3.2.

$$G = \frac{\Delta V \cdot C}{e} \tag{3.2}$$

The way in which a SiPM operates makes it possible to fairly accurately measure its gain. This is done through the fact that each detected particle results in a highly quantized output pulse, as can be seen in Figure 3.1a, where the first pulse density seen at around negative 10 millivolts correspond to a single photon being detected, while the next density corresponds to two photons etc. If one were to integrate

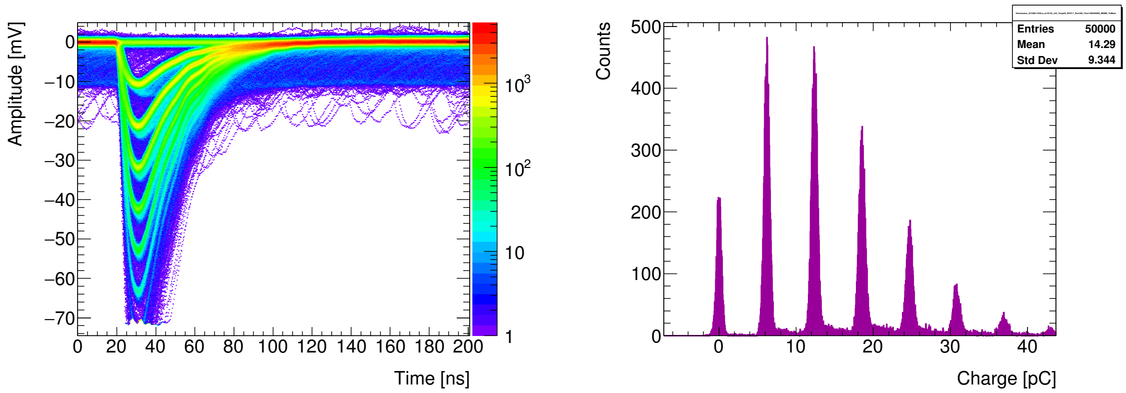

(a) Density plot of several photon pulses generated by a SiPM.

(b) Integrated photon pulses yield photoelectron spectra like these.

Figure 3.1: These plots are both made using the Hamamatsu detector S13360 1325CS serial number 10143.

each of these pulses, one would end up with a charge spectrum like the one shown in Figure 3.1b, where one can clearly see the different numbers of photons being detected and the charges that were recorded from each avalanche. The separation between each adjacent peak in this figure should ideally be constant and should correspond to the charge generated by a single fired pixel, and in turn this distance can be used to determine the gain of the SiPM. In Figure 3.1b the intrinsic gain of the SiPM has not been separated from the system, as such it displays the absolute gain.

The absolute gain, which is a combination of the intrinsic gain of the SiPM and the preamplifier used, is determined through dividing the obtained integrated charge by the electron charge. We were unable to accurately determine the gain of the preamplifiers and as such we could not decouple the intrinsic gain of the detectors. Hence all the displayed charge on plots corresponds to the absolute gain of the system, and is given in units of pico Coulomb unless otherwise specified.

3.4 Dark Rate Count

The dark count rate originates primarily from a free charge carrier which triggers an avalanche. The source of this free charge carrier is mainly from two sources. The first is when an electron transfers from the valence to the conduction band via a state/trap within the band gap. This is sensitive to temperature and density of the traps as well as the relative energy of the traps. These traps commonly occur due to lattice imperfections or impurities. The second way is through direct and trap-assisted band-to-band tunneling, this is only slightly sensitive to temperature, but instead is sensitive to the applied bias voltage. The dark rate count is the main source of noise in a SiPM.

3.5 Optical Crosstalk

Optical crosstalk occurs when a primary discharge (avalanche) in a pixel triggers secondary discharges in one or more adjacent pixels. This can either happen nearly simultaneously as the primary avalanche or it can be delayed by a several 10's of nanoseconds. The probability of crosstalk is dependent on the pixel size, the shielding between said pixels, as well as increasing with an applied overvoltage.

Overvoltage is as aforementioned the difference between the applied bias voltage and the breakdown voltage. Since this is the only factor that is variable in a specific sensor, the crosstalk can only be minimized through limiting the increase of the bias voltage. The Hamamatsu detectors with trenches, namely the LCT and S13360, should reduce the optical crosstalk.

3.6 Afterpulses

During breakdown, carriers can become trapped in the sensor. After a delay of up to several nanoseconds, the trapped carriers are released, potentially initiating an avalanche and creating an afterpulse in the same pixel. Afterpulses with short delay that occur during the recovery time of the pixel tend to have negligible impact as the pixel is not fully charged. However, longer delay afterpulses can impact measurements done with the SiPM if the rate is high enough. Afterpulse probability increases indirectly with overvoltage, this is due to the increased avalanche initiation probability by the processes previously discussed. Afterpulses were a contributing factor to why the determination of a proper integration window was difficult to achieve, and also its importance.

Chapter 4

Data Acquisition and Handling

4.1 Waveform Contributions

The signal contributions in the waveforms come from avalanches triggered by the QRLED used. The trigger in the setup is set so that these should always occur after the same fixed time interval for each recorded waveform. This results in almost all pulses starting to rise at the same point. The background is mostly noise, such as dark count rate, optical crosstalk and afterpulsing. However, there was also discovered another source of parasitic pickup signal in the recorded signal, which is explained in section 4.2.

4.2 Parasitic Pickup Signal

During data acquisition it was discovered that we had a signal which was picked up by the system. After a lengthy exploration of different potential causes; cellphones and other electronic communication devices were removed, and we discovered that one of the CAN Bus cables, used to communicate between the PC running LabView and the voltage source, were faulty and was generating noise. Since this was a component that we were unable to find a replacement for, it was necessary to develop a tool that was able to minimize the effect of this Parasitic Pickup Signal (PPS) and also determine what impact this would have on the analysis.

We tried to remove the Parasitic Pickup Signal by recreating the shape of this signal to be able to successfully suppress its effects. Since the shape of the Parasitic Pickup Signal was seemingly different in each of the data files this rendered it moot trying to just record a few samples without using any photon source and subsequently removing this signal from all the other data samples. As this turned out to be something that would have to be done individually to each recorded data file, we needed a clever system to automate this procedure.

One of the attempted methods was to look at only the Pedestal Contributions (PCon) in the 50 000 waveforms since this should ideally only contain noise and the Parasitic Pickup Signal. This was done by trying to isolate the Pedestal Contributions as much as possible to minimize any signal shapes influencing the Parasitic Pickup Signal shape that needed to be subtracted.

We had a natural trigger offset in time where we had roughly 40–60 sampling points (16–30 nanoseconds) of data taking before the QRLED was triggered. This resulted in a small window which should only contain Pedestal Contributions like signal shapes. Yielding to caution, only the first 21 data sampling points were used. The amplitude of the antecedent points were first plotted in a binned histogram before it was fitted with a Gaussian to determine its mean and sigma, as seen in Figure

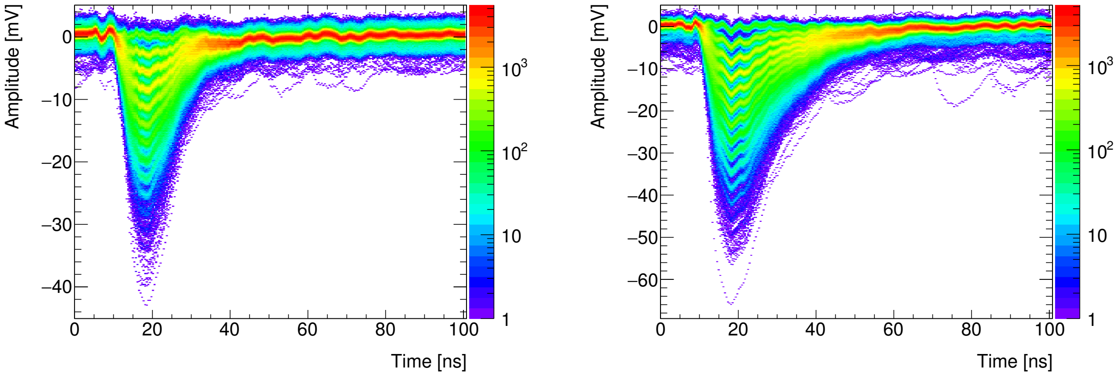

(a) S12571 010C serial number 271

(b) S12571 015C serial number 136

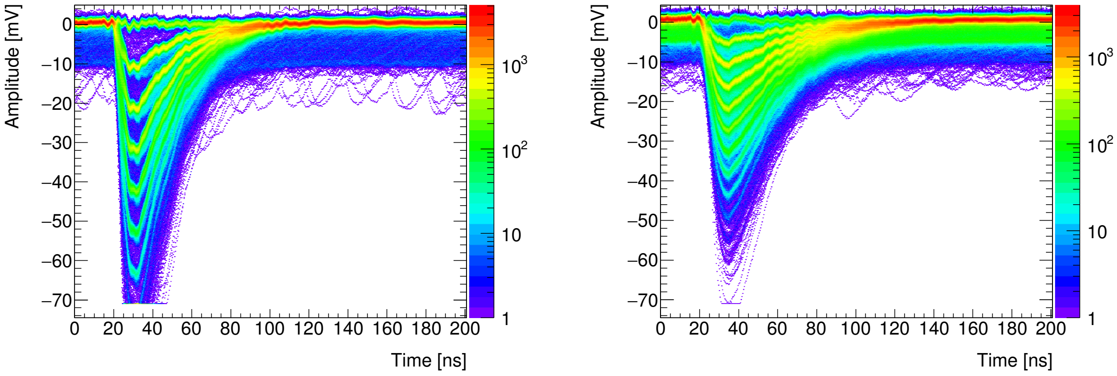

(c) S13360 1325CS serial number 10143

(d) S13360 3025cs serial number 10103

Figure 4.1: In these density plots of waveforms from the Hamamatsu detectors it is possible to see how the Parasitic Pickup Signal affected a few of the different detectors we tested. The Parasitic Pickup Signal can be seen as this wiggle that permeates the waveform, and one can clearly see that it is less pronounced in the higher gain detectors which led us to exclude the pre-amp and detectors as the culprit. The gain of these detectors go from lowest in 4.1a to highest in 4.1d

.

4.2. Using these two values we could then filter out the non-Pedestal Contributions waveforms by requiring that the average amplitude in one waveform was below $\mu+\sigma$, since anything higher than this should not be a Pedestal Contributions, and that the amplitude in each data sampling point in the waveform was below $\mu+3\times\sigma$, this to take care of sudden and short spikes in the data that the first condition would ignore. Plotting the remaining waveforms yield what you see in Figure 4.3a.

Using the waveforms which only contain the Parasitic Pickup Signal and Pedestal Contributions we can then make an average waveform signal shape of these by simply averaging the amplitude in each data sampling point, and then subtracting this signal shape from all other waveforms, as seen in Figure 4.3. This method also had the added benefit of removing the DC voltage offset induced in the measurements, which shifted the pedestals mean from 0 to an either positive or negative value depending on the detector.

While this successfully removed the effects of the Parasitic Pickup Signal which made some of the further analyses easier, especially when it came to the determination of the integration window, we decided to do all of the analyses utilizing the subtracted and the non-subtracted Parasitic Pickup Signal waveforms. This was to further make sure that we did not introduce any major impacting bias into the results by removing it. At all points in the analysis process we checked that both

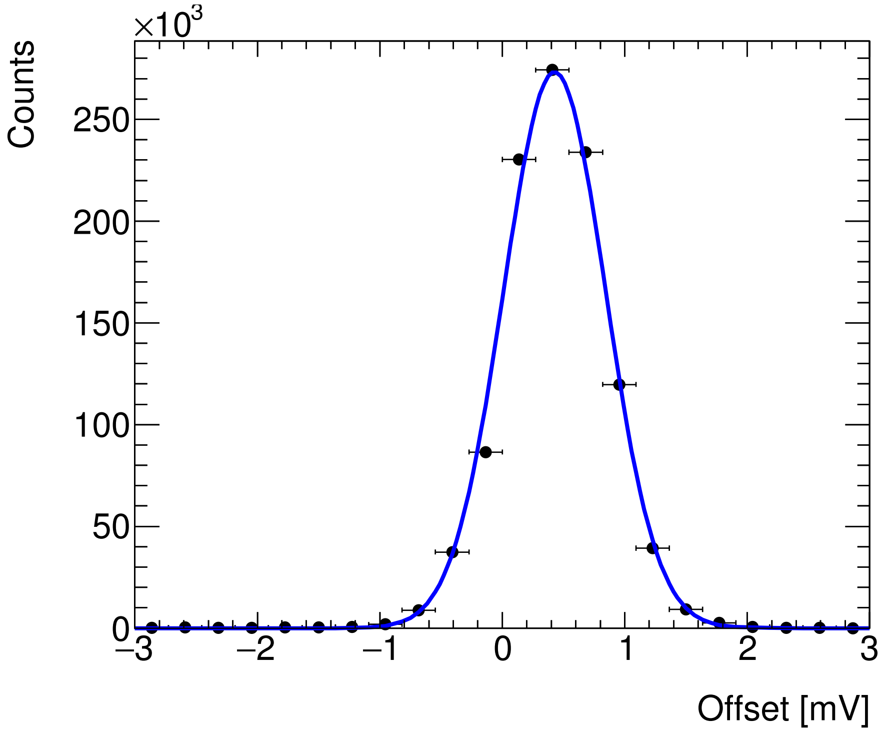

(a) Fit on the amplitudes of the first 21 data sampling points.

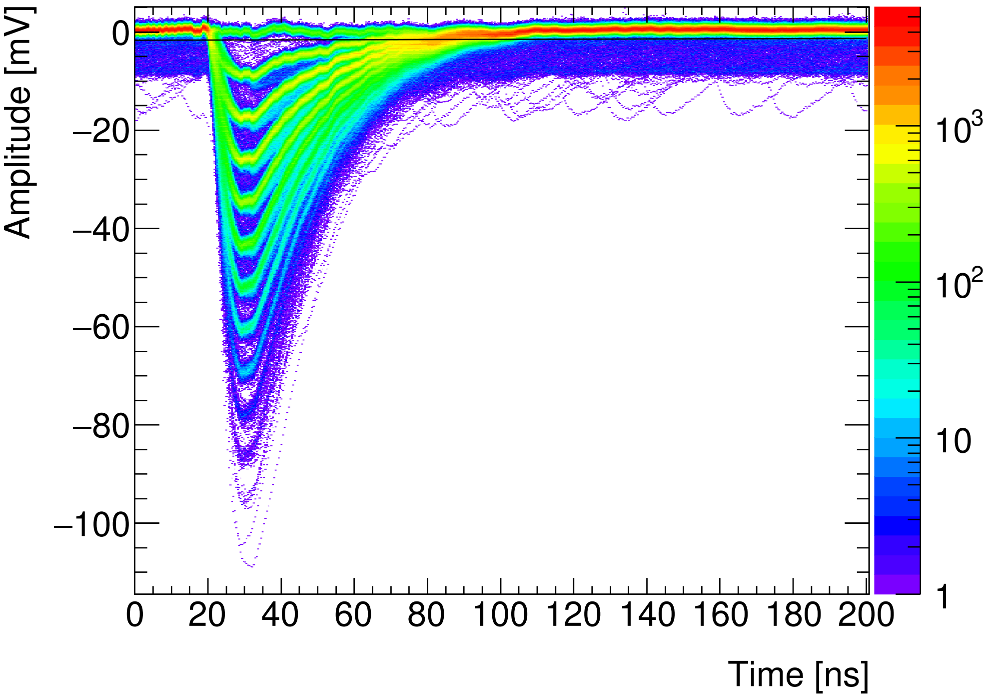

(b) Waveform density distribution with a black line overlain, waveforms contained below this line were considered to be Pedestal Contributions.

Figure 4.2: Gaussian fit on a binned histogram which contains all amplitudes for the first 21 data sampling points in each Pedestal Contributions waveform can be seen in 4.2a. The vertical black line seen in 4.2b near $-2\,\mathrm{mV}$ shows the amplitude which corresponds to the negative of $\mu + 2 \times \sigma$ which is extracted from the Gaussian fit. Waveforms are recorded by the Hamamatsu detector S13360 1325CS serial number 10143.

methods yielded similar results and were not skewing one way or another.

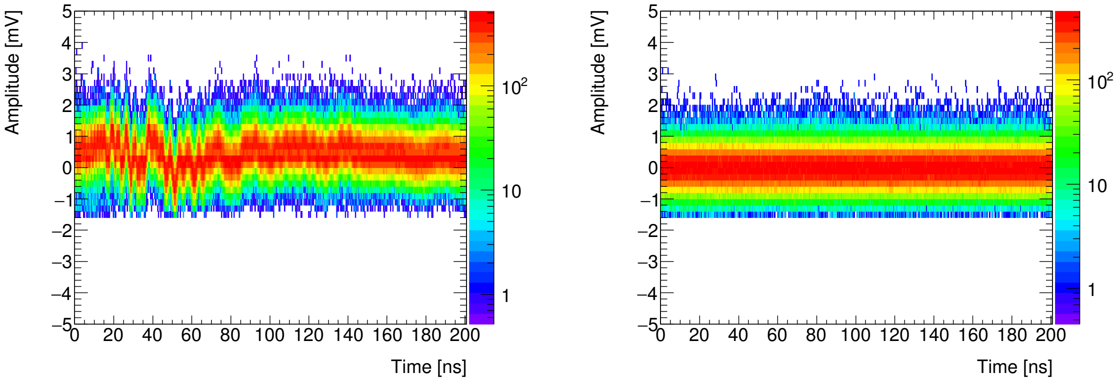

(a) Pedestal waveforms with Parasitic Pickup Signal visible.

(b) Pedestal waveforms with Parasitic Pickup Signal removed.

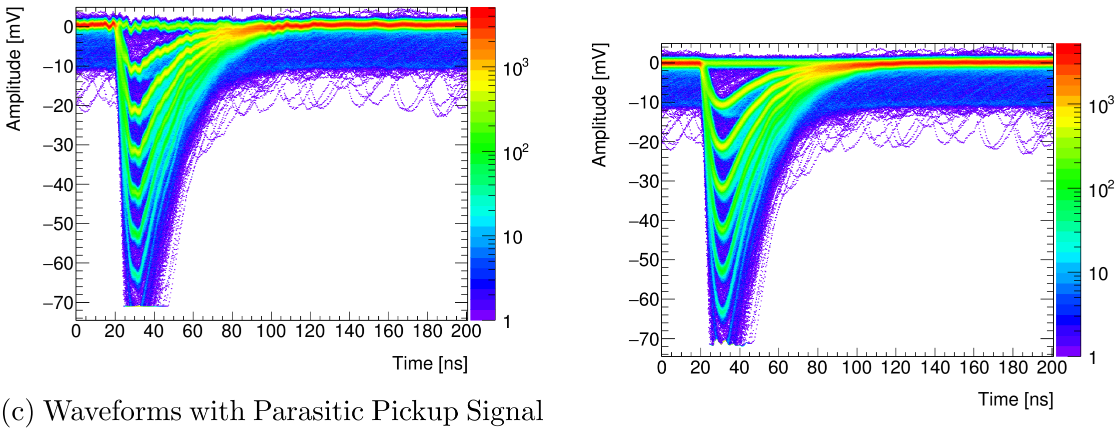

(c) Waveforms with Parasitic Pickup Signal visible.

(d) Parasitic Pickup Signal subtracted.

Figure 4.3: In these density plots one can see the Parasitic Pickup Signal along with the Pedestal Contributions in 4.3a, while you can see the result after averaging and subtracting in 4.3b. The before and after subtraction can respectively be seen in 4.3c and 4.3d. These are all of the Hamamatsu detector S13360 1325cs serial number 10143.

4.3 Integration Window

Since we have well over 2×10^9 waveforms it would be impractical to manually inspect each waveform by eye to determine the points where we should start and stop integration. As such it was deemed necessary to develop a small and robust algorithm to determine these points. The way that this was performed relies heavily on the method used to remove the Parasitic Pickup Signal. Utilizing the mean and the sigma determined from that method we could find both the point at which the waveforms had a rising pulse and at which point it had then receded.

To determine the start point of integration we went through each of the waveforms one by one and extracted a integration window starting value for each of them. This was done by starting at the point where the 50 000 waveforms had a global maximum amplitude and go backwards through the data sampling points until the amplitude returned to the fit determined mean value. For Parasitic Pickup Signal subtracted the mean was set to 0 since this method removes the voltage offset induced by the signal. The reason we did not use the maximum value for each individual waveform is to minimize computational time, and to also remove the effect of cases where severe afterpulsing occurred. These could potentially yield a higher amplitude than the triggered peak itself.

The sampling point corresponding to where the signal had started to rise would be filled into a histogram, and from all of the values we determined a mean integration starting point, while also having the individually starting points for the waveforms, as seen in Figure 4.5.

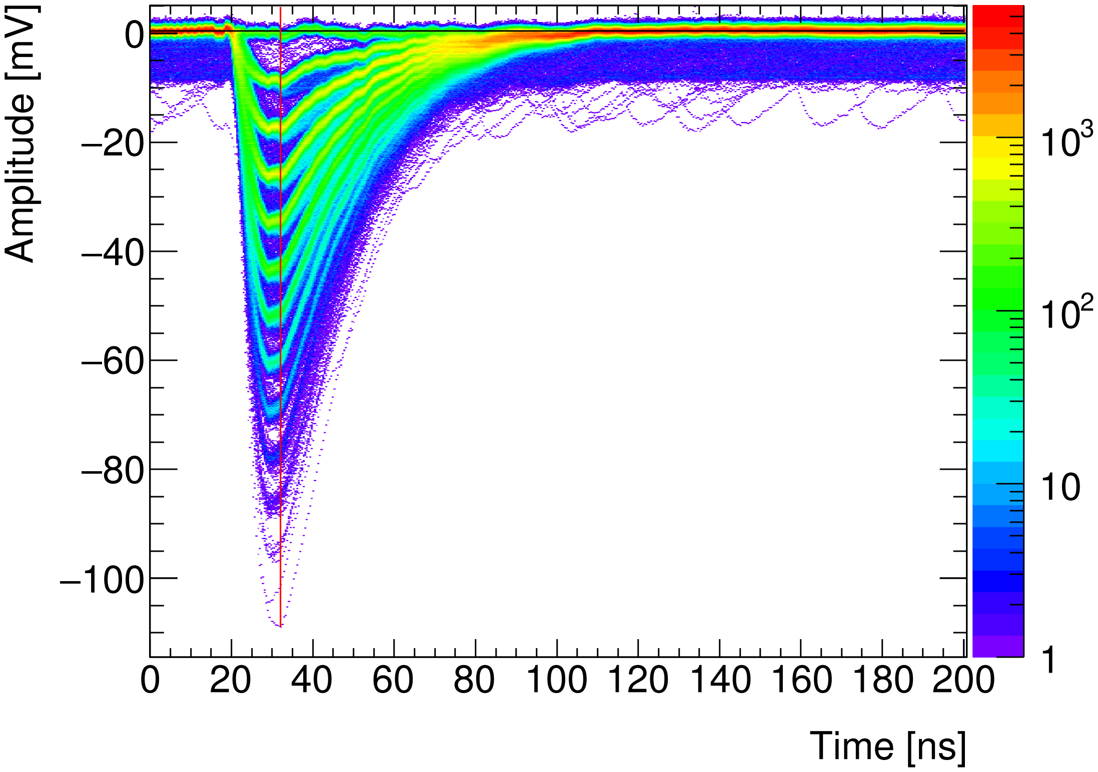

Figure 4.4: The horizontal red line corresponds to the peak position of the waveform with the highest amplitude, while the vertical black line near 0 shows the DC offset determined through the Parasitic Pickup Signal subtraction technique. Waveforms recorded by the Hamamatsu detector S13360 1325CS serial number 10143.

We determined endpoints in a similar fashion, though here the individually recorded endpoints can be affected by afterpulsing. Which would push the determined integration end point towards a higher value since it would delay the receding of the signal pulse. As this could be a contributing factor to systematic changes to the gain, it was decided we should compare different integration windows to see what the effect may be. Further analysis on the effects of this chosen starting point, and variations on it, showed that using the mode of the starting and end point distributions yielded a higher rate of successful fits on the p.e. spectra. Every mention of mean start or end point refers to the mode of the distributions shown in Figure 4.5 unless it is stated otherwise. The main reasoning behind this choice was the fact that some of the start and end point distributions showed several discrete peaks instead of a singular continuous distribution. This would shift the mean value in a way that could potentially end in the integration yielding a smaller value of the charge.

Several integration windows were established and compared:

Mean Start Mean End (MSME) All waveforms are integrated from the bin corresponding with the mode observed in the histogram seen in Figure 4.5a and 4.5b. Until the bin corresponding to the mode in the histogram shown in Figure 4.5c and 4.5d. These histograms are determined separately for each data sample containing 50 000 waveforms.

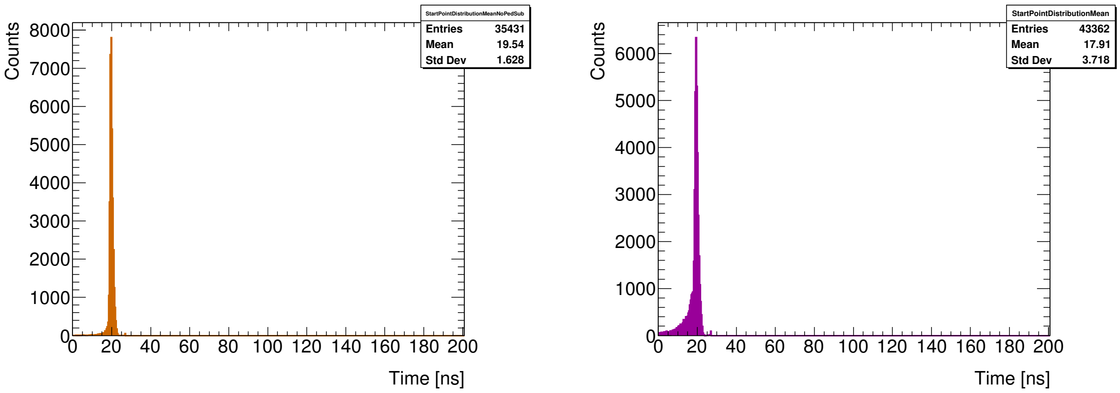

(a) Start point distribution of non-Pedestal Contributions waveforms without Parasitic Pickup Signal subtracted.

(b) Start point distribution of non-Pedestal Contributions waveforms with Parasitic Pickup Signal subtracted.

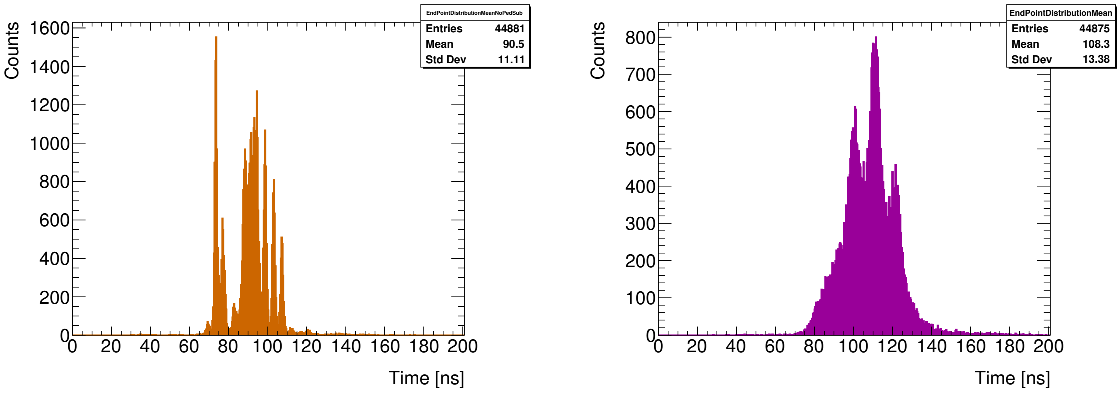

(c) End point distribution of non-Pedestal Contributions waveforms without Parasitic Pickup Signal subtracted.

(d) End point distribution of non-Pedestal Contributions waveforms with Parasitic Pickup Signal subtracted.

Figure 4.5: We can in 4.5c see that there are several distinctive peaks, while the majority of these peaks have merged in 4.5d. This is due to the fact that the Parasitic Pickup Signal introduce sever wiggles in the waveforms which shifts the position in time at for when they have receded. As one can see this effect is negligible in the determination of the start point. These are all of the Hamamatsu detector S13360 1325cs serial number 10143.

Variable Start Mean End (VSME) All waveforms are integrated from its own waveform specific determined starting point as seen in Figure 4.5a and 4.5b, up to the bin corresponding to the mode in a histogram similar to the bottom two pictures in Figure 4.5.

Mean Start Variable End (MSVE) All waveforms are integrated from the bin corresponding with the mode observed in the histogram. Until its own waveform specific determined end point as seen in Figure 4.5c and 4.5d.

Variable Start Variable End (VSVE) All waveforms are integrated from its own waveform specific determined starting point, until its own waveform specific determined end point.

These different determination methods were tested for the integration windows for both Parasitic Pickup Signal subtracted and non-subtracted waveforms. We also changed where these values occurred by recording them not only when they crossed the μ, but also $\mu + \sigma$ and $\mu - \sigma$. Here the μ is set to 0 for Parasitic Pickup Signal subtracted waveforms. One can see an example of this in Figure 4.6. We then fitted these to determine the gain as well as the σ, χ^2, and the relative standard error [12] for the different integration windows.

We found that MSME integration window showed the most stable performance yielding the lowest systematic uncertainty. AS such it was chosen as our default integration window. While no in-depth study was carried out to show this (mainly due to not having dedicated data samples in which one could do it), the comparison studies of the different windows indicate a sharper photoelectron peak (p.e. peak) for this method compared to the MSVE method which would include any afterpulses in its integration window. This lead us to the conclusion that MSME would have the most robust performance, as it would set the same integration window for all waveforms, although it would mean that waveforms with afterpulses are only partially integrated.

Since the choice of integration technique fell upon the Composite Simpson's rule which requires that you have an even number of partitions which are integrated over; if the integration window was found to have an odd number of bins there was added one extra bin to the determined endpoint. The choice of adding instead of subtracting is due to the fact that we would rather integrate too much of the signal than too little, though, as can be seen in the comparison of integration windows, this should have a negligible effect.

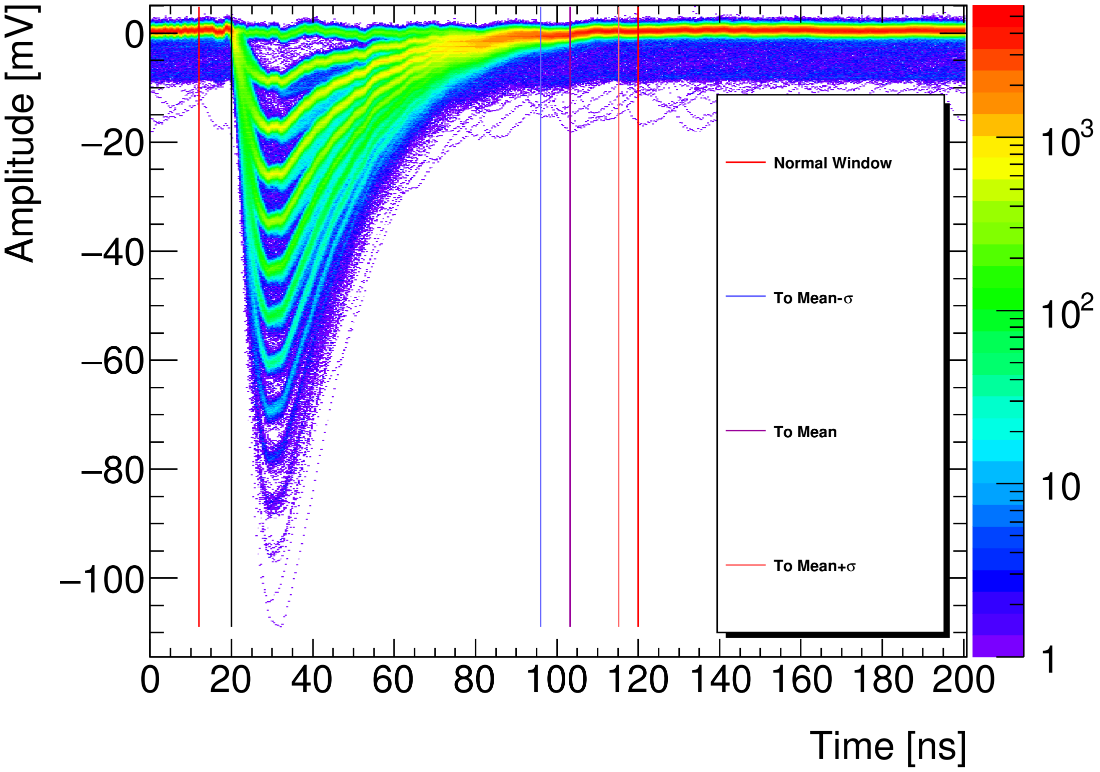

Figure 4.6: The black vertical line seen at 20ns corresponds to the mean starting value determined by the signal receding to its mean value, the ones determined by the other methods only differ by 0-1ns as such it would not be visible. The light blue, magenta and light red vertical lines seen on the right hand side corresponds to the mean of the endpoints determined with the three different receding conditions. The two red lines referred to as Normal Window corresponds to an early integration adaption used before the automatic integration window method was developed.

Pedestal Contributions waveforms were not included to contribute to this determination of the integration windows by requiring that the average amplitude of the waveform was at least $\mu + 2 \times \sigma$, also here the μ is set to 0 for Parasitic Pickup Signal subtracted waveforms. Since the Pedestal Contributions were not included we used the determined MSME for these waveforms.

4.4 Determination of Photoelectron Spectra

Since we were using an oscilloscope for the data collection, all data was taken as waveforms that were stored as binary files. These only contained the number of waveforms recorded, the number of data points taken, the width of each data point in time; followed by amplitudes of each data point. Due to storage capacity issues we went from storing the data as doubles into utilizing shorts. This was in order to further reduce the files size by factor four. However the shorts had to be converted into doubles again in the scripts using metadata that was recorded from the oscilloscope. This metadata contained the offset in millivolts and the corresponding conversion factors to go from a short to the recorded amplitude in mV.

As we did not have a DAQ with an integrated charge integration, we had to carry out the integration ourselves. To determine the optimal technique for integrating the waveforms, several different methods were tested. As we had a fixed partition for all the data points we tried Riemann integration, Rectangle, Trapezoidal, Simpson's, Simpson's 3/8, Alternative extended Simpson's, and Composite Simpson's rule.

The methods were tested by integrating a small sample of files from each of the detectors where we knew we had stable and optimal operational conditions, i.e. temperature and bias voltage, such as not to distort the signals. These were also carried out with the different integration windows discussed. These integrated waveforms result in a p.e. peak spectrum which we can fit to extract the gain, and its error, and use these values as a measure of how well the individual techniques performed. We also tried integrating only from the rise of the signal up till the maximum amplitude, but since this method did not show any promising results it was not pursued any further.

The tests showed that the Composite Simpson's rule yielded the least artifacts on the p.e. peak distributions which made fitting of the spectra easier and more successful. The gain determined from these spectra yielded the least variance in its distributions and was especially proficient in producing more defined peaks in the high noise samples. As such it was the one selected and was subsequently applied to all of the data in this analysis.

4.5 Fitting routine

The fitting routine that was used in this analysis to determine the gain, was initially developed by Justas Zalieckas, using the available RooFit classes for ROOT. Changes were made to it in consort with him due to several different bugs which were discovered during the work carried out within this thesis. Parameters and other adjustable variables was changed on a case by case basis, although it was initially aimed to finding a set of variables that would be applicable to all data files for a certain detector model due to the data volume. Though some tweaking were necessary especially for the very low/high temperature runs, as well as some low/high bias runs.

The p.e. spectra were fitted using the likelihood function in Eq. 4.1.

$$L = \prod_{i=1}^{50000} f_{sig} F_{sig}(v^i) + (1 - f_{sig}) F_{bkg}(v^i) \tag{4.1}$$

$$F_{sig}(v^i) = f_{ped} G_{ped}(v^i) + \sum_{j=1}^{n-1} f_j G_j(v^i) + (1 - f_{ped} - \sum_{j=1}^{n-1} f_j) G_n(v^i) \tag{4.2}$$

$$G_\alpha(v^i) = \frac{1}{\sigma_\alpha \sqrt{2\pi}} \exp\left[-\frac{(v^i - v_0)^2}{2\sigma_\alpha^2} \right] \tag{4.3}$$

f_{sig} = Signal fraction of model
n = Maximum number of p.e. peaks to be fit
G_α = Gaussian α
f_α = Fraction of contributing Gaussian α
σ_α = Width of Gaussian α
v^i = Measured voltage amplitude
v_0 = Fitted mean

The signal model consisted of a Probability Distribution Function (PDF) where we had several Gaussian functions corresponding to the number of p.e. peaks that we wished to fit, and one additional Gaussian used to model the pedestal. The background PDF is parameterized by a sensitive nonlinear iterative peak (SNIP) clipping algorithm [13], [14] that is implemented in the ROOT TSpectrum class. The TSpectrum also has a one-dimensional peak search algorithm with advanced spectra processing functions which were used to determining how many p.e. peaks we had in the spectra, and their respective position [15], [16]. This search function has two parameters which influence how it finds p.e. peaks by scanning the integrated spectrums over several attempts. The first of which is called Sigma and its value influences how close two peaks are allowed to be. If two peaks are found within this Sigma distance, the peak with the highest amplitude is picked. The second term is called Threshold and its value corresponds to a percentage of the maximum amplitude of the found peaks, and subsequent scans afterwards ignores peaks found with an amplitude below this value. The positions which TSpectrum locates are then used to define the analytic peak model. The parameters of the Gaussian functions are not constrained in the fit and this also applies to the fractions used.

We carried out binned fits of the p.e. spectra, where we required that the spectrum has a visible pedestal as well as at least two distinctive p.e. peaks. This is due to the fact that determining the gain by the distance of the first two p.e. peaks yield a more reliable result than using the distance between the pedestal and the first p.e. peaks, since this distance is often smaller. Tests were also done on this, as well as measuring the distance between second and third p.e. peak, and the distance between third and first divided by two, to make certain that they all agreed with each other. A typical fit of a p.e. spectrum for the Hamamatsu detectors can be seen in Figure 4.7 and the gain determined with these different peaks shows similar results as the legend reflects.

The statistical error on the gain is obtained by the uncertainties of the peak positions of both p.e. peaks used in the gain measurement.

$$\sigma_{gain} = \sqrt{\sigma_1^2 + \sigma_2^2} \tag{4.4}$$

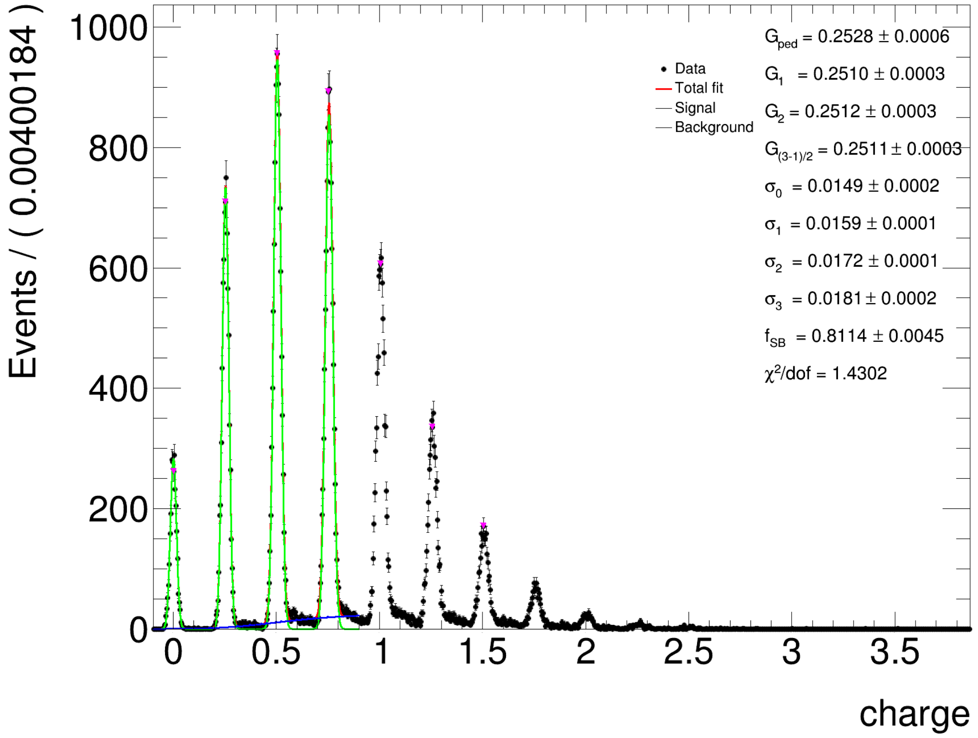

Figure 4.7: Here one can see a typical fit of the pedestal and the first three p.e. peaks. The charge here is in arbitrary units. All measurements are recorded by the Hamamatsu detector S13360 1325CS serial number 10143.

This fitting routine was even further modified to be used in the automatic determination of bin sizes used for each set of 50 000 waveforms. This method of determining the fixed bin numbers per p.e. peak is discussed in section 4.6.

4.6 Issues with integration

Since we were doing binned fits to determine the gain as well as using the TSpectrum class for ROOT to determine the peak position and background estimation, the choice of a suitable bin size was a crucial component. Having too coarse bin widths yielded rather poor separation of the p.e. peaks and therefore a poor gain determination, and having too fine a bin size resulted in the TSpectrum failing to find the position of the p.e. peaks, and instead finding several peaks within each. To combat these issues a method to automatically determine the optimal bin width for each spectrum was developed where we required that each p.e. peak had as close to a fixed pre-determined number of bins to it as possible. This means that the bin sizes were individual component for each spectrum, rather than varying the bin width throughout a single spectrum. Typical number of bins per peak were roughly 10 for Hamamatsu, while closer to 5 for KETEK and CPTA.

Several different ways were tested before it fell on the choice of using a coarse bin width at first. We can then apply a modified version of the gain fitting routine to extract the position and sigma of each p.e. peak. These values were used to extract the necessary bin width to enable the pre-selected number of fixed bins within $\pm 1\sigma$ of the peak position. The initial choice of the number used for this coarse bin determination varied for the detectors used and were discovered through trial and error earlier during the software development. The number of bins within $\pm 1\sigma$ of the peak positions were determined through testing different values, and fitting the resulting p.e. spectra with the gain routine to compare the resulting χ^2 and relative errors for different temperatures and bias voltages as well as stabilization runs. This was done for each detector until we found a fixed bin number that yielded all around good fits. Typically this value was the same for all detectors by a specific manufacturer, but there were also a few odd ones out. There was also carried out in-depth studies to estimate the effect of changing the determined bin width by a factor ten up or down. We looked at the gain, sigma, relative error, and the χ^2 distributions for different stability runs and detectors. These tests showed that there was little to no impact on the gain or sigma determined, and therefore also the relative error, while the χ^2 distribution suffered once the bin width got too large, while TSpectrum fails finding the peaks if the bin width was set too low. As we were only using fits which yielded a χ^2 of below 5 for the Hamamatsu detectors and below 15 for KETEK and CPTA, the importance of finding a middle ground between the two effects observed was crucial.

Unfortunately most of the CPTA data had so poorly defined waveform peaks at non-optimal bias voltage and temperatures that integration yielded non-usable results, with all peaks being smeared into one large Guassian. Only after several iterations of trying to improve the integration technique, window and bin widths did we get fitable p.e. peak distributions. Aside from this, due to data storage issues we were forced to maintain a small sampling window on the oscilloscope, which unfortunately did not contain the full waveform of detectors from both CPTA and KETEK, as can be seen in the waveform density plots in Figure 4.8. This would imply that if we were to use the integrated spectrum we would only be getting an incalculable partial charge, which would yield varying results. As such most of the CPTA and KETEK data was analyzed using the maximum amplitude distributions, which in most cases also simplified the issues we had with TSpectrum being unable to locate the p.e. peaks for these detectors.

Note that neither the improved integration methods nor the maximum amplitude method were able to produce distinctive p.e. peaks for all of the CPTA and KETEK detectors. It proved especially difficult at non-optimal bias voltages or temperature. As such we did not get as many samples as we'd like in the gain determination in the bias scans nor in the subsequent stabilization runs.

4.7 Determination of dV/dT

One of the prime characteristics of a SiPM is that the gain varies with temperature. This occurs since the breakdown voltage has a heavy dependence on the temperature while the capacitance of the pixels should be moderately affected, which the measurements seems to confirm. It can easily be seen from Eq. 3.2 that a change in these two variables would in turn influence the gain.

So in order to successfully stabilize the gain of a SiPM one first needs to accurately gauge the temperature dependence of the breakdown voltage. This was achieved through measurements done of the gain at several different temperatures and applied bias voltages. This was carried out using what we refer to as bias scans, where we typically scanned over a symmetric $\pm 5\,\mathrm{V}$ region around the recommended operational bias voltage for the current temperature selected. Most of these scans were done in steps of $0.1\,\mathrm{V}$ where we recorded 50 000 waveforms at each step, though there were cases where the step size were increased and the scanning region was wider. The light intensity of the QRLED was adjusted down according to the increase in voltage, this is to not oversaturate the detectors and to try to enable the same number of p.e. peaks observed in each scanned voltage point and temperature. The temperature was increased in $5\,^\circ\mathrm{C}$ steps, and we typically scanned

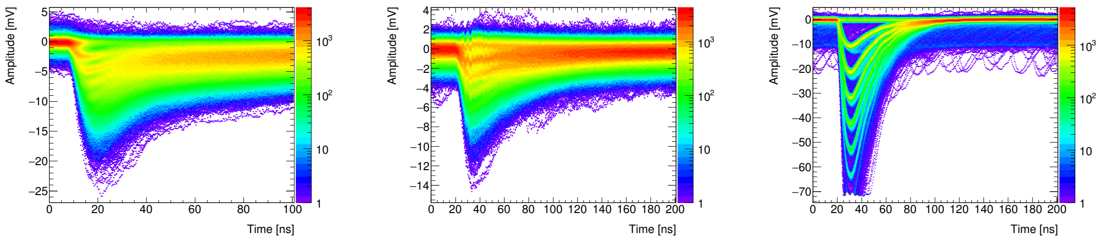

(a) CPTA have fairly smeared signals, but can see distinctive waveform densities.

(b) KETEK have also fairly smeared signals, but can see distinctive waveform densities.

(c) From the Hamamatsu detectors we can observe distinctive well separated waveform densities.

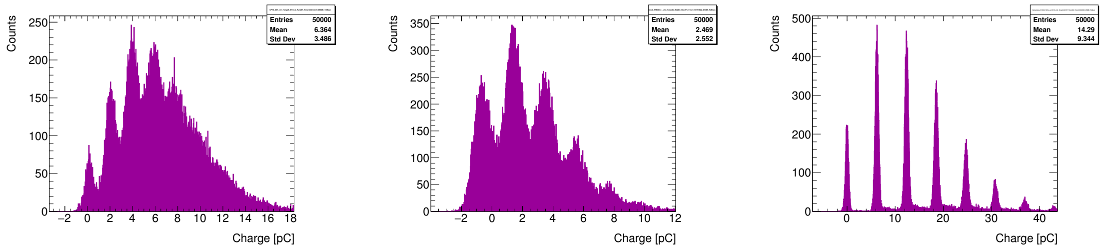

(d) Earlier adaption of integration yielded no distinctive p.e. peaks.

(e) Integrated spectrum for KETEK, with distinctive peaks.

(f) Integrated spectrum for Hamamtsu, with well separated distinctive peaks.

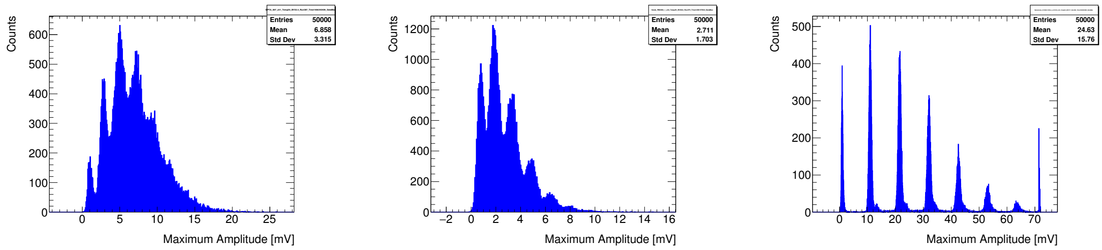

(g) Maximum amplitude spectrum of CPTA detector, which was initially the only way to determine gain.

(h) Maximum amplitude spectrum of KETEK detector show similar structure as the integrated spectrum.

(i) Maximum amplitude spectrum of Hamamtsu detector show similar structure as the integrated spectrum.

Figure 4.8: The detectors used in these plots are CPTA serial number 857, KETEK PM33 50 serial number 1 and Hamamatsu S13360 1325CS serial number 10143. Data taken under detectors nominal operational bias voltage while the temperature was 25 °C. Only after several iterations of the analysis software were we able to achieve distinctive p.e. peaks for CPTA and KETEK. The far right effect seen in 4.8i arises from the fact that the maximum amplitude generated was larger than the recording window and was therefore clipped.

over the temperature region of 1–50 °C. Though for some detectors this was done in a smaller temperature range due to observed effects and the step sizes were then correspondingly changed.

These different scans yield the dependence of gain-versus-bias voltage (dG/dV) as seen in Figure 4.9, and gain-versus-temperature (dG/dT) as seen in Figure 4.10. The relation of dV/dT, which is what we wish to obtain, can be acquired using several methods. The method which were used is discussed towards the end of this section. Before this we will discuss other methods which has certain drawbacks.

While the dV/dT could be calculated from a linear fit to the breakdown voltage as a function of the temperature distribution, another more accurate method is to combine the measurements of dG/dV and dG/dT. Then one can calculate dV/dT as seen in Eq. 4.5.

$$dV/dT = -\frac{dG/dT}{dG/dV} \tag{4.5}$$

However, this way of determining the dV/dT yields values which are accurate only at the nominal temperature, and since the goal is to stabilize the gain over what would be considered normal operational conditions, we need a third method. One can for instance see that the operational ambient temperatures of the ATLAS detector at the LHC is between 17–25 °C according to an analysis performed [17]. While in most other cases this would be near room temperature, which should fluctuate between 20–30 °C. As such we have had most of the focus on achieving stable gain in this temperature range, although we still analyzed the data in the full scanning range described, in order to ascertain its full potential.

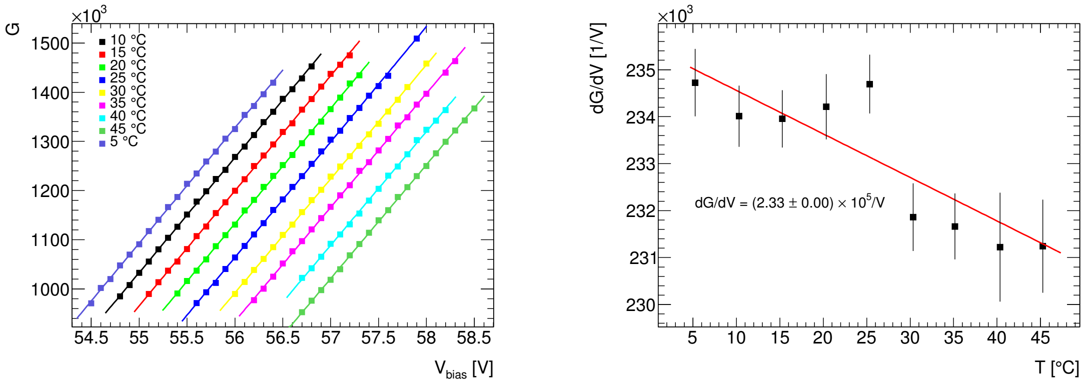

(a) Measurements of gain-versus-bias voltage (dG/dV) for fixed temperatures.

(b) Plot shows the obtained values of the dG/dV versus fixed temperature.

Figure 4.9: All measurements are recorded by the Hamamatsu detector S13360 1325CS serial number 10144.

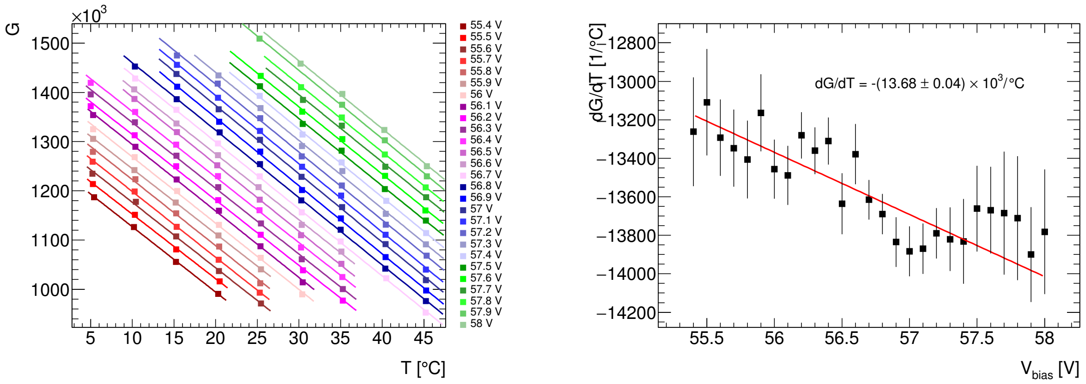

(a) Measurements of gain-versus-temperature (dG/dT) for fixed bias.

(b) Plot shows the obtained values of the dG/dT versus fixed bias voltage.

Figure 4.10: All measurements are recorded by the Hamamatsu detector S13360 1325CS serial number 10144.

The third method involves dividing a set of dG/dT slopes by a dG/dV for a given temperature, this should give us a sample of different dV/dT values that correspond to each temperature point that we scanned. We can then estimate the dV/dT using all the data taken from all temperature points measured. Each sample is averaged by first assigning a weight for each dV/dT, this weight is defined as $w_i = \frac{1}{\delta(dV/dT)^2}$. Plotting these values should give us a distribution where each point represents the weighted mean of the corresponding temperature scanned samples. The error that has been assigned to each value comes from the variance in the weighted mean sample. The expected $\langle \mathrm{dV/dT} \rangle$ is estimated through modeling of the distribution with a uniform function, and its value and error is given by the fit parameters, an example of this can be seen in Figure 4.11.

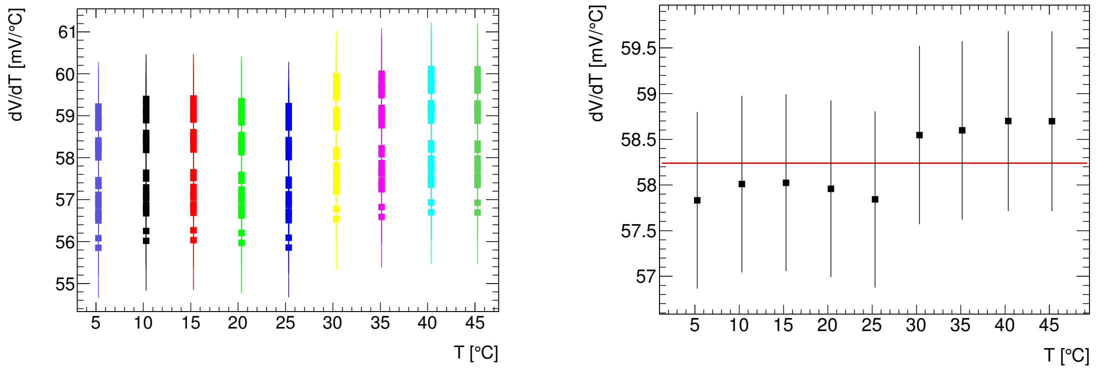

(a) Shows the measured dV/dT as a function of temperature.

(b) Weighted average distribution of dV/dT as a function of temperature.

Figure 4.11: All measurements are recorded by the Hamamatsu detector S13360 1325CS serial number 10144. the uniform fit used to determine the dV/dT can be seen in plot 4.11b.

The error on the bias voltage measured by the Keithley multimeter is neglected in all fits where it would be applicable, as its value is given by $\delta V_{bias} \approx 0.001\%$ from the data sheet for the range in which we are measuring, which is far smaller than any other source of error which we have.

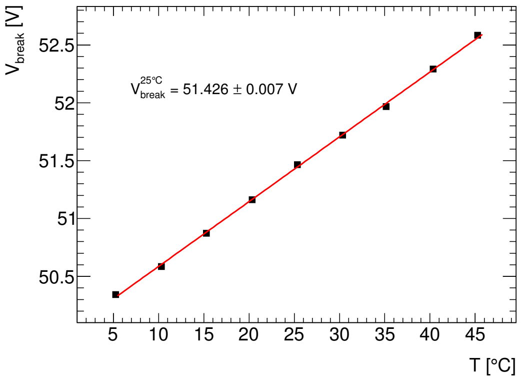

Figure 4.12: The fits yields a breakdown voltage of $51.426 \pm 0.007V$ while official Hamamatsu data sheets show a value of $53 \pm 5V$ at the same temperature. All measurements are recorded by the Hamamatsu detector S13360 1325CS serial number 10144.

4.7.1 Analytical description of V_{bias} versus Temperature

The analytical description used to determine the V_{bias} versus temperature dependence can be estimated through individually considering the gain changes with respect to temperature and bias voltage, this is given by Eq. 4.6.

$$dG(V,T) = \frac{\partial G(V,T)}{\partial T} \cdot dT + \frac{\partial G(V,T)}{\partial V} \cdot dV \tag{4.6}$$

For a constant gain $dG = 0$, as we are trying to achieve in this analysis, it yields the following Eq. 4.7.

$$dV/dT = \frac{\partial G(V,T)/\partial T}{\partial G(V,T)/\partial V} \tag{4.7}$$

As can be seen in Figure 4.10 and 4.9, we observe linear dependencies of dG/dT and dG/dV, and those distributions are modeled with first-order polynomials which yield the following system of differential equations seen in Eq. 4.8.

$$\begin{gathered} \frac{\partial G(V,T)}{\partial T} = a + b \cdot V \\ \\ \frac{\partial G(V,T)}{\partial V} = c + d \cdot T \end{gathered} \tag{4.8}$$

Where the constants a and c corresponds to the offset, while b and d is the slope parameter and all of these values are determined from the fits shown in section 4.7. The analytical solution where $b \neq 0$ and $d \neq 0$ is shown in Eq. 4.9, where the C corresponds to the integration constant.

$$V(T) = -\frac{a}{b} + \frac{C}{(c + d \cdot T)^{\frac{b}{d}}} \tag{4.9}$$

A typical plot of this equation for the Hamamatsu detectors can be seen in Figure 4.13.

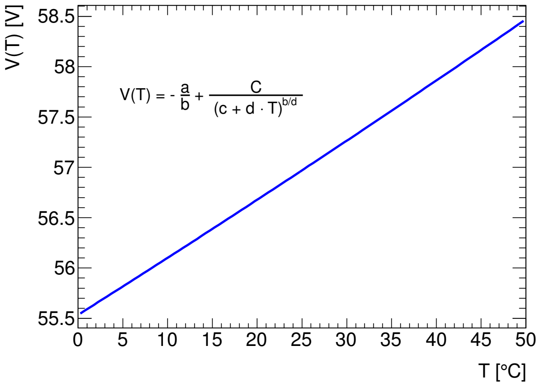

Figure 4.13: The fits yields a correction factor of $58.24 \pm 0.32 mV/$°C while official Hamamatsu data sheets show a value of $54mV/$°C at the recommended operational voltage. All measurements are recorded by the Hamamatsu detector S13360 1325CS serial number 10144.

Chapter 5

Silicon Photomultiplier Results

All fits have been visually inspected to improve the fit parameters over as large a range of temperatures and bias voltages as possible. Some of the features seen in the different plots stem from the fact that the fitting routine either fails to find peaks or it does not fit the correct peaks. This tends to happen at certain thresholds and is not necessarily due to properties of the detector itself.

5.1 Bias Scans

The prior knowledge of the relation voltage-versus-temperature (dV/dT), known as a compensation constant, is necessary to carry out the gain stabilization. Therefore, we characterize each SiPM by first determining the temperature dependence of the gain and then its bias voltage dependence. The method to which we have done this is explained in-depth in section 4.7. The scans were carried out in the climate chamber where we had a black box filled with the detectors, sensors and preamplifiers. Table 5.1 show all the results from the bias scans for all the different detectors tested, the LCT4 detectors had already been characterized from a previous run and was not tested along with the new setup.

5.1.1 Hamamatsu

The Hamamatsu detectors originally had another step of 1 °C, but the climate chamber does not seem to be able to successfully stabilize this temperature point. It fluctuates between 0–2 °C quite rapidly leading to inconclusive results, as such the samples that were done at this temperature has not been included in these studies. Bias scans for the cluster containing the four S13360 detectors did not have proper bias voltages set for the 40 °C as such the data taken for this temperature is not usable and has been disregarded. Aside from these facts all of the Hamamatsu detectors have very stable conditions and integrating their waveforms yield well-defined p.e. spectra from which it is fairly straight forward to extract the gain. One can observe the different distributions measured by the A1 20 µm detector in Figure 5.1 while the rest can be found in appendix A.

Table 5.1: This table list all the different results obtained through the bias scan characterization process for the different detectors. We had already done a scan of the LCT4 detectors during a previous run and the values listed are from this run.

Type	**Model**	**Serial#**	**Pixel Pitch** [μm]	**Ch #**	**Temperature range** [°C]	dG/dV [$10^5\mathrm{V}^{-1}$]	dG/dT [$10^3{}^\circ\mathrm{C}^{-1}$]	dV/dT [mV]	$V_{break}^{25\,^\circ\mathrm{C}}$
					Hamamatsu				
A	1		20	1	2–48 °C	42.59 ± 0.02	-254.72 ± 0.37	59.69 ± 0.37	64.514 ± 0.004
A	2		20	2	2–48 °C	36.32 ± 0.01	-218.30 ± 0.32	59.83 ± 0.38	64.529 ± 0.004
A	1		15	3	2–48 °C	35.13 ± 0.02	-206.38 ± 0.35	59.06 ± 0.42	64.612 ± 0.004
A	2		15	4	2–48 °C	35.08 ± 0.02	-207.07 ± 0.33	59.23 ± 0.30	64.530 ± 0.004
B	1		20	1	5–45 °C	43.24 ± 0.02	-248.68 ± 0.40	56.88 ± 0.51	71.161 ± 0.004
B	2		20	2	5–45 °C	36.69 ± 0.02	-215.68 ± 0.38	57.90 ± 0.64	71.254 ± 0.004
B	1		15	3	5–45 °C	32.99 ± 0.02	-186.38 ± 0.32	57.10 ± 0.45	71.397 ± 0.004
B	2		15	4	5–45 °C	33.31 ± 0.02	-186.31 ± 0.30	56.46 ± 0.60	71.208 ± 0.004
S13360	1325CS	10143	25	1	5–45 °C	55.18 ± 0.03	-310.68 ± 0.59	55.80 ± 0.29	51.440 ± 0.004
S13360	1325CS	10144	25	2	5–45 °C	46.36 ± 0.02	-267.63 ± 0.40	57.76 ± 0.19	51.416 ± 0.005
LCT	4	6	50		5–45 °C	109.35 ± 0.05	-577.05 ± 0.03	53.9 ± 0.5	
LCT	4	9	50		5–45 °C	108.02 ± 0.05	-562.81 ± 0.02	54.0 ± 0.7	
S12571	010C	271	10	1	5–45 °C	11.96 ± 0.01	-76.50 ± 0.11	63.99 ± 0.18	65.341 ± 0.005
S12571	010C	272	10	2	5–45 °C	10.07 ± 0.01	-65.70 ± 0.10	65.22 ± 0.18	65.370 ± 0.006
S12571	015C	136	15	3	5–45 °C	28.71 ± 0.01	-182.30 ± 0.23	63.46 ± 0.32	64.482 ± 0.005
S12571	015C	137	15	4	5–45 °C	29.38 ± 0.01	-183.73 ± 0.24	62.38 ± 0.36	64.404 ± 0.005
S13360	3025CS	10103	25	1	5–45 °C	53.52 ± 0.02	-296.10 ± 0.69	56.17 ± 0.36	52.442 ± 0.004
S13360	3025CS	10104	25	2	5–45 °C	44.82 ± 0.03	-260.39 ± 0.66	58.27 ± 0.41	51.799 ± 0.005
S13360	1325CS	10143	25	3	5–45 °C	62.53 ± 0.01	-347.20 ± 0.43	56.22 ± 0.63	51.534 ± 0.004
S13360	1325CS	10144	25	4	5–45 °C	62.26 ± 0.01	-349.13 ± 0.45	56.24 ± 0.28	51.468 ± 0.004
					KETEK				
W12	A		20	1	1–40 °C	70.15 ± 0.03	-146.20 ± 0.29	21.17 ± 0.40	26.871 ± 0.002
W12	B		20	2	1–40 °C	60.85 ± 0.02	-138.26 ± 0.23	23.02 ± 0.25	26.873 ± 0.002
PM33	50	1	50	3	1–40 °C	116.98 ± 0.14	-227.19 ± 1.26	20.43 ± 0.28	27.176 ± 0.004
PM33	50	2	50	4	1–40 °C	109.67 ± 0.16	-206.84 ± 1.37	20.45 ± 0.41	27.362 ± 0.004
PM33	50	5	50	1	1–30 °C	105.99 ± 0.17	-192.37 ± 1.43	18.74 ± 0.21	27.106 ± 0.005
PM33	50	6	50	2	1–30 °C	93.63 ± 0.14	-169.80 ± 1.08	18.84 ± 0.28	27.239 ± 0.005
PM33	50	7	50	3	1–30 °C	111.55 ± 0.21	-247.59 ± 1.65	20.94 ± 0.38	27.159 ± 0.005
PM33	50	8	50	4	1–30 °C	104.00 ± 0.18	-205.22 ± 1.48	20.00 ± 0.34	27.125 ± 0.005
					CPTA				
		857	40	1	1–45 °C	78.13 ± 0.57	-141.41 ± 4.11	19.33 ± 0.74	31.568 ± 0.015
		922	40	2	1–45 °C	163.52 ± 0.41	-413.57 ± 2.61	25.25 ± 0.51	31.362 ± 0.005
		972	40	3	1–45 °C	169.40 ± 0.52	-394.47 ± 2.72	23.95 ± 0.90	31.492 ± 0.007
		1065	40	4	1–45 °C	186.74 ± 0.41	-421.02 ± 2.42	22.67 ± 0.51	31.306 ± 0.005

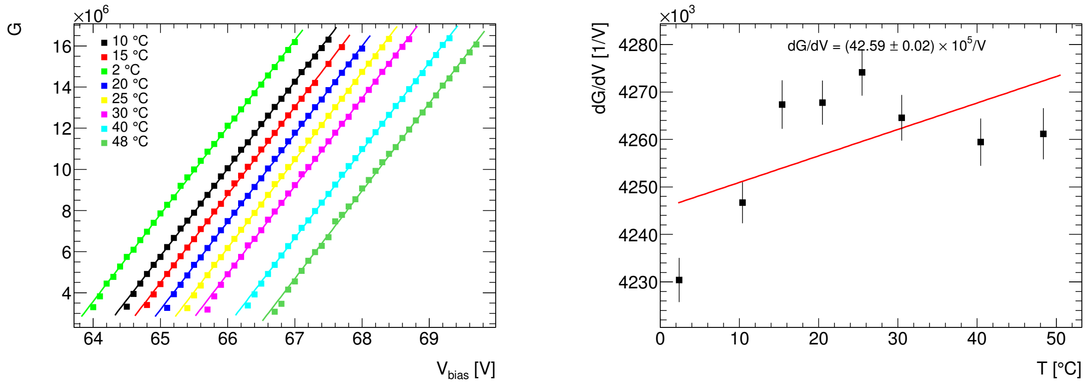

(a) Measurements of gain-versus-bias voltage (dG/dV) for fixed temperatures.

(b) Plot shows the obtained values of the dG/dV versus fixed temperature.

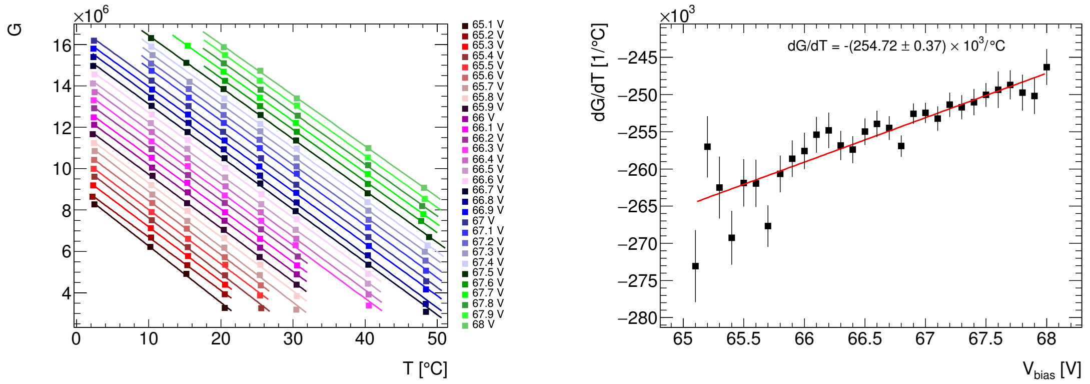

(c) Measurements of gain-versus-temperature (dG/dT) for fixed bias.

(d) Plot shows the obtained values of the dG/dT versus fixed bias voltage.

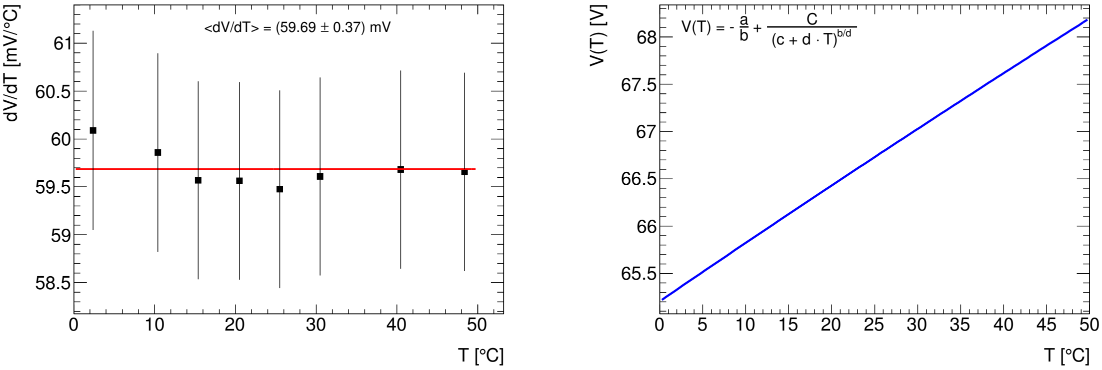

(e) Weighted average distribution of dV/dT as a function of temperature.

(f) Plot illustrates the bias voltage as a function of temperature.

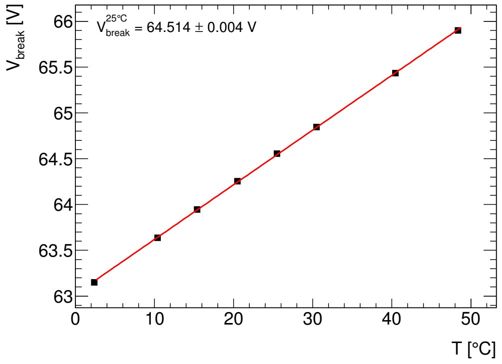

(g) Plot shows the determined breakdown voltage at different temperatures.

Figure 5.1: All measurements are taken with the Hamamatsu detector A1 20 µm.

5.1.2 KETEK

The KETEK detectors have a smaller temperature range that they were tested which is due to initial testing showing that they do not show distinctive p.e. peaks at temperatures higher than 40 °C for the W12 and 30 °C for the PM3350 detectors. However the PM3350 detectors experience quite noisy signals around and above 25 °C and as such only the data scanned below this value has been used to determine its dV/dT. All of the KETEK detectors seem to be better suited for lower temperature operations as they start to struggle once they get closer to room temperature before breaking down entirely. The available information found in presentations by KETEK seem to also indicate that they are meant for sub 15 °C temperatures [18]. When it comes to the bias scans performed there were certain aspects that made us take notice. For the first cluster of the two W12 and two PM3350 run we had several scans which showed data that was not useful in the determination of a proper dV/dT value needed for stabilization of the gain.

Lending credence to the idea that these detectors are indeed meant for lower temperature operations, which both the data and the presentations seem to suggest, we have chosen to neglect the scans where the impact of the higher temperature skews the data. This effect is so dominating that applying the resulting correction factor would end in the gain not being stabilized in the temperature range where these detectors should be operated. While unfortunately we did not know that this was such a persistent issue when we carried out the stabilization runs. Apart from the fact that we saw that the temperature range for the KETEK detectors had to be lowered for them to produce results from which we could extract a gain measurement. These things rings especially true for the PM series which seem to show these signs already at room temperature while the W12 detectors seem to operate at a fair level up to the point where they fail completely. The PM3350 serial number 1 does not have viable data from both of the bias scans performed at 27 and 30 °C as such these were not included in the estimations. One can also observe a change in the gain at the higher bias voltages for the data taken at 25 °C as well though these have not been removed. Meanwhile for the PM3350 serial number 2 these issues had an even larger extent where they experienced increasing amounts of instability at an even lower temperature stage in the bias scans. This resulted in that the data taken in the 25–30 °C range was not included as it would skew the data towards an incorrect dV/dT estimate. Furthermore one can see that this specific detector also seem to experience this to a lesser extent in the 17–23 °C range, although only the data in the higher bias voltage measurements for the 23 °C scan had to be removed. In Figure 5.2 we can see the measurements done with the W12 A detector while the rest of the KETEK can be viewed in appendix B.

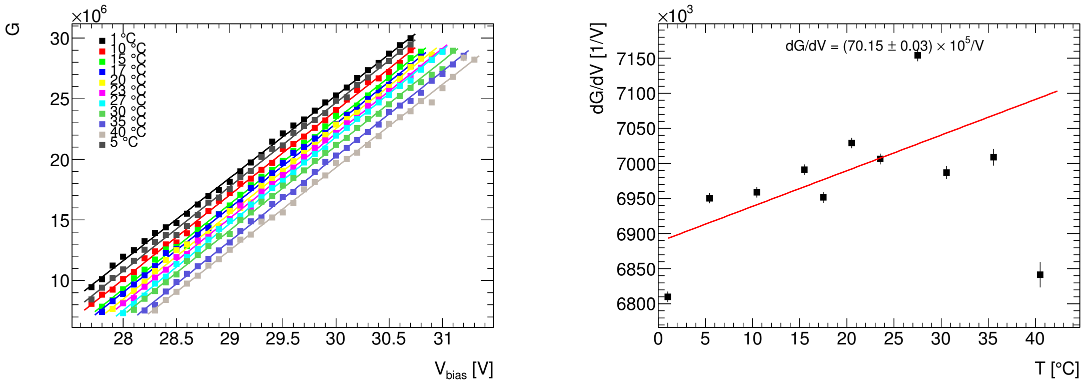

(a) Measurements of gain-versus-bias voltage (dG/dV) for fixed temperatures.

(b) Plot shows the obtained values of the dG/dV versus fixed temperature.

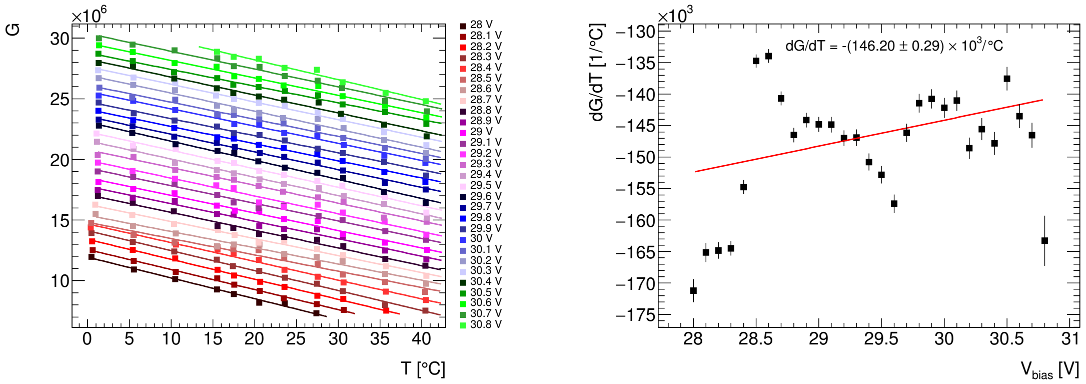

(c) Measurements of gain-versus-temperature (dG/dT) for fixed bias.

(d) Plot shows the obtained values of the dG/dT versus fixed bias voltage.

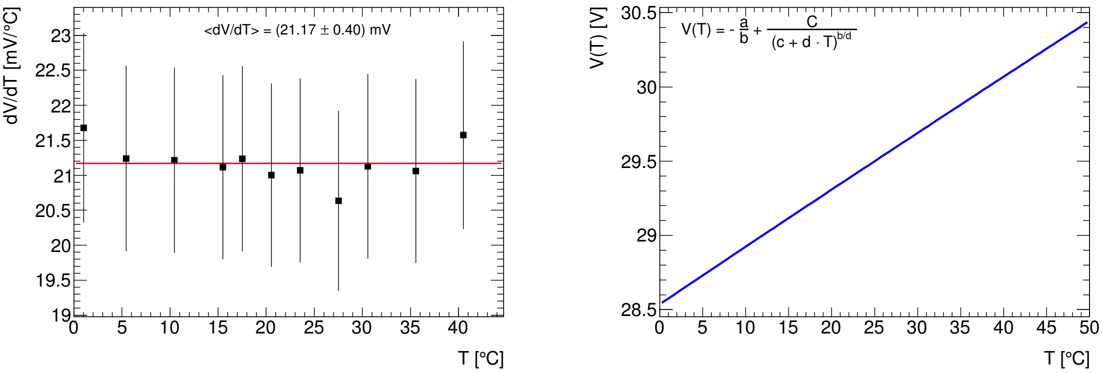

(e) Weighted average distribution of dV/dT as a function of temperature.

(f) Plot illustrates the bias voltage as a function of temperature.

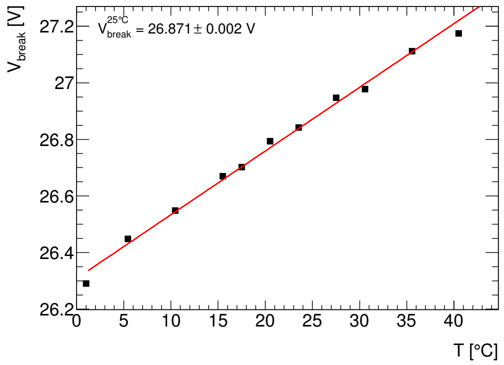

(g) Plot shows the determined breakdown voltage at different temperatures.

Figure 5.2: All measurements are taken with the KETEK detector W12 A.

5.1.3 CPTA

Unfortunately when it comes to the CPTA detectors there appears that something happened during the data-taking period. The bias scans were done over two subsequent days where the ones carried out the first day have a completely different dependence on temperature and bias voltage for the gain than the scans done the next day. One might consider that perhaps the voltage applied to the preamplifiers were changed by accident in order for this to occur. There really is no way to determine what caused this to happen without scheduling another data taking sessions to troubleshoot this issue. Though since we had so few CPTA detectors and the dV/dT had already been determined for the CPTA 857 in advance so we settled on applying this value to the CPTA stabilization runs.

The values listed for the CPTA detectors should be taken with quite a bit of salt as we had very few scans from which to extract the estimates. This holds especially true for the CPTA 857 which seems to experience extremely noisy waveforms and highly unstable gain estimates has been observed in all of the tests. While the CPTA 1065 has the most stable conditions of these detectors and as a result has the most accurate values listed. Although these should be viewed with reservations and the measurements itself should still be further scrutinized. The plots showcasing the results of CPTA 1065 can be seen in Figure 5.3 while the rest can be seen in appendix C.

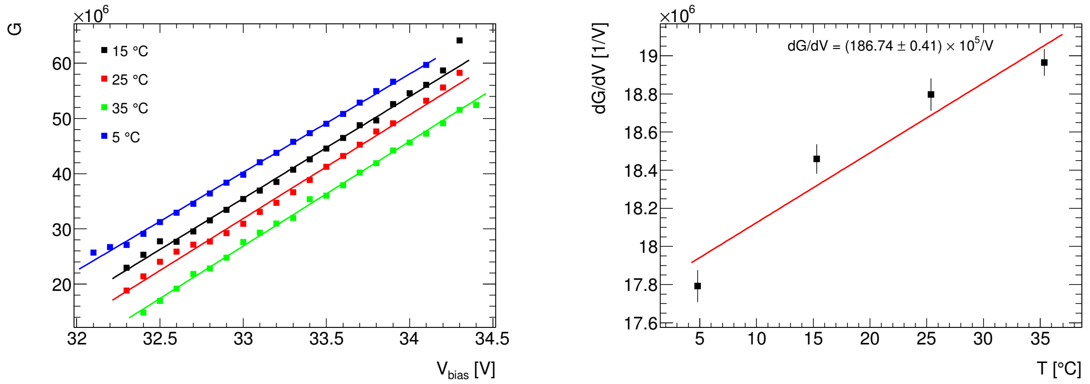

(a) Measurements of gain-versus-bias voltage (dG/dV) for fixed temperatures.

(b) Plot shows the obtained values of the dG/dV versus fixed temperature.

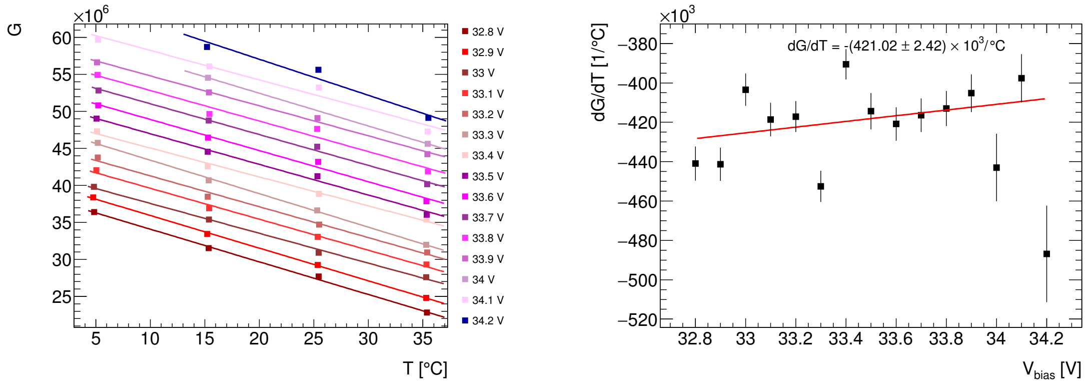

(c) Measurements of gain-versus-temperature (dG/dT) for fixed bias.

(d) Plot shows the obtained values of the dG/dT versus fixed bias voltage.

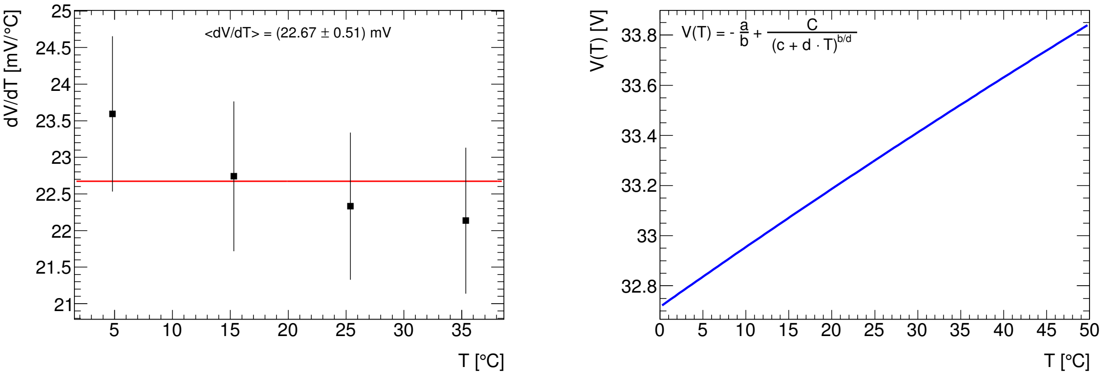

(e) Weighted average distribution of dV/dT as a function of temperature.

(f) Plot illustrates the bias voltage as a function of temperature.

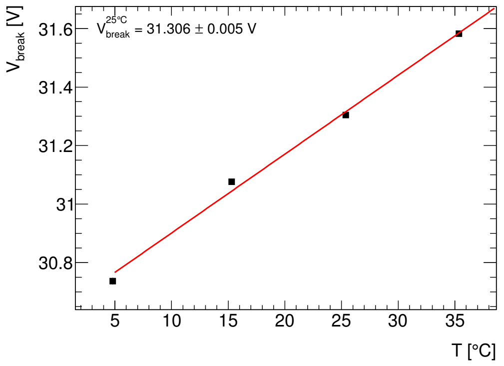

(g) Plot shows the determined breakdown voltage at different temperatures.

Figure 5.3: All measurements are taken with the CPTA detector 1065.

5.2 Stabilization

We had a limited window of data recording since we could only book the climate chamber for a short fixed period, as such most of the stabilization runs were done overnight using the own programmed temperature profile with the climate chamber. While checks, optimizations, and bias scans were carried out during the day. One of these programmed profiles was a stepwise function which incremented by 5 °C in the 1–20 °C and 30–50 °C ranges, while incrementing by 2 °C in the 20–30 °C range. It was done this way in order to get increased statistics in the temperature region of interest; other similar temperature profiles were used for different detector, for instance the run using four KETEK PM3350 had a much shorter range of 1–35 °C. The stepwise profile which was used for most of the runs can be seen in Figure 5.4a.

Since we are continuously recording the data using a step wise function instead of manually moving to each temperature, and then starting the data-taking process, it means that we end up with a lot of samples where the temperature fluctuation is rather large. Since this is something one would typically not experience in normal operational conditions we have removed the data points corresponding to the rapid ramp up from 25 °C seen at the start, as well as the rapid ramp up from 1 °C seen at the end. We also try remove any data samples taken in the start of each step if the temperature does not seem to settle and is seen to be fluctuating. After the temperature has stabilized we completely stop removing any possible data samples even if the temperature would start to fluctuate again. This process is done individually for each detector as they have their own temperature monitoring sensor. The temperature measured by the three remaining non-detector sensors are used to cross-check that the temperature measurements are correct and that there are no apparent issues in relation to this. The data that remains after this procedure has been applied can be seen in Figure 5.4b.

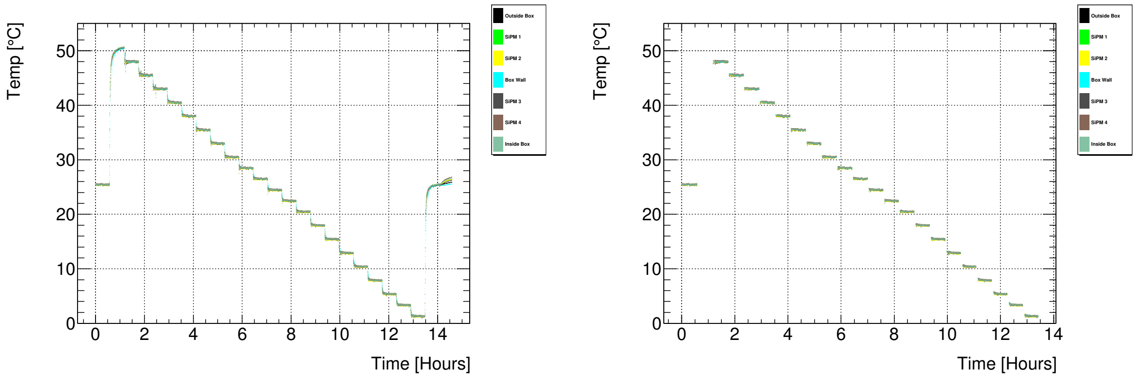

(a) Measurements of the step wise temperature profile.

(b) Only showing measurements used in analysis.

Figure 5.4: One can in 5.4a observe the temperature data recorded by the different PT1000. The temperature profile shown here is the one which was used for most the analysis and was programmed through the touchscreen interface of the climate chamber. The plot in 5.4b shows an example of the profile after the removal of any data samples where the temperature is ramping quickly.

The stabilization is carried out through using the Adaptive Power Supply Board (ADA Board). This system continually measures and adjusts the bias voltage based on temperature using the dV/dT correction factor that we previously determined using the bias scan method. The ADA Board did not have four channels in which to perform this adjustment separately for each detector, and a voltage divider was used to give each detector a fixed percentage of the bias voltage that was supplied to the detector with the highest specified operational bias voltage. This fixed percentage used was determined by dividing the specific detector's bias voltage by the one with the highest. However, for detectors which have very similar bias voltage this divider was not used. This means we performed the gain stabilization of four different detectors using a single dV/dT correction factor in order to show the viability of a small system setup.

Using this method we hope to attain a uniform gain distribution regardless of temperature. The stability achieved through utilizing the methods described in this thesis is estimated by measuring the non-uniformity. This is given as ΔU through the Eq. 5.1 where the dG/dT and the nominal gain, G_{nom}, is estimated by a linear fit to the gain distribution in the selected temperature range. Even though we typically fitted the entire temperature range in which we took data there were cases where the detectors experienced non-linear effects at high temperature, and in these cases the fits were done in a smaller range. Since it is the room temperature stability that is the main focus we have also extracted the values corresponding to the non-uniformity in the 20–30 °C range. For the case of the detectors were the first fit does not cover the 20–30 °C range there is done a separate fit to cover this region. The Table 5.2 reflect the values used in the non-room temperature fit range.

$$\Delta U = \frac{dG/dT}{G_{nom}} \times \Delta T \tag{5.1}$$

G_{nom} = The estimated nominal gain at 25°C by the fit

ΔT = Temperature range of interest

The temperature profiles used by the Hamamatsu detectors typically had stable data in the 1–50 °C range, where the 50 °C points typically showed that the climate chamber had in most cases not properly stabilized the temperature and was fluctuating. The KETEK detectors, especially the PM3350, appeared to show that they were meant for lower temperature operations as they displayed rather defined waveforms at lower temperatures - while for instance the Hamamatsu seemed to struggle when it neared the lower ranges - albeit they rarely showed any useful results above 30 °C, although the W12 detectors did not appear to show much issues before nearing the 50 °C mark. The temperature profile used for the four PM3350 detectors were decided to be 1–35 °C, while the run showcasing the W12 and PM3350 went from 1–50 °C. CPTA showed similar results as the with the KETEK W12 detectors albeit a bit less defined peaks as such the data was taken with the full 1–50 °C range although not all of the detectors showed the same promise at higher temperatures. At each temperature step we typically recorded $\sim$ 40 data samples each with 50 000 waveforms after stable temperature was achieved. It was carried out this way to enable a lot more statistics in order to increase the accuracy of the results, this is similar to how we treated the bias scans. Also for the stabilization runs we only plot the weighted average; where its uncertainty is given by the variance of the weighted samples, here each point consists of the $\sim$ 40 data samples taken per temperature step. Though, both the stabilization run with the four B's and the the four S13360 detectors consists of $\sim$ 20 data samples. The Table 5.2 lists the measured dV/dT value extracted from the bias scan and which dV/dT value that was applied to the detector during the stabilization run, it also includes the temperature range which were used to determine the non-uniformity of the gain, ΔU, and the non-uniformity achieved in the 20–30 °C range, $\Delta U_{20-30\,°C}$. This temperature range can be smaller for some of the detectors, even within the four detector cluster, this is due to some of them experiencing non-operational conditions which results in recorded data with no - or not enough - discernible p.e. peaks, these points are promptly removed from the analysis as it would be impossible to fit these and hence no gain measurements can be extracted.

5.2.1 Hamamatsu

The Hamamatsu detectors as a whole are very well stabilized in the temperature region of interest with all of the detectors having a gain non-uniformity well within the required 1 %. Most of the detectors also fulfill this requirement in the whole temperature range as well. The figures showing the measured gain stability for all of the detectors can be seen in Appendix D. The A prototypes perform extraordinarily in the whole temperature range with an estimated non-uniformity of less than 0.2 %, as seen in Figure 5.5. This is mostly due to the fact that all of these detectors have very similar dV/dT compensation factors and they show few non-linear effects in the extremities of the temperature range although these are still present. However for most of other Hamamatsu detectors there are very clear non-linear effects observed at temperatures above ~40 °C.

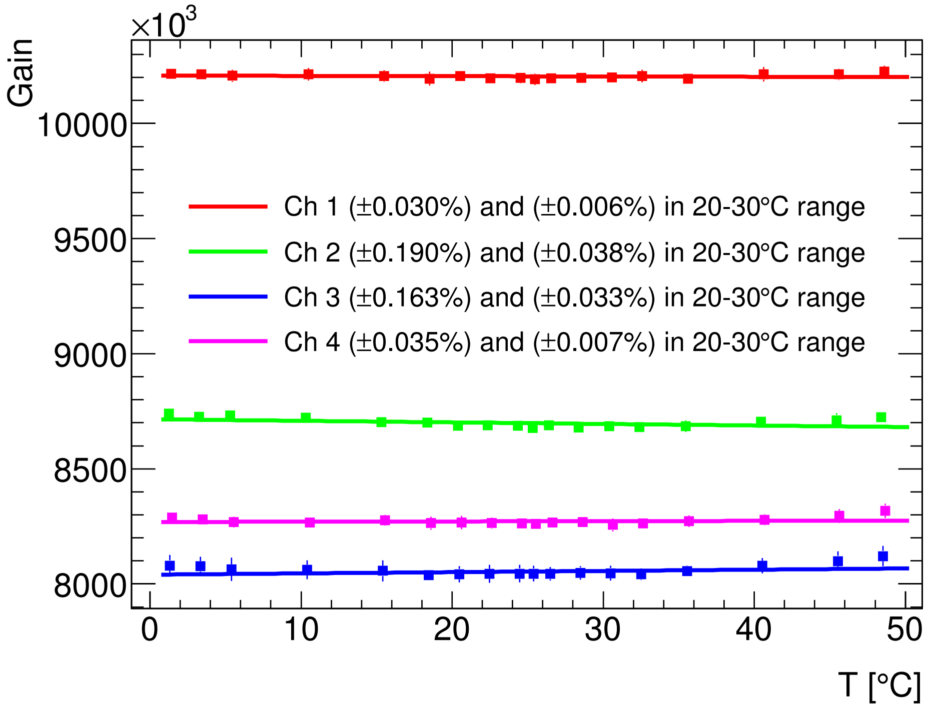

Figure 5.5: For the Hamamatsu A prototypes we had a rather good coincident between the measured and applied dV/dT as can be seen in the extraordinary stabilization results achieved for these detectors.

The B prototypes does not achieve as good a non-uniformity as the rest of the detectors tested. During the stabilization run we find that the measured gain is stable and is rising throughout the whole run which mights suggest that we have applied a too high compensation factor for these detectors. This is further backed by looking at Table 5.2 for the B detectors. Where one can see that the non-uniformity achieved is best for the detector which has a measured compensation factor that matches the one applied. Also for these prototypes there does not appear to any non-linear effects present in the gain measurements due to temperature. The plots for these detectors can be found in Figure D.2.

Table 5.2: The ΔU here refers to the non-uniformity of the measured gain, as determined through Eq. 5.1. It is specified both for the value extracted in the $20-30$°C range, and the whole temperature range listed. These runs were all done with four detectors in the system which were stabilized by a single dV/dT correction factor. Due to some of the detectors operating at a subpar level compared to the others it was tested along with, not all four detectors reflect the same temperature range for gain non-uniformity fit. The range is different due to certain temperatures where the p.e. spectra cannot be fitted. The temperature range column will reflect the range used in this fit determination for the ΔU for each specific detector. Although, for the ranges where it is below 20 °C a separate fit is done in the 20-30 °C range, as for the KETEK detectors. The W12 detectors are listed twice, with the gain non-uniformity extracted from using both the MSME, which is the first two values listed, and the Maximum Amplitude method.

Type	**Model**	**Serial#**	**Pixel Pitch** [μm]	**Ch.#**	**Temperature range** [°C]	**Measured** dV/dT [mV °C^{-1}]	**Applied** dV/dT [mV °C^{-1}]	ΔU [%]	$\Delta U_{20-30\,°C}$ [%]
					Hamamatsu				
A	1		20	1	1–50 °C	59.69 ± 0.37	59.00	0.030	0.006
A	2		20	2	1–50 °C	59.83 ± 0.38	59.00	0.190	0.038
A	1		15	3	1–50 °C	59.06 ± 0.42	59.00	0.163	0.033
A	2		15	4	1–50 °C	59.23 ± 0.30	59.00	0.035	0.007
B	1		20	1	1–50 °C	56.88 ± 0.51	57.80	1.250	0.257
B	2		20	2	1–50 °C	57.90 ± 0.64	57.80	0.393	0.080
B	1		15	3	1–50 °C	57.10 ± 0.45	57.80	1.052	0.216
B	2		15	4	1–50 °C	56.46 ± 0.60	57.80	2.140	0.444
S13360	1325CS	10143	25	1	1–50 °C	55.80 ± 0.29	57.20	0.739	0.151
S13360	1325CS	10144	25	2	1–50 °C	57.76 ± 0.19	57.20	0.234	0.047
LCT	4	6	50	3	1–50 °C	53.9 ± 0.5	53.997	0.251	0.051
LCT	4	9	50	4	1–50 °C	54.0 ± 0.7	53.997	0.247	0.050
S12571	010C	271	10	1	1–43 °C	63.99 ± 0.18	64.8	0.629	0.150
S12571	010C	272	10	2	1–43 °C	65.22 ± 0.18	64.8	0.026	0.006
S12571	015C	136	15	3	1–36 °C	63.46 ± 0.32	63.12	0.752	0.216
S12571	015C	137	15	4	1–43 °C	62.38 ± 0.36	63.12	1.128	0.270
S13360	3025CS	10103	25	1	1–50 °C	56.17 ± 0.36	57.0	1.380	0.284
S13360	3025CS	10104	25	2	1–50 °C	58.27 ± 0.41	57.0	0.434	0.089
S13360	1325CS	10143	25	3	1–50 °C	56.22 ± 0.63	57.0	1.063	0.218
S13360	1325CS	10144	25	4	1–50 °C	56.24 ± 0.28	57.0	0.898	0.184
					KETEK				
W12	A		20	1	1–35 °C	21.17 ± 0.40	17	1.497	0.435
W12	B		20	2	1–35 °C	23.02 ± 0.25	17	2.742	0.791
W12	A		20	1	1–15 °C	21.17 ± 0.40	17	0.734	0.786
W12	B		20	2	1–15 °C	23.02 ± 0.25	17	1.331	1.426
PM33	50	1	50	3	1–15 °C	20.43 ± 0.28	18.15	0.917	0.983
PM33	50	2	50	4	1–15 °C	20.45 ± 0.41	18.15	0.726	0.777
PM33	50	5	50	1	1–15 °C	18.74 ± 0.21	18.3	1.075	1.152
PM33	50	6	50	2	1–15 °C	18.84 ± 0.28	18.3	0.698	0.748
PM33	50	7	50	3	1–15 °C	20.94 ± 0.38	18.3	0.659	0.706
PM33	50	8	50	4	1–15 °C	20.00 ± 0.34	18.3	0.699	0.749
					CPTA				
		857	40	1	1–50 °C	19.33 ± 0.74	21.2	5.972	1.279
		922	40	2	1–50 °C	25.25 ± 0.51	21.2	1.758	0.353
		972	40	3	1–50 °C	23.95 ± 0.90	21.2	2.586	0.517
		1065	40	4	1–50 °C	22.67 ± 0.51	21.2	0.510	0.103

For the case of the S12571 there is a very clear drop in the gain measured at 45 and 48 °C, the gain quickly drops by ~0.5 % over the course of this temperature change. These effects are present without any analysis software being applied to the data and appears to be detector intrinsic in nature. As seen from Figure D.3 we observe that for the rest of the stabilization run the gain appears to be rising and stable, aside from a few measurements showing some fluctuations.

The trenched detectors, both the S13360 and the LCT, appear to have rather linear behaviour observed in the 1–30 °C range. The measured gain increases steadily with the temperature in this range for these detectors. While after this point clear non-linear effects seem to come into play and the gain starts to decrease with the increasing temperature. This appears to be a detector intrinsic feature for these detectors as well and does not seem to be introduced by the analysis carried out within this thesis.

5.2.2 KETEK

The PM3350 detectors did not produce as much usable results from integrating the waveforms, as such we have used the maximum amplitude method for the determination when it comes to these detectors. The W12 detectors have usable results from both methods, but display clear non-linear effects above 34 °C using the integrated spectra as can be seen in Figure 5.6. However, if one utilize the results from the maximum amplitude method these effects come into play at a much lower temperature for the W12 detectors, and we observe two different linear ranges where the first one is around 1–15 °C and the second is seen at 15–30 °C which is not seen from the MSME method. It is unclear whether this effect would be fully mitigated also for the PM3350 detectors if one was able to successfully integrate the waveforms since these effects do not appear to be as prominent for the integrated spectra from the W12 detectors. Unfortunately there is not any separation observed in integrated p.e. spectra above 18 °C for the PM3350.

We have not been able to determine the recommended operational temperature range for the PM3350 as the range is not shown in its data sheets from the manufacturer. The only temperature plot found for these detectors is contained in a presentation from KETEK which seems to indicate that they are meant for low temperature operations, as these plots only go from −35–15 °C and this plot shows that the dV/dT is supposed to be linear in this range [18]. While we do not go to a low enough temperature to confirm this, the results seem to back up the idea that they are indeed linear at the lower registry and meant for these temperatures. For the PM3350 we have chosen to fit the ranges 1–15 °C and 15–30 °C separately. The plots for the combined W12 and PM3350 run can be seen in Figure 5.7 while the rest of the results can be found in appendix E.

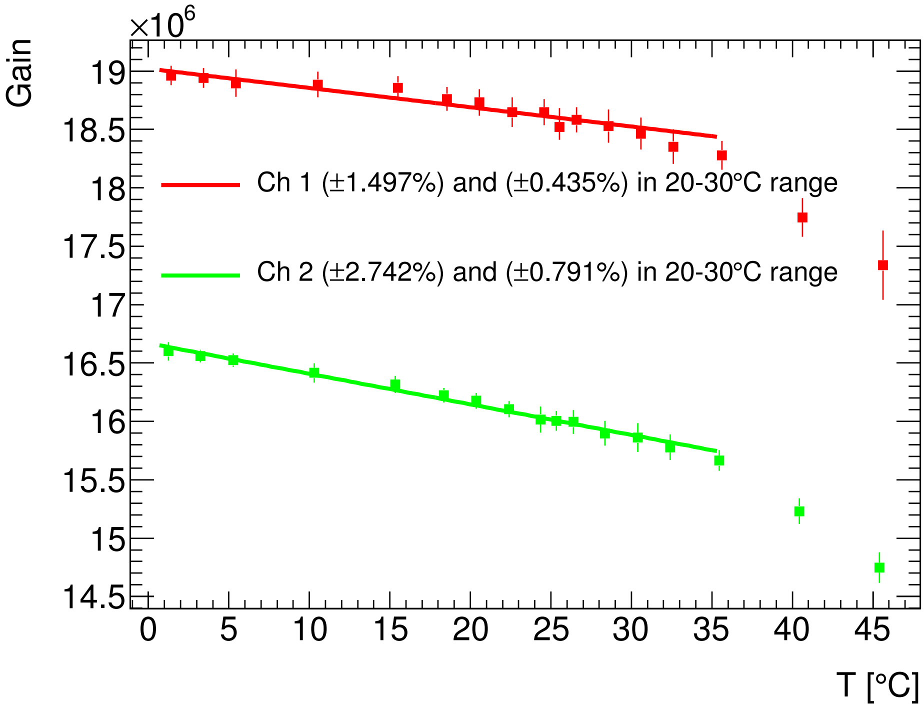

Figure 5.6: These plots show the gain stability achieved for the KETEK W12 detectors as measured using the MSME method. Any non-linear component does not appear before after 35 °C. We achieve decent results for these detectors, though as can be seen from the negative slope we have undercorrected these detectors which is reflected in Table 5.2.

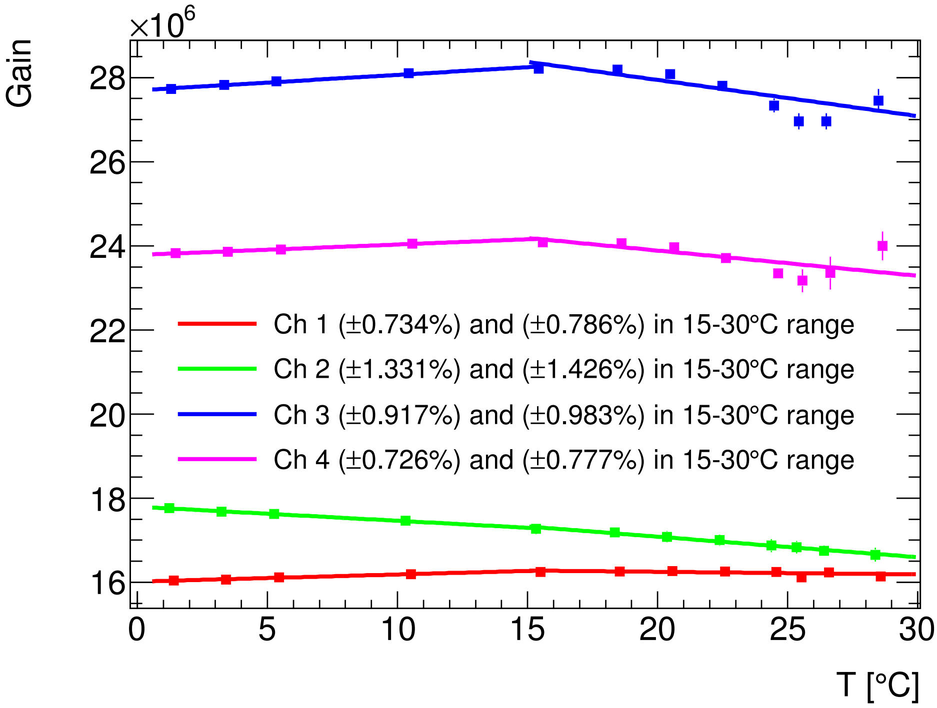

Figure 5.7: The Maximum Amplitude method does not yield as stable results for the W12 detectors with a clear shift in temperature dependence seen around 15 °C. This is not quite as drastic for the two PM3350 although we chose to fit these with two separate linear polynomials as well. Overall the stability achieved is quite decent however for the W12 it is less than what was observed with the MSME method.

5.2.3 CPTA

The CPTA detectors experienced unstable operation during the start of the stabilization run. This seemingly occurred due to bias voltage not being properly ramped to the correct values before data recording was started. Based on the fact that the gain in the beginning of the run is twice as high as it was for the rest of the run. Due to these effects those data samples have been rejected for this analysis. These samples correspond to the 25 °C point.

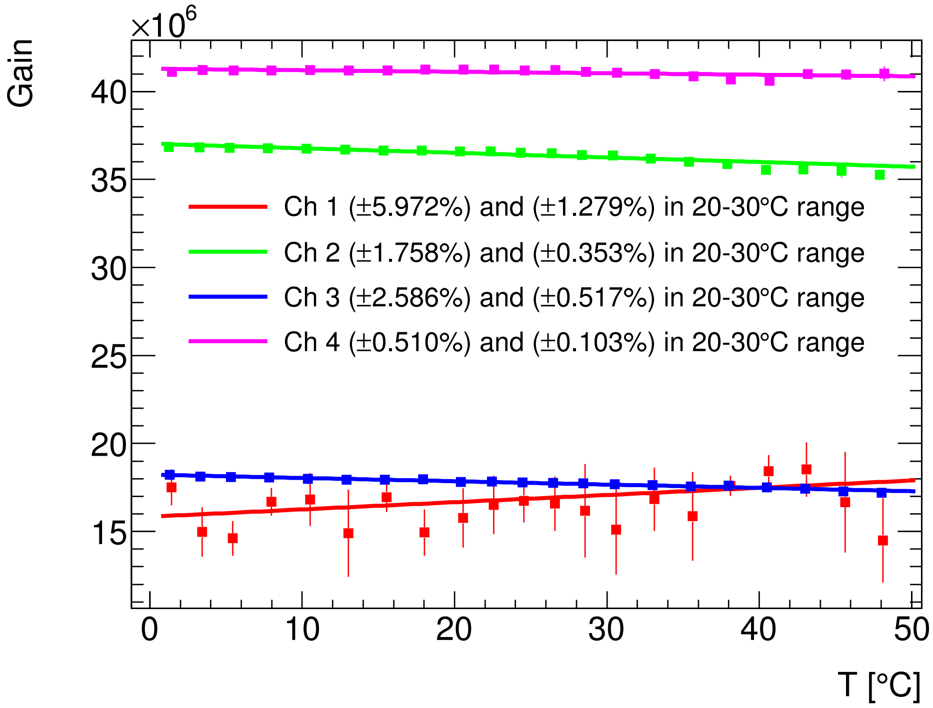

Figure 5.8: One can clearly see the amount of noise and instability the CPTA 857 experienced during the run, while the other three CPTA detectors keep themselves rather stable and achieving decent results in the 20–30 °C range. The CPTA 1065 is as aforementioned seemingly a good detector which can been seen from the fact that it experiences very few fluctuations compared to the others.

5.3 Comparison of integration methods

We utilized the different Hamamatsu detectors as a reference when we developed all of the software tools discussed in this thesis, this is mainly due to their far superior waveform separation and how clean the signals were. Though some tools were tested on the different CPTA and KETEK detectors as they were the only ones displaying the features which we had to mitigate. Earlier adaptations of the different integration window determination methods, i.e. MSME, utilized the actual mean value of their respective distributions, though this was discovered later on to typically yield a less favourable result than using the bin corresponding to the maximum occurrence, as such it really should be called something along the lines of the Mode Start and Mode Endpoint, but for continuity it retained its original name. For most of the Hamamatsu detectors there was not that big a difference between the resulting p.e. spectra for different integration window determinations which can be seen in Figure 5.9. As such the choice in the end fell on MSME mainly due to its increased ability to successfully suppress the afterpulsing contributions, which is also one of the reasons why it was changed to using the mode instead of the mean

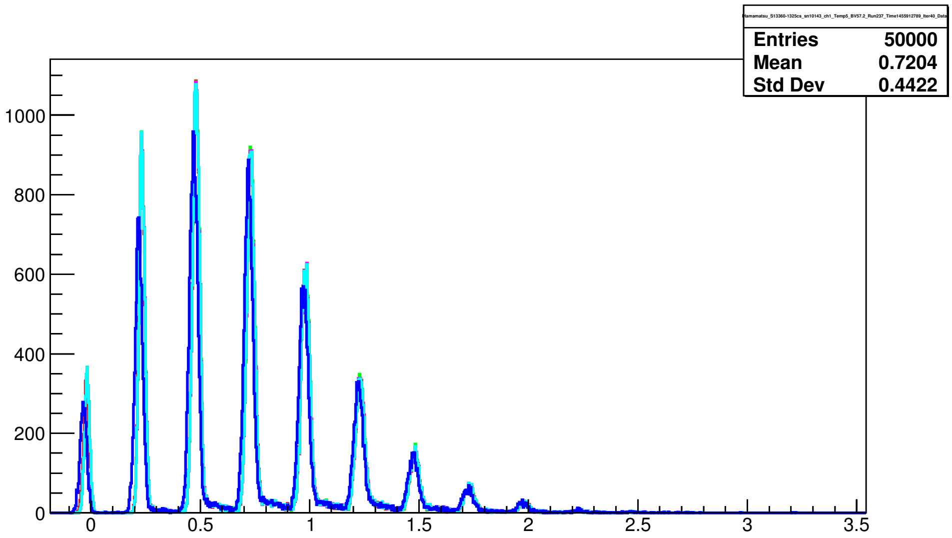

Figure 5.9: The dark blue p.e. spectrum represents an integration window selected by visually inspecting the corresponding waveform density plot and trying to determine its optimal values through trial and error. The rest of the four different methods of automatic integration window determination seem to overlap nearly perfectly, and as one can easily see, it ends up with more sharply defined p.e. peaks. All measurements are recorded by the Hamamatsu detector S13360 1325CS serial number 10143.

of the point distributions as seen in Figure 5.10.

The method of removing the Parasitic Pickup Signal (PPS) showed promise, as there did not appear to be any major differences in the gain nor the error on the gain by removing, this is both for the MSME and the MSVE methods. Though it resulted in overall increasing the number of data files where we were able to successfully fit the resulting p.e. spectra, and therefore also in extracting the values we needed and hence the results accuracy. Due to the vast amount of data we had taken it was not really an option to individually fit each spectra with its own specific fit parameters, as such each detectors had the same ones for a large fraction of the samples, though there was some tweaking needed for some of the bias scan data files. This typically was for data files taken during either too high a temperature, high bias voltage, or where the bias voltage came close to the current breakdown voltage. Since the Parasitic Pickup Signal subtraction method increased the number of fits which did not fail, we deemed that the subtraction was a resounding successful even though it would have been even better to remedy this before any data was taken. The subtraction was especially useful when it came to the CPTA and KETEK detectors as it massively improved the resulting spectra from the Maximum Amplitude technique, which in turn yielded a far larger amount of data from which we could extract the necessary values. One can see the examples of the difference yielded by the subtraction of the Parasitic Pickup Signal for a stabilization run in Figure 5.11. The rest of the Hamamatsu detectors showed similar results to this one, albeit a slightly stronger indication of a more stable gain for the Parasitic Pickup Signal subtraction case.

Several tests were performed to see if correcting for the observed DC offset would yield better or worse results. This was done for all integration windows and also for most of the Hamamatsu detectors - with the exception of the A and B prototypes - all detectors from this manufacturer show similar results as the ones displayed in Figure 5.12. In the first three rows of this figure the different ranges are fixed, as

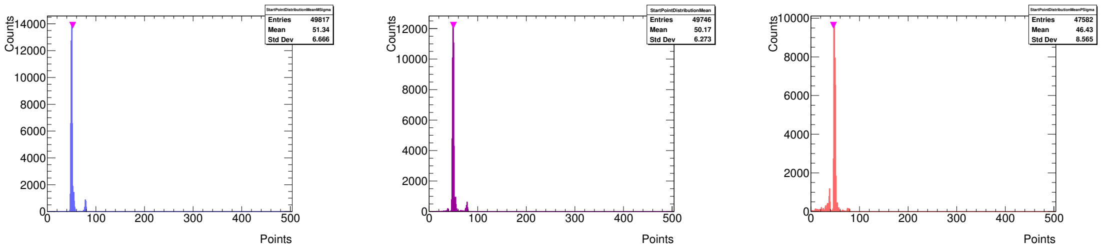

(a) Start points for $\mu - \sigma$.
(b) Start points for μ.
(c) Start points for $\mu + \sigma$.

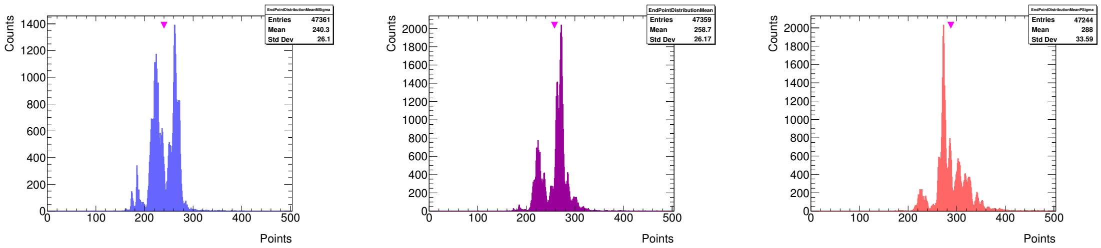

(d) End points for $\mu - \sigma$.
(e) End points for μ.
(f) End points for $\mu + \sigma$.

Figure 5.10: These distributions are for the MSME method, which is the one that ended up being used for the analysis. The shift by $1 \times \sigma$ is in regards to the requirement of when we consider that a waveform has properly receded, and it is the cause of the observed difference in these distributions. The upside down triangle indicates the calculated mean value of the distribution, which was used in the early software iterations before it was changed to the maximum peak value. An example of where these different maxima occur can be seen in Figure 4.6

such one can quickly compare the different plots and see that all four methods for the integration window yields rather similar results. The reason for why these four methods end up so similar is mostly due to the effect of the Parasitic Pickup Signal subtraction, as this ends up reducing the variance on the integration window size and therefore no big difference is seen, while plots where it is not removed yield varied results. In the plots where we refer to 'no offset' this reflects that there was not taken any steps to mitigate the DC offset that was observed in the waveforms - and one can see that this seem to yield rather drastic non-linear effects in the higher temperature region, some of which are seen no matter what we would do, but not to the same extent. While this may be due to how the fit model is defined, as this would result in the mean of the p.e. peak in the spectra being shifted, there was taken steps to include this in the model to try to correct for it, but it did not change what was observed from the data. As such it was deemed more suiting to try to correct for this fact through the integration procedure. Since the method of Parasitic Pickup Signal subtraction already yields this DC offset value and the estimated sigma, what was done was to compare no offset to μ offset and $\mu \pm \sigma$ offsets. The former two are displayed in Figure 5.12 and the latter two are not as they do not differ much from the displayed μ offset. The percentage values which are shown in the plots are taken from the linear fits and corresponds to the overall gain stability in the range of 1–50 °C, this method is discussed in-depth in section 5.2. From the plots one can see that the non-linear effects observed in the no offset method yields better non-uniformity estimates. However, since the offset corrections seem to reduce the non-linear effect, as seen in Figure 5.12e, the observed magnitude of this effect seem to be a mostly software introduced feature and does not appear to be solely due to the detector intrinsic properties. It should be noted that these effects are rather small for most of the Hamamatsu detectors, and we can only observe them due to the high precision of our measurements. As such, these effects can be mostly ignored

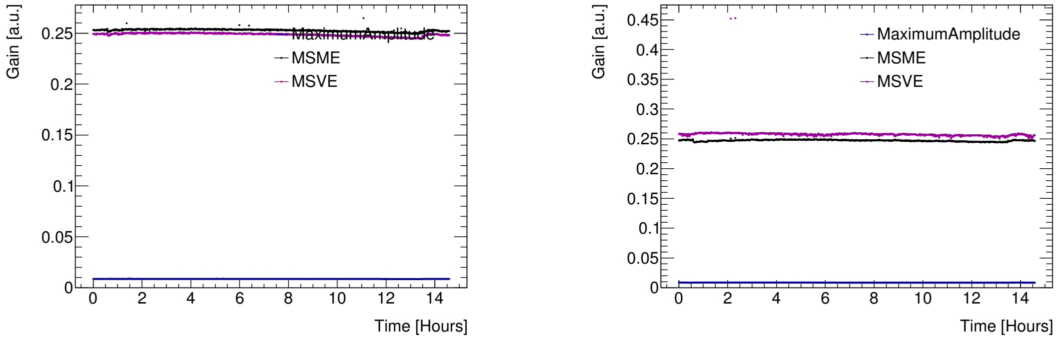

(a) Gain (b) Gain

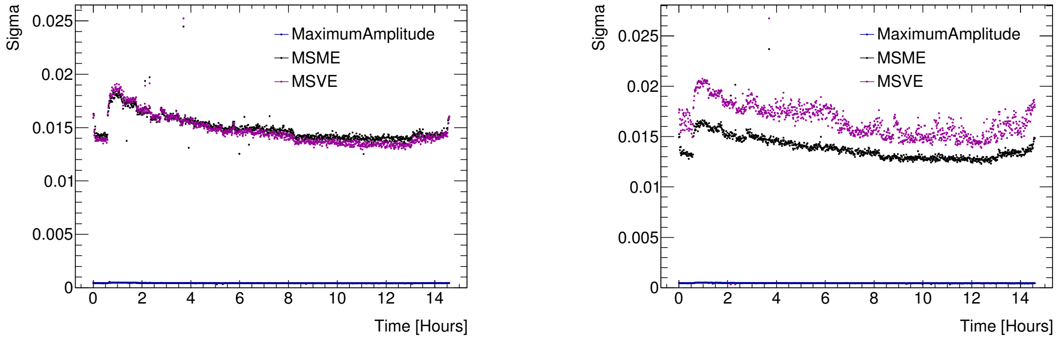

(c) σ_{gain} (d) σ_{gain}

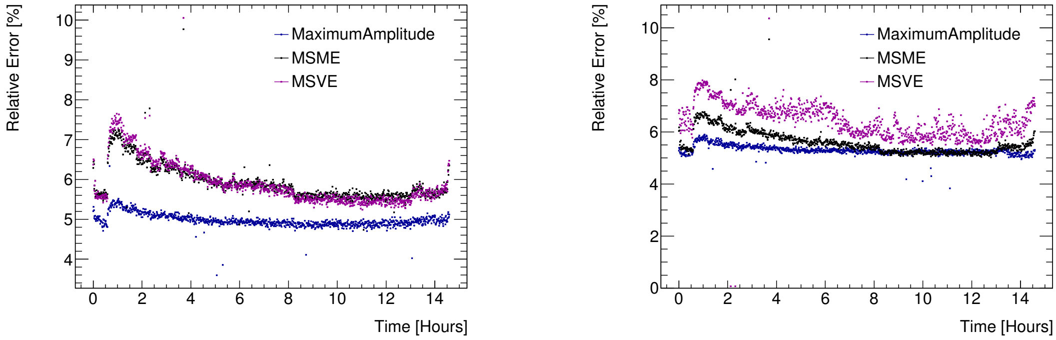

(e) Relative Error (f) Relative Error

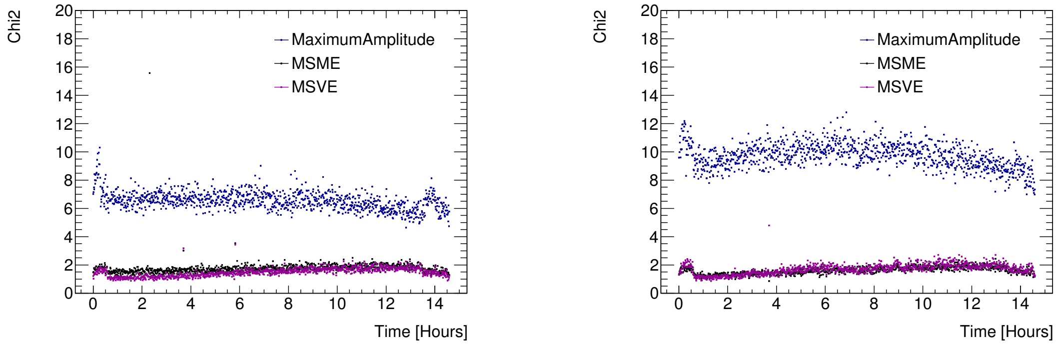

(g) χ^2 (h) χ^2

Figure 5.11: The left hand plots illustrate the different distributions with the Parasitic Pickup Signal (PPS) removed, while the right hand plots still have it intact. These are all fits done on the p.e. spectra from the stabilization runs taken by the Hamamatsu S13360 1325CS serial number 10143 detector. The magenta points relate to the MSVE, black to MSME, and blue to the Maximum Amplitude method. All other Hamamatsu detectors, even the other S13360 1325CS detector displayed reduced relative errors and less variance in the distributions than this particular detector.

for these detectors. However they should be studied to be certain that they are not introduced through the used analysis methods.

We observe non-linear effect at higher temperatures for all of the detectors which we tested, and even though this is not reported by most sources. We have confirmed these results through visual inspections of the waveforms and p.e. spectra, this to remove any software introduced bias. The upward trend of the gain symbolizes that we overcorrected by applying a too large value for the dV/dT constant which can be seen in Table 5.2. The different values referred to as 'int. $\mu \pm \sigma$' is in regards to the integration window determination method, and at what point we consider a waveform to have fully receded, as discussed in section 4.3. One can see that the $\mu - \sigma$ method seem to yield the most linear effects in the gain, however as one can see in Figure 4.6 it cuts a little into the waveforms. For other detectors this cut was even larger, as such we chose to err on the safe side by using the μ method. Even though this method does not fully mitigate the non-linear effects that we observed and that have not been reported. One reason why these non-linear effects are not mentioned in most sources might be due to the fact that they do not tend to go above 40 °C and as we can see the effects are mostly seen after this point. Another might be that these are simply stated as approximately linear as these effects are rather small and can typically only be observed by zooming in on the distributions. As one can see from the observed non-uniformity for the stability runs in Figure 5.12 the linear correction still give results where the gain difference is less than 0.5%.

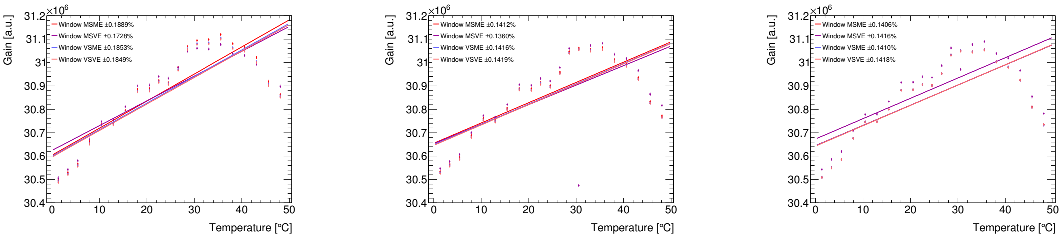

(a) No offset, int. $\mu - \sigma$.

(b) No offset, int. μ.

(c) No offset, int. $\mu + \sigma$.

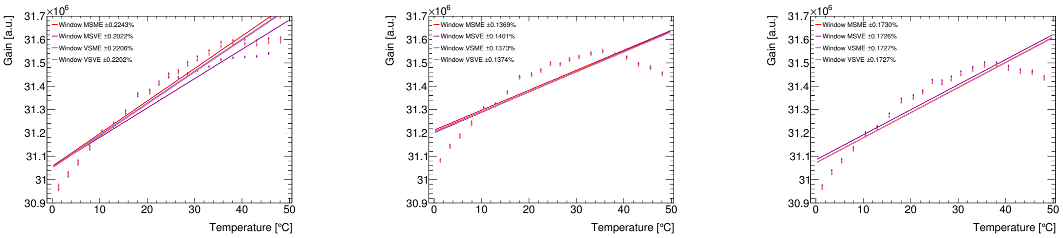

(d) μ offset, int. $\mu - \sigma$.

(e) μ offset, int. μ.

(f) μ offset, int. $\mu + \sigma$.

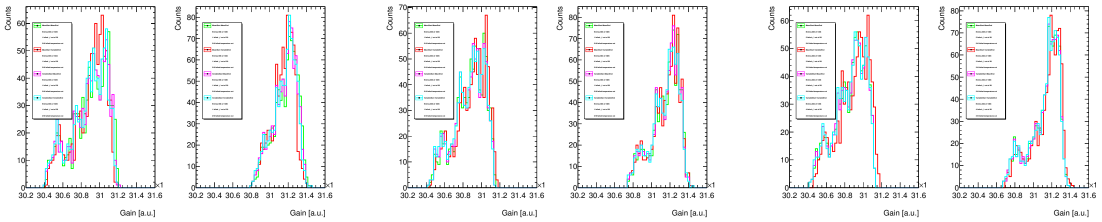

(g) Gains, $\mu - \sigma$ offset.

(h) Gains, μ offset.

(i) Gains, $\mu + \sigma$ offset.

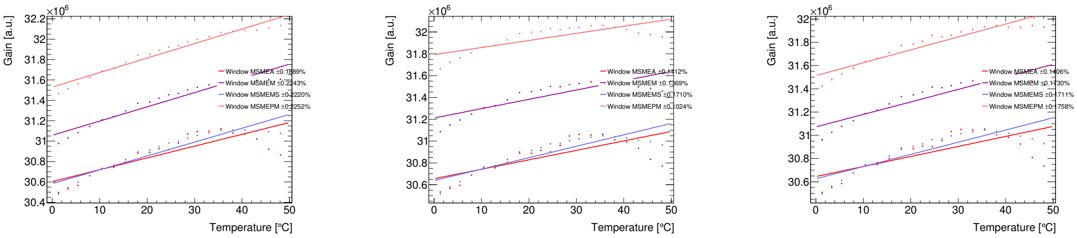

(j) MSME, int. $\mu - \sigma$.

(k) MSME, int. μ.

(l) MSME, int. $\mu + \sigma$.

Figure 5.12: These plots are all of a gain stabilization run done by the Hamamatsu S13360 1325CS serial number 10143. The row with 5.12a and 5.12b show a comparison of the gain achieved with the different integration window determinations. Each plot contains the MSME, MSVE, VSME, and VSVE methods. The offset refers to the DC offset observed in the recorded waveforms, where in no offset we have not done anything to it, while the μ offset refers to the fact that we added the mean value of the distribution show in Figure 4.2a. The row with 5.12g show the gain distribution in a histogram of the methods, the leftmost of the two show in a single figure corresponds to the gain by using the first and second p.e. peak, while the rightmost is by using the second and third. Bottom row 5.12j shows the different distributions for the selected method.

Chapter 6

Conclusion and Outlook for SiPM Gain Stabilization

Most of the issues in regards to the integration which is discussed in this thesis, was ironed out post the data taking period. As such the issues which were discovered during the analysis was attempted to be solved in the different ways explained. Though unfortunately some of these issues were unrecoverable, such as the waveforms of CPTA and KETEK not being fully recorded. In hindsight, we would have needed longer time to properly develop the software used for the analysis, as well as several more days of DAQ to mediate any issues faced. Though since we are not in possession of a climate chamber of our own, we had to abide by the schedule which we were allowed to use it.

From the plots of the gain stabilization run one can observe that the corrections achieved by the ADA Board reach fairly decent non-uniformity in the whole range of 1–50 °C for all of the Hamamatsu detectors. This was achieved even though some of the dV/dT constants were not precisely known at the time and quick approximately determined values were used. Since the initial goal was to achieve less than 1% non-uniformity in the 20–30 °C range, we surely have gone beyond and above the goals by looking in the entirety of the 1–50 °C range and managed to surpass the goal even in this region for some detectors. Hence we have shown the viability of the methods used. In this thesis it has been presented results that show that one can in fact retain precise gain throughout normal operational conditions through very simple means, and one of the next logical steps would be to test this on a larger complete detector system to determine if this method is still as effective. Though to carry this out successfully we would have to adjust several things, both in terms of storage capabilities, but also the DAQ system requires a complete overhaul, as the one we have been using has a maximum of four channels.

As shown we observed non-linear effects in the gain stabilization, where the non-prototype Hamamatsu detectors in particular seem to be linear up to around 40 °C. While for the KETEK detectors these effects come into play at a much lower temperature. However, these effects are rather small for most of the Hamamatsu detectors, and is on the order of less than 0.001% for most of these detectors. As such these effects are far below the requirement that we had set out to achieve in this study. Although, the S12571 do experience a more significant drop in the gain at higher temperature. One would have to conduct more in-depth studies, with new data acquisition runs, in order to conclude whether these are introduced by issues in our analysis or whether they are detector intrinsic in nature. When it comes to the KETEK detectors, the non-linearity is quite noticeable, however these detectors do not appear to be suitable for these temperatures and as such they should be operated in the linear temperature range.

Although, in order to achieve better stabilization results one would need to include these effects to alleviate them. This could possibly be carried out by utilizing a higher order polynomial correction for the dV/dT or through defining several linear regions where one would apply different compensation factors. One of the potential extensions of the work done within this thesis is to also include these effects in the dV/dT estimations such that one can be able to successfully mitigate them, doing this would prove especially useful for improving the viability of detectors from KETEK at higher temperatures.

Chapter 7

ATLAS Experiment

7.1 Large Hadron Collider

Situated at world's largest laboratory Conseil Européen pour la Recherche Nucléaire (CERN) we find the end step in the accelerator complex namely the Large Hadron Collider (LHC). A total of seven experiments are found along the LHC although the only one of interest to this thesis is the A Toroidal LHC ApparatuS (ATLAS) experiment. The accelerator supplies the protons which are squeezed together in order to induce the hard scattering processes which leads to the particles observed by ATLAS. The LHC performs this by circulating two proton beams in opposite directions and accelerating these to an energy of 6.5 TeV. This corresponds to a total center-of-mass energy of $\sqrt{s} = 13\,\text{TeV}$ in the proton-proton collisions which takes place at the interaction point where ATLAS is located. The whole of the accelerator complex found at CERN in 2016 can be seen in Figure 7.1.

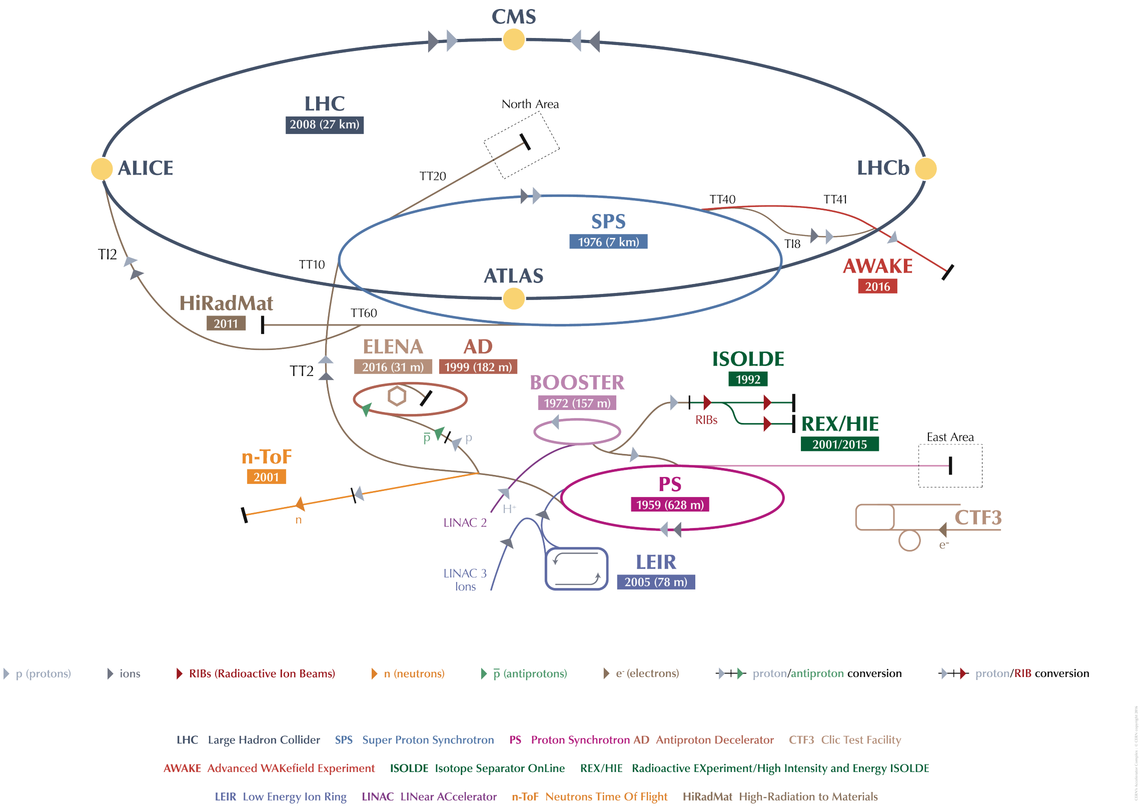

Figure 7.1: Shows the state of the accelerator complex at CERN in 2016. The accelerator chain that leads into the LHC starts with LINAC2 and its hydrogen gas source. Picture taken from [19].

7.2 Luminosity and cross section

In particle physics we describe the number of interesting collisions in terms of an integrated luminosity. This luminosity can in turn be converted into the expected number of interesting physic events which we would observe in our data as long as we know the cross section of the interaction.

$$N = \sigma \times \mathcal{L}_{int} \tag{7.1}$$

In order to get a correct number of expected events, an accurate determination of both the cross section and integrated luminosity is required. The cross section refers to the likelihood of an event taking place and is typically calculated analytically by using a Quantum Field Theory (QFT), although for more complicated processes a numerical lattice theory is applied instead. While the recorded integrated luminosity is typically measured using detectors at the experiment where the data was taken. The measurements and calculations needed to determine this recorded luminosity is a rather complicated matter, hence there is a full task force delegated to accomplish this at ATLAS. The luminosity for ATLAS in 2015 and 2016 can be seen in Figure 7.2.

Although there are several contributing factors to accurately determine the precise luminosity at ATLAS [20], one can dumb down the process to a simple formula, as given in Eq. 7.2. With this forumla one can effectively calculate the luminosity for any circular collider experiment.

$$\begin{gathered}\mathcal{L}_{int} = \int \mathcal{L} dt \\ \mathcal{L} = \frac{N_1 N_2 f N_b}{4\pi\sigma_x\sigma_y}\end{gathered} \tag{7.2}$$

N_1 = Number of particles per bunch in beam 1
N_2 = Number of particles per bunch in beam 2
f = Revolution frequency, how often the same bunch in the beams collide
N_b = Number of bunches in the beams
σ_x = Gaussian width of beam in x-direction
σ_y = Gaussian width of beam in y-direction

In turn we could swap the Eq. 7.1 around such that we could measure the cross section by determining the number of events observed in the data. One can then compare the measured and the calculated cross section, and with this one can determine the accuracy of the theory used to calculate the cross section. This is one of the most common ways to determine that a theory used in particle physics explains the full picture and that it does not need to be modified to accommodate for any observed effects.

7.3 The ATLAS detector

A Toroidal LHC ApparatuS (ATLAS) is an omnipurpose detector and as such it is used to probe for new physics. It is built shell by shell with subsystems around the interaction point where the *pp* collisions take place. This is to maximize the fiducial volume capable of detecting any newly created particles escaping the collision

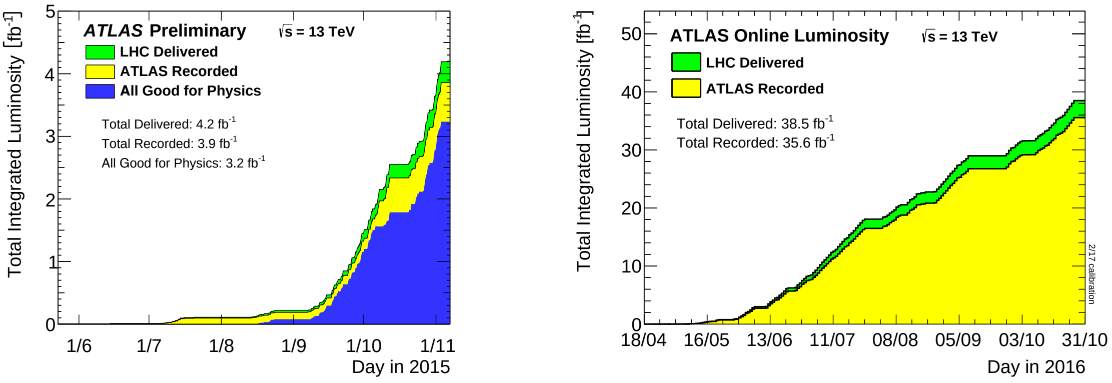

(a) 2015

(b) 2016

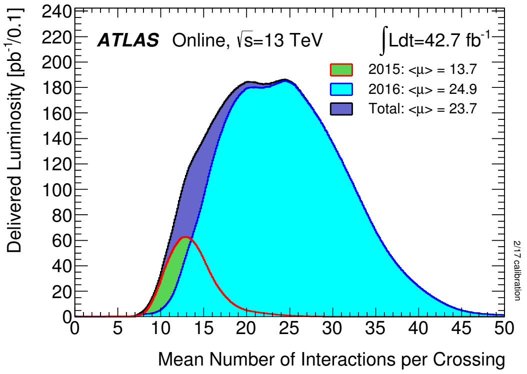

(c) μ interactions per crossing

Figure 7.2: 7.2a and 7.2b shows the luminosity supplied by the LHC in light green and the luminosity recorded by the ATLAS detector in dark yellow. The lower dark blue observed in 7.2a corresponds to the luminosity which is approved for use in common physics analysis. The plot in 7.2c illustrated the mean number of collisions observed per bunch crossing and therefore the amount of pile-up experienced.

point. Innermost we have the detectors used for vertex reconstruction and the other subsystems used to measure the particles track. Further out we first have the solenoid magnet used to curve the charged particles, this is to measure the momentum of the particles transversing the detector. Then comes the calorimeters which are used to measure the energy of particles absorbed in them. Typically photons and electrons are stopped in the Electron Magnetic Calorimeter (ECAL) while hadrons like pions and kaons continue on to the Hadronic Calorimeter (HCAL) before they are stopped. After this we find the magnet system from which ATLAS is named. The toroidal magnets are used to curve the path of the muons escaping the detector in order for the Muon Spectrometers (MS) to perform a more accurate transverse momentum measurement.

7.3.1 Observables and Geometry

As mentioned ATLAS is built with the interaction point as its center. The coordinate system used in ATLAS is defined has having its origin at this point and from this all other observables are defined. When it comes to the Cartesian coordinates the beam pipe is defined as the z-axis and the forward direction is defined as positive. The positive direction of the x-axis is towards the center of the LHC ring. While the y-axis goes through the center of the detector with the positive direction towards ground level. Using this one can then define the xy-plane which is then transverse

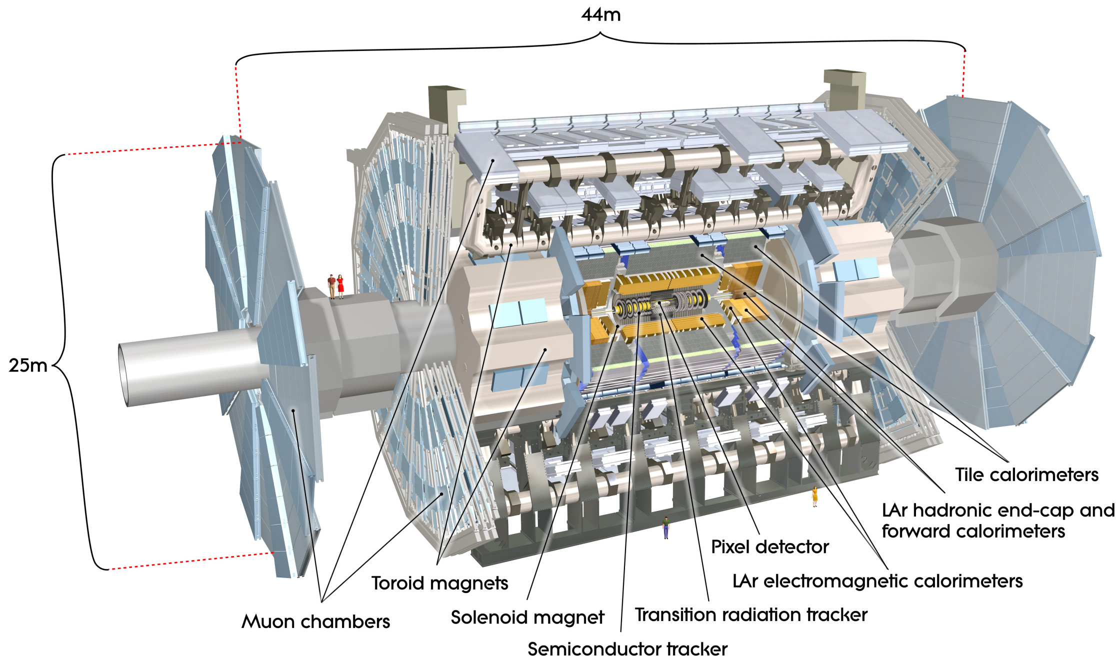

Figure 7.3: Shows a cross section of the ATLAS detector.

to the beam pipe and therefore also the interaction point. From this one can then define that the component of the particle momentum that moves in this plane as the transverse momentum p_T. This is one of the most used observables in searches done with ATLAS. The reason for this is that the beams themselves should not have any p_T components and therefore any product produced after the collisions have to conserve the transverse momentum of 0.

Since ATLAS is built almost like a cylindrical onion around the interaction point we also have to include the cylindrical coordinate system. Where the azimuthal angel ϕ is measured around the beam pipe and is defined by Eq. 7.3.

$$\phi = \tan^{-1}\frac{p_y}{p_x} \tag{7.3}$$

The polar angel θ is further defined as the scattering angle of the particle with respect to the y-axis. Although, most of the searches at ATLAS are typically interested in particles that have a low value for θ. Hence another variable is more often used, namely the psuedorapidity η. This is defined by Eq. 7.4.

$$\eta = -\ln\tan^{-1}\frac{\theta}{2} \tag{7.4}$$

ATLAS is typically divided into its three structural components with a barrel in the middle near the beam pipe with its two endcaps on either side. The detector covers the full azimuthal range up to a psuedorapidity of $|\eta| = 2.5$ for the inner detectors and up to $|\eta| = 4.9$ for the calorimeters.

7.3.2 Subsystems

Following we detail a short coverage of the different subsystems in ATLAS. Although, due to the nature of the decays of interest in this thesis the main focus will be on the Inner Detector (ID) and on the measurements of muons with the MS. While the rest of the subsystems will only be briefly mentioned.

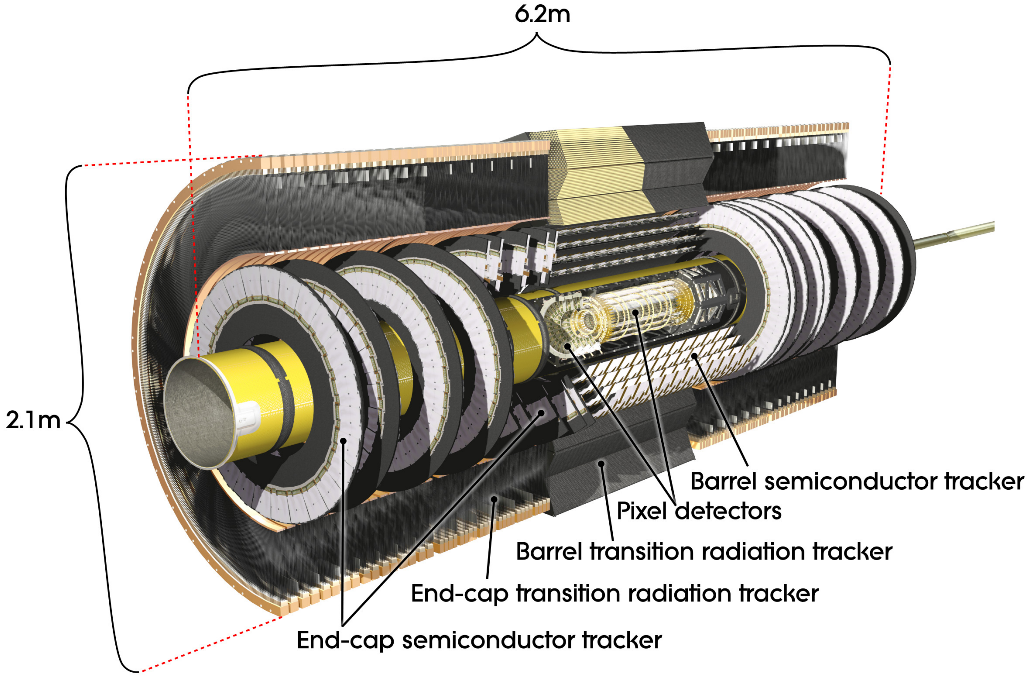

Figure 7.4: Shows a cross section of the ATLAS Inner Detector.

Inner Detector

The innermost part of the detector is used to take extraordinarily accurate position measurements of charged particles emerging from the collisions. Contained in this part of the detector we find three subsystems: the innermost pixel layers, the silicon microstrip layers, and the Transition Radiation Tracker. These are all immersed in an 2 T uniform magnetic field produced by the solenoid magnet. The position measurements from each layer is combined and through fits to these measurements particle tracks are estimated. These measurements are further used in the determination of the p_T, the charge of the particle, and its direction. Together all the tracks from a single event are combined in order to reconstruction the origins of the different particles created, this is referred to as a vertex. The primary vertex indicates the initial pp collision while any short lived particles created here each travel until they decay in what is called a secondary vertex, and any subsequent particles can go on to create tertiary vertices after this point.

Currently due to the high luminosity observed at ATLAS there is an Insertable B-layer, IBL, between the previous layers of the pixel detectors and the beam pipe. This additional subsystem has been introduced due to concerns of significant radiation damage to the pixel layers in LHC Run 2. Since this would end in reduced tracking efficiencies, and especially the ability of tagging possible b-quark decays.

All of this culminates in the ability to successfully determine the how the particles behave in the enclosure of the beam pipe. This proves crucial for most B-physics analysis, as most of the particles we are searching for decays only a few hundreds of µm from the primary vertex. The track reconstruction efficiencies can be found in Table 7.1 and vertex efficiencies in Table 7.2.

Calorimetry

Outside the ID sits the solenoid magnet and is subsequently followed by the electromagnetic and hadronic calorimeters. Due to the sheer size of this subsystem most of its components has been chosen on a cost-efficiency basis. Hence these are both sampling calorimeters and where they are constructed from several alternating

Table 7.1: Summary of key performance numbers for the loose, loose-primary and tight-primary selections for ⟨µ⟩ = 40. These are given for all tracks passing the selections as well as for tracks with $p_T > 2\,\text{GeV}$. The efficiency is only calculated for tracks from the hard scattering interaction while the fake fraction is for the whole event [21]. In comparison the ⟨µ⟩ = 23.7 for the combined data of 2015 and 2016.

	Efficiency	**Fake fraction**
	All tracks / $p_T > 2\,\text{GeV}$	
Loose	84.60 % / 87.12 %	14.43 % / 7.79 %
Loose-primary	83.92 % / 86.77 %	13.56 % / 7.54 %
Tight-primary	77.38 % / 82.11 %	3.67 % / 1.13%

Table 7.2: Vertex match and fake rates for ⟨µ⟩ = 60 using the tracks from the tight-primary selection but in addition requiring either an IBL or a B-Layer hit, or either of the two [21]. This is well above the ⟨µ⟩ = 23.7 for the combined data of 2015 and 2016. Hence one would expect better match rates than what this table shows.

Require hit in:	**Match Rate**	**Fake Rate**
IBL or B-Layer	42.99 %	0.41 %
IBL	43.42 %	0.29 %
B-Layer	42.96 %	0.39 %
Baseline for Run 1	42.63 %	2.03 %

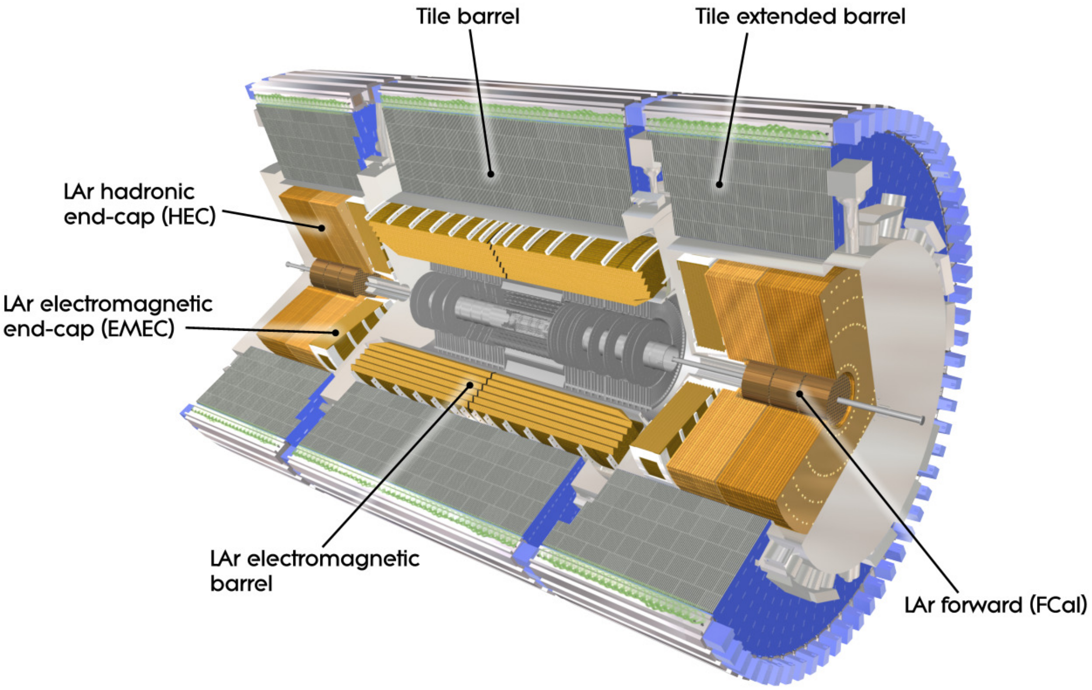

Figure 7.5: Shows a cross section of the Calorimetry Detectors used within the ATLAS detector.

layers of active and passive materials. This is in order to minimize the depth and money required to measure the energy of particles. A combination of techniques allows these detectors to accommodate for the broad degree of physics processes that are of interest. The ECAL is designed with a fine granularity in mind and this makes it ideally suited for precision measurements of both electrons and photons. The HCAL is a much coarser defined system. This has been done to better satisfy the requirements needed in jet reconstruction and to improve measurements of the missing transverse energy, E_t^{miss}. Both of these systems have been designed to ensure that their corresponding particle showers are well contained within the detectors, and to allow as little punch through as possible into the muon detectors.

Muon Spectrometers

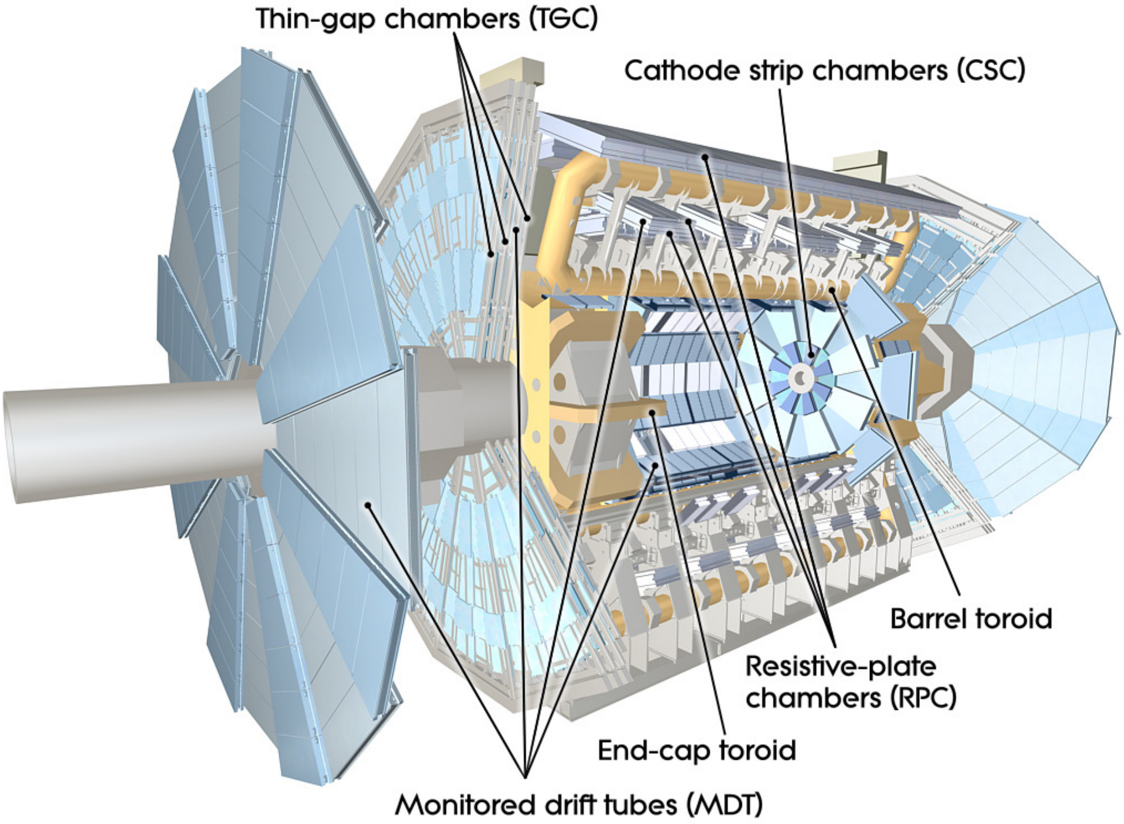

Figure 7.6: Shows a cross section of the Muon Spectrometers located in the ATLAS detector.

The Muon Spectrometers (MS) is the outermost subsystem on ATLAS. It has been designed with the goal in mind to be able to detect muons in the psuedorapidity region of $|\eta| \leq 2.7$ and to provide precise momentum measurements. The relative resolution on the momentum measurements are within 3 % over a wide p_T range, however they rise to 10 % at $p_T \approx 1$ TeV. The Monitored Drift Tubes (MDT) is the detectors which provide the high precision measurements in this η region. While the Resistive-Plate Chambers (RPC) and Thin-Gap Chambers (TGC) are responsible for the muon triggers as well as complementing with additional spatial measurements.

Muon reconstruction

The muons can be reconstructed several different ways. The reconstruction can either be performed through combining the measurements of the ID and the MS or through utilizing only the hits recorded by the MS. For this analysis we have chosen to only use the combined muons. To determine these, track reconstruction is performed independently in the ID and MS, and a combined track is formed with a global refit that uses the hits from both the ID and MS subsystems. During the global fit procedure, MS hits may be added to or removed from the track to improve the fit quality. Most muons are reconstructed following an outside-in pattern recognition, in which the muons are first reconstructed in the MS and then extrapolated inward and matched to an ID track. An inside-out combined reconstruction, in which ID tracks are extrapolated outward and matched to MS tracks, is used as a complementary approach to confirm results.

The performance group responsible for the MS reports a muon reconstruction close to 99 % over most of the psuedorapidity region of $|\eta| \leq 2.5$ for muon $p_T > 5\,\mathrm{GeV}$. While the relative muon p_T resolution for J/ψ is found to be 1.7 % in the barrel and 2.3 % in the endcaps [22].

Chapter 8

Standard Model

The Standard Model (SM) has been slowly developed over the years since Sheldon Glashow discovered a way to combine the electromagnetic and weak interactions in 1961. Since then advances in both theory and experiments have pushed the Standard Model (SM) to what it is today. It is the theory which formulates the majority of the present knowledge on known particle physics. While there are several extensions beyond the SM which covers hypothetical particles and the like. The SM describes the behaviour of particles on the most fundamental level. Its mathematical formulations allow for very detailed and precise calculations of physics processes at high energy. Several of these calculations have been measured and confirmed with extraordinary precision and the SM has to this day not been proven wrong. Within this chapter we will cover several of the general concepts of this model. All values for the elementary particles and interactions are taken from the Particle Data Group (PDG) [23].

8.1 Elementary particles and their interactions

8.1.1

8.1.2 Elementary particles

Everything we see around us is made up by elementary particles. These particles have a spin $^1/_2$ and are denoted *fermions*. We have two groups of fermions, *leptons* and *quarks*, which are further arranged into three generations which are sometimes referred to as *flavour*. Each generation has two members and common for all of them is that their electric charge differ by the elementary charge e. These members are typically referred to as the up or down type of their respective generation. Additionally, each member has their own anti-particle which has the exact same mass, but opposite charges.

Leptons

For the down type leptons we find the electrically charged particles. The three generations of these down type leptons are, in ascending order: the electron e^-, the muon μ^-, and the tau τ^-. While for the electrically neutral particles we find, in ascending order: the electron neutrino ν_e, the muon neutrino ν_μ, and the tau neutrino ν_τ. Although all of these particles differ in mass and lifetimes, common for all leptons is that they couple to bosons with the same strength, known as *lepton universality.* Since the neutrinos are electrically neutral they only couple to the weak interactions. It was long believed that neutrinos were massless, however recent observations of neutrino oscillations require that they are massive. There are

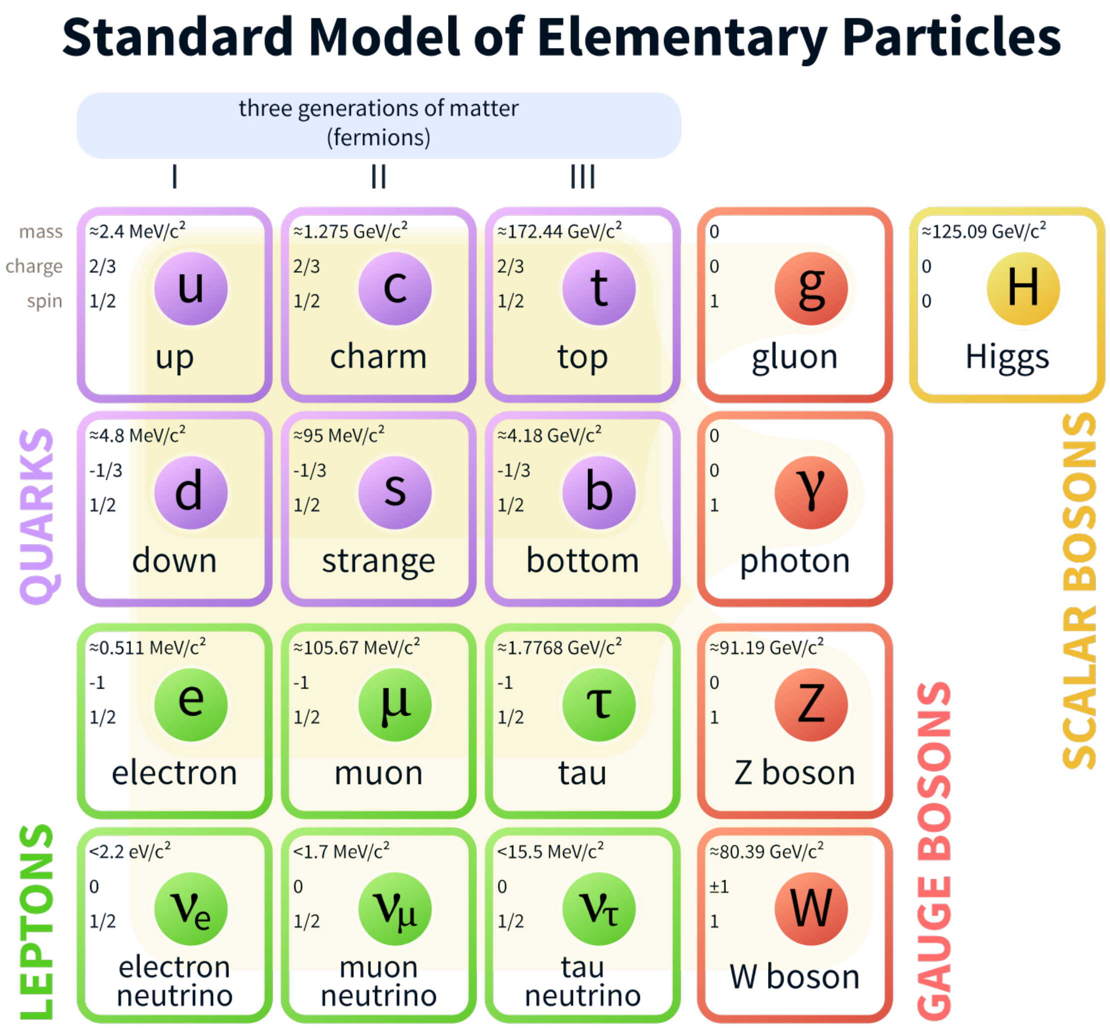

Figure 8.1: Illustrating the simplicity when it comes to the elementary particles of the SM. These simple building blocks can be used to make the entirety of the particle zoo.

three known discrete neutrino masses which does correspond uniquely to a single flavoured neutrino. Although we only have measurements of the differences between these masses and not of the masses themselves, experiments show that the magnitude of the masses is small [24] [25]. The leptons are listed in Table 8.1.

Quarks

The quarks are characterized by the fact that they are massive and carry three different charges: the electric charge of Quantum Electrodynamics (QED), the weak isospin charge of Electro Weak (EW) theory, and the colour charge of Quantum Chromodynamics (QCD). Thus they can interact through all of the four known fundamental forces. The concept of colour charge requires that a quark is in one of three possible quantum states. These three states are by convention labeled as red, green, or blue. Their corresponding anti-particles carry anti-colour, namely anti-red, anti-green, and anti-blue. In nature we never directly observe any coloured particles, and all known composite particles consisting of quarks are colourless, these are typically referred to as the colour white. This is known as *confinement* and as a consequence of this all coloured objects must be in pairs in order to produce white particles. Confinement forces all known coloured particles to undergo instantaneous

Table 8.1: The values listed for the masses of the charged leptons and lifetimes are taken from the PDG [23] while the neutrino masses are from another source [25]. Q symbolizes the electric charge of the particles, while the L_α is the lepton number of the corresponding particle. Both the electron and muon mass measurements have extraordinary high precision.

Generation	**Particle**	**Symbol**	**Q** [e]	**Spin**	L_e	L_μ	L_τ
First	Electron Neutrino	ν_e	0	½	1	0	0
	Electron	e	-1	½	1	0	0
Second	Muon Neutrino	ν_μ	0	½	0	1	0
	Muon	μ	-1	½	0	1	0
Third	Tau Neutrino	ν_τ	0	½	0	0	1
	Tau	τ	-1	½	0	0	1

Generation	**Particle**	**Mass** [MeV c^{-2}]	τ[µs]
First	Electron Neutrino	$< 0.000\,002$ (90% C.L.)	Unknown
	Electron	$0.510\,998\,946\,1 \pm 0.000\,000\,003\,1$	Stable
Second	Muon Neutrino	< 0.190 (90% C.L.)	Unknown
	Muon	$105.658\,374\,5 \pm 0.000\,002\,4$	$2.196\,981\,1 \pm 0.000\,002\,2$
Third	Tau Neutrino	< 18.2 (95% C.L.)	Unknown
	Tau	1776.86 ± 0.12	$(2.903 \pm 0.5) \times 10^{-7}$

Table 8.2: The **Q** symbolizes the electric charge of the particles, the I_3 corresponds to the isospin, **B** is the baryon quantum number of the particles, **C** is the charm, **S** strangeness, **T** topness, and **B'** the bottomness of the corresponding particles. All values are taken from the PDG [23].

Generation	**Particle**	**Symbol**	**Q** [e]	**Spin**	I_3	**B**	**C**	**S**	**T**	**B'**	**Mass** [MeV c^{-2}]
First	Up	u	⅔	½	½	⅓	0	0	0	0	$2.2^{+0.6}_{-0.4}$
	Down	d	-⅓	½	-½	⅓	0	0	0	0	$4.7^{+0.5}_{-0.4}$
Second	Charm	c	⅔	½	0	⅓	1	0	0	0	$(1.28 \pm 0.03) \times 10^3$
	Strange	s	-⅓	½	0	⅓	0	-1	0	0	$3.5^{+0.7}_{-0.3}$
Third	Top	t	⅔	½	0	⅓	0	0	1	0	$(173.1 \pm 0.6) \times 10^3$
	Bottom	b	-⅓	½	0	⅓	0	0	0	-1	$(4.18^{+0.04}_{-0.03}) \times 10^3$

hadronization at the point of their creation. The t-quark is the only known particle that does not undergo this treatment, as it decays before this can occur. There are only two known methods of creating colourless particles. This can either be achieved through combining three different (anti-)quarks with the colours (anti-)red, (anti-)green, and (anti-)blue, known as $(\bar{q}\bar{q}\bar{q})qqq$ or (anti-)baryons. Or one may combine a quark and an anti-quark, i.e. red and anti-red creates white particles, known as $q\bar{q}$ or mesons. The quarks are listed in Table 8.2

8.1.3 Forces

All elementary particles are effected by one or more of the four fundamental forces which are mediated by particles known as bosons. All bosons have integer spin. The electromagnetic force is mediated by quanta known as photons γ and it only interacts with electrically charged particles. The photon is massless, has no charge of any kind, and has an infinite range where the strength of the electromagnetic force is proportional to the inverse of the distance, i.e. $\propto {}^{1}/_{r}$. The interaction between

Table 8.3: The **Q** symbolizes the electric charge of the particles, the T_3 corresponds to the weak isospin. Values taken from PDG [23]. The massless bosons does not have confirmed masses of 0, only limits which are incredibly small, still they have been listed as 0 within this thesis.

Force	**Particle**	**Symbol**	Anti-Particle	**Q** [e]	T_3	**Colour Charged**	**Mass** [MeV c^{-2}]
Eletrcomagnetic	Photon	γ	Self	0	0	No	0
Weak	W boson	W^-	W^+	-1	1	No	80.385 ± 0.015
	Z boson	Z^0	Self	0	0	No	91.1876 ± 0.0021
Strong	Gluon	g	Self	0	0	Yes	0
Gravity	Graviton	G	Self	0	0	No	0

coloured particles is mediated by the gluon g and is referred to as the strong force. The gluon is also massless, though it is not without charge as it has two colour charges. Since the gluons carry colour charge it can self-interact, this along with the principles of colour confinement limits the interaction range of the strong force to roughly 1 fm. The weak interaction is special in that it has three massive mediators, namely the charged $W^{\pm}$ and the neutral Z^0. Since the mediators are massive and unstable the range of the weak force is constrained by the mediators lifetime, and is on the order of 10^{-3} fm. In the electroweak theory of the SM, the weak and the electromagnetic forces are treated as different manifestations of a single electroweak interaction. The SM does not describe the interaction between fundamental particles and gravity, as this is still a poorly understood topic and the impact of gravity would be negligible compared to the other forces. The forces and the corresponding boson properties are listed in Table 8.3.

8.1.4 The gauge principles

In order to be able to describe the behaviour of high-energy particles one has to involve both quantum mechanics and special relativity. When one combine these two mathematical concepts we end up with Quantum Field Theory (QFT) where particles are considered as quantized excitations of their corresponding field. The nomenclature, symbols, and the procedure used within this thesis for QFT is conforms to the ones used in [26]. The Minkowski metric signature used in this thesis conforms to the $(+,-,-,-)$ notation. In the confines of QFT the number of particles of a given system is not a conserved quantity. This allows for the creation and annihilation of particles within a system. For every interaction described by the SM there exists a *gauge theory* which provides the rules necessary to calculated the probabilities of interaction processes. The term gauge theory is used for any theory in which a Lagrangian is invariant under a phase, or gauge as it were, transformation. If one were to write down the most general form of how such a transformation changes a field ψ when it is applied to the field it would yield Eq. 8.1.

$$\psi(x) \rightarrow U\psi(x) \qquad\qquad U = \exp\big(ig\Sigma_{\alpha=1}^{N}\epsilon_\alpha\chi_\alpha\big) \tag{8.1}$$

χ_α = Hermitian operators

ϵ_α = Continuous real parameters

$$U = U(x) = \exp\big(ig\Sigma_{\alpha=1}^{N}\epsilon_\alpha(x)\chi_\alpha(x)\big) \tag{8.2}$$

The ϵ_α in Eq. 8.1 are continuous real parameters that change the phase of the field by an equal amount for each space-time coordinate. This is considered a *global* transformation. However the SM Lagrangian requires invariance of *local* transformations as well, where the $\epsilon_a lpha$ are a function of space-time x. This causes the transformation to be modified as Eq. 8.2 shows. According to Noethers theorem the invariance of the Lagrangian implies that there is a conserved quantity, this quantity is what we refer to as the charge of a QFT and it reflects the underlying symmetric nature of the system. The properties and dimensions of the transformation matrix U specifies in which symmetry group the theory belongs. Generally we speak of a set of $n \times n$ unitary matrices which we refer to as U(n). If the determinant of one of these matrices is +1 it is referred to as a special unitary matrix, SU(n).

8.1.5 Quantum Electrodynamics

The QFT which describes the electromagnetic interactions are referred to as Quantum Electrodynamics (QED). It is considered to be the simplest of the gauge theories, however it has been a major success since its creation and its properties has been very accurately measured. The free-field Lagrangian for QED is given by Eq. 8.7. QED is an U(1) gauge theory where the fermion fields transform as in Eq. 8.4.

$$\mathcal{L}_0 = \bar{\psi}(x)(i\gamma^\mu\partial_\mu)\psi(x) \tag{8.3}$$

$$\begin{aligned} \psi(x) &= U(x)\psi(x) = \exp(-ieQ\epsilon(x))\psi(x) \\ \bar{\psi}(x) &= U(x)\bar{\psi}(x) = \exp(ieQ\epsilon(x))\bar{\psi}(x) \end{aligned} \tag{8.4}$$

Simply inserting these transformations into the QED Lagrangian will not leave it invariant. To restore the invariance of the Lagrangian one has to replace the ordinary particle derivative with a new covariant derivative as seen in Eq. 8.5.

$$\partial_\mu \to \mathcal{D}_\mu = \partial_\mu + ieQA_\mu \tag{8.5}$$

$$A_\mu \to A_\mu + \partial_\mu\epsilon(x) \tag{8.6}$$

The conserved quantity in QED is of course the electric charge, while the strength of the interacting fields is given by the elementary charge e. In case of QED, the A_μ observed in Eq. 8.5 can be interpreted as the photon field. This field further transforms as given by Eq. 8.6. In order to fully restore the invariance of the Lagrangian the transformations given by these two equations are combined and inserted into it. When the covariant derivative $\mathcal{D}_\mu$ is inserted into the free-field Lagrangian $\mathcal{L}_0$ one ends up with a new Lagrangian. This can be further separated into the original $\mathcal{L}_0$ and a completely new part $\mathcal{L}_{int}$. This new Lagrangian is responsible for the interaction between photons and electrically charged fermions. It is then possible to also include the terms for the pro$\mathcal{L}_A$, which leads to the full QED Lagrangian as given by Eq. 8.7.

$$\mathcal{L}_{QED} = \mathcal{L}_0 + \mathcal{L}_{int} + \mathcal{L}_A = \bar{\psi}(x)(i\gamma^\mu\partial_\mu)\psi(x) - eQ\bar{\psi}(x)\gamma^\mu\psi(x)A_\mu(x) - \frac{1}{4}F^{\mu\nu}F_{\mu\nu} \tag{8.7}$$

$$F_{\mu\nu} = \partial_\mu A_\nu - \partial_\nu A_\mu \tag{8.8}$$

8.2 Standard Model

When one further extends the principle of gauge invariance to all other fundamental interactions it leads to the Standard Model (SM). It is based on the combined system of $SU(3)_C \times SU(2)_L \times U(1)_Y$ gauge groups. The indices on these refer to the charge of the interaction: C for colour charge, L for the left-handedness - otherwise known as chirality - and the Y is for the hypercharge.

8.2.1 Quantum Chromodynamics

Quantum Chromodynamics (QCD) is gauge theory for the strong interactions. The transformation matrix for QCD is the $SU(3)$, and gauge invariance of this matrix requires that there are eight independent real gluon fields. These fields carry both a colour and an anti-colour, thus they can couple to each other or perform self-interactions. The coupling strength α_s for these fields is highly dependent on the momentum transfer q^2 of the interaction in question. For a high q^2, which corresponds to short distance between the interacting particles, the coupling strength tends towards 0. This is known as asymptotic freedom. Conversely, if one were to attempt a separation of one quark in a bound state, the strength of the interaction increases. When the distance between the quarks becomes high enough, the interaction between the quarks causes a situation where it is energetically favourable to instead create another $q\bar{q}$ pair. The initial quarks then hadronize and two new bound states are formed. Since we are required to apply perturbation theory in order to successfully calculate amplitudes and for these we require infinitesimal strengths in order for these to converge. As such it is only possible to apply perturbation theory to QCD above a certain threshold. This threshold is referred to as Λ_{QCD} and its value is scale dependent, however it is typically taken at $\Lambda_{QCD} \approx 200\,\text{MeV}$.

8.2.2 Electro Weak Theory

All experiments that has been performed on weak interactions seem to indicate that only left-handed fermion fields interact. For anti-particles only right-handed fields occur. The definition of a right- or left-handed field is given by Eq. 8.9.

$$\begin{aligned} \psi^L(x) &= \frac{1}{2}\left(1-\gamma_5\right)\psi(x) \\ \psi^R(x) &= \frac{1}{2}\left(1+\gamma_5\right)\psi(x) \end{aligned} \tag{8.9}$$

For Electro Weak (EW) a $SU(2)$ gauge symmetry is needed. The corresponding conserved quantity is the weak isospin T_α, $\alpha = 1, 2, 3$. The left-handed structure of the weak interaction is generated by setting the isospin components of the right-handed leptons and quarks to be 0. Hence they are not affected by the $SU(2)_L$ transformation. However the electromagnetic interaction does not differentiate the handedness of particles. Thus in order to successfully unify the weak and electromagnetic interactions we have to introduce a new conserved quantity called hypercharge Y. This gives rise to the $U(1)_Y$ gauge symmetry. The hypercharge is related to the electric charge Q and the third component of the weak isospin T_3 as shown in Eq. 8.10.

$$Y = \frac{Q}{e} - T_3 \tag{8.10}$$

When combining these gauge transformations one gets the combined fermion fields as given by Eq. 8.11. The σ_α corresponds to the 2×2 Pauli matrices, while ϵ_α and ϵ are real differentiable functions. Since the Pauli matrices do not commute the theory is said to be non-Abelian, which results in a more complicated Lagrangian than for QED. The combined $SU(2)_L \times U(1)_Y$ group yields a total of four gauge fields. These can be turned into two which are charged, namely the $W^\pm$, and the other two can be combined into the neutral Z^0 and γ. One of the main reasonings behind combining the electromagnetic and weak interactions were due to seemingly both the Z^0 and γ contributing to the same interaction amplitudes. All of this leads to there being a mixing angle between these two particles, which is known as the weak mixing angle θ_W.

$$\begin{aligned} \psi^L(x) &\to \exp\left[ig\frac{\sigma_\alpha}{2}\epsilon_\alpha(x) + ig'Y\epsilon(x)\right]\psi^L(x) \\ \psi^R(x) &\to \exp\left[ig'Y\epsilon(x)\right]\psi^R(x \end{aligned} \tag{8.11}$$

8.2.3 The Higgs Model

The electroweak theory as it was presented in the previous section does not contain massive interacting bosons nor fermions. Instead these were formulated to be massless. However we know from experiments that the $W^\pm$ and Z^0 bosons, and fermions, do indeed have mass, hence something must be missing. The reason behind this is that mass terms of the form $m\psi^L\psi^R$ breaks the gauge invariance constructed in the EW theory and destroys its renormalizability. This further leads to divergences in high-order calculations. As such the Higgs model was introduced to give particles masses. The process through which this happens is known as *spontaneous symmetry breaking.*

If we were to consider a system where the Lagrangian $\mathcal{L}$ is invariant under a certain symmetry transformation. Then every state of the system, including the vacuum, is unique and shares the invariance of the $\mathcal{L}$ as long as the system has no degenerate energy levels. However, if the energy levels are indeed degenerate then there is no explicitly unique group state representing the vacuum. Hence one can arbitrarily select a ground state from amongst the degenerate levels and is no longer invariant under the transformation. This is the case for a symmetry being spontaneously broken. The implications of this in QFT leads to a non-vanishing vacuum expectation value for a quantized field.

In order to fix the massless particles of the EW theory we have to introduce new fields, as given by Eq. 8.12. This is referred to as a weak isospin doublet which contains two complex fields, and it transforms in the same way as ψ^L in Eq. 8.11 .

$$\Phi(x) = \begin{pmatrix} \psi_a(x) \\ \psi_b(x) \end{pmatrix} \tag{8.12}$$

The Higgs field of the vacuum state is not invariant under $SU(2)_L \times U(1)_Y$ hence it breaks the symmetry. However, it is invariant under pure $U(1)$ transformations which leaves the photon massless. The Higgs doublet adds an additional four degrees of freedom to the Lagrangian. These degrees of freedom can be removed through applying a selective and convenient gauge transformation. When this transformation is applied the degrees of freedom can be realized as the longitudinal polarization components of the $W^\pm$ and Z^0, hence giving them mass, and a new scalar particle H, namely the Higgs boson. The mass terms for the remaining fermions are acquired through Yukawa interactions with the Higgs field. These mass terms appear in the theory as free parameters and as such they have to be measured through experiments.

8.2.4 Quark Mixing

The EW Lagrangian also describes the interaction between quarks and its gauge bosons. It has two main components, or currents, the first is the charged current mediated by $W^{\pm}$, and the second for the neutral current as mediated by the Z^0 and γ. Looking at the charged current we encounter the bilinear terms of Eq. 8.13.

$$\sum_{q=1}^{3} \bar{u}_q^L \gamma^\mu d_q^L \tag{8.13}$$

The terms u_q^L, d_q^L are eigenstates of the weak interaction. The weak interaction does not directly couple to the mass eigenstates of the quarks, but instead it couples to linear combinations of them. These can be constructed into unitary matrices for the up and down type quarks separately, as given by Eq. 8.14.

$$\begin{pmatrix} u_1 \\ u_2 \\ u_3 \end{pmatrix}_{L,R} = U_{L,R} \begin{pmatrix} u \\ c \\ t \end{pmatrix}_{L,R} \qquad \begin{pmatrix} d_1 \\ d_2 \\ d_3 \end{pmatrix}_{L,R} = D_{L,R} \begin{pmatrix} d \\ s \\ b \end{pmatrix}_{L,R} \tag{8.14}$$

Using the results of Eq. 8.14 one can then rewrite Eq. 8.13, yielding Eq. 8.15. This equation seem to indicate that the charged currents causes quark mixing. One can then construct a matrix to describe this mixing, this matrix is known as the Cabibbo-Kobayashi-Maskawa (CKM) matrix and is shown in Eq. 8.16.

$$\begin{pmatrix} \bar{u} & \bar{c} & \bar{t} \end{pmatrix}_L U_L^\dagger D_L \gamma^\mu \begin{pmatrix} d \\ s \\ b \end{pmatrix}_L \tag{8.15}$$

$$V_{CKM} \equiv U_L^\dagger D_L = \begin{pmatrix} V_{ud} & V_{us} & V_{ub} \\ V_{cd} & V_{cs} & V_{cb} \\ V_{td} & V_{tc} & V_{tb} \end{pmatrix} \tag{8.16}$$

The CKM V_{CKM} has four free parameters, which are typically parameterized by three angels and one complex phase. The diagonal entries in this matrix has values close to unity. This is interpreted as an indication that charged-current weak interaction are most likely to occur within a generation. These transitions are typically referred to as *CKM favoured transitions.*

The neutral currents yield bilinears on the form as seen in Eq. 8.17. The fact that $U_L^\dagger U_L = 1$ implies that there does not exist any flavour changing neutral currents to the first order.

$$\begin{pmatrix} \bar{u} & \bar{c} & \bar{t} \end{pmatrix}_L U_L^\dagger U_L \gamma^\mu \begin{pmatrix} d \\ s \\ b \end{pmatrix}_L + \text{Right-handed terms} \tag{8.17}$$

8.2.5 CP Violation

The existence of a complex phase in the CKM matrix implies the possibility of particles and anti-particles behaving differently. The fact the $W^{\pm}$ bosons only couple to left-handed particles suggests that the weak interaction is not symmetric under a parity transformation P. Under such a transformation the handedness of the spatial coordinates are reversed. It can also be shown that the weak interaction is not symmetric under a charge transformation C. A charge transformation transforms a particle to its anti-particle. However, most weak interactions are symmetric under a combined transformation of these two, namely a CP transformation. The first known exception to this was observed in $K^0 - \bar{K^0}$ mixing in 1964 [27]. In such a mixing the K^0 is able to oscillate into its anti-particle $\bar{K^0}$ and vice versa. This implies that all observable neutral kaons are linear combinations of two other states. These states are simply referred to as K_S (short lifetime, CP even) and K_L (long lifetime, CP odd) due to their respective lifetimes. If one were to have CP conservation then the CP odd K_L should always decay into a set of three pions as these are also CP odd. However experiments show that the K_L can also decay into a two pions with branching ratios of $\mathcal{B}(K_L \to \pi^+\pi^-) = 0.20\%$ and $\mathcal{B}(K_L \to \pi^0\pi^0) = 0.08\%$, hence CP is violated. It was also discovered mixing in both the $B^0 - \bar{B^0}$ in 2001 [28] [29] and $D^0 - \bar{D^0}$ in 2007 [30] system.

However, CP violation is not only found in the mixing sector. It can also arise through the decay of particles. This happens if the decay amplitudes for a process and its CP conjugated process are different. One can measure this CP asymmetry through observing the decay of charged mesons M into a CP eigenstate f, the asymmetry is given by Eq. 8.18. While for neutral mesons, the interference between decays with and without mixing is an additional source of CP violation.

$$\mathcal{A}_{CP} = \frac{\Gamma\left(M^- \to f\right) - \Gamma\left(M^+ \to f\right)}{\Gamma\left(M^- \to f\right) + \Gamma\left(M^+ \to f\right)} \tag{8.18}$$

Chapter 9

B Physics

Studies performed on B mesons offer a throve of valuable insight into the processes and parameters of the SM, such as measurements of the CKM elements, CP violating phases, and flavour changing neutral processes. This chapter wll cover the production and decay of B mesons, with emphasis on the two heavy-quark system of B_c.

9.1 Heavy quark production

When the mass of a quark $\mathcal{Q}$ is much larger than the corresponding QCD energy scale, $\Lambda_{QCD} \approx 200\,\mathrm{MeV}$, it is defined as a heavy quark. In *pp* collisions at the LHC, the leading-order QCD processes for production of heavy quarks $\mathcal{Q}$ are light quark annihilation and gluon-gluon-fusion. These processes are shown in Eq. 9.1 and their corresponding Feynman diagram contributions can be seen in Figure 9.1. There are also equivalent processes for Electroweak interactions although their contributions are negligible in comparison. The production of heavy quarks through gluon fusion and quark annihilation are collectively called *flavour creation* processes.

$$q\bar{q} \rightarrow \mathcal{Q}\bar{\mathcal{Q}} \qquad\qquad gg \rightarrow \mathcal{Q}\bar{\mathcal{Q}} \tag{9.1}$$

The production can also be carried out through *flavour excitation* processes. In these the heavy quark is scattered from the quark sea in one of the incident hadrons. The lowest-order diagrams for these processes can be seen in figure 9.2. However, in order to successfully calculate the final state of many typical decays one needs to include higher-order QCD processes which will involve $g \rightarrow \mathcal{Q}\bar{\mathcal{Q}}$ vertices. These are known as gluon fragmentation or splitting. The ratio between the rate of gluon fragmentation or fusion is energy dependent, where the gluon fragmentation is dominating at center-of-mass energies much higher than the mass of the heavy quarks.

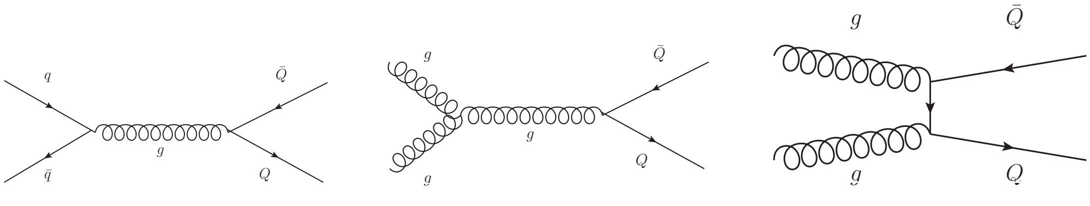

(a) Light quark annihilation. (b) Gluon fusion - s-channel. (c) Gluon fusion - t-channel.

Figure 9.1: Leading-order Feynman diagrams for flavour creation processes.

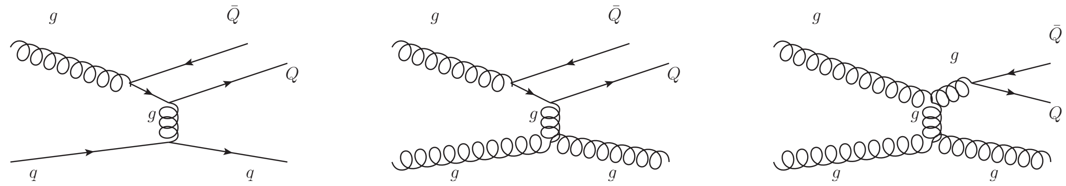

(a) Heavy sea quark scattering off another quark.

(b) Heavy sea quark scattering off another gluon.

(c) Gluon fragmentation.

Figure 9.2: Leading-order Feynman diagrams for flavour excitation processes.

9.2 Decay of heavy quarks

For decays of composite particles consisting of a light and a heavy quark, such as the $D^+(c\bar{d})$ or $B^+(u\bar{b})$ mesons, the energy released by the heavy quark is of a much greater magnitude than its lighter partner. In such cases it is safe to neglect the contributions of the light quark if one needs only a naïve estimate on the decay amplitude. One can look at the lighter partner as a passive spectator in the decay, this is called the *spectator* model. Hence we are left with the interaction of a single heavy quark decaying, which can be perturbatively solved. However, if this naïvety holds it would indicate that all decays involving a heavy and a like quark should in principle have equal lifetimes. While this is true to some regard, as the lifetime is typically of the same order, to end up with a more precise estimate one would have to include QCD effects.

Hadronic B decays are theoretically difficult to determine due to the complexity of the QCD contributions. Thus one often evocate the usage of other tools to simplify this process. Effective field theories and heavy quark expansion are often used tools as this allows for a viable treatment of these processes. These tools require a specific energy scale as an input parameters, this scale is often chosen to be equal to the energy of the system in question, and the results are typically only valid near this chosen scale. When it comes to the decays of general B-meson, where there are typically only a single heavy quark, it is quite reasonable to choose an energy scale μ which is equal to the b-quark mass. These effective field theories are often constructed using the technique of the operator product expansion. Several possible Feynman diagrams that contribute to these hadronic B decays can be seen in Figure 9.3.

9.3 Operator Product Expansion

In the framework of the Operator Product Expansion (OPE) we find that the product of two fields at different points are expanded to a sum of local operators $\mathcal{O}_i$. These can be used to describe the long-distance QCD effects which are responsible for the binding of the quarks inside the hadron. While each operator is further multiplied with a scale-dependent coefficient $C_i(\mu)$. These are known as Wilson coefficients and they are included to deal with the short-distance perturbatively calculable effects of QCD. As an example one can look to Figure 9.4 to see how a relatively simple Feynman diagram is impacted by the inclusion of gluons. Using the simple spectator model observed in this figure one can then construct the effective Hamiltonian for the system, as given by Eq. 9.2. Although as the Wilson coefficients are scale dependent whereas the operators are not, any calculations done with OPE are only valid at the chosen scale μ. One typically vary the scale in the range of $\frac{m_q}{2} < \mu < 2m_b$ to determine the error on these calculations.

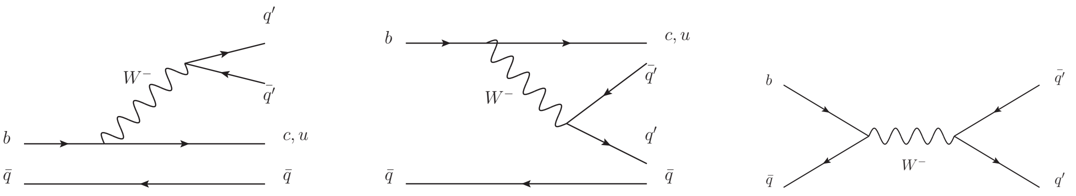

(a) Spectator.

(b) Colour suppressed.

(c) Annihilation.

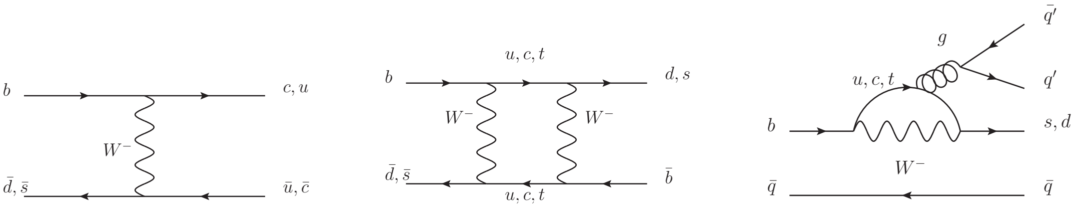

(d) W boson exchange.

(e) Box diagram showcasing neutral B mixing.

(f) QCD penguin.

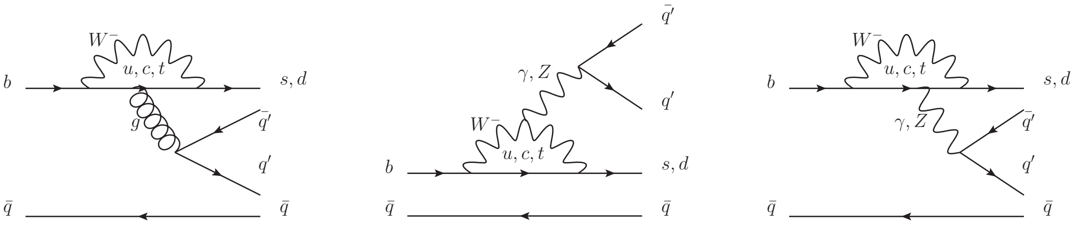

(g) QCD penguin.

(h) EW penguin.

(i) EW penguin.

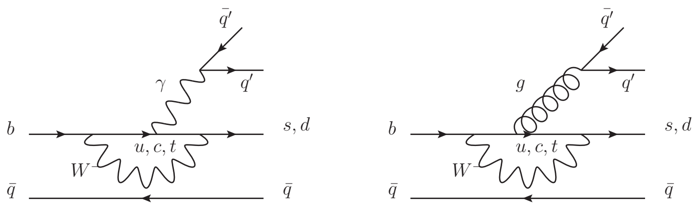

(j) Magnetic dipole penguin.

(k) Chromomagnetic dipole penguin.

Figure 9.3: These Feynman diagrams showcase several methods for which a B meson can decay hadronically.

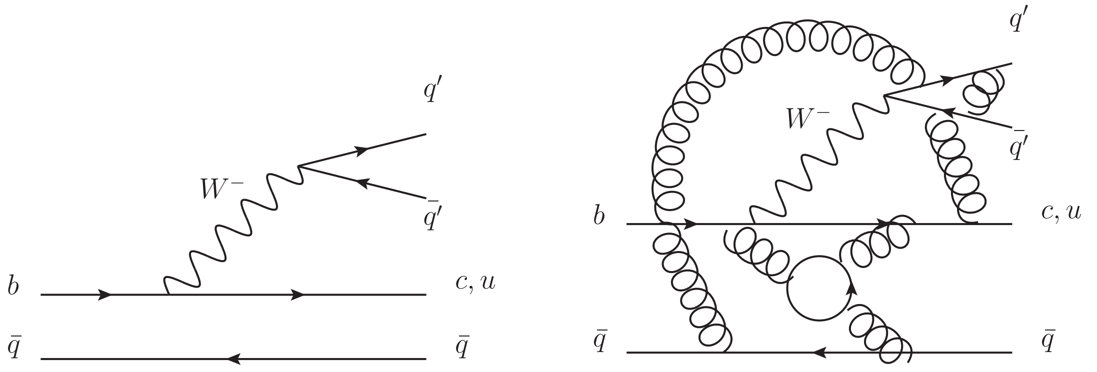

(a) Clean hadronic spectator decay.

(b) Can observe gluon radiation between quarks.

Figure 9.4: Spectator Feynman diagram with and without QCD effects included.

$$\mathcal{H} = \frac{G_F}{\sqrt{2}} V_{cb} V_{ud}^* \left[C_1(\mu)\mathcal{O}_1 + C_2(\mu)\mathcal{O}_2 \right] \tag{9.2}$$

G_F = Fermi constant
V_{cb} = CKM element
V_{ud}^* = CKM element

$$\begin{aligned} \mathcal{O}_1 &= \left(\bar{d}_i \gamma^\mu \left(1-\gamma^5\right) u_i\right) \left(\bar{b}_j \gamma^\mu \left(1-\gamma^5\right) c_j\right) \\ \mathcal{O}_2 &= \left(\bar{d}_i \gamma^\mu \left(1-\gamma^5\right) c_j\right) \left(\bar{b}_j \gamma^\mu \left(1-\gamma^5\right) u_i\right) \end{aligned} \tag{9.3}$$

The roman indices in Eq. 9.3 indicate the QCD colour of each participating quark. In addition to the current-current operators as shown in this equation we can also construct similar to describe semileptonic decays and penguins.

9.4 The B_c meson

The B_c and B_c^* are the ground state and the first excited state of the $\bar{b}c$ quarkonium system. While charmonium and bottomonium states have hidden flavours, the B_c meson contain two explicit flavours. Hence the B_c mesons decay only through weak interactions. While in the production of B_c mesons by strong or electromagnetic interactions, two additional heavy quarks are always produced. The production cross-sections for the B_c mesons are suppressed compared with the production cross-sections for the hidden-flavour quarkonia. This is due to the leading-order diagrams which are of a higher order in coupling constants and furthermore the phase-space is suppressed, owing to the presence of the two additional heavy quarks.

When it comes to the decay of the B_c meson there are to the lowest-order three main paths through which this can occur. Either heavy quark can appear as a spectator while the remaining quark decays, or they can both annihilate. It is expected that the c-quark decays are dominating, with an inclusive branching fraction of $\sim$70 %. While the b-quark contributes with an additional $\sim$20 % and the remaining $\sim$10 % is through weak annihilation [31], [32].

The calculations of decay amplitudes for B mesons with one light quark is often done by utilizing theories where the b-quark mass is taken at the limit where $m_b \to$

∞ as, i.e. Heavy Quark Effective Theory (HQET). Since we have two heavy quarks in the B_c meson this is unfortunately not applicable. However it can be calculated in the same way as other heavy quarkonium, by using different potential models or through various types of non-relativistic QCD. The methodology behind this is discussed thoroughly in [31], [33] and the remaining sections in this chapter will contain excerpts from these sources.

Exclusive rates for non-leptonic two-body decays can be calculated using the hypothesis of naïve factorization. This hypothesis is based on colour transparency – the assumption that for processes with a high recoil both the initial and final state interactions are suppressed. Since the products of B decays are energetic, the color transparency argument states that a $q\bar{q}$ pair stay close together, and has a small chromomagnetic dipole moment until it is far away from the other decay products. Therefore we have two energetic $q\bar{q}$ pairs who are thereby transparent to each other, and form final-state mesons without participating in any soft gluon exchanges. This is fortuitous since these effects would otherwise require an extremely complicated description. The two hadronic currents in Eq. 9.2 can therefore be factorized into a product of two matrix elements. For the decay of a $B_c^+ \to J/\psi\pi^+$ the amplitude can be expressed as in Eq. 9.4.

$$\mathcal{A}^{fact} = \frac{G_F}{\sqrt{2}} V_{cb} V^*_{ud} a_1(\mu) \left\langle \pi^+ \right| \left(\bar{d}\gamma^\mu \left(1-\gamma^5\right) u \right) \left|0\right\rangle \left\langle J/\psi \right| \left(\bar{c}\gamma_\mu \left(1-\gamma_5\right) b \right) \left|B^+\right\rangle \tag{9.4}$$

G_F = Fermi constant
V_{cb} = CKM element
V^*_{ud} = CKM element
$a_1(\mu) = C_1(\mu) + \frac{1}{N_c} C_2(\mu)$
N_c = Number of quark colours
$C_{1,2}$ = Wilson coefficients

The numerical value of a_1 is expected to be process-independent and its value would be equal to 1 if QCD corrections were neglected. This spectator, or colour-allowed, transition is dominated by contributions from $\mathcal{O}_1$ and is typically referred to as a Class I Decay. Class II Decays, which represents the colour-suppressed diagrams, are dominated by $\mathcal{O}_2$ and have a corresponding parameter a_2 which is equal to a_1 with the numerical indices swapped. There also exists a Class III Decay in which both $\mathcal{O}_1$ and $\mathcal{O}_2$ can generate the same finale state, this causes Pauli interference which can be either constructive or destructive.

Obtaining values for the matrix elements require some additional parameterizations. For instance, the amplitude for creating a pion from vacuum can be expressed by the decay constant f_π, resulting in Eq. 9.5. This decay constant has be accurately measured in semi-leptonic decays.

$$\left\langle \pi^+ \right| \bar{d}\gamma^\mu\gamma^5 u \left|0\right\rangle = -i f_\pi q^\mu \tag{9.5}$$

$q_\mu = \left(p_{B_c^+} + p_{J/\psi} \right)_\mu$
q_μ = momentum transfer satisfying $q^2 = m_\pi^2$

Additionally, the matrix elements for the $B(J^P) = 0^-$ to $J/\psi(J^P = 1^-)$ transition can be parametrized by four form factors, namely: V, A_0, A_1 and A_2. V enters into the vector contributions, as seen in Eq. 9.6, while the three A_i are used in the axial-vector part in Eq. 9.7. These form factors can be derived within the confines of several models of strong interactions, such as quark models or QCD sum rules.

$$\left\langle \pi^+ \right| \bar{c}\gamma_\mu b \left| B_c \right\rangle = \frac{2i}{m_B + m_{J/\psi}} \epsilon^{\mu\nu\rho\sigma} \epsilon^{J/\psi} p_{B_\rho} p_{J/\psi_\sigma} V(q^2) \tag{9.6}$$

$$\begin{aligned} \left\langle \pi^+ \right| \bar{c}\gamma_\mu \gamma_5 b \left| B_c \right\rangle = & 2m_{J/\psi} \frac{\epsilon^{J/\psi} \cdot q}{q^2} q_\mu A_0(q^2) \\ & + \left(m_{B_c^+} + m_{J/\psi}\right) \left(\epsilon^{J/\psi} - \frac{\epsilon^{J/\psi} \cdot q}{q^2} q_\mu\right) A_1(q^2) \\ & - \frac{\epsilon^{J/\psi} \cdot q}{m_{B_c^+} + m_{J/\psi}} \left(p_B + p - \frac{m_{B_c^+}^2 - m_{J/\psi}^2}{q^2} q\right)_\mu A_2(q^2) \end{aligned} \tag{9.7}$$

$m_{B_c^+}$ = The mass of the B_c

$m_{J/\psi}$ = The mass of the J/ψ

$\epsilon^{J/\psi}$ = The polarization vector of the J/ψ

For HQET, if one takes the limit where $m_Q \to \infty$ then the $b \to c$ transition for the $B^\pm$, B^0 or B_s^0 decays essentially becomes a symmetric operation under which the system of light quarks and gluons are left invariant. For these cases the hadronic matrix elements can be expressed in terms of the universal Isgur-Wise function ξ. This function only depends on the initial and final velocities of the heavy quark. In this heavy-quark mass limit the spin of the heavy and light degrees of freedom decouple. This spin is then separately conserved by the strong interactions. The consequence of this for B decays into vector states is that the form factor for both the vector and the axial-vector current are dependent on ξ. As such one can calculate the matrix elements by parameterizing this function. This is effective for single heavy hadrons, however the spin symmetry assumption is not directly applicable to the B_c meson decays, as these can involve a heavy spectator. Although, the form factors are expected to be closely related between decays involving a low recoil momenta. Calculations performed in the approximation of 0 recoil are in good agreement with other models. The q^2 dependence of the form factors are typically estimated by assuming a pole dominance, as seen in Eq. 9.8 which can be expanded into higher orders of q^2/M_{pole}. This mass pole is chosen by considering the exchange of the nearest lying particle in the t-channel.

$$f(q^2) = \frac{f(0)}{1 - q^2/M_{pole}} \tag{9.8}$$

Since there has been few measurements of the branching ratio for $B_c^+ \to J/\psi\pi^+$ and mostly only observations confirming the existence of the decay [34] [35] [36] [37] [38] [39] [40]. We have instead chosen to use a theory value listed in a review of theoretical predictions for this ratio [32]. Eq. 9.9 shows the calculated value for the branching ratio.

$$\mathcal{B}\left(B_c^+ \to J/\psi\pi^+\right) = (0.13 \pm 0.05)\,\% \tag{9.9}$$

9.4.1 Exclusive decays of $B^{\pm} \to J/\psi K^{\pm}$ and $B_c^{\pm} \to J/\psi\pi^{\pm}$

The decay of a B_c^+ meson into a J/ψ and a π^+ is an attractive decay channel to study due to the clean di-muon signature of the J/ψ and the simple decay topology. In the case of a Class I Decay of the B_c^+, the spectating c-quark combines with the $\bar{c}$-quark from the decaying $\bar{b}$-quark, while the emitted W^+ forms a π^+ through produced pair of $u\bar{d}$. For the normalization channel of this analysis we have chosen the $^{\pm} \to J/\psi K^{\pm}$ decay due to its similar topology, especially considering that ATLAS does not have any particle identification systems. This decay is colour suppressed and its amplitude is proportional to a_2 and the kaon production matrix element can be substituted by the kaon decay constant f_K. Eq. 9.10 shows the decay amplitude for the $B^{\pm}$.

$$\mathcal{A}^{fact} = \frac{G_F}{\sqrt{2}} V_{cb} V_{cs}^* a_2 \left\langle K^+ \right| \left(\bar{s}\gamma^{\mu}\left(1-\gamma^5\right) c \right) |0\rangle \left\langle J/\psi \right| \left(\bar{c}\gamma_{\mu}\left(1-\gamma_5\right) b \right) \left| B^+ \right\rangle \tag{9.10}$$

The decay of the $B^{\pm}$ is CKM favoured due to the fact that the relevant elements are close to unity. Hence the relatively large $B^{\pm}$ production cross section provides a high number of observed events. This exclusive decay is well studied as it is often used as a normalization channel for other decays as well. Thus the Monte Carlo (MC) samples are expected to represent the data reasonably well, and to provide a precise yield estimate.

When it comes to the $B_c^{\pm}$ production, the expected number of observed particles for a given integrated luminosity $\mathcal{L}_{int}$ is given by Eq. 9.11. The number of observed particles depend on the fragmentation probability f_c which is difficult to measure as it requires the precise knowledge of the total $b\bar{b}$ production cross section. However, if one were to take the ratio $N_{B_c^+}/N_{B^+}$ then the cross section factor cancels and we are left with Eq. 9.12.

$$N_{B_c^+} = \sigma_{pp\to b\bar{b}} f_c \mathcal{B}\left(B_c \to J/\psi\pi\right) \mathcal{B}\left(J/\psi \to \mu^+\mu^-\right) \epsilon_{B_c^+} \mathcal{L}_{int} \tag{9.11}$$

$\sigma_{pp\to b\bar{b}}$ = Cross section for $b\bar{b}$ pair production

f_c = Probability for a b-quark to hadronize into B_c, called Fragmentation Probablity

$\epsilon_{B_c^+}$ = Reconstruction efficiency for B_c

$$\frac{f_c}{f_u} = \frac{N_{B_c^+}}{N_{B^+}} \frac{\mathcal{B}\left(B^+ \to J/\psi K\right)}{\mathcal{B}\left(B_c \to J/\psi\pi\right)} \frac{\epsilon_{B^+}}{\epsilon_{B_c^+}} \frac{\mathcal{L}_{B^+}^{int}}{\mathcal{L}_{B_c^+}^{int}} \tag{9.12}$$

If one were to use samples were there is equal luminosities for both decays and expressing the branching fractions in terms of factorized amplitudes we end up getting Eq. 9.13. The only disadvantage of using the $B^+ \to J/\psi K^+$ as a normalization channel is the fact that it is colour suppressed while the B_c^+ decay is colour allowed so we end up with the ratio $\frac{a_1}{a_2}$. The Feynman diagrams for both decays can be seen in Figure 9.5.

$$\frac{f_c}{f_u} = \frac{N_{B_c^+}}{N_{B^+}} \frac{|V_{ud}|^2}{|V_{cs}|^2} \left(\frac{a_1}{a_2}\right)^2 \left(\frac{f_{\pi}}{f_K}\right)^2 \frac{\left|\langle J/\psi| \left(\bar{c}\gamma_{\mu}\left(1-\gamma_5\right) b\right) |B_c^+\rangle\right|^2}{\left|\langle J/\psi| \left(\bar{c}\gamma_{\mu}\left(1-\gamma_5\right) b\right) |B^+\rangle\right|^2} \frac{\epsilon_{B^+}}{\epsilon_{B_c^+}} \tag{9.13}$$

Seeing as the branching ratio of the B^+ channel [41], Eq. **??** has been measured with quite high precision the main contribution on the uncertainty on the measurement of f_c/f_u comes from the B_c branching fraction.

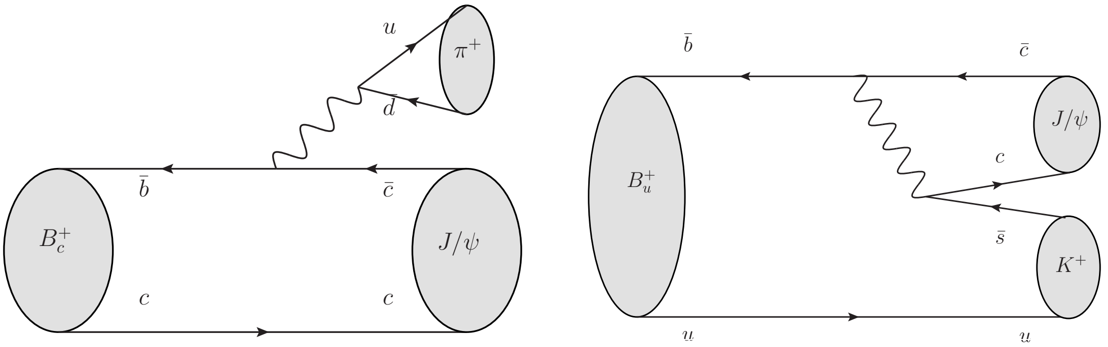

(a) Colour allowed decay for $B_c^+ \to J/\psi\pi^+$ (b) Colour suppressed decay for $B^+ \to J/\psi K^+$

Figure 9.5: Feynman diagrams for the two decays of study in this thesis.

Table 9.1: Values of the fragmentation probabilities taken from from [42]. The last column includes measurements performed at LEP, Tevatron and LHC.

Quantity	**Z decays**	**Tevatron**	**LHCb**	**Combined**
$f_u = f_d$	0.407 ± 0.007	0.344 ± 0.021		0.404 ± 0.006
f_s	0.101 ± 0.008	0.115 ± 0.013		0.103 ± 0.005
f_{baryon}	0.084 ± 0.011	0.196 ± 0.046		0.088 ± 0.012
f_s/f_d	0.249 ± 0.023	0.333 ± 0.041	0.259 ± 0.015	0.256 ± 0.013

$$\mathcal{B}\left(B^+ \to J/\psi K^+\right) = (1.026 \pm 0.031) \times 10^{-3} \tag{9.14}$$

While the fragmentation probabilities may in principle depend on transverse momentum, rapidity, and the beam particle of choice. The Heavy Flavor Averaging Group (HFLAV) [42] calculates averages of the measurements done on these probabilities under the assumption that the values are universal. The justification behind these assumptions is that size of the hadronization scale compared to the b-quark production interaction is rather small, $\left(\lambda_{QCD}^2 \ll q^2\right)$. Though there has not been performed enough studies on this to get a final confirmation on validity of this assumption. However, through combining these measurements the separate fragmentation probabilities are extracted, as seen in Table 9.1. Given the low production cross section of B_c mesons yields a very small value for f_c comparable to the other probabilities and as such it is given as 0 by HFLAV. The averages are constrained by the following identities as given in Eq. 9.15. As the B_c meson is indeed confirmed by several independent experiments, the fragmentation probability f_c cannot be exactly 0.

$$f_u = f_d \qquad f_c \sim 0 \qquad f_u + f_d + f_s + f_{baryon} = 1 \tag{9.15}$$

Chapter 10

Event Selection

The goal of any analysis is to maximize the number of signal events compared to any background contributions, while there are different methods of accomplishing this, the choice of strategy within this analysis ended up on utilizing a cut-based approach. Here one tries to maximize the significance of the MC datasets by cutting out events based on the different parameters related to the interacting particles, where the significance is defined by Eq. 10.1.

S = Number of signal events

B = Number of background events

$$Significance = \frac{S}{\sqrt{S+B}} \tag{10.1}$$

10.1 Monte Carlo Samples

Almost all MC samples used in this analysis has been officially generated in Pythia8 under the 2015 MC production campaign by the ATLAS Production Group, aside from the signal sample of B_c^+ which was produced privately. This signal sample was produced utilizing a Pythia8 script made for B^+ where the lifetime and mass was modified to the corresponding values of B_c^+. ATLAS has moved away from supporting FORTRAN in their latest software builds which makes this the only available method to get B_c^+ MC samples. This of course impacts the success of the MC used for the event selection optimization. However, according to the people in the B-physics MC production team, due to the similarity in the topology of the two decays it should still attain results which are usable. The commands used for the generation and simulation of these events were supplied by Semen Turchikhin from the production team. All MC samples used are listed in Table 10.1.

Each MC sample contains a fixed generated number of events, N_{gen}, corresponding to a set production cross section, σ_{gen}, which is calculated by Pythia. Since it's computationally heavy to generate the same number of events that one would expect to find in the real data, the MC samples needs to be scaled such that the integrated luminosity of these samples matches the luminosity which has been collected by ATLAS. The weight that is used to do this corresponds to the equation below:

N_{gen} = Number of generated events

σ_{gen} = Cross-section of generated events

$$\mathcal{L}_{gen} = \frac{N_{gen}}{\sigma_{gen}} \tag{10.2}$$

Table 10.1: The corrected cross-sections σ_{corr} include the branching ratio of forced decays, the filter efficiencies and a factor two for particle anti-particle symmetry. All the MC samples are created under the 2015 MC Production Campaign, and there were no available MC for these samples for 2016.

Sample	N_{gen}	$\sigma_{gen}[\text{nb}^{-1}]$	σ_{corr}	$\mu p_T thresholds[\text{GeV}]$
$B^+ \to J/\psi K^+$	989800	112440	1.7	3.5, 3.5
$B_c^+ \to J/\psi \pi^+$	964000	8097600	0.0126	3.5, 3.5
$b\bar{b} \to J/\psi X$	9909000	19568	61	3.5, 3.5
$b\bar{b} \to \mu^+\mu^- X$	49539000	78563	6327	3.5, 3.5
$pp \to J/\psi X$	4954989	3498.9	209	2.5, 2.5

$$w = \frac{\mathcal{L}_{Data}}{\mathcal{L}_{MC}} \tag{10.3}$$

10.1.1 Signal Samples

The signal samples used are generated by forcing the B-meson to undergo a decay through the channel of interest, this is to save both computational, time and space resources. So in order to get a correct value for the generated cross-section one has to apply the different branching fractions and generation efficiencies which are used for each sample. The signal samples are further scaled by a factor of two since only positively charged B-mesons are generated to account for the missing contributions from its anti-particle. All officially produced samples contain pileup corrections, as such one has several B-meson candidates per bunch crossing, this has not been applied to the privately generated B_c^+ signal sample as the GRID jobs failed repeatedly when this was attempted.

Table 10.2: Branching ratios for the relevant decay modes. All of B_c^+ values are theoretical predictions.

Decay Channel	$\mathcal{B}$ [%]
$J/\psi \to \mu^+\mu^-$	5.93 ± 0.06
$B^+ \to J/\psi K^+$	0.1016 ± 0.0033
$B_c^+ \to J/\psi \pi^+$	0.13 ± 0.05

In order to get the same number of events in the truth-matched MC as we do in the Data, we have defined a $\sim \pm 3\sigma$ range around the signal peak as the signal region. The B^+ signal peak was modeled using three different Gaussians centered around the same mass m_B, where two of them are to account for physics and detector resolution effects. This in turn is made into a PDF which is fitted to unbinned data by maximizing the likelihood function shown in Eq. 10.4.

$$L = \prod_{i=1}^{N} f_1 G_1(m^i_{J/,h}) + f_2 G_2(m^i_{J/\psi,h}) + (1 - f_1 - f_2) G_3(m^i_{J/\psi,h}) \tag{10.4}$$

$$G_\alpha(m^i_{J/\psi,h}) = \frac{1}{\sigma_\alpha \sqrt{2\pi}} \exp\left[-\frac{(m^i_{J/\psi,h} - m_B)^2}{2\sigma_\alpha^2}\right] \tag{10.5}$$

N = Maximum number of data points
G_α = Gaussian α
f_α = Fraction of contributing Gaussian α
σ_α = Width of Gaussian α
$m_{J/\psi,h}$ = Invariant mass of J/ψ and hadron (K^+ for B^+ or π^+ for B_c) in dataset
m_B = Gaussian peak center, corresponds to B-meson mass

The width that is used to determine the signal region band is a weighted sum of the corresponding Gaussian widths. While the lower and higher masses outside this region is respectively referred to as upper and lower sidebands.

$$\sigma_{SR} = f_1\sigma_1 + f_2\sigma_2 + (1 - f_1 - f_2)\sigma_3 \tag{10.6}$$

The signal model used for the B_c^+ uses one Gaussian instead of three, but the whole procedure is otherwise identical as for the B^+.

10.1.2 Background Samples

For the signal decays in question in this analysis we always have a secondary vertex from which a J/ψ and a separate hadron track originates. Though to mimic the continuous mass spectrum background one expects in data, one selects a J/ψ candidate and try to pair it with another random charged track. Then the pair is backtracked to see if they might originate from the same vertex, if they do then they are recreated as a B-meson with a mass corresponding to the invariant mass of the pair.

Another possible background contribution comes from other proper B-meson decays which causes a distribution with peaking structures; one typically refer to these as peaking background if its mass peak interferes with the signal peak.

In order to properly model the expected background from data one utilizes several different MC samples, which is then analyzed and further construct a background fit model to describe it. In these MC samples, any signal event is truth-matched away so one avoid double counting of signal events. Furthermore in the background sample where two random muons are being combined to a J/ψ candidate, any truth-matched J/ψ is removed in order to avoid double counting background events.

Direct J/ψ production

While there are a lot of decays that can produce a J/ψ as a secondary particle, it is also possible for two protons to produce a J/ψ directly. Since the production cross-section for this to take place is rather large, as it can arise through several possible QCD processes, it has significant contribution to the background. Though, while the B^+ ($\tau = 1.6 \times 10^{-12}$ s), and less so, the B_c^+ ($\tau = 0.5 \times 10^{-12}$ s) do exist for a long enough time-frame that they can "fly" from the primary vertex quite a bit before decaying, the negligible-in-comparison lifetime of the J/ψ ($\tau = 7.2 \times 10^{-21}$ s) makes it so that it decays almost immediately. Since these are produced by the protons in the initial interaction they are found fairly close to the primary vertex, as such they are highly sensitive to any cuts done on the distance between the primary and secondary vertex, otherwise known as L_{xy}.

Combinatorial $b\bar{b}$ background

In combinatorial backgrounds we have no J/ψ, but instead we find two muons from different sources which has been randomly combined along with a charged track. The main source of these muons are from semi-leptonic b-quark decays which produce a c-quark in the form of $b \to c\mu^- \bar{\nu_\mu}$ or $\bar{b} \to \bar{c}\mu^+\nu_\mu$. These c-quarks can further decay semi-leptonically or produce charmed hadrons which in turn can decay semi-leptonically. Since the two muons and the charged track are randomly picked, they typically don't have any structure in the χ^2 of the vertex reconstruction fit. As such a large number of these events are removed through a cut on this variable. Furthermore, since the products are picked randomly, a cut on the angle between the p_T and L_{xy} vectors remove another sizable contribution seeing as these particles don't necessarily originate from the same decay and are therefore not boosted in the same direction. As mentioned earlier, truth-matched J/ψ have been removed from this background sample.

Inclusive $b\bar{b} \to J/\psi$ decays

Within the inclusive sample one can find all possible decays involving $b\bar{b} \to J/\psi X$, where X can be any possible particle. While the other backgrounds can mostly be removed through restrictions on one or two variables, these background events mimic the characteristics of the signal events which leads to it being difficult to fully remove the background contributing events. As such it needs to be properly parameterized.

While all of the decays of B^+ and B_c^+ to a J/ψ and at least one hadron track can be miss-reconstructed as the signal channels; there are some which should require special attention, though since there is no dedicated samples for the B^+ and no samples at all for B_c^+, it is not possible to construct specialized fit models to correctly attribute to these decays.

The exclusive decay of $B^+ \to J/\psi\pi^+$, where the π is reconstructed as a K, leads to a visible broad peak which is shifted to the higher side of the signal region. We have attempted to parametrize this feature with a Crystal-Ball function, within the combined background sample. Seemingly no other decays appear to warrant its own specific model to be successfully parametrized. The relative ratio between this channel and the signal decay is given by Eq. 10.7.

$$R = \frac{\mathcal{B}\,(B^+ \to J/\psi\pi^+)}{\mathcal{B}\,(B^+ \to J/\psi K^+)} = (4.8 \pm 0.4)\,\% \tag{10.7}$$

There is an equivalent decay for the B_c^+. This is the exclusive decay $B_c^+ \to J/\psi K^+$ which will lead to a peak with lower mass than the signal. However, since there are no exclusive MC to model this on, and neither is there enough statistics to do this through the background MC. As such we are unable to parametrize this effect. This relative ratio is given by Eq. 10.8.

$$R = \frac{\mathcal{B}\,(B_c^+ \to J/\psi K^+)}{\mathcal{B}\,(B_c^+ \to J/\psi\pi^+)} = (8.5 \pm 0.5)\,\% \tag{10.8}$$

10.2 Selection Methods

10.2.1 First Event Selection

Before one starts doing any sort of further analysis on the different MC samples, there is typically imposed certain minimum requirements on the different variables used. While most of these come from the different subsystem groups of ATLAS, i.e. the Muon Combined Performance (PC) Group or Inner Tracker PC Group, who have their own studies done to determine which parameters requirements of that subsystem one would need to get events which are of interest to Physics analysis.

The sum of all these recommended cuts are referred to as the generic requirements. Events that pass all of these cuts are further scrutinized using different conditions in order to optimize the significance of the samples in question.

At the ATHENA level the minimum requirements for an the events is that we have J/ψ candidates which are reconstructed from two oppositely charged muons. Fits are required to have a $\chi^2 < 10$ and the muons have to be combined, meaning that the reconstruction algorithm utilizes both the Muon Spectrometer and the Inner Tracking Detector to tag them. To get the B-meson candidates we require that along with the J/ψ there is an additional track, and that these have to share a common vertex. The same χ^2 requirement apply to the B-meson reconstruction fit, along with an $|\eta| < 2.5$ requirement on the B-meson decay products, this in order to remove events which are not within the fiducial volume of the detector. Furthermore the mass of the secondary track is set to correspond to either the K^+ or π^+ mass depending on the decay in question.

Table 10.3: Generic requirements cuts, as advised by the Inner Detector [43] and Muon CP groups [44], corresponding to the loose requirements for both charged hadron track and muons. The pseudorapidity requirement on the muons shown in this table came by recommendation from the B-physics J/ψ group conveners. Events that satisfy the require cuts are kept.

Particle	$\|\eta\|$	p_T	Silicone Hits	SCT Hits	Pixel Hits
μ_1, μ_2	< 2.3	$\geq 4000, \geq 4000$		≥ 5	≥ 1
π, K	< 2.5	> 400	≥ 7		
	IBL Hits	Silicone Shared Hits	Silicone Holes	SCT Holes	Pixel Holes
μ_1, μ_2			≤ 2		
π, K		≤ 1	≤ 2		≤ 1

10.2.2 J/ψ Candidate Selection

After the ATHENA level cuts and the generic cuts has been applied to the samples the next order is to minimize the number of J/ψ candidates. This is done by imposing a resolution requirement on its mass. Using truth-matched signal events we perform an unbinned maximum likelihood fit on the J/ψ mass distribution. The model for this fit is given by Eq. 10.9. From the fit we can extract the mean value, the sigmas and the fraction of the distribution. We define a weighted three sigma cut around the fitted mean which is then applied to all candidates, this cut is given by Eq. 10.11. This is performed separately for the two different decays, and for 2015 and 2016 data.

$$L = \prod_{i=1}^{N} f_1 G_1(m^i_{\mu,\mu}) + (1 - f_1) G_2(m^i_{\mu,\mu}) \tag{10.9}$$

$$G_\alpha(m^i_{\mu,\mu}) = \frac{1}{\sigma_\alpha \sqrt{2\pi}} \exp\left[-\frac{(m^i_{\mu,\mu} - m_{J/\psi})^2}{2\sigma_\alpha^2}\right] \tag{10.10}$$

N = Maximum number of data points
G_α = Gaussian α
f_α = Fraction of contributing Gaussian α
σ_α = Width of Gaussian α
$m_{\mu,\mu}$ = Invariant mass of muons in dataset
$m_{J/\psi}$ = Gaussian peak center, corresponds to J/ψ mass

$$\sigma_w = f_1\sigma_1 + (1 - f_1)\sigma_2 \tag{10.11}$$

Table 10.4: Fitted peak and width of the J/ψ from truth-matched signal MC for the corresponding decays. All values are in MeV c^{-2}.

Decay		$m_{J/\psi}$	σ_w
$B^+ \to J/\psi K^+$	2015		
	2016		
$B_c^+ \to J/\psi\pi^+$	2015		
	2016		

10.2.3 Observables

As has already been mentioned in Section 10.1, we have several observables from which we can apply different cuts in order to select a subset of the recorded data. Herein we apply these cuts to optimize on the significance, as defined in Eq. 10.1. Through this we aim to discriminate as high a yield of signal events as possible out of the datasets. To accomplish this goal we have chosen four observable capable of greatly separating background and signal events.

- The transverse momentum of the hadron track p_T
- The goodness-of-fit from the vertex reconstruction of the hadron and muon tracks χ^2
- The transverse decay length of the B-mesons L_{xy}
- The pointing angle α

The relatively long lifetime of the b-quark allows the composite B-meson to fly a short distance away from the primary vertex before decaying. This allows ATLAS to reconstruct a secondary vertex by triangulating the track of two oppositely charged muons and a single hadron track backwards towards a common origin. There is then applied a fit to determine how good these tracks align to this vertex. From this fit we can extract the χ^2. Since there are several possible B-meson candidates from each primary vertex and we have a $\langle\mu\rangle = 23.7$ for the data samples. This means we have a large number of primary vertices and therefore also B-meson candidates. Previous studies done in the B-physics group shows that the candidate with the best χ^2 typically yield the truth-matched particle. As such the χ^2 is the only observable used in the determination of which candidate to select, and all the rest are used to discriminate amongst these.

The L_{xy} is defined as the distance between the primary and secondary vertex in the transverse plane. We only use the distance in xy-plane since ATLAS has a much better spatial resolution in this plane compared to along the z-axis. In some cases the L_{xy} can be resolved to have negative values. This happens when its vector points in the opposite direction of the B-meson momentum vector. The cause of the aforementioned problem is due to the fact that the secondary vertex appears to have been reconstructed behind the primary vertex. Since this should not happen for signal candidates one can then apply cuts on the pointing angle α between the L_{xy} and the B-meson p_T vectors, as given in Eq. 10.12. For signal events the value of this angle should be fairly close to 0.

$$\alpha = \left|\phi_{p_T} - \phi_{L_{xy}}\right| \tag{10.12}$$

Finally the requirements we impose on the transverse momentum of the hadron track is in order to remove soft pions, which are abundantly produced at the LHC. All of these cuts are optimized separately using MC for both the B^+ and B_c samples, where the MC has been scaled to either 2015 or 2016 luminosities. The obtained optimized cuts are listed in Table 10.5 for B^+ and in Table 10.6 for B_c. The significance distributions obtained for these different discriminating variables can be seen in Figure 10.1 and 10.2.

Efficiencies

To be able to determine the ratio f_c/f_u one of the necessary components is the ratios of selection efficiency. This is determined through the use of truth-matched information from the signal MC samples. Also here we estimate these for each sample separately. The determination of the efficiency ϵ is carried out by simply counting the number of events that are present after a cut and dividing this number by the initial sum. These cuts are carried out successively as such it is the difference between two listed efficiencies that shows how much signal events the cut removes. The efficiency is calculated using Eq. 10.13 and its uncertainty is given by Eq. 10.14 [45].

$$\epsilon = \frac{n}{N} \tag{10.13}$$

$$\sigma_\epsilon = \frac{\sqrt{n(1 - n/N)}}{N} \tag{10.14}$$

Table 10.5: Optimized selection criteria for the $B^{\pm} \rightarrow j/\psi K^{\pm}$ decay channel. For each requirement we calculate the cumulative signal efficiency. The *generic requirements* refer to the sum of all generic requirements as stated by the Muon and ID CP groups, and truth-matching cuts on J/ψ and $B^{\pm}$. Events that satisfy the require cuts are kept.

	2015		2016	
Observables	Cut	Efficiency	Cut	Efficiency
After ATHENA		$72.45\% \pm 0.04\%$		$72.45\% \pm 0.04\%$
Truth-matching J/ψ		$72.45\% \pm 0.04\%$		$72.45\% \pm 0.04\%$
Truth-matching $B^{\pm}$		$52.00\% \pm 0.05\%$		$52.00\% \pm 0.05\%$
Trigger		$18.02\% \pm 0.04\%$		$9.94\% \pm 0.03\%$
π $\lvert\eta\rvert$	< 2.5	$18.02\% \pm 0.04\%$	< 2.5	$9.94\% \pm 0.03\%$
μ_1 p_T [MeV c^{-1}]	≥ 4000	$17.66\% \pm 0.04\%$	≥ 4000	$9.91\% \pm 0.03\%$
μ_1 p_T [MeV c^{-1}]	≥ 4000	$17.29\% \pm 0.04\%$	≥ 4000	$9.89\% \pm 0.03\%$
μ_1 Inner Detector Hits		$17.26\% \pm 0.04\%$		$9.87\% \pm 0.03\%$
μ_2 Inner Detector Hits		$17.23\% \pm 0.04\%$		$9.85\% \pm 0.03\%$
π Inner Detector Hits		$17.23\% \pm 0.04\%$		$9.89\% \pm 0.03\%$
J/ψ χ^2	< 10	$17.23\% \pm 0.04\%$	< 10	$9.89\% \pm 0.03\%$
J/ψ p_T [MeV c^{-1}]	≥ 7000	$17.23\% \pm 0.04\%$	≥ 7000	$9.89\% \pm 0.03\%$
Generic requirements		$17.23\% \pm 0.04\%$		$9.89\% \pm 0.03\%$
$B^{+}p_T$ [MeV c^{-1}]	> 12500	$14.40\% \pm 0.04\%$	> 14000	$8.73\% \pm 0.03\%$
p_T [MeV c^{-1}]	> 5100	$9.90\% \pm 0.03\%$	> 5100	$8.73\% \pm 0.02\%$
χ^2	< 2.4	$9.70\% \pm 0.03\%$	< 2.4	$5.83\% \pm 0.02\%$
L_{xy} [mm]	> 0.14	$9.39\% \pm 0.03\%$	> 0.15	$5.61\% \pm 0.02\%$
α [rad]	< 0.1	$9.33\% \pm 0.03\%$	< 0.1	$5.55\% \pm 0.02\%$

Table 10.6: Optimized selection criteria for the $B_c^\pm \to j/\psi\pi^\pm$ decay channel. For each requirement we calculate the cumulative signal efficiency. The *generic requirements* refer to the sum of all generic requirements as stated by the Muon and ID CP groups, and truth-matching cuts on J/ψ and $B_c^\pm$. Events that satisfy the require cuts are kept.

	2015		2016	
Observables	Cut	Efficiency	Cut	Efficiency
After ATHENA		$67.50\% \pm 0.05\%$		$65.40\% \pm 0.05\%$
Truth-matching J/ψ		$67.50\% \pm 0.05\%$		$65.40\% \pm 0.05\%$
Truth-matching $B_c^\pm$		$30.33\% \pm 0.05\%$		$29.39\% \pm 0.05\%$
Trigger		$25.75\% \pm 0.04\%$		$24.94\% \pm 0.04\%$
π $\lvert\eta\rvert$	< 2.5	$25.74\% \pm 0.04\%$	< 2.5	$24.94\% \pm 0.04\%$
μ_1 p_T [MeV c^{-1}]	≥ 4000	$21.54\% \pm 0.04\%$	≥ 4000	$20.87\% \pm 0.04\%$
μ_1 p_T [MeV c^{-1}]	≥ 4000	$18.08\% \pm 0.04\%$	≥ 4000	$17.51\% \pm 0.04\%$
μ_1 Inner Detector Hits		$18.02\% \pm 0.04\%$		$17.45\% \pm 0.04\%$
μ_2 Inner Detector Hits		$17.97\% \pm 0.04\%$		$17.41\% \pm 0.04\%$
π Inner Detector Hits		$17.97\% \pm 0.04\%$		$17.41\% \pm 0.04\%$
J/ψ χ^2	< 10	$17.97\% \pm 0.04\%$	< 10	$17.41\% \pm 0.04\%$
J/ψ p_T [MeV c^{-1}]	≥ 7000	$17.97\% \pm 0.04\%$	≥ 7000	$17.40\% \pm 0.04\%$
Generic requirements		$17.97\% \pm 0.04\%$		$17.40\% \pm 0.04\%$
p_T [MeV c^{-1}]	> 5100	$5.28\% \pm 0.02\%$	> 5100	$5.11\% \pm 0.02\%$
χ^2	< 2.4	$4.85\% \pm 0.02\%$	< 2.4	$4.50\% \pm 0.02\%$
L_{xy} [mm]	> 0.14	$4.26\% \pm 0.02\%$	> 0.15	$3.90\% \pm 0.02\%$
α [rad]	< 0.1	$4.07\% \pm 0.02\%$	< 0.1	$3.74\% \pm 0.02\%$

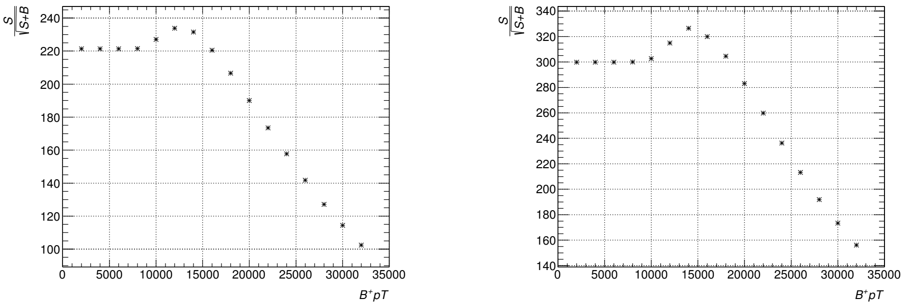

(a) Significance versus p_T.

(b) Significance versus p_T.

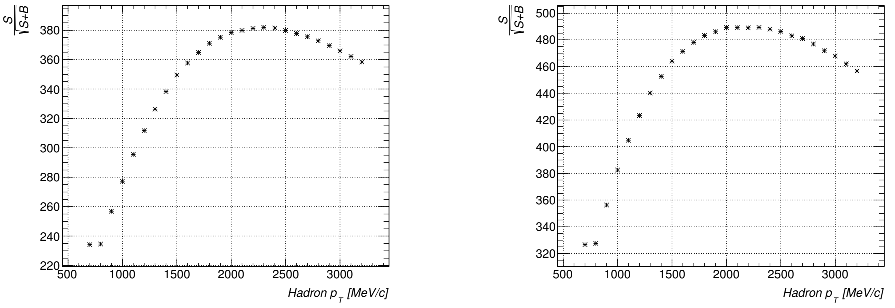

(c) Significance versus p_T.

(d) Significance versus p_T.

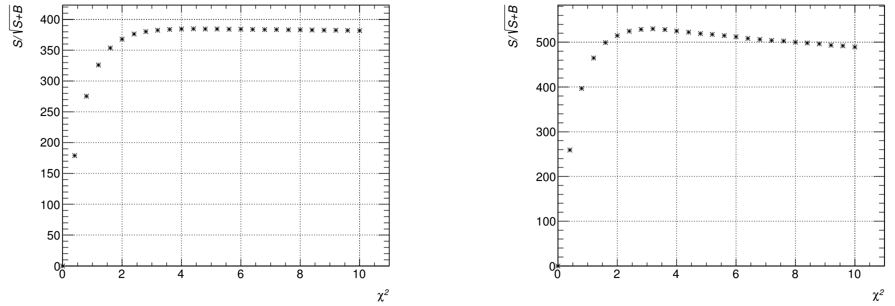

(e) Significance versus χ^2.

(f) Significance versus χ^2.

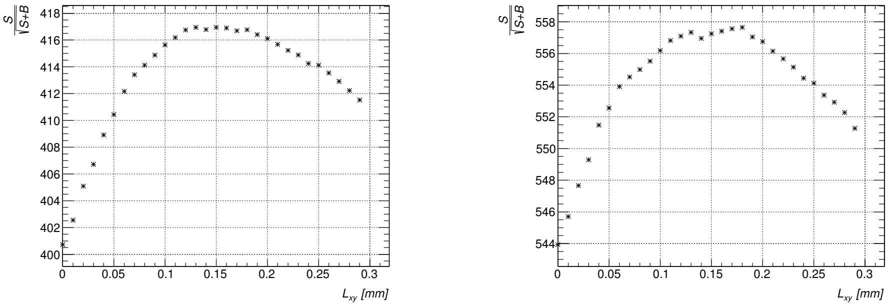

(g) Significance versus L_{xy}.

(h) Significance versus L_{xy}.

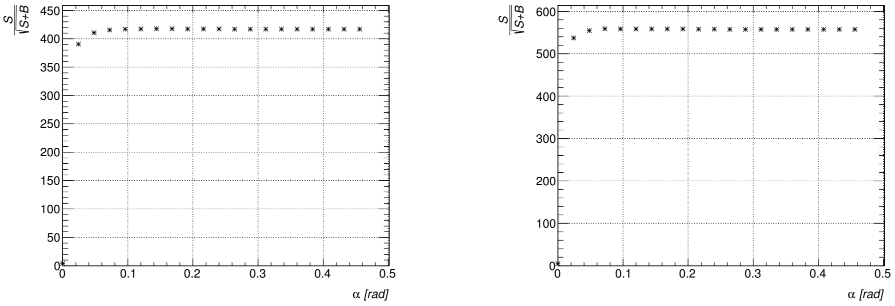

(i) Significance versus pointing angle.

(j) Significance versus pointing angle.

Figure 10.1: Significance distributions of the variables used to optimize cuts for the B^+. Left plots shows 2015, while right hand side showcases 2016.

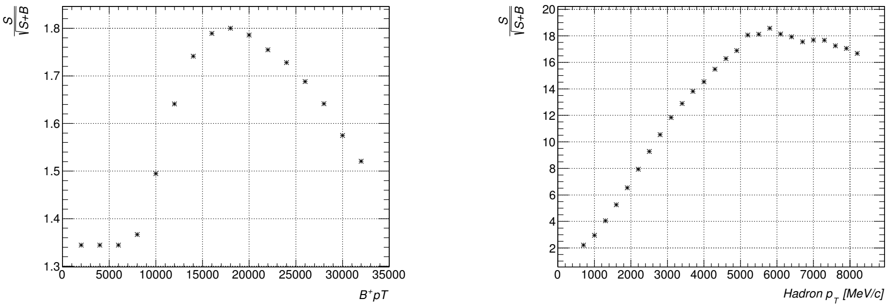

(a) Significance versus p_T.

(b) Significance versus p_T.

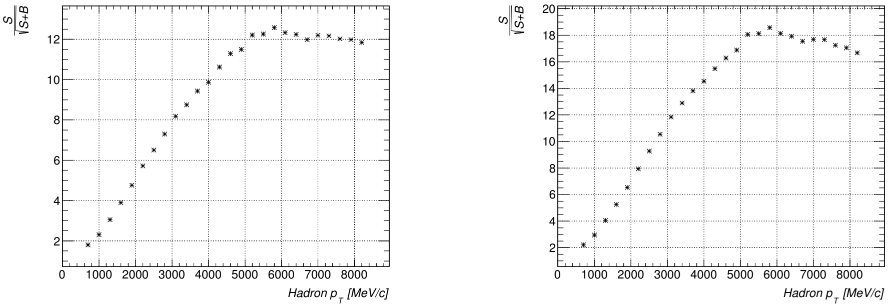

(c) Significance versus p_T.

(d) Significance versus p_T.

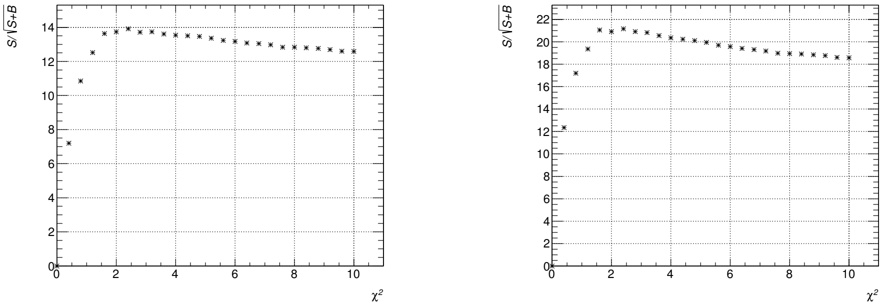

(e) Significance versus χ^2.

(f) Significance versus χ^2.

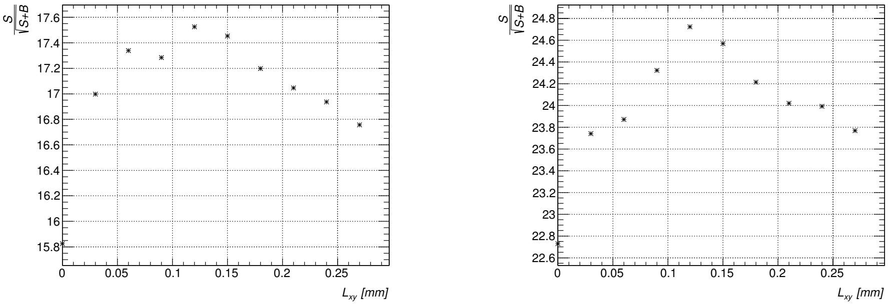

(g) Significance versus L_{xy}.

(h) Significance versus L_{xy}.

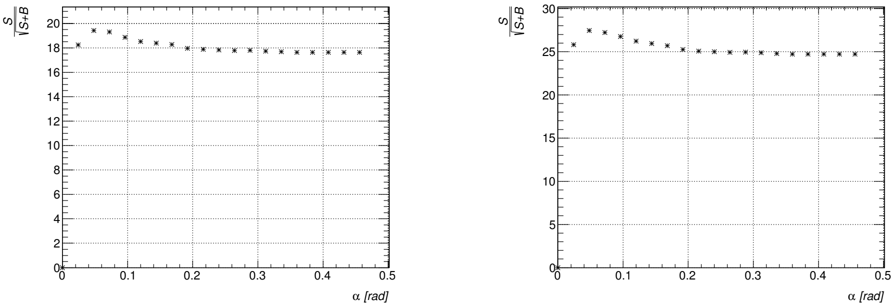

(i) Significance versus pointing angle.

(j) Significance versus pointing angle.

Figure 10.2: Significance distributions of the variables used to optimize cuts for the B_c^+. Left plots shows 2015, while right hand side showcases 2016.

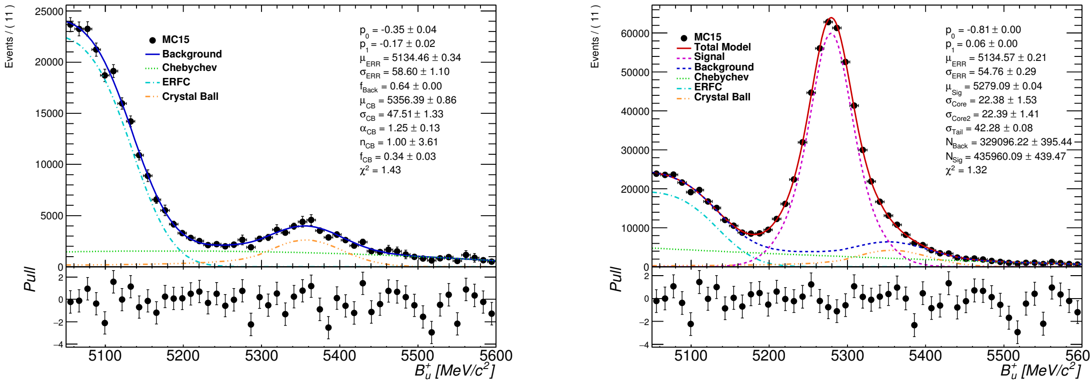

(a) Combined MC background scaled to 2015 $\mathcal{L}_{int}$

(b) Combined MC background and signal scaled to 2015 $\mathcal{L}_{int}$

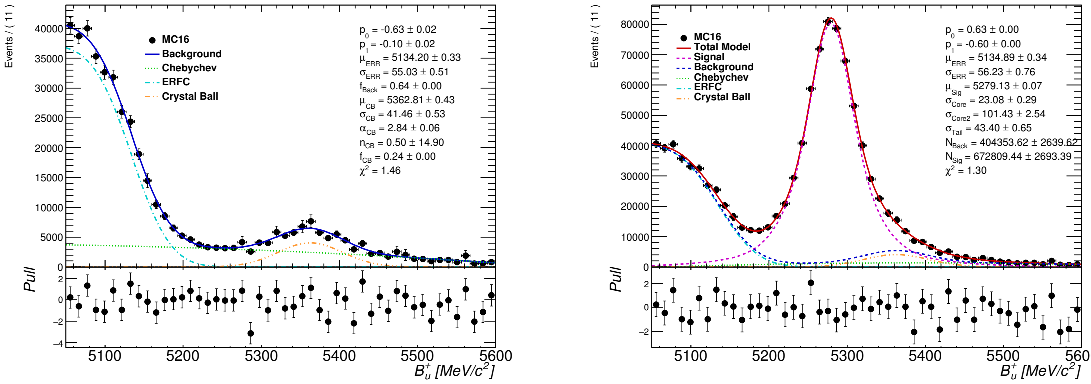

(c) Combined MC background scaled to 2016 $\mathcal{L}_{int}$

(d) Combined MC background and signal scaled to 2016 $\mathcal{L}_{int}$

Figure 10.3: The obtained fits on the 2015 and 2016 MC samples for the $B^{\pm} \rightarrow J/\psi K^{\pm}$ decay.

10.3 Modeling of the Background and Signal

10.3.1 B^{+} Model

The mass distribution that remain, after all of the selection cuts have been applied, are modeled by several background and signal PDFs. To successfully describe the observed background structures a mix of three different PDFs are used. One of the sources of peaking background is through the miss reconstruction of $B^{+} \rightarrow J/\psi\pi^{+}$. Here the pion is reconstructed with a kaon mass, creating a broad visible peak in the signal region which is modeled by a Crystall-Ball (CB) function, Eq. 10.15. Since we do not have a specific MC sample in which to model this peak to fix its parameters. We have instead attempted to fit this broad peak in the combined background samples in order to estimate its parameters. We then fix the CB parameters to these determined values when we fit our total model on the combined background and signal MC, as well as for the data.

$$M_{CB}(m_{J/\psi K}) = \begin{cases} \frac{1}{\sqrt{2\pi}\sigma_{CB}} \exp\left(-\frac{(m_{J/\psi K}-\mu_{CB})^2}{2\sigma_{CB}^2}\right), & m_{J/\psi K} > \mu_{CB} - \alpha_{CB}\sigma_{CB} \\ \frac{1}{\sqrt{2\pi}\sigma_{CB}} \frac{(\frac{n_{CB}}{\alpha_{CB}})^2 \exp\left(\frac{-\alpha_{CB}^2}{2}\right)}{(\frac{(\mu_{CB}-m_{J/\psi K})}{\sigma_{CB}}+\frac{n_{CB}}{\alpha_{CB}}-\alpha_{CB})^n}, & m_{J/\psi K} \leq \mu_{CB} - \alpha_{CB}\sigma_{CB} \end{cases} \tag{10.15}$$

μ_{CB} = Mean of the Gaussian core

σ_{CB} = Width of the Gaussian core

α_{CB} = Determines which side of the Gaussian that has a power law tail

n_{CB} = Decides the length of the tail

The lower end of the background spectrum, below 5200 MeV c^{-2}, features partially reconstructed B decays. This background contribution is modeled with a complementary error function (ERFC), Eq. 10.17. The ERFC is a sigmoid shaped function with the mean value m_{ERFC} and width σ_{ERFC} as defined by Eq. 10.16.

$$\mathrm{erfc}\,(x) = \frac{2}{\sqrt{\pi}} \int_x^\infty \mathrm{e}^{-t^2}, \qquad x = \frac{m_{J/\psi K} - \mu_{ERFC}}{\sigma_{ERFC}} \tag{10.16}$$

$$M_{ERFC}(m_{J/\psi K}) = \mathrm{erfc}\left(\frac{m_{J/\psi K} - \mu_{ERFC}}{\sigma_{ERFC}}\right) \tag{10.17}$$

The remaining background is modeled with a second-order Chebychev (C) polynomial of the first kind, Eq. 10.18 [46].

$$M_C(m_{J/\psi K}) = 2p_1 m_{J/\psi K}^2 + p_0 m_{J/\psi K} \tag{10.18}$$

The combined background PDF is given by Eq. 10.19. Using this model we then perform an unbinned maximum likelihood fit on the luminosity scaled combined background MC samples.

$$M_{Back}(m_{J/\psi K}) = f_{CB} M_{CB}(m_{J/\psi K}) + f_{ERFC} M_{ERFC}(m_{J/\psi K}) + f_C M_C(m_{J/\psi K}) \tag{10.19}$$

f_i = Fraction of each PDF component, $f_{CB} + f_C + f_{ERFC} = 1$

In order to complete the model to determine the expected invariant mass distribution we also have to include the signal PDF from Eq. 10.4. With this model we then perform an unbinned extended maximum likelihood fit on the luminosity scaled combined background and signal MC samples.

$$M_{B^+}(m_{J/\psi K}) = N_{Sig} M_{Sig}(m_{J/\psi K}) + N_{Back} M_{Back}(m_{J/\psi K}) \tag{10.20}$$

10.3.2 B_c^+ Model

We do not attempt to construct an equally complex model for the B_c^+. Due to the low production cross-section of this particle the background is simply modeled using a second-order Chebychev of the first kind, the same as in Eq. 10.21. While the signal is modeled by a single Gaussian, Eq. 10.22, yielding the total model of Eq. 10.23. Also here we perform an unbinned extended maximum likelihood fit on the luminosity scaled combined background and signal MC samples.

$$M_{Back}(m_{J/\psi pi}) = 2p_1 m_{J/\psi\pi}^2 + p_0 m_{J/\psi\pi} \tag{10.21}$$

$$M_{Sig}(m_{J/\psi pi}) = \frac{1}{\sqrt{2\pi}\sigma} \exp\left(-\frac{(m_{J/\psi\pi} - m_{B_c^+})^2}{2\sigma^2}\right) \tag{10.22}$$

$$M_{B_c^+}(m_{J/\psi K}) = N_{Sig} M_{Sig}(m_{J/\psi\pi}) + N_{Back} M_{Back}(m_{J/\psi\pi}) \tag{10.23}$$

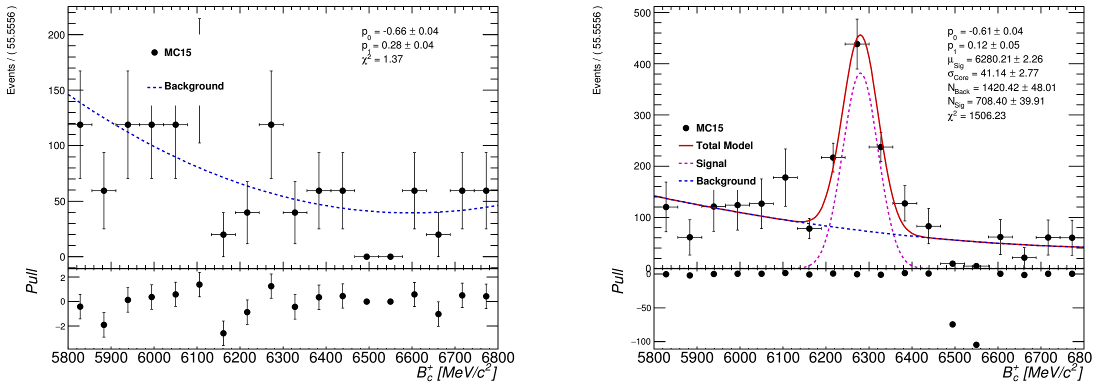

(a) Combined MC background scaled to 2015 $\mathcal{L}_{int}$

(b) Combined MC background and signal scaled to 2015 $\mathcal{L}_{int}$

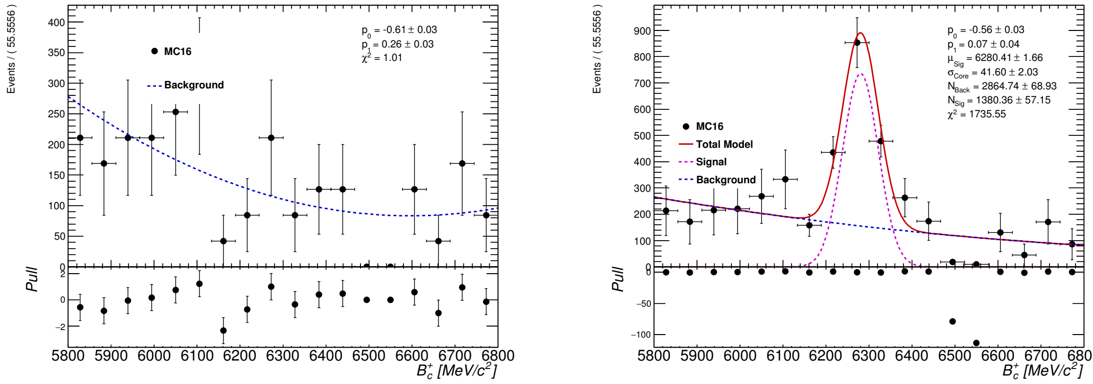

(c) Combined MC background scaled to 2016 $\mathcal{L}_{int}$

(d) Combined MC background and signal scaled to 2016 $\mathcal{L}_{int}$

Figure 10.4: The obtained fits on the 2015 and 2016 MC samples for the $B_c^{\pm} \to J/\psi\pi^{\pm}$ decay.

Chapter 11

Results of the Fragmentation Ratio

After optimizing the selection requirements on the MC samples we can then apply the same set of cuts on both the 2015 and 2016 data sets. The 2015 data corresponds to total of integrated luminosity of $3.22\,\mathrm{fb}^{-1}$ while the 2016 has a total of $6.85\,\mathrm{fb}^{-1}$. From these data sets we can extract a mass and yield estimate for both the B^+ and B_c^+ mesons. We can then estimate the fragmentation probability ratio f_c/f_u. This ratio is given by Eq. 9.12, however since the integrated luminosity and luminosity uncertainty is the same for both the B^+ and B_c^+ samples, the equation can be simplified to Eq. 11.1. The efficiency ratio $\epsilon_{B^+}/\epsilon_{B_c^+}$ is extracted from truth-matched MC signal samples, and is given by Eq. 10.13. Due to time constraint we have only obtained results in the full psuedorapidity region of $|\eta| < 2.5$.

$$\frac{f_c}{f_u} = \frac{N_{B_c^+}}{N_{B^+}} \frac{\mathcal{B}\left(B^+ \to J/\psi K\right)}{\mathcal{B}\left(B_c \to J/\psi \pi\right)} \frac{\epsilon_{B^+}}{\epsilon_{B_c^+}} \tag{11.1}$$

11.1 $B^\pm \to J/\psi K^\pm$ Results

To extract the mass and yield for the $B^\pm$ we perform an unbinned extended maximum likelihood fit on the mass distribution. The model is defined in Section 10.3.1. Most of the parameters of the fit are variable, aside from the fixed parameters to fit the peaking background contributions from $B^\pm \to J/\psi\pi^\pm$, where the pion is reconstructed with a kaon mass hypothesis. This is to let the statistical uncertainty of the measurement be determined through the fitting procedure. While the fixed parameters of the peaking background model are varied and are added as a source of systematic uncertainty. The fits are carried out separately for both the 2015 and 2016 data samples. The results can seen in Figure 11.1, while the parameters can be found in Table **??**. The pull distribution of the fit versus data can be seen below each figure, and it is an indication of how well the model fits the data and the accuracy of the error estimates [47]. The pulls can be seen to fluctuate around 0 which indicates that the model imitates the data well.

From the 2015 data we extract a total of $321\,158 \pm 1772(\mathrm{stat})$ signal events, and a mass estimate of $5279.23 \pm 0.10(\mathrm{stat})\,\mathrm{MeV}\,c^{-2}$. In the 2016 data set we observe a total of $1\,226\,013 \pm 5125(\mathrm{stat})$ events and we get a mass estimate of $5279.00 \pm 0.05(\mathrm{stat})\,\mathrm{MeV}\,c^{-2}$. The ATLAS B-physics group is currently working on an official analysis for the $B^\pm$ mass measurement for 2015 and 2016 data samples, however their results are not available for the 2016 data yet. The analysis on the $B^\pm$ mass measurement uses the same 2015 data samples as we have done. They obtain a mass estimate of $5279.31 \pm 0.11(\mathrm{stat})\,\mathrm{MeV}\,c^{-2}$ [48]. The results shows good

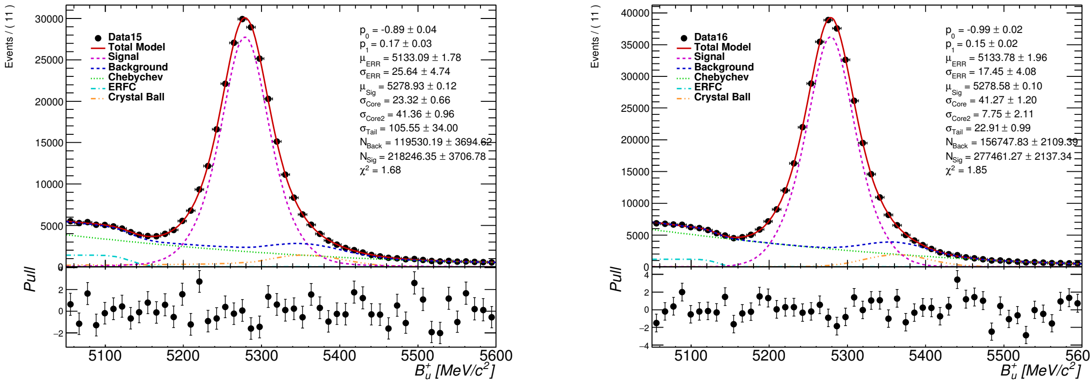

(a) B^+ fit on 2015 data

(b) B^+ fit on 2016 data

Figure 11.1: The obtained fits on the 2015 and 2016 data samples for the $B^\pm \to J/\psi K^\pm$ decay.

consistency, seeing as their result is within one σ of the measurement we have carried out. There are slight differences to the applied threshold cuts used between their analysis and the ones we've used. They use a general di-muon trigger with a muon transverse momentum cut of $p_T > 4\,\mathrm{GeV}\,c^{-1}$ and a $p_T > 15\,\mathrm{GeV}\,c^{-1}$ on the $B^\pm$. While our trigger is a di-muon and J/ψ trigger with a cut of $p_T > 6\,\mathrm{GeV}\,c^{-1}$ for the muons and a $B^\pm$ cut of $p_T > 2\,\mathrm{GeV}\,c^{-1}$. Their fit model is also very different, as such these results illustrates that fit model systematics should be rather small. This and other systematics are discussed in-depth in Section 11.3.3.

11.2 $B_c^\pm \to J/\psi\pi^\pm$ Results

The method used for the extraction of the mass and signal yield is the same as for the $B^\pm$, however the fit model is not as complex. This model is defined in Section 10.3.2. In this model we leave all fit parameters free. Figure 11.2 shows fit results on both the 2015 and 2016 data samples. From the 2015 data we extract a signal yield of $156 \pm 38(\mathrm{stat})$ and the mass estimate is $6276.83 \pm 7.48(\mathrm{stat})\,\mathrm{MeV}\,c^{-2}$. While the 2016 data yield $1149 \pm 110(\mathrm{stat})$ signal events and an estimated mass of $6265.13 \pm 4.47(\mathrm{stat})\,\mathrm{MeV}\,c^{-2}$. The $B_c^\pm$ mass has been measured by both the LHCb [37] and CMS [34] Collaborations through the same decay channel $B_c^\pm \to J/\psi\pi^\pm$ using Run1 LHC data. LHCb quotes a mass estimate of $6273.7 \pm 1.3(\mathrm{stat})\,\mathrm{MeV}\,c^{-2}$ from 2470 ± 350 efficiency-corrected signal events. The efficiency-corrected signal events that we observe are $3833 \pm 934(\mathrm{stat})$ for 2015 and $30\,722 \pm 2941(\mathrm{stat})$ for 2016. While CMS list the mass as $6267 \pm 3(\mathrm{stat})\,\mathrm{MeV}\,c^{-2}$ from 176 ± 19 signal events, and the current world average as performed by PDG is $6274.9 \pm 0.8\,\mathrm{MeV}\,c^{-2}$.

The measurements that we obtain are within one σ of each other, however both measurements have large uncertainties. The 2016 data is fairly similar to the measurement quoted by CMS, although it is several σ away from the world average. Yet, all these results are rather concise considering the small number of signal events. Thus leading to the conclusion that our obtained estimate of the B_c^+ mass is in rather good consensus.

As discussed in Section 10.1 the MC samples for the $B_c^\pm$ has been produced by using a modified Pythia8 script. This script was initially meant for the $B^+ \to J/\psi K^+$ decay channel, where the B^+ mass and lifetime has been exchanged by the corresponding values for the B^+ taken from PDG, and the kaon has been exchanged with a pion. Since the topology of these decays are similar, they should be able to

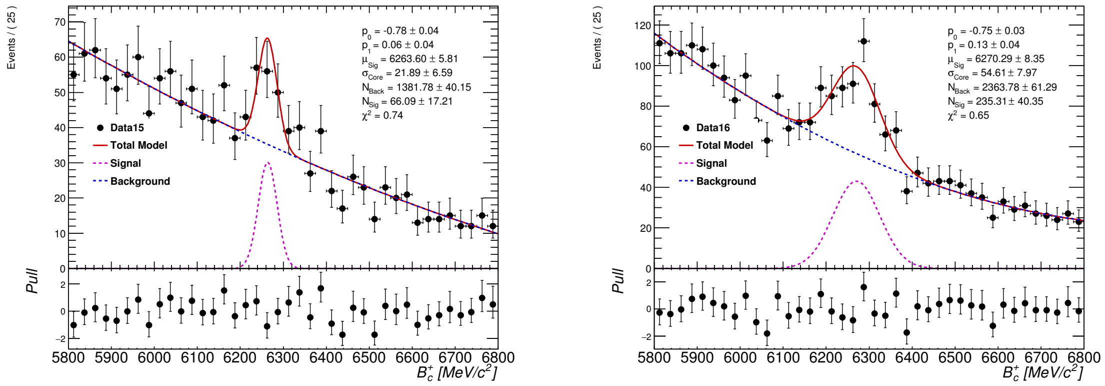

(a) B_c^+ fit on 2015 data

(b) B_c^+ fit on 2016 data

Figure 11.2: The obtained fits on the 2015 and 2016 data samples for the $B_c^\pm \to J/\psi\pi^\pm$ decay.

reproduce the signal shapes. However, if one compares the fits performed on the MC, Figure 10.4, with the ones performed on the data, Figure 11.2, one can observe different background slopes although the signal are somewhat similar. Unfortunately this is nothing something that can be amended since ATLAS does not have any capability to make true B_c^+ MC samples. Hence, since the MC does not appear to be fully accurate, and we use it to perform the optimization cuts, these cuts are most likely not optimal. However, the pull shows that the model fits the data rather well.

11.3 Systematic Uncertainties

Systematic uncertainties are measurement errors which are not due to statistical fluctuations in data samples.

11.3.1 Mass Measurements

There are several contributing sources to systematic uncertainties for the mass estimation.

- **Fit model**. The choice of specific PDF to model the observed mass distribution can introduce systematic uncertainties on the mass estimate. In order to successfully quantize this effect one has to vary the used background and signal model PDF which are used.

- **Momentum scale calibration**. An incorrect calibration of track momentum can result in a shifted mass peak. This could be probed by comparing the fitted J/ψ mass to the world average. As a shift in muon momentum would directly influence the estimated J/ψ mass and would be quite precise due to its narrow mass distribution. A corresponding estimate for the charged hadron track would have to be conducted in specialized tracking efficiencies studies. They have not been performed in ATLAS for the 2015 nor 2016 data, although studies are underway from the Inner Detector Combined Performance Group. Recent study performed by ATLAS for the mass measurement of $B^\pm$ have ignored the uncertainties due to momentum scale and vertexing as they necessary information is not yet available [48]. However, if the uncertainty of the hadron momentum was known one could shift the track momentum by this uncertainty in the MC samples. One can then perform a fit on the new mass distribution, and take the shift in the mass as a systematic uncertainty.

11.3.2 f_c/f_u uncertainties

When computing the ratio f_c/f_u some of the contributing systematic uncertainties will cancel while others remain. The following sources of systematic uncertainties has been given extra consideration.

- **MC sample size**. A small sample size may impact the measured efficiencies ϵ_{B^+} and $\epsilon_{B_c^+}$. Their uncertainties have been calculated using Eq. 10.14.
- **$B^\pm$ and $B_c^\pm$ reconstruction**. Since ATLAS do not have particle identification the decay topology of the two decay channels are identical. As such the efficiencies on the vertex and track reconstruction should cancel. However, the lifetime difference between the kaons and pions can introduce lower reconstruction efficiency for the kaons. Although this is modeled in the MC and therefore included in the total signal efficiency.
- **Fit model**. Different PDF models can affect the signal yield estimates and introduces a model specific uncertainty.
- **Luminosity**. Since the luminosity of the two data samples are identical for both the $B^\pm$ and $B_c^\pm$, the luminosity uncertainty should cancel in the ratio. The relative luminosity uncertainty is determined by the ATLAS Luminosity Taskforce and is estimated to be 2.12 % in 2015 and 2.21 % in 2016. Since the note with these results have not been published yet we are unable cite a proper source, however the latest luminosity tag *OflLumi-13TeV-009* which was updated 2017.06.17 shows these results.
- **Fake $B_c^\pm$ MC**. The uncertainties introduced by the private production of these fake $B_c^\pm$ MC samples are incalculable. Since there is no other means of producing $B_c^\pm$ MC samples in ATLAS one cannot use any tools to estimate this. As such, for a proper analysis the tools necessary to produce these samples must be constructed. Both LHCb and CMS uses the BCVEGPY package to produce such samples [49]. This package is not included in the ATLAS Software Framework currently, however there are plans to implement in at some point.
- **$B_c^\pm$ lifetime uncertainty**. The uncertainty on the lifetime for the $B_c^\pm$ is rather large. It can lead to incorrectly determined efficiency with the MC samples. Ideally the systematic uncertainty contribution from this effect should be measured by varying the $B_c^\pm$ lifetime by its uncertainties in the MC and redoing the efficiencies. However due to limited time and no officially produced MC samples, we have been unable to estimate this effect. The equivalent contribution from the $B^\pm$ lifetime would be negligible in comparison as it is measured with higher precision. Articles which have performed the same analysis indicate that this effect is roughly 10%, and it is the dominating systematic in their studies [37] [34].

11.3.3 Introduced uncertainties due to choice of fit model

The sensitivity in the signal yield and mass estimate due to the choice of total fit PDF is determined through testing alternative models. Since the background and

Table 11.1: Absolute and relative signal yield and mass for the $B^{\pm}$ from the 2015 data. All fits have $\chi^2 < 2.5$.

Model		$N_{B_c^{\pm}}$	$\Delta N_{B_c^{\pm}}$	$\frac{\Delta N_{B_c^{\pm}}}{N_{B_c^{\pm}}^{Base}}$ [%]	$m_{B_c^{\pm}}$ [MeV c^{-2}]	$\Delta m_{B_c^{\pm}}$ [MeV c^{-2}]	$\frac{\Delta m_{B_c^{\pm}}}{m_{B_c^{\pm}}^{Base}}$ [%]
Base		218 246.35	-	-	5278.93	-	-
Background	Hyperbolic Tangent	209 202.78	-9043.56	-4.14	5278.69	-0.24	-0.005
	Gaussian	227 586.58	9340.24	4.28	5278.92	-0.01	0.000
	Exponential	228 980.98	10 734.64	4.92	5278.99	0.06	0.001
Signal	Double Gaussian	207 819.30	$-10\,427.05$	-4.78	5278.85	-0.07	-0.001

signal models are uncorrelated sources of systematic uncertainties these models can be freely exchanged. We have performed this exchange of fit models on the 2015 and 2016 data samples separately. The relative yield difference is estimated through Eq. 11.2 and is listed as the corresponding systematic uncertainty due to the fit model.

$$\frac{\Delta N_B}{N_B^{Base}} = \frac{N_B^{Test} - N_B^{Base}}{N_B^{Base}} \tag{11.2}$$

The N_B^{Base} refers to the estimated signal yield from the fit models outlined throughout this thesis, while the N_B^{Test} refers to the signal yield extracted when we use a different fit model. The equivalent relative mass difference is defined by Eq. 11.3, and is only carried out for the $B_c^{\pm}$.

$$\frac{\Delta m_{B_c}}{m_{B_c}^{Base}} = \frac{m_{B_c}^{Test} - m_{B_c}^{Base}}{m_{B_c}^{Base}} \tag{11.3}$$

Model-induced for B^{+}

We take the largest estimated relative uncertainty amongst the background, and add it in quadrature with the signal model relative uncertainty. This value is taken as the systematic uncertainty due to the fit model. For the signal yields we find this contribution to be 6.86 % for the 2015 data, while the 2016 data gives us 15.09 %.

From Table 11.1 and Table 11.2 one can easily see that the fit model systematics are dominated by the exponential and hyperbolic tangent. There is a substantial observed increase in the signal yield for these background models. This seems to occur due to a too small fraction estimation for the Crystal-Ball. This contribution is supposed to take care of the $B^{\pm} \to J/\psi\pi^{\pm}$ miss constructed events, and should consequently decrease the number of signal yield according to the understood physics. Since the branching ratio is supposed to be 4.8% for these two decay channels, one would expect that the Crystal-Ball contribution should be much larger. It appears that in addition to the other fixed parameters, we should have also fixed the fraction contribution of this Crystal-Ball, or have carried out a simultaneous fit. However since we do not have any dedicated MC sample for this decay we have been unable to do so. This effect is more pronounced in the 2016 than the 2015 data. A comparison between the Double-Gaussian signal, the hyperbolic tangent, Gaussian for the $B^{\pm} \to J/\psi\pi^{\pm}$ contribution, and an exponential fit performed on the 2016 data can be seen in Figure 11.3. This showcases how the signal yield estimate is influenced by the different models, especially the contribution of the miss reconstructed pions, and we feel it illustrates the need for a dedicated MC sample.

Table 11.2: Absolute and relative signal yield and mass for the $B^{\pm}$ from the 2016 data. All fits have $\chi^2 < 2.5$.

Model		$N_{B_c^{\pm}}$	$\Delta N_{B_c^{\pm}}$	$\frac{\Delta N_{B_c^{\pm}}}{N^{Base}_{B_c^{\pm}}}$ [%]	$m_{B_c^{\pm}}$ [MeV c^{-2}]	$\Delta m_{B_c^{\pm}}$ [MeV c^{-2}]	$\frac{\Delta m_{B_c^{\pm}}}{m^{Base}_{B_c^{\pm}}}$ [%]
Base		277 461.27	-	-	5278.58	-	-
Background	Hyperbolic Tangent	277 694.35	233.08	0.08	5278.51	-0.07	-0.001
	Gaussian	307 640.21	30 178.94	10.88	5278.71	0.13	0.002
	Exponential	319 317.49	41 856.22	15.09	5278.73	0.15	0.003
Signal	Double Gaussian	277 314.74	-146.53	-0.05	5278.58	0.00	0.000

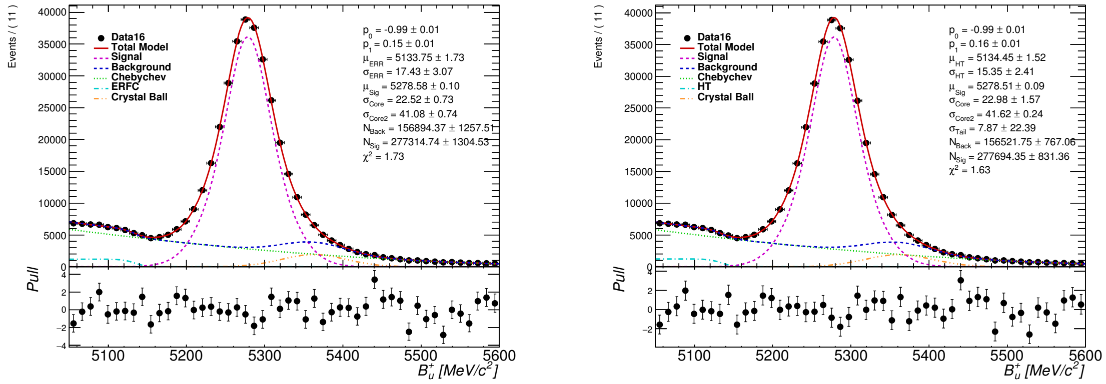

(a) Double Gaussian signal fit

(b) Hyperbolic tangent fit

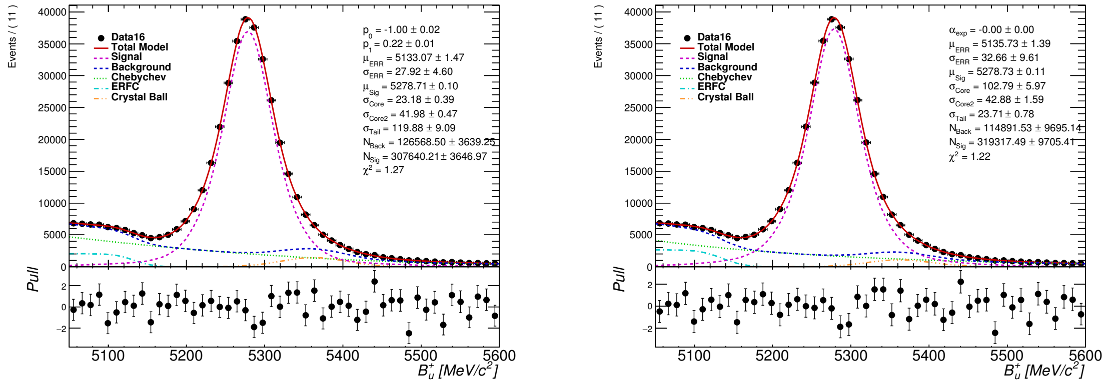

(c) Gaussian for the miss reconstructed pion contribution

(d) Exponential fit

Figure 11.3: Here we can see four of the different fit models on the 2016 data. A double Gaussian signal fit is in 11.3a. In 11.3c we have used a Gaussian instead of a Crystal-Ball for the $B^{\pm} \rightarrow J/\psi\pi\pm$ contribution. Both of these have roughly the same number of events for the miss reconstructed pions. While the Crystal-Ball contribution has been greatly suppressed in 11.3d. Along with a too large fraction of the partially reconstructed B decays found in the lower mass region for both 11.3c and 11.3d, which causes the background estimation in the signal region to be too low. This causes the signal yield to artificially increase, which directly increases our systematic uncertainty. This shows that to obtain better systematics estimate one should have MC specifically for this feature, in order to fix the fit parameters to a proper sample, or perform a simultaneous fit.

Table 11.3: Absolute and relative signal yield and mass for the $B_c^\pm$ from the 2015 data. All fits have $\chi^2 < 2.5$.

Model		$N_{B_c^\pm}$	$\Delta N_{B_c^\pm}$	$\frac{\Delta N_{B_c^\pm}}{N_{B_c^\pm}^{Base}}$ [%]	$m_{B_c^\pm}$ [MeV c^{-2}]	$\Delta m_{B_c^\pm}$ [MeV c^{-2}]	$\frac{\Delta m_{B_c^\pm}}{m_{B_c^\pm}^{Base}}$ [%]
Base		66.09	-	-	6263.60	-	-
Background	3rd Order Chebychev	57.78	-8.31	-12.58	6264.13	0.53	0.008
	Exponential	130.66	64.57	97.70	6266.69	3.10	0.049
Signal	Crystal Ball	72.69	6.60	9.99	6263.58	-0.01	0.000

Model-induced for B_c^+

We take the largest estimated relative uncertainty amongst the background, and add it in quadrature with the signal model relative uncertainty. This value is taken as the systematic uncertainty due to the fit model. For the signal yields we find this contribution to be 98.21 % for the 2015 data, if one were to not include the systematics from the exponential this would drop greatly down to 16.06 %, which indicates that something needs further attention. While the 2016 data gives us a reasonable 7.25 %.

The exponential fit model seem to overestimate the number of signal yields. In the 2015 data the relative yield of this fit gives a 97.70 % discrepancy, however in the 2016 data the same gives a relative yield difference by 6.23 %. This seems to occur due to lack of statistics for the 2015 sample. The three fits performed on the 2015 data all give a narrow mass window, while the exponential gives a much wider mass window. This wide mass range is also present in all four fits done on the 2016 data. Thus we are inclined to conclude the narrow mass window observed by the three fits done on the 2015 data are due to low statistics. Hence, it appears that if one were to combine the events from these two samples, and perform the fits on this combined sample, the systematic uncertainty due to this fit model would decrease greatly. Since the $\sqrt{s} = 13$ TeV and the 25 ns bunch spacing is the same for both the 2015 and 2016 data samples, as long as one apply the correct triggers for the corresponding years, it should be fine.

However, it does appear that the exponential model does not really suit the data as it performs poorly on both data samples. A wider mass region of study would show if the model is indeed lackluster, or if its parameters simply needs to be adjusted, this could be performed in a proper sideband study. Figure 11.4 shows the different fit models for the two data samples used. We also tried to model the signal region using two Gaussian function, however these fits fail to converge, and has been left out of this analysis. A double-sided Crystal-Ball function would have been another model to attempt if time could have been found.

11.4 Mass Measurement

We have assumed a systematic uncertainty due to the momentum scale, which was reported by a similar study to be 0.05%, as there are no official studies carried out within ATLAS which would allow us to measure this value ourselves. From the fit model we use the highest deviation from the background and signal models. These are added in quadrature with the momentum scale yielding a systematic uncertainty of 0.070% for 2015, and 0.056% for the 2016 data, which is applied as our systematic sources for the $B_c^\pm$ mass measurement. Applying the same to the

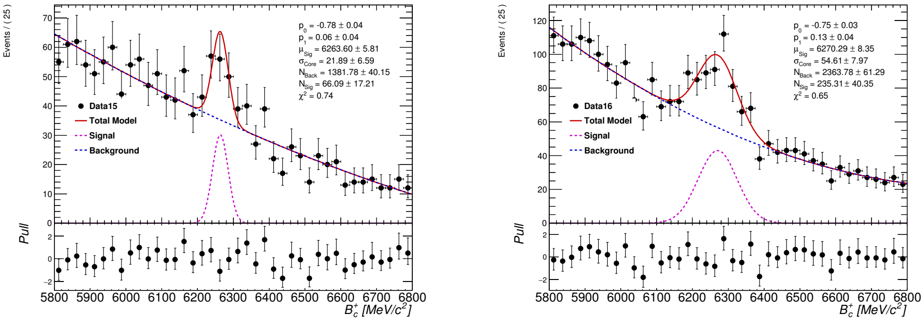

(a) Background modeled with a 2nd Order Chebychev of the first kind. Signal modeled with a single Gaussian.

(b) Background modeled with a 2nd Order Chebychev of the first kind. Signal modeled with a single Gaussian.

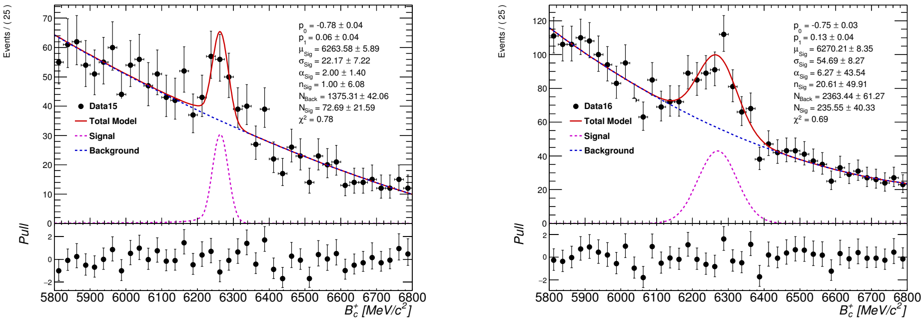

(c) Background modeled with a 2nd Order Chebychev of the first kind. Signal modeled with a single Crystal-Ball.

(d) Background modeled with a 2nd Order Chebychev of the first kind. Signal modeled with a single Crystal-Ball.

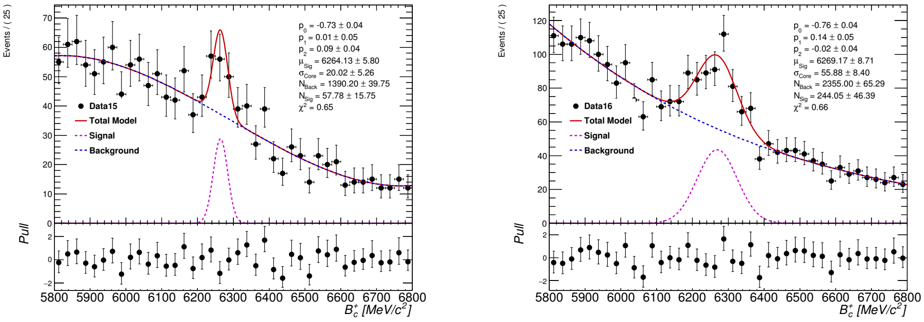

(e) Background modeled with a 3nd Order Chebychev of the first kind. Signal modeled with a single Gaussian.

(f) Background modeled with a 3nd Order Chebychev of the first kind. Signal modeled with a single Gaussian.

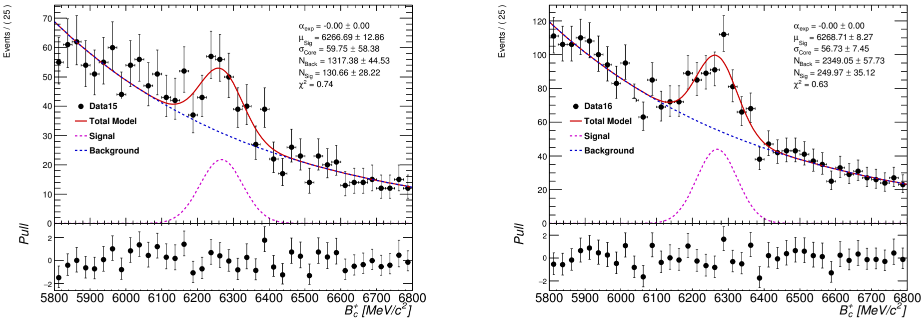

(g) Background modeled with a Exponential function. Signal modeled with a single Gaussian.

(h) Background modeled with a Exponential function. Signal modeled with a single Gaussian.

Figure 11.4: Left hand side shows the 2015 data, and right hand side the 2016 data. The nominal fits can be seen in 11.4a and 11.4b

Table 11.4: Absolute and relative signal yield and mass for the $B_c^\pm$ from the 2016 data. All fits have $\chi^2 < 2.5$.

Model		$N_{B_c^\pm}$	$\Delta N_{B_c^\pm}$	$\frac{\Delta N_{B_c^\pm}}{N_{B_c^\pm}^{Base}}$ [%]	$m_{B_c^\pm}$ [MeV c^{-2}]	$\Delta m_{B_c^\pm}$ [MeV c^{-2}]	$\frac{\Delta m_{B_c^\pm}}{m_{B_c^\pm}^{Base}}$ [%]
Base		235.31	-	-	6270.29	-	-
Background	3rd Order Chebychev	244.05	8.74	3.71	6269.17	-1.13	-0.018
	Exponential	249.97	14.66	6.23	6268.71	-1.58	-0.025
Signal	Crystal Ball	235.55	0.24	0.10	6270.21	-0.08	-0.001

$B^\pm$ mass measurements yield the following systematic uncertainty of 0.05026 for 2015, 0.05009 for 2016 data. The final mass values are given in Table 11.5, while a comparison between our and other measurements can be found in Table 11.6. These systematic uncertainties are considered to be fully correlated.

Table 11.5: The combined mass values were estimated using the method of generalized weighted average as outlined in [50] [51] [52].

	2015 [MeV c^{-2}]	2016 [MeV c^{-2}]
m_B	5278.93 ± 0.12(stat) ± 2.65(syst)	5278.58 ± 0.09(stat) ± 2.64(syst)
	5278.75 ± 0.07(stat) ± 2.63(syst)	
m_{B_c}	6263.60 ± 8.35(stat) ± 4.38(syst)	6270.29 ± 5.81(stat) ± 3.51(syst)
	6268.32 ± 4.77(stat) ± 3.78(syst)	

Table 11.6: Both LHCb and CMS uses the same decay channel $B_c^\pm \to J/\psi\pi^\pm$ that we do to extract the mass estimates. CMS only lists the statistical error on the mass. The world average is taken from the PDG.

Experiment	m_{B_c}[MeV c^{-2}]	
Our measurement	6268.32 ± 4.77(stat) ± 3.78(syst)	6268.32 ± 6.08
LHCb [37]	6273.7 ± 1.3(stat) ± 1.6(syst)	6273.7 ± 2.06
CMS [35]	6267 ± 3(stat)	6267 ± 3
World average [53]		6274.9 ± 0.8

11.5 f_c/f_u Determination

The obtained signal yields and efficiencies can then be entered into Eq. 11.1 in order to determine the fragmentation ratio f_c/f_u. The results for the 2015 and 2016 data sets are collected in Table 11.8, while Table 11.9 lists the obtained uncertainties for the different samples.

11.6 Final Remarks

A proper determination of the signal efficiencies are needed to obtain precise measurements in any analysis where the signal yield is used. However to be able to do

Table 11.7: Efficiencies determined for the $B^{\pm}$ and $B_c^{\pm}$ using truth-truth matched MC samples.

	2015	2016
ϵ_B	$9.39\% \pm 0.03\%$	$5.61\% \pm 0.02\%$
ϵ_{B_c}	$4.07\% \pm 0.02\%$	$3.74\% \pm 0.02\%$

Table 11.8: The $f_c/f_u \times \mathcal{B}_\rfloor \to \mathcal{J}\psi\pi$ was combined using the method of generalized weighted average as outlined in [50] [51] [52]. The f_c/f_u value was also attempted to be combined using this method, however it return a value which were lower than either, and hence a simple approximate formula was used instead. Both values are listed below.

Datasets	$f_c/f_u \times \mathcal{B}_c\,(\to J\psi\pi)\,[10^{-7}]$
2015	$2.83 \pm 0.74_{\text{stat}} \pm 0.02^{\text{uncorr}}_{\text{syst}} \pm 2.80^{\text{corr}}_{\text{syst}}$
2016	$8.62 \pm 1.48_{\text{stat}} \pm 0.06^{\text{uncorr}}_{\text{syst}} \pm 1.48^{\text{corr}}_{\text{syst}}$
Combined	$8.31 \pm 0.66_{\text{stat}} \pm 1.98_{\text{syst}}$ 8.31 ± 2.09

Datasets	$f_c/f_u[10^{-4}]$
2015	$2.18 \pm 0.57_{\text{stat}} \pm 0.01^{\text{uncorr}}_{\text{syst}} \pm 2.59^{\text{corr}}_{\text{syst}}$
2016	$6.66 \pm 1.13_{\text{stat}} \pm 0.04^{\text{uncorr}}_{\text{syst}} \pm 2.86^{\text{corr}}_{\text{syst}}$
Combined	$1.19 \pm 0.51_{\text{stat}} \pm 2.58_{\text{syst}}$
Generalized	1.19 ± 2.63
Combined	$3.06 \pm 0.51_{\text{stat}} \pm 2.72_{\text{syst}}$
Approximate	3.06 ± 2.77

Table 11.9: Shows the list of all systematic uncertainties which goes into the measurement of the fragmentation ratio f_c/f_u. The total uncertainty of the 2015 measurement is clearly dominated by the fit model systematics for the $B_c^{\pm}$, and should be mitigated by more statistics. The fit model uncertainty is not negligible for the 2016 data either, but here the uncertainty is mainly dominated by the theoretical branching fraction prediction. Further MC samples would be needed to better estimate the $B^{\pm}$ fit model contribution.

Source		Relative uncertainty	
		2015	2016
Branching fraction	$\mathcal{B}(B^{\pm} \to J/\psi K^{\pm}$	3.25%	
	$\mathcal{B}(B_c^{\pm} \to J/\psi\pi^{\pm}$	38.46%	
Mass fit	N_B	6.86 %	15.09 %
	N_{B_c}	98.21 %	7.25 %
Efficiencies	ϵ_B	0.02%	0.03%
	ϵ_{B_c}	0.02%	0.02%
Total		105.74 %	42.07 %

this one needs MC samples that reproduce the signal decay and background contributions accurately. Where a large number of simulated events are preferred as it reduces any uncertainties. As there are no verified nor officially produced MC samples for the $B_c^{\pm}$, these have been privately produced. Having a dedicated sample for the $B^{\pm} \to J/\psi\pi^{\pm}$ would prove invaluable as it could potentially reduce the obtained fit model systematics greatly. As similar studies which have a dedicated sample for these events report a fit model systematic of maximum $\sim 2\%$, while we obtain a maximum value of 18% due to these effects. However, the dominating contributing systematic is from the uncertainty on the $B_c^{\pm} \to J/\psi\pi^{\pm}$ branching fraction, as this has a value of 38.5%.

Chapter 12

Conclusion on the Fragmentation Ratio Measurement

Within this thesis we have studied events from decaying $B_c^{\pm}$ particles. These are not very well measured nor are they theoretically well known. However proper studies of these particles would probe our knowledge of heavy quarks, and the SM. We have observed a total of 156 $B_c^{\pm}$ candidates from the $\mathcal{L}_{int} = 3.22\,\text{fb}^{-1}$ 2015, and 1149 from $\mathcal{L}_{int} = 6.85\,\text{fb}^{-1}$ 2016 data using ATLAS. These candidates have been selected through several optimization steps determined through MC samples. We have also performed mass estimation fits, which yields a $m_{B_c^{\pm}} = 6268.32 \pm 6.08$ MeV c^{-2} which is consistent with the world average of $6274.9 \pm 0.8\,\text{MeV}\,c^{-2}$, a comparison of different measure masses can be found in Table 11.6.

Using the obtained efficiency-corrected signal yield for the $B_c^{\pm}$ and $B^{\pm}$ we performed a measurement on the fragmentation ratio f_c/f_u. From our measurements, in Table 11.8, we have determined the following value for this ratio.

$$\frac{f_c}{f_u} = (3.06 \pm 0.51_{\text{stat}} \pm 2.72_{\text{syst}}) \times 10^{-4} \tag{12.1}$$

LHCb, Eq. 12.3 and CMS, 12.4, has performed a measurement of the ratio $\mathcal{R}_{c/u}$, Eq. 12.2.

$$\mathcal{R}_{c/u} = \frac{\sigma(B_c^{\pm})\mathcal{B}(B_c\pm \to J/psi\pi^{\pm})}{\sigma(B^{\pm})\mathcal{B}(B^{\pm} \to J/psiK^{\pm})} = \frac{N_{B_c^{\pm}}}{\epsilon_{B_c^{+}}}\frac{\epsilon_{B^{+}}}{N_{B^{\pm}}} \tag{12.2}$$

The LCHb measurement cannot be directly compared as it uses a psuedorapidity range of $2.5 < \eta < 4.5$ while we have $|\eta| < 2.5$ and the B_c is known to produce more availably in the central region [54].

$$\mathcal{R}_{c/u} = 0.68 \pm 0.10(\text{stat}) \pm 0.03(\text{syst}) \pm 0.05(\text{lifetime})\,\% \tag{12.3}$$

However CMS has a rapidity range of $|y| < 1.6$ which should be more comparable to our result, given in Eq. 12.5.

Table 12.1: My caption

Datasets	$R_{c/u}[10^{-4}]$
2015	$2.78 \pm 0.73_{\text{stat}} \pm 0.02^{\text{uncorr}}_{\text{syst}} \pm 2.75^{\text{corr}}_{\text{syst}}$
2016	$8.49 \pm 1.46_{\text{stat}} \pm 0.05^{\text{uncorr}}_{\text{syst}} \pm 1.43^{\text{corr}}_{\text{syst}}$
Combined	$8.18 \pm 0.65_{\text{stat}} \pm 1.93_{\text{syst}}$ 8.18 ± 2.04

$$\mathcal{R}_{c/u} = 0.48 \pm 0.05(\text{stat}) \pm 0.03(\text{syst}) \pm 0.05(\text{lifetime})\,\% \tag{12.4}$$

Our result is within errors.

$$\mathcal{R}_{c/u} = 0.082 \pm 0.006(\text{stat}) \pm 0.019(\text{syst})\,\% \tag{12.5}$$

This measurement is almost an order in magnitude lower than what LHCb reports, while half an order in magnitude from the result of CMS. It might be that reduction of the systematic effects would increase the measurement, to levels near their listed measurements. However, the fragmentation probabilities on the B-meson kinematics are not well understood. We have assumed that there is no dependence on $|\eta|$ and p_T on the fragmentation probability in our measurements. We have also assumed that the fragmentation ratio is independent of $\sqrt{s}$, and this might be justified. Another master thesis measure f_c/f_u on $\sqrt{s} = 7\,\text{MeV}\,c^{-2}$ and $\sqrt{s} = 8\,\text{MeV}\,c^{-2}$ using ATLAS. They list the following value $f_c/f_u = (5.98 \pm 0.72_{\text{stat}} \pm 0.47_{\text{syst}} \pm 2.70_{\text{theory}}) \times 10^{-4}$ which is fairly close to ours. Still one are unable to draw any proper conclusion on the $\sqrt{s}$ based on these measurements alone.

The 2015 measurement is dominated by the systematic uncertainty of the fit model, however the data from 2016 seem to indicate that this is due to low statistics. As such we believe that combining these two data samples, redoing the fits would greatly reduce the systematics such that only the theoretical value on the $B_c^{\pm} \to J/\psi\pi^{\pm}$ branching fraction would dominate. Since the $\sqrt{s} = 13\,\text{TeV}$, and the 25 ns bunch spacing, is the same for both the 2015 and 2016 data samples, they should be fine to combine. As long as one applies the correct triggers for the corresponding years, and measure the efficiency ratio directly in the MC samples.

Unfortunately there was not enough time to properly determine the systematic uncertainties, and to combine the two data samples, as the data was only given to us by ATLAS on the 17th of July 2017. While the $B_c^{\pm}$ samples completed on the 26th of July 2017. Before this we were only able to use a small sample of roughly 8000 events which we were unable to perform any proper optimization step on. This has led to the later part of this thesis being quite rushed, and the proper level of detail has not been obtained.

Sometimes the fitting procedure performed by MIGRAD falls into local minima and is unable to find the global minimum. By varying certain parameters in the different tested fit models we can then help MIGRAD in finding the global minimum, though there was no time to perform this. Since these models are included as a source of systematic error, we could potentially decrease the fit model induced systematic uncertainties by performing this operation. However, having a dedicated $B^{\pm} \to J/\psi\pi^{\pm}$ might make the need for this parameter tweaking unnecessary. As most of the systemic uncertainties seems to stem from fits not being able to find an optimal fraction between the PDFs used. One of these effects comes from the fact this peaking background is not being well modeled. Another is that the hyperbolic tangent, and the complimentary error function, sometimes has a too large fraction which causes the combinatorial background underneath the signal region to be underestimated. Through proper sideband studies one might have been able to mediate these introduced issues.

Overall the results seem quite promising and warrants further polishing of certain key aspects. As for instance, a proper estimation of all systematic uncertainties would increase the measurement precision. Also it would be nice to perform the measurements in the different psuedorapdities, which were mentioned earlier in this thesis. As the $B_c^{\pm}$ is dependent on this value. Proper sideband studies should also be performed, though there was not enough time to include this in the thesis.

However, the data used in this thesis does not included the delayed physics stream, and as such the majority of the 2016 data samples are not included. It could be reasonable to blind the remaining unused data, and perform sideband studies before performing final fits, and then unblinding the results.

References

[1] R. Brun and F. Rademakers, "Root—an object oriented data analysis framework," *Nuclear Instruments and Methods in Physics Research Section A: Accelerators, Spectrometers, Detectors and Associated Equipment*, vol. 389, no. 1-2, pp. 81–86, 1997.

[2] W. Verkerke and D. Kirkby, "The roofit toolkit for data modeling," Jun. 14, 2003. arXiv: `physics/0306116v1 [physics.data-an]`.

[3] D. K. W. Verkerke. (2017). Roofit users manual v2.07, [Online]. Available: `http://roofit.sourceforge.net/docs/RooFit_Users_Manual_2.07-29.pdf` (visited on 07/10/2017).

[4] M. Morhac. (2017). Tspectrum class reference, [Online]. Available: `https://root.cern.ch/doc/v608/classTSpectrum.html` (visited on 07/10/2017).

[5] I. Polák and J. Kvasnička, "A fast uv-led qrdriver for calibration system for sipm based scintillator hcal detector," *Journal of Instrumentation*, vol. 9, no. 03, p. C03015, 2014. [Online]. Available: `http://iopscience.iop.org/article/10.1088/1748-0221/9/03/C03015/meta;jsessionid=569F4F8B09F7D7682BF9338B05F0A961.c2.iopscience.cld.iop.org` (visited on 07/10/2017).

[6] T. LeCroy. (2017). Do6000a oscilloscopes datasheet, [Online]. Available: `http://cdn.teledynelecroy.com/files/pdf/hdo6000a-oscilloscopes-datasheet.pdf` (visited on 07/10/2017).

[7] T. LeCroy. (2017). Operator's manual hdo6000 / hdo6000a high definition oscilloscopes, [Online]. Available: `http://cdn.teledynelecroy.com/files/manuals/hdo6000a-operators-manual.pdf` (visited on 07/10/2017).

[8] J. Cvach, M. Janata, M. Kovalcuk, *et al.*, "Opticle fibre calibration system and adaptive power supply," Mar. 24, 2015. arXiv: `1503.06940v1 [physics.ins-det]`.

[9] Hamamatsu. (2017). Mppc s12571-010, -015c/p, [Online]. Available: `http://www.hamamatsu.com/resources/pdf/ssd/s12571-010_etc_kapd1044e.pdf` (visited on 07/10/2017).

[10] Hamamatsu. (2017). Mppc s13360 series, [Online]. Available: `https://www.hamamatsu.com/resources/pdf/ssd/s13360_series_kapd1052e.pdf` (visited on 07/10/2017).

[11] KETEK. (2017). Pm3325-eb pm3350-eb datasheet, [Online]. Available: `https://4b0vz81vun5u2kaw7x3w6ptl-wpengine.netdna-ssl.com/wp-content/uploads/2017/01/KETEK-PM3325-EB-PM3350-EB-Datasheet.pdf` (visited on 07/10/2017).

[12] E. W. Weisstein. (2017). Relative error, [Online]. Available: `http://mathworld.wolfram.com/RelativeError.html` (visited on 07/10/2017).

[13] M. Morhac, J. Kliman, V. Matousek, M. Veselsky, and I. Turzo, "Background elimination methods for multidimensional coincidence γ-ray spectra," *Nuclear Instruments and Methods in Physics Research Section A: Accelerators, Spectrometers, Detectors and Associated Equipment*, vol. 401, no. 1, pp. 113–132, 1997.

[14] M. Morhac and V. Matousek, "Peak clipping algorithms for background estimation in spectroscopic data," *Applied spectroscopy*, vol. 62, no. 1, pp. 91–106, 2008.

[15] M. Morháč, J. Kliman, V. Matoušek, M. Veselsky, and I. Turzo, "Identification of peaks in multidimensional coincidence γ-ray spectra," *Nuclear Instruments and Methods in Physics Research Section A: Accelerators, Spectrometers, Detectors and Associated Equipment*, vol. 443, no. 1, pp. 108–125, 2000.

[16] M. Morhac, "Multidimensional peak searching algorithm for low-statistics nuclear spectra," *Nuclear Instruments and Methods in Physics Research Section A: Accelerators, Spectrometers, Detectors and Associated Equipment*, vol. 581, no. 3, pp. 821–830, 2007.

[17] E. Vigo-Castellví, "Study of the ventilation at ATLAS cavern UX15: air velocity and temperature around the muon chambers," CERN, Geneva, Tech. Rep. CERN-ST-2000-063. CERN-ST-CV-2000-145-EVC, 2000. [Online]. Available: `https://cds.cern.ch/record/476676`.

[18] C. Dietzinger, T. Ganka, W. Gebauer, *et al.* (2012). Silicon photomultipliers with enhanced blue-light sensitivity, KETEK Gmbh and Technische Universität München, [Online]. Available: `https://indico.cern.ch/event/164917/contributions/1417113/attachments/198506/278655/PhotoDet2012-KETEK-14-June-2012.pdf` (visited on 07/10/2017).

[19] C. De Melis, "The CERN accelerator complex. Complexe des accélérateurs du CERN," 2016, General Photo. [Online]. Available: `https://cds.cern.ch/record/2197559`.

[20] G. Aad *et al.*, "Measurement of the inclusive jet cross section in pp collisions at sqrt(s)=2.76 TeV and comparison to the inclusive jet cross section at sqrt(s)=7 TeV using the ATLAS detector," *Eur. Phys. J.*, vol. C73, no. 8, p. 2509, 2013. DOI: `10.1140/epjc/s10052-013-2509-4`. arXiv: `1304.4739 [hep-ex]`.

[21] A. Collaboration, "Performance of the atlas track reconstruction algorithms in dense environments in lhc run 2," Apr. 26, 2017. arXiv: `1704.07983v1 [hep-ex]`.

[22] A. Collaboration, "Muon reconstruction performance of the atlas detector in proton–proton collision data at $\sqrt{s}$=13 tev," *Eur. Phys. J. C (2016) 76:292*, Mar. 17, 2016. DOI: `10.1140/epjc/s10052-016-4120-y`. arXiv: `1603.05598v2 [hep-ex]`.

[23] C. P. et al. (Particle Data Group), *Chin. Phys. C*, 100001 (2016) and 2017 update.

[24] F. Capozzi, E. Lisi, A. Marrone, D. Montanino, and A. Palazzo, "Neutrino masses and mixings: Status of known and unknown 3ν parameters," Jan. 28, 2016. DOI: `10.1016/j.nuclphysb.2016.02.016`. arXiv: `1601.07777v1 [hep-ph]`.

[25] E. W. Otten and C. Weinheimer, "Neutrino mass limit from tritium beta decay," *Rept.Prog.Phys.71:086201,2008*, Sep. 11, 2009. arXiv: `0909.2104v1 [hep-ex]`.

[26] G. S. Franz Mandl, *Quantum Field Theory.* JOHN WILEY & SONS INC, Jun. 11, 2010, 478 pp., ISBN: 0471496847. [Online]. Available: `http://www.ebook.de/de/product/7349270/franz_mandl_graham_shaw_quantum_field_theory.html`.

[27] J. H. Christenson, J. W. Cronin, V. L. Fitch, and R. Turlay, "Evidence for the 2π decay of the K_2^0 meson," *Phys. Rev. Lett.*, vol. 13, pp. 138–140, 4 Jul. 1964. DOI: `10.1103/PhysRevLett.13.138`. [Online]. Available: `https://link.aps.org/doi/10.1103/PhysRevLett.13.138`.

[28] K. Abe, K. Abe, R. Abe, *et al.*, “Observation of large *CP* violation in the neutral B meson system,” *Phys. Rev. Lett.*, vol. 87, p. 091 802, 9 Aug. 2001. DOI: `10.1103/PhysRevLett.87.091802`. [Online]. Available: `https://link.aps.org/doi/10.1103/PhysRevLett.87.091802`.

[29] B. Aubert, D. Boutigny, J.-M. Gaillard, *et al.*, “Observation of *CP* violation in the B^0 meson system,” *Phys. Rev. Lett.*, vol. 87, p. 091 801, 9 Aug. 2001. DOI: `10.1103/PhysRevLett.87.091801`. [Online]. Available: `https://link.aps.org/doi/10.1103/PhysRevLett.87.091801`.

[30] B. Aubert, M. Bona, D. Boutigny, *et al.*, “Evidence for D^0–$\overline{D}^0$ mixing,” *Phys. Rev. Lett.*, vol. 98, p. 211 802, 21 May 2007. DOI: `10.1103/PhysRevLett.98.211802`. [Online]. Available: `https://link.aps.org/doi/10.1103/PhysRevLett.98.211802`.

[31] N. Brambilla, M. Krämer, R. Mussa, *et al.*, “Heavy quarkonium physics,” *CERN Yellow Report, CERN-2005-005, Geneva: CERN, 2005.- 487 p.*, Dec. 13, 2004. arXiv: `hep-ph/0412158v2 [hep-ph]`.

[32] V. V. Kiselev, “Decays of the B_c meson,” Aug. 21, 2003. arXiv: `hep-ph/0308214v1 [hep-ph]`.

[33] A. J. Bevan *et al.*, “The Physics of the B Factories,” *Eur. Phys. J.*, vol. C74, p. 3026, 2014. DOI: `10.1140/epjc/s10052-014-3026-9`. arXiv: `1406.6311 [hep-ex]`.

[34] C. Collaboration, “Measurement of the ratio of the production cross sections times branching fractions of Bc+/- to J/psi pi+/- and B+/- to J/psi K+/- and B(Bc+/- to J/psi pi+/- pi+/- pi-/+)/B(Bc+/- to J/psi pi+/-) in pp collisions at sqrt(s) = 7 TeV,” *JHEP 01 (2015) 063*, Oct. 21, 2014. DOI: `10.1007/JHEP01(2015)063`. arXiv: `1410.5729v2 [hep-ex]`.

[35] “Observation of the decays B_c to $J/\psi\ \pi$ and B_c to $J/\psi\ \pi\ \pi\ \pi$ in pp collisions at $\sqrt{s} = 7TeV$,” CERN, Geneva, Tech. Rep. CMS-PAS-BPH-11-003, 2012. [Online]. Available: `http://cds.cern.ch/record/1461944`.

[36] G. Yuan-Ning, H. Ji-Bo, P. Robbe, M.-h. Schune, and Y. Zhen-Wei, “Experimental prospects of the B_c studies of the lhcb experiment,” *Chinese Physics Letters*, vol. 27, no. 6, p. 061 302, 2010. [Online]. Available: `http://stacks.iop.org/0256-307X/27/i=6/a=061302`.

[37] L. collaboration, “Measurements of B_c^+ production and mass with the $B_c^+ \rightarrow J/yp^+$ decay,” *Phys. Rev. Lett. 109, 232001 (2012)*, Sep. 25, 2012. DOI: `10.1103/PhysRevLett.109.232001`. arXiv: `1209.5634v3 [hep-ex]`.

[38] C.-H. Chang and X.-G. Wu, “Uncertainties in estimating hadronic production of the meson B_c and comparisons between tevatron and lhc,” *Eur.Phys.J.C38:267-276,2004*, Sep. 11, 2003. DOI: `10.1140/epjc/s2004-02015-0`. arXiv: `hep-ph/0309121v5 [hep-ph]`.

[39] T. Aaltonen, S. Amerio, D. Amidei, *et al.*, “Measurement of the B_c production cross section in $p\overline{p}$ collisions at $\sqrt{s} = 1.96$ TeV,” *Phys. Rev. D*, vol. 93, p. 052 001, 5 Mar. 2016. DOI: `10.1103/PhysRevD.93.052001`. [Online]. Available: `https://link.aps.org/doi/10.1103/PhysRevD.93.052001`.

[40] R. Aaij *et al.*, “Measurement of the B_c^+ meson lifetime using $B_c^+ \rightarrow J/\psi\mu^+\nu_\mu X$ decays,” *Eur. Phys. J.*, vol. C74, no. 5, p. 2839, 2014. DOI: `10.1140/epjc/s10052-014-2839-x`. arXiv: `1401.6932 [hep-ex]`.

[41] (Jul. 29, 2017), [Online]. Available: `http://pdg.lbl.gov/2017/listings/rpp2017-list-B-plus-minus.pdf`.

[42] H. F. A. Group, “Averages of b-hadron, c-hadron, and τ-lepton properties as of summer 2016,” Jun. 12, 2017. arXiv: `1612.07233v2 [hep-ex]`.

[43] R. J. A. Whartona W. Yaob, “Atlas inner detector track quality cuts for run 2,” Tech. Rep., Jul. 30, 2017. [Online]. Available: `https://cds.cern.ch/record/1752536/files/ATL-COM-PHYS-2014-1084.pdf`.

[44] “Tracking cp pre-recommendations for 2017 winter conferences,” Tech. Rep., Jul. 30, 2017. [Online]. Available: `https://twiki.cern.ch/twiki/bin/view/AtlasProtected/TrackingCPMoriond2017`.

[45] D. Casadei, “Estimating the selection efficiency,” *JINST*, vol. 7, P08021, 2012. DOI: `10.1088/1748-0221/7/08/P08021`. arXiv: `0908.0130 [physics.data-an]`.

[46] E. W. Weisstein. (Jul. 30, 2017). Chebyshev polynomial of the first kind., [Online]. Available: `http://mathworld.wolfram.com/ChebyshevPolynomialoftheFirstKind.html`.

[47] L. Demortier and L. Lyons, “Everything you always wanted to know about pulls,” CDF, Tech. Rep. CDF/ANAL/PUBLIC/5776, Feb. 2002. [Online]. Available: `http://physics.rockefeller.edu/luc/technical_reports/cdf5776_pulls.pdf`.

[48] “$B^{\pm}$ mass reconstruction in $B^{\pm} \to J/\psi K^{\pm}$ decay at ATLAS at 13 TeV pp collisions at the LHC,” CERN, Geneva, Tech. Rep. ATLAS-CONF-2015-064, Dec. 2015. [Online]. Available: `https://cds.cern.ch/record/2114830`.

[49] C.-H. Chang, C. Driouichi, P. Eerola, and X.-G. Wu, “Bcvegpy: An event generator for hadronic production of the B_c meson,” *Comput.Phys.Commun.159:192-224,2004*, Sep. 11, 2003. DOI: `10.1016/j.cpc.2004.02.005`. arXiv: `hep-ph/0309120v1 [hep-ph]`.

[50] M. K. Bugge, A. Read, and O. M. Røhne. (Aug. 4, 2017). Mean or average of two partially correlated measurements, [Online]. Available: `https://wiki.uio.no/mn/fys/epf/index.php/Mean_or_average_of_two_partially_correlated_measurements`.

[51] L. Lyons, D. Gibaut, and P. Clifford, “How to combine correlated estimates of a single physical quantity,” *Nuclear Instruments and Methods in Physics Research Section A: Accelerators, Spectrometers, Detectors and Associated Equipment*, vol. 270, no. 1, pp. 110–117, 1988, ISSN: 0168-9002. DOI: `http://dx.doi.org/10.1016/0168-9002(88)90018-6`. [Online]. Available: `http://www.sciencedirect.com/science/article/pii/0168900288900186`.

[52] M. G. Cox, C. Eiø, G. Mana, and F. Pennecchi, “The generalized weighted mean of correlated quantities,” *Metrologia*, vol. 43, no. 4, S268, Aug. 4, 2017. [Online]. Available: `http://stacks.iop.org/0026-1394/43/i=4/a=S14`.

[53] (Aug. 4, 2017), [Online]. Available: `http://pdg.lbl.gov/2017/listings/rpp2017-list-Bc-plus-minus.pdf`.

[54] A. V. Berezhnoy, V. V. Kiselev, A. K. Likhoded, and A. I. Onischenko, “B_c meson at lhc,” *Phys.Atom.Nucl.60:1729-1740,1997; Yad.Fiz.60N10:1889-1900.1997*, Mar. 17, 1997. arXiv: `hep-ph/9703341v1 [hep-ph]`.

[55] G. Eigen, A. Træet, J. Zalieckas, *et al.*, “Sipm gain stabilization studies for adaptive power supply,” Feb. 29, 2016. arXiv: `1603.00016v1 [physics.ins-det]`.

[56] A. Collaboration, “Determination of the ratio of b-quark fragmentation fractions f_s/f_d in pp collisions at $\sqrt{s} = 7$ tev with the atlas detector,” *Phys. Rev. Lett. 115, 262001 (2015)*, Jul. 31, 2015. DOI: `10.1103/PhysRevLett.115.262001`. arXiv: `1507.08925v2 [hep-ex]`.

[57] "Studies of the ATLAS Inner Detector material using $\sqrt{s}$ =13 TeV *pp* collision data," CERN, Geneva, Tech. Rep. ATL-PHYS-PUB-2015-050, 2015. [Online]. Available: `https://cds.cern.ch/record/2109010`.

[58] J. Heinrich, "Pitfalls of Goodness-of-Fit from Likelihood," *eConf*, vol. C030908, MOCT001, 2003, [,52(2003)]. arXiv: `physics/0310167 [physics.data-an]`.

[59] J. Heinrich. (2017). Goodness of fit recommendations, [Online]. Available: `https://www-cdf.fnal.gov/physics/statistics/recommendations/goodnessoffit.html` (visited on 07/10/2017).

[60] S. Piatek. (2017). A technical guide to silicon photomultipliers (sipm), [Online]. Available: `https://www.hamamatsu.com/us/en/community/optical_sensors/articles/technical_guide_to_silicon_photomultipliers_sipm/index.html` (visited on 07/10/2017).

[61] P. Eckert, H.-C. Schultz-Coulon, W. Shen, R. Stamen, and A. Tadday, "Characterisation studies of silicon photomultipliers," *Nucl.Instrum.Meth.A620:217-226,2010*, Mar. 31, 2010. DOI: `10.1016/j.nima.2010.03.169`. arXiv: `1003.6071v2 [physics.ins-det]`.

[62] A. Ghassemi, K. Sato, and K. Kobayashi, "Mppc," Hamamatsu Photonics K.K., Solid State Division, Tech. Rep., 2017. [Online]. Available: `https://www.hamamatsu.com/resources/pdf/ssd/mppc_kapd9005e.pdf` (visited on 07/10/2017).

[63] A. e. a. Vacheret, "Characterization and Simulation of the Response of Multi Pixel Photon Counters to Low Light Levels," *Nucl. Instrum. Meth.*, vol. A656, no. 1, pp. 69–83, 2011. DOI: `10.1016/j.nima.2011.07.022`. arXiv: `1101.1996 [physics.ins-det]`.

[64] Otte, Adam Nepomuk et al., "Characterization of Three High Efficiency and Blue Sensitive Silicon Photomultipliers," *Nucl. Instrum. Meth.*, vol. A846, pp. 106–125, 2017. DOI: `10.1016/j.nima.2016.09.053`. arXiv: `1606.05186 [physics.ins-det]`.

[65] *Data Analysis in High Energy Physics*. Wiley VCH Verlag GmbH, Jun. 26, 2013, ISBN: 3527410589. [Online]. Available: `http://www.ebook.de/de/product/20188461/data_analysis_in_high_energy_physics.html`.

[66] K. K. Konrad Kleinknecht, *Detectors for Particle Radiation*. CAMBRIDGE UNIV PR, Dec. 11, 2003, 260 pp., ISBN: 0521648548. [Online]. Available: `http://www.ebook.de/de/product/4061575/konrad_kleinknecht_k_kleinknecht_detectors_for_particle_radiation.html`.

[67] N. B. S. Andrew Webb, *Introduction to Medical Imaging*. Cambridge University Press, Nov. 18, 2010, 298 pp., ISBN: 0521190657. [Online]. Available: `http://www.ebook.de/de/product/11904691/andrew_webb_nadine_barrie_smith_introduction_to_medical_imaging.html`.

[68] *Subatomic Physics*. World Scientific Publishing Company, Jul. 13, 2007, 642 pp., ISBN: 9812700579. [Online]. Available: `http://www.ebook.de/de/product/6456326/subatomic_physics.html`.

[69] J. D. Walecka, *Topics in Modern Physics*. World Scientific Publishing Company, Jan. 21, 2013, 500 pp., ISBN: 9814436895. [Online]. Available: `http://www.ebook.de/de/product/19884261/john_dirk_walecka_topics_in_modern_physics.html`.

[70] D. Griffiths, *Introduction to Elementary Particles*. Wiley VCH Verlag GmbH, Aug. 11, 2008, ISBN: 3527406018. [Online]. Available: `http://www.ebook.de/de/product/4008107/david_griffiths_introduction_to_elementary_particles.html`.

[71] S. Prata, *C++ Primer Plus*. Addison Wesley, Sep. 11, 2011, 1200 pp., ISBN: 0321776402. [Online]. Available: `http://www.ebook.de/de/product/15355139/stephen_prata_c_primer_plus.html`.

[72] J. Zelle, *Python Programming: An Introduction to Computer Science*. Franklin, Beedle & Associates, 2010, ISBN: 9781590282410. [Online]. Available: `https://www.amazon.com/Python-Programming-Introduction-Computer-Science/dp/1590282418?SubscriptionId=0JYN1NVW651KCA56C102&tag=techkie-20&linkCode=xm2&camp=2025&creative=165953&creativeASIN=1590282418`.

[73] F. W. Byron, *Mathematics of Classical and Quantum Physics*. DOVER PUBLICATIONS, Aug. 11, 1992, ISBN: 048667164X. [Online]. Available: `http://www.ebook.de/de/product/3303148/frederick_w_byron_mathematics_of_classical_and_quantum_physics.html`.

[74] W. R. Leo, *Techniques for Nuclear and Particle Physics Experiments*. Springer-Verlag GmbH, Jan. 11, 1994, ISBN: 3540572805. [Online]. Available: `http://www.ebook.de/de/product/3236631/william_r_leo_techniques_for_nuclear_and_particle_physics_experiments.html`.

[75] H. Spieler, *Semiconductor Detector Systems*. OXFORD UNIV PR, Oct. 11, 2005, 489 pp., ISBN: 0198527845. [Online]. Available: `http://www.ebook.de/de/product/4443566/helmuth_spieler_semiconductor_detector_systems.html`.

[76] F. Mandl, *Quantum Mechanics*. Wiley-Blackwell, Mar. 11, 1992, ISBN: 0471931551. [Online]. Available: `http://www.ebook.de/de/product/3236938/franz_mandl_quantum_mechanics.html`.

[77] A. Beiser, *Concepts of Modern Physics*. McGraw-Hill Europe, 2002, ISBN: 0071234608. [Online]. Available: `https://www.amazon.com/Concepts-Modern-Physics-Arthur-Beiser/dp/0071234608?SubscriptionId=0JYN1NVW651KCA56C102&tag=techkie-20&linkCode=xm2&camp=2025&creative=165953&creativeASIN=0071234608`.

[78] C. Grupen and B. Shwartz, *Particle Detectors*. Cambridge University Press, Mar. 3, 2011, 676 pp., ISBN: 0521187958. [Online]. Available: `http://www.ebook.de/de/product/13945458/claus_grupen_boris_shwartz_particle_detectors.html`.

[79] P. Hofmann, *Solid State Physics: An Introduction*. Wiley-VCH, 2011, ISBN: 9783527408610. [Online]. Available: `https://www.amazon.com/Solid-State-Physics-Philip-Hofmann-ebook/dp/B006H31NT6?SubscriptionId=0JYN1NVW651KCA56C102&tag=techkie-20&linkCode=xm2&camp=2025&creative=165953&creativeASIN=B006H31NT6`.

[80] K. Wille, *The Physics of Particle Accelerators: An Introduction*. OXFORD UNIV PR, Feb. 11, 2001, 328 pp., ISBN: 0198505493. [Online]. Available: `http://www.ebook.de/de/product/2758400/klaus_wille_the_physics_of_particle_accelerators_an_introduction.html`.

[81] *Elementary Differential Equations and Boundary Value Problem.* WILEY ACADEMIC, Dec. 4, 2012, ISBN: 1118323610. [Online]. Available: `http://www.ebook.de/de/product/20512024/elementary_differential_equations_and_boundary_value_problem.html`.

[82] *Introduction to High Energy Physics.* Cambridge University Press, Apr. 13, 2000, 442 pp., ISBN: 0521621968. [Online]. Available: `http://www.ebook.de/de/product/3620669/donald_h_university_of_oxford_perkins_introduction_to_high_energy_physics.html`.

[83] J. D. Bjorken and S. D. Drell, *Relativistic Quantum Mechanics (Pure & Applied Physics).* Mcgraw-Hill College, 1965, ISBN: 978-0070054936. [Online]. Available: `https://www.amazon.com/Relativistic-Quantum-Mechanics-Applied-Physics/dp/0070054932?SubscriptionId=0JYN1NVW651KCA56C102&tag=techkie-20&linkCode=xm2&camp=2025&creative=165953&creativeASIN=0070054932`.

[84] J. D. Bjorken and S. D. Drell, *Relativistic Quantum Fields.* Mcgraw-Hill College, 1965, ISBN: 978-0070054943. [Online]. Available: `https://www.amazon.com/Relativistic-Quantum-Fields-James-Bjorken/dp/0070054940?SubscriptionId=0JYN1NVW651KCA56C102&tag=techkie-20&linkCode=xm2&camp=2025&creative=165953&creativeASIN=0070054940`.

[85] J. Pequenao, "Computer generated image of the whole ATLAS detector," 2008, [Online]. Available: `https://cds.cern.ch/record/1095924`.

[86] C. Collaboration, "Measurement of the total and differential inclusive B^+ hadron cross sections in pp collisions at $\sqrt(s) = 13$ tev," Sep. 3, 2016. DOI: `10.1016/j.physletb.2017.05.074`. arXiv: `1609.00873v1 [hep-ex]`.

Appendix A

Bias scan measurements for Hamamatsu

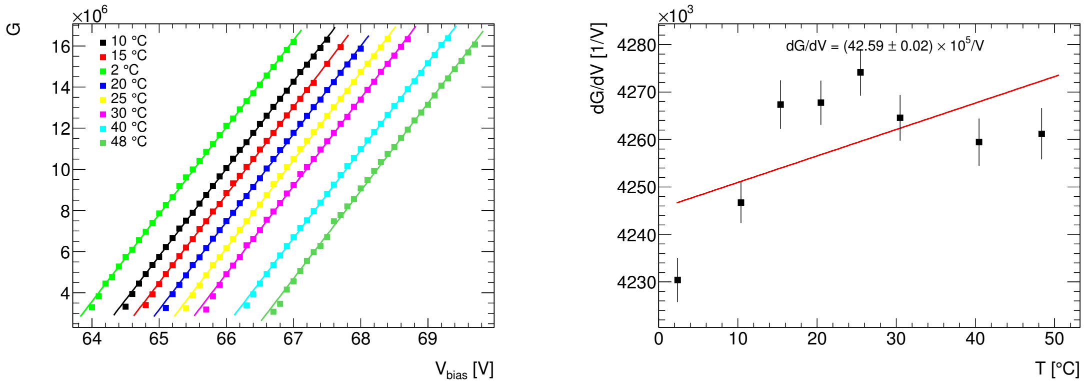

(a) Measurements of gain-versus-bias voltage (dG/dV) for fixed temperatures.

(b) Plot shows the obtained values of the dG/dV versus fixed temperature.

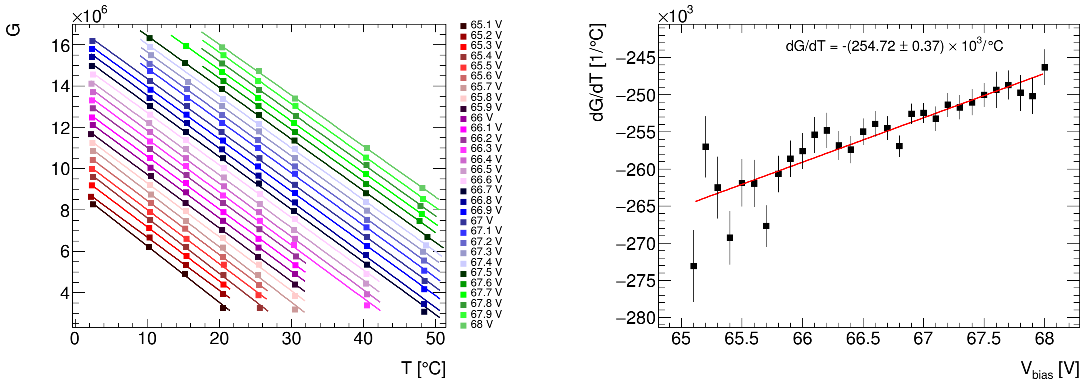

(c) Measurements of gain-versus-temperature (dG/dT) for fixed bias.

(d) Plot shows the obtained values of the dG/dT versus fixed bias voltage.

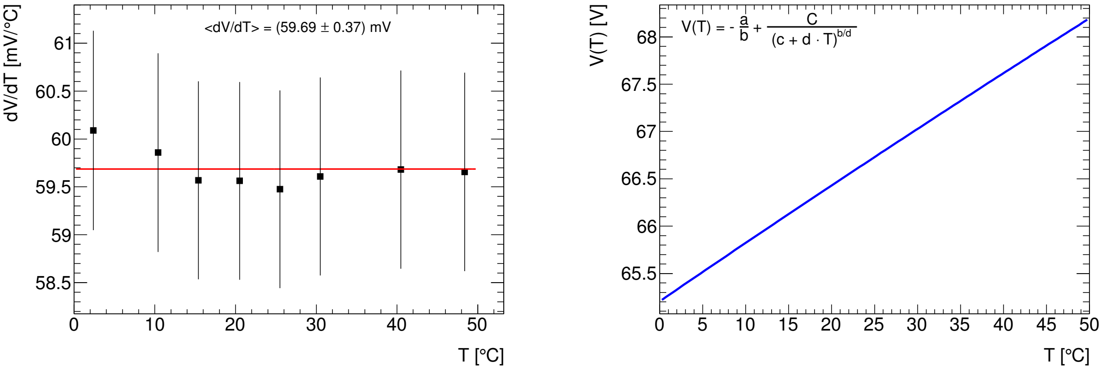

(e) Weighted average distribution of dV/dT as a function of temperature.

(f) Plot illustrates the bias voltage as a function of temperature.

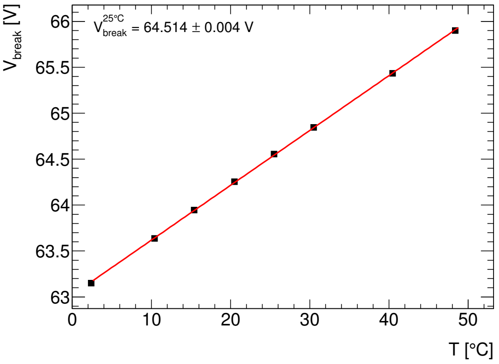

(g) Plot shows the determined breakdown voltage at different temperatures.

Figure A.1: All measurements are taken with the Hamamatsu detector A1 20µm with channel 1 preamplifier.

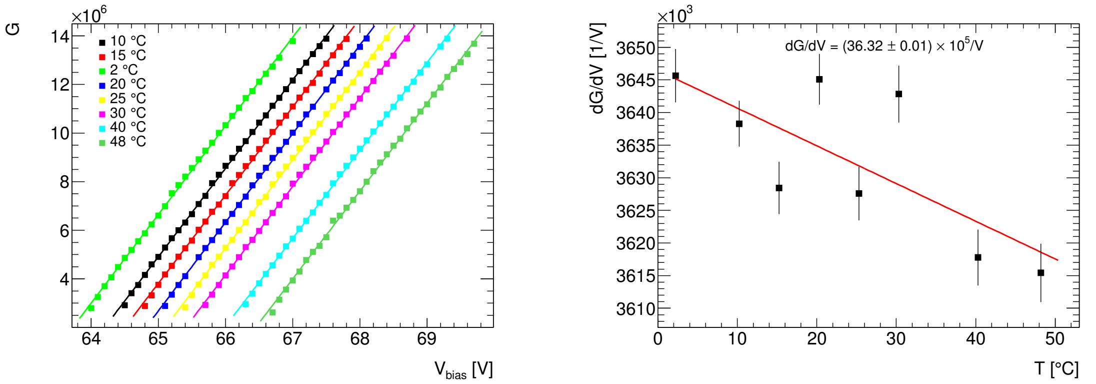

(a) Measurements of gain-versus-bias voltage (dG/dV) for fixed temperatures.

(b) Plot shows the obtained values of the dG/dV versus fixed temperature.

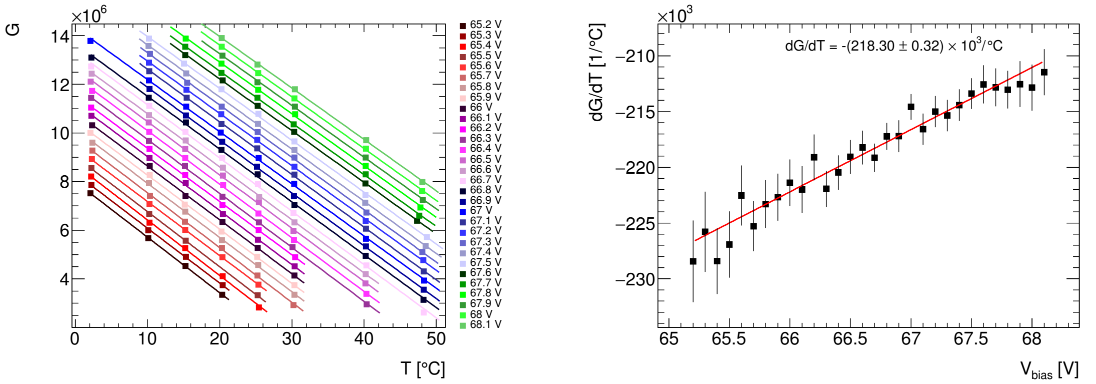

(c) Measurements of gain-versus-temperature (dG/dT) for fixed bias.

(d) Plot shows the obtained values of the dG/dT versus fixed bias voltage.

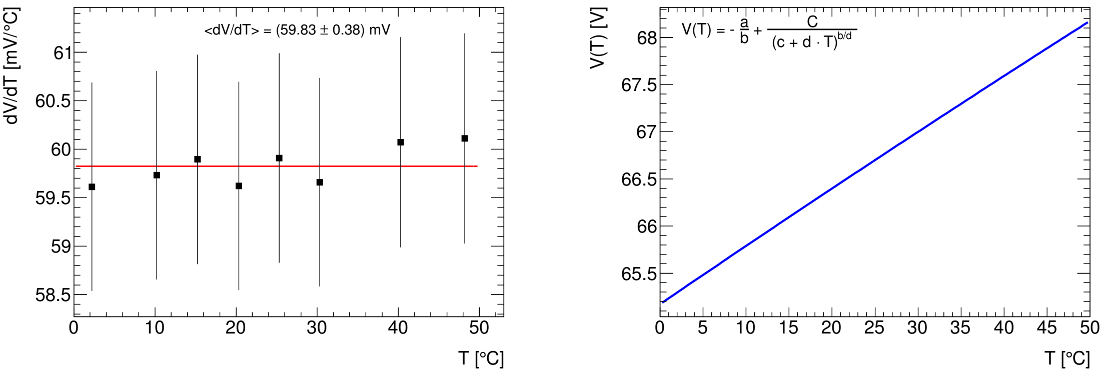

(e) Weighted average distribution of dV/dT as a function of temperature.

(f) Plot illustrates the bias voltage as a function of temperature.

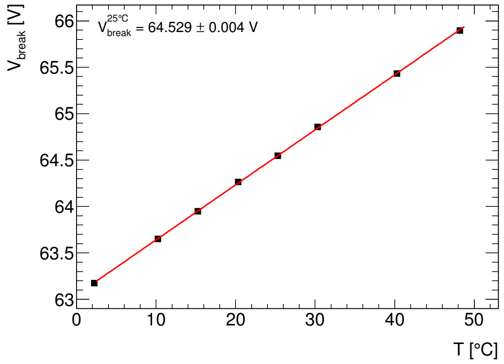

(g) Plot shows the determined breakdown voltage at different temperatures.

Figure A.2: All measurements are taken with the Hamamatsu detector A2 20µm with channel 2 preamplifier.

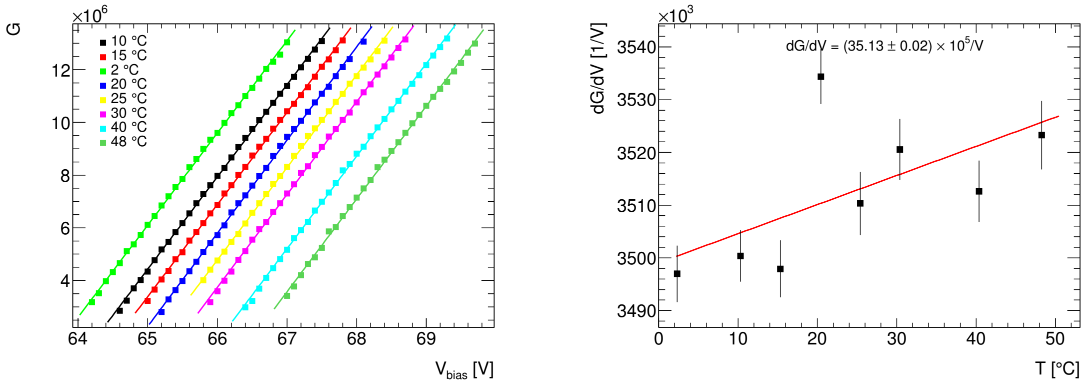

(a) Measurements of gain-versus-bias voltage (dG/dV) for fixed temperatures.

(b) Plot shows the obtained values of the dG/dV versus fixed temperature.

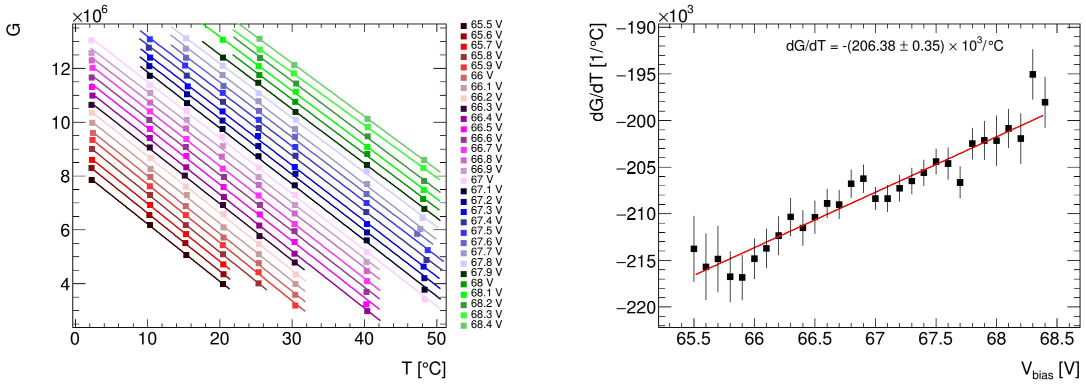

(c) Measurements of gain-versus-temperature (dG/dT) for fixed bias.

(d) Plot shows the obtained values of the dG/dT versus fixed bias voltage.

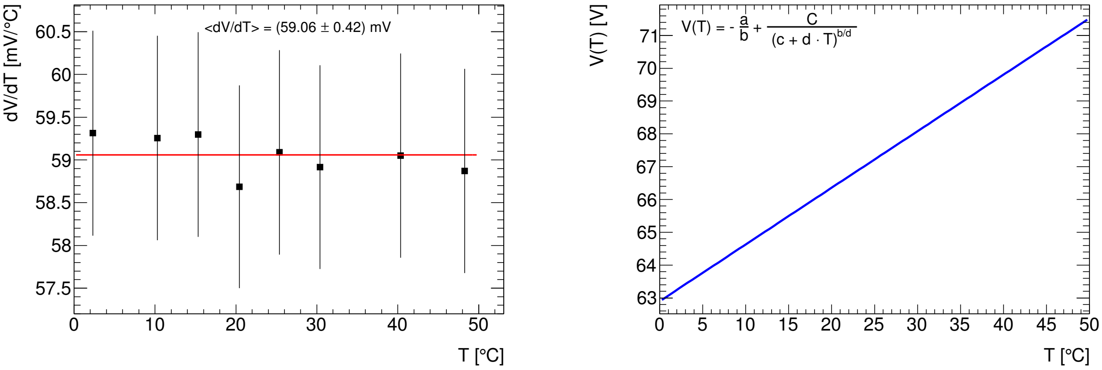

(e) Weighted average distribution of dV/dT as a function of temperature.

(f) Plot illustrates the bias voltage as a function of temperature.

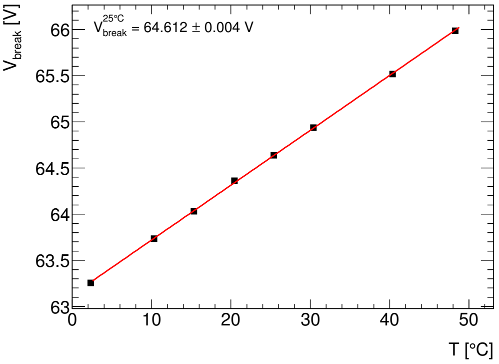

(g) Plot shows the determined breakdown voltage at different temperatures.

Figure A.3: All measurements are taken with the Hamamatsu detector A1 15µm with channel 3 preamplifier.

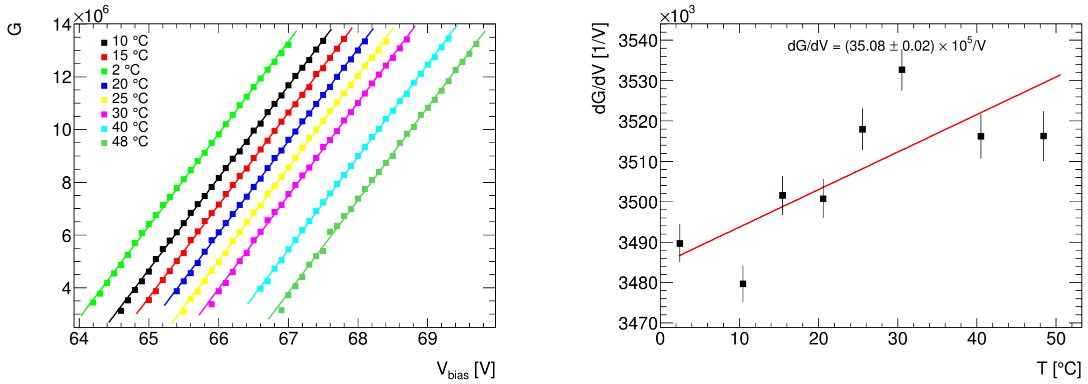

(a) Measurements of gain-versus-bias voltage (dG/dV) for fixed temperatures.

(b) Plot shows the obtained values of the dG/dV versus fixed temperature.

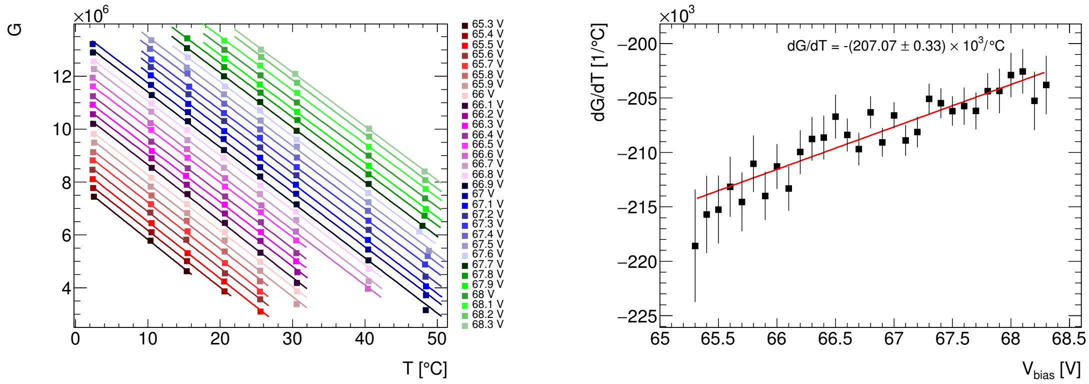

(c) Measurements of gain-versus-temperature (dG/dT) for fixed bias.

(d) Plot shows the obtained values of the dG/dT versus fixed bias voltage.

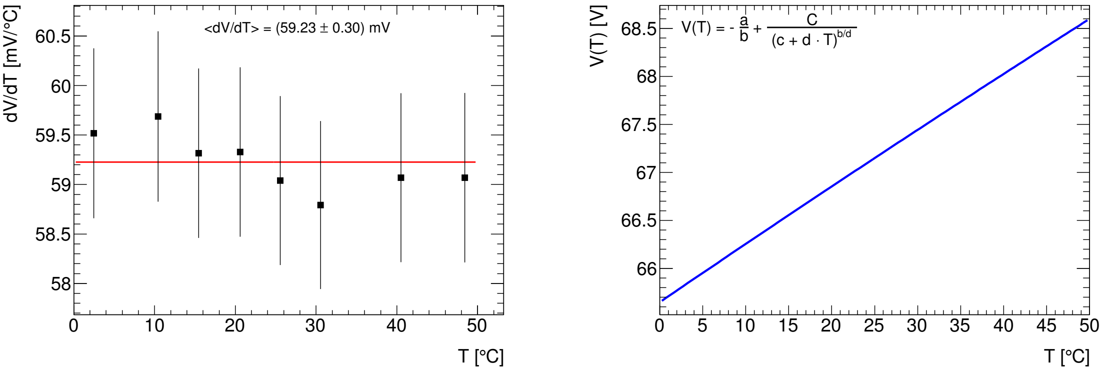

(e) Weighted average distribution of dV/dT as a function of temperature.

(f) Plot illustrates the bias voltage as a function of temperature.

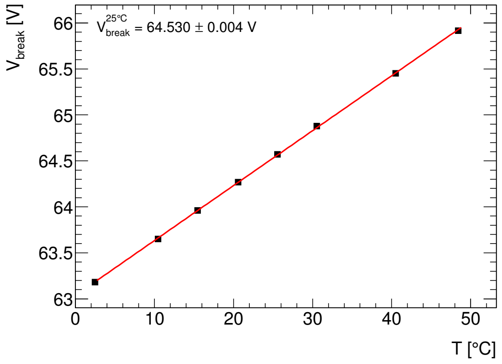

(g) Plot shows the determined breakdown voltage at different temperatures.

Figure A.4: All measurements are taken with the Hamamatsu detector A2 15µm with channel 4 preamplifier.

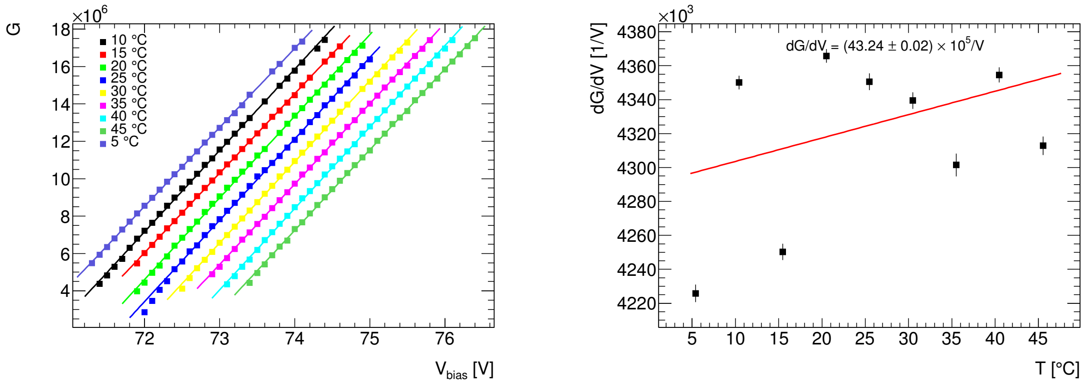

(a) Measurements of gain-versus-bias voltage (dG/dV) for fixed temperatures.

(b) Plot shows the obtained values of the dG/dV versus fixed temperature.

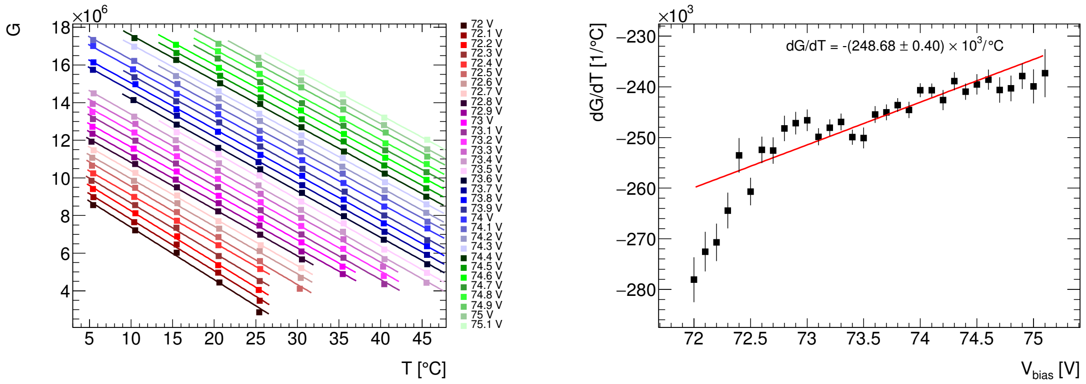

(c) Measurements of gain-versus-temperature (dG/dT) for fixed bias.

(d) Plot shows the obtained values of the dG/dT versus fixed bias voltage.

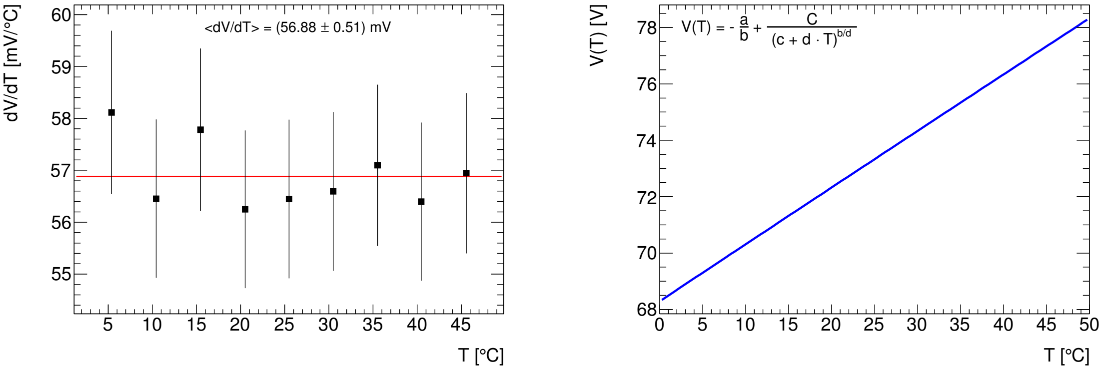

(e) Weighted average distribution of dV/dT as a function of temperature.

(f) Plot illustrates the bias voltage as a function of temperature.

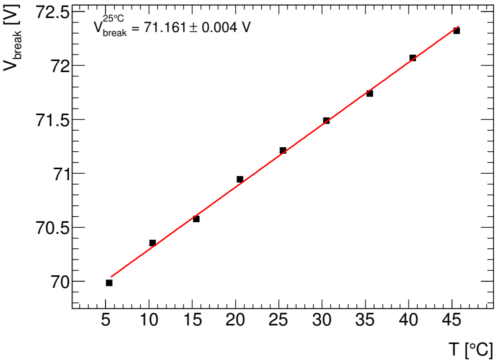

(g) Plot shows the determined breakdown voltage at different temperatures.

Figure A.5: All measurements are taken with the Hamamatsu detector B1 20µm with channel 1 preamplifier.

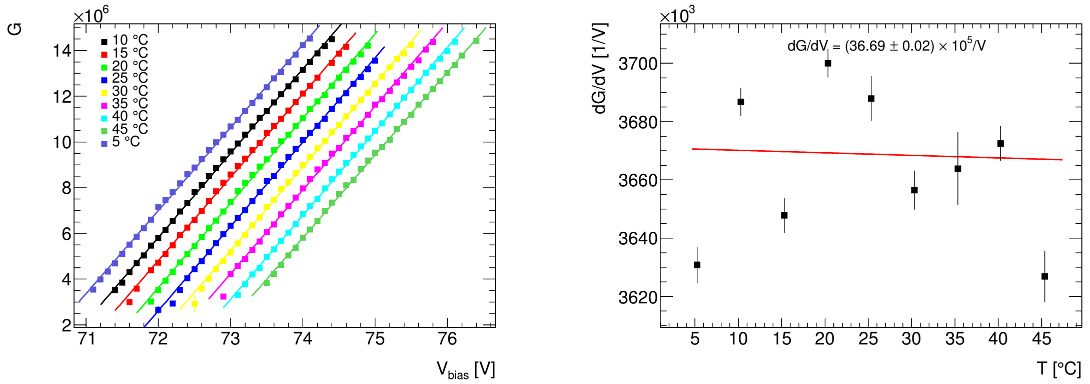

(a) Measurements of gain-versus-bias voltage (dG/dV) for fixed temperatures.

(b) Plot shows the obtained values of the dG/dV versus fixed temperature.

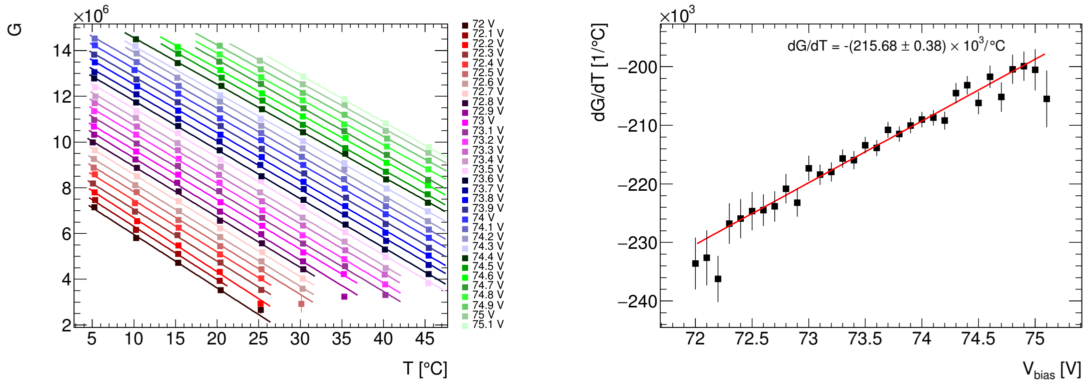

(c) Measurements of gain-versus-temperature (dG/dT) for fixed bias.

(d) Plot shows the obtained values of the dG/dT versus fixed bias voltage.

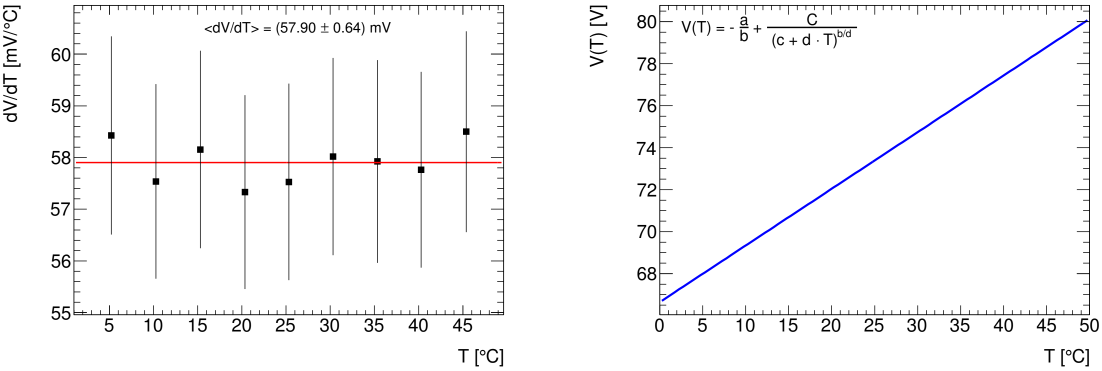

(e) Weighted average distribution of dV/dT as a function of temperature.

(f) Plot illustrates the bias voltage as a function of temperature.

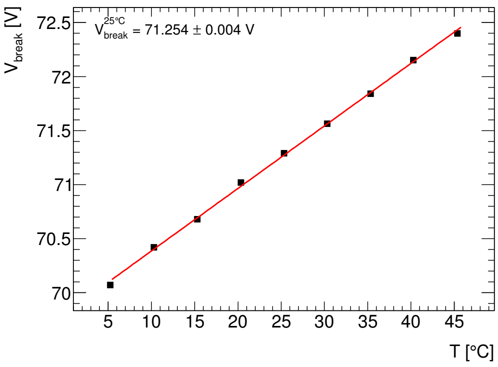

(g) Plot shows the determined breakdown voltage at different temperatures.

Figure A.6: All measurements are taken with the Hamamatsu detector B2 20µm with channel 2 preamplifier.

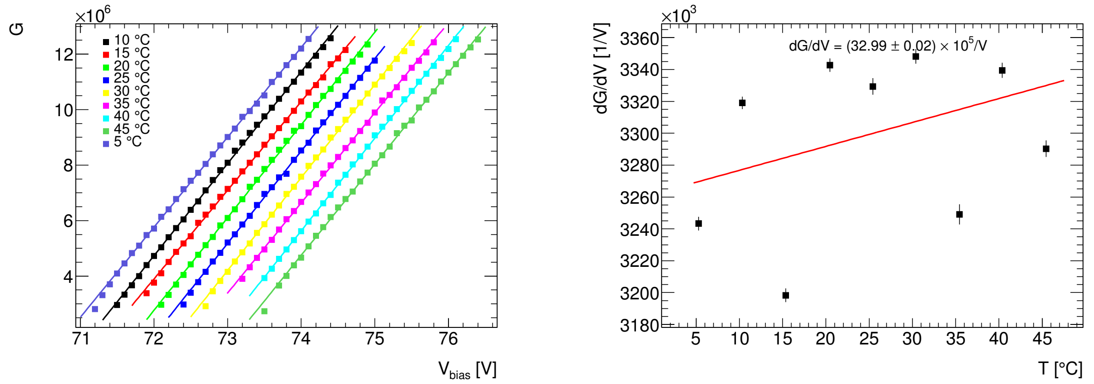

(a) Measurements of gain-versus-bias voltage (dG/dV) for fixed temperatures.

(b) Plot shows the obtained values of the dG/dV versus fixed temperature.

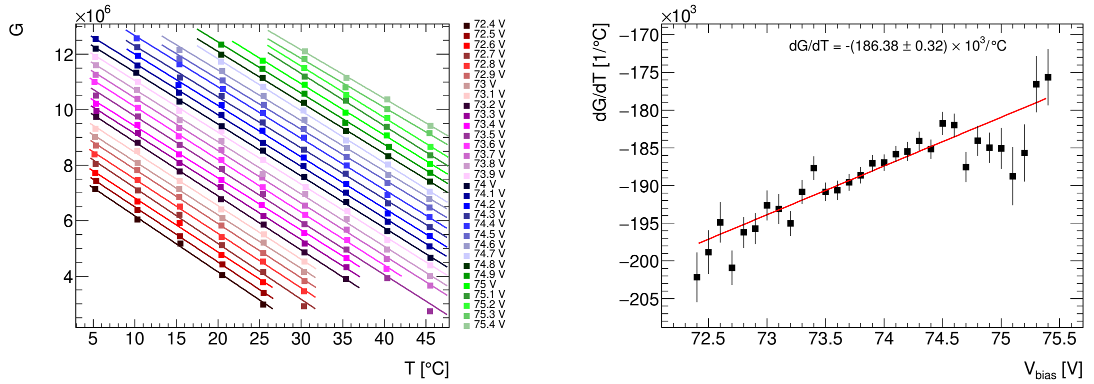

(c) Measurements of gain-versus-temperature (dG/dT) for fixed bias.

(d) Plot shows the obtained values of the dG/dT versus fixed bias voltage.

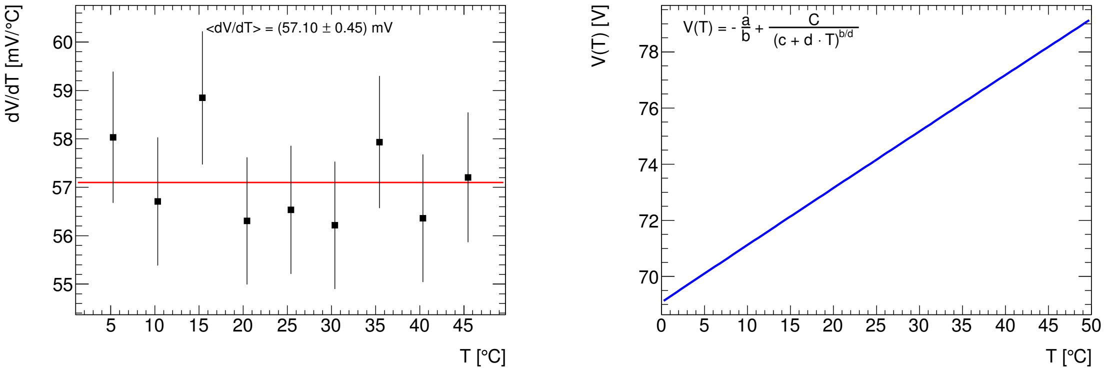

(e) Weighted average distribution of dV/dT as a function of temperature.

(f) Plot illustrates the bias voltage as a function of temperature.

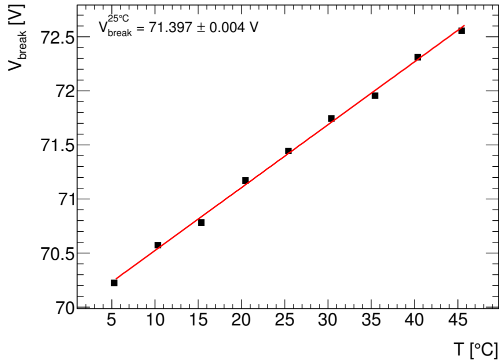

(g) Plot shows the determined breakdown voltage at different temperatures.

Figure A.7: All measurements are taken with the Hamamatsu detector B1 15µm with channel 3 preamplifier.

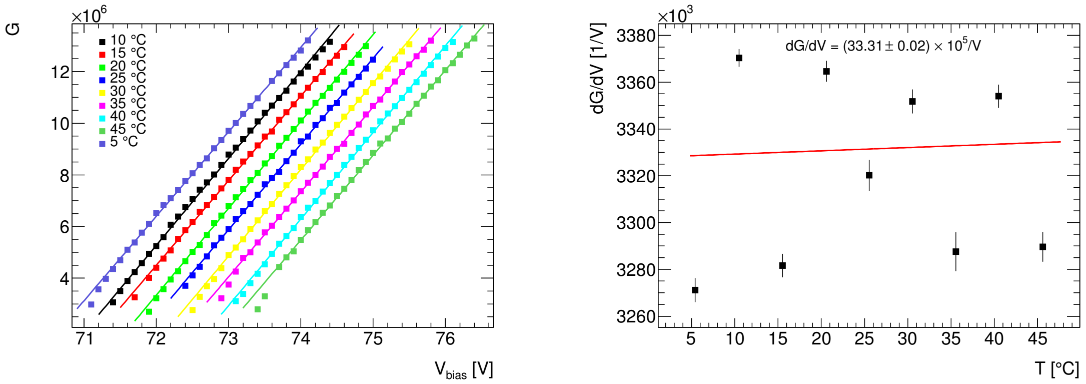

(a) Measurements of gain-versus-bias voltage (dG/dV) for fixed temperatures.

(b) Plot shows the obtained values of the dG/dV versus fixed temperature.

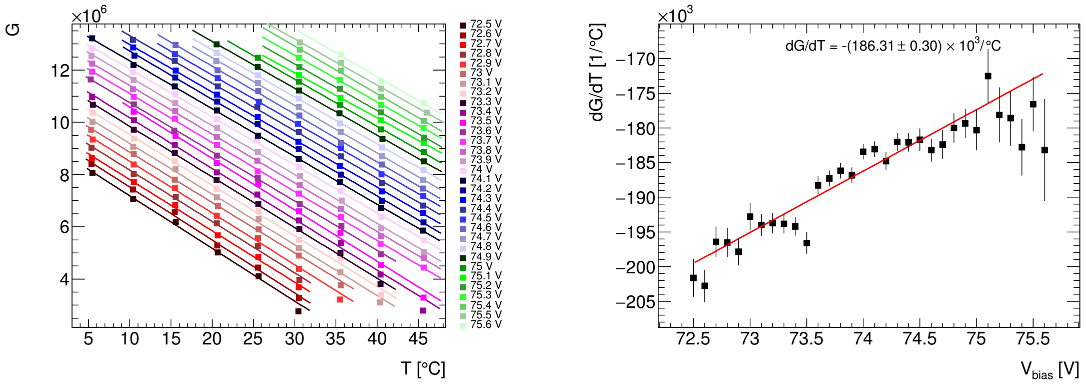

(c) Measurements of gain-versus-temperature (dG/dT) for fixed bias.

(d) Plot shows the obtained values of the dG/dT versus fixed bias voltage.

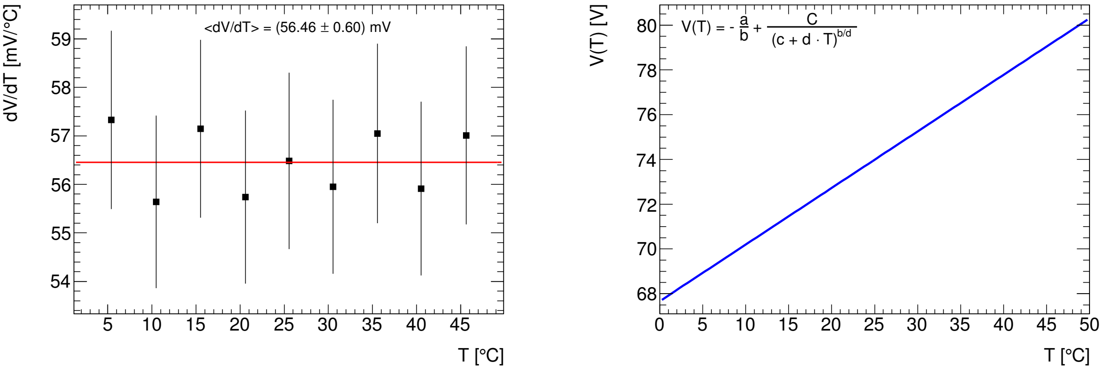

(e) Weighted average distribution of dV/dT as a function of temperature.

(f) Plot illustrates the bias voltage as a function of temperature.

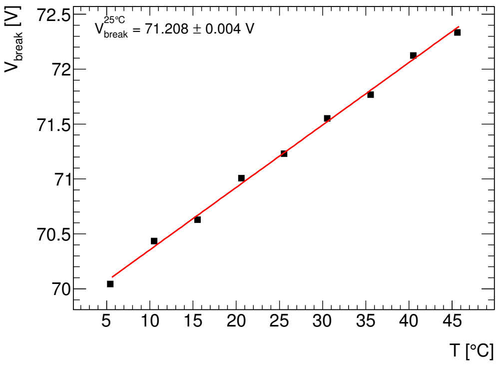

(g) Plot shows the determined breakdown voltage at different temperatures.

Figure A.8: All measurements are taken with the Hamamatsu detector B2 15µm with channel 4 preamplifier.

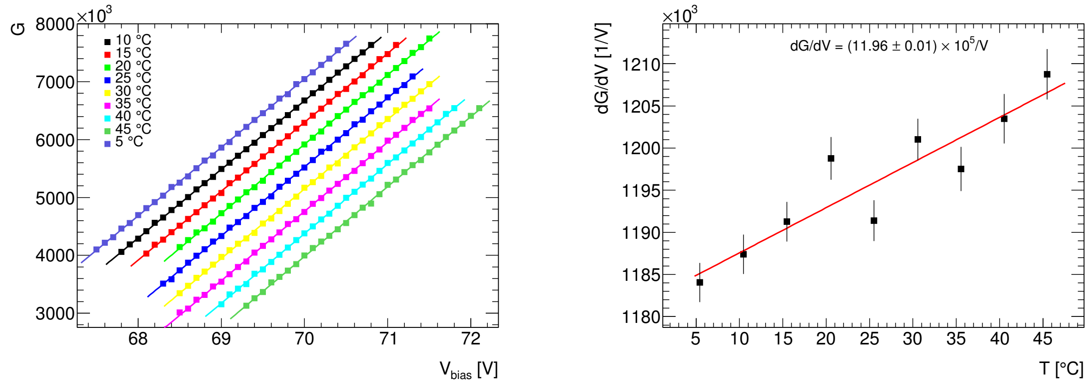

(a) Measurements of gain-versus-bias voltage (dG/dV) for fixed temperatures.

(b) Plot shows the obtained values of the dG/dV versus fixed temperature.

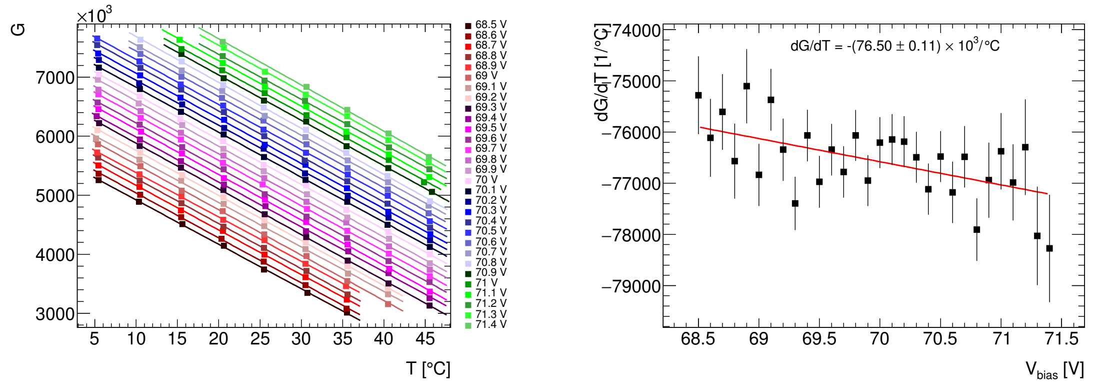

(c) Measurements of gain-versus-temperature (dG/dT) for fixed bias.

(d) Plot shows the obtained values of the dG/dT versus fixed bias voltage.

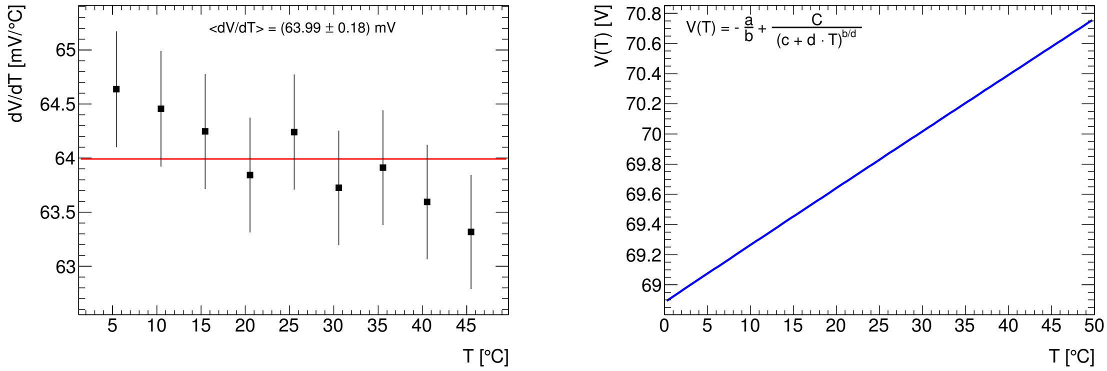

(e) Weighted average distribution of dV/dT as a function of temperature.

(f) Plot illustrates the bias voltage as a function of temperature.

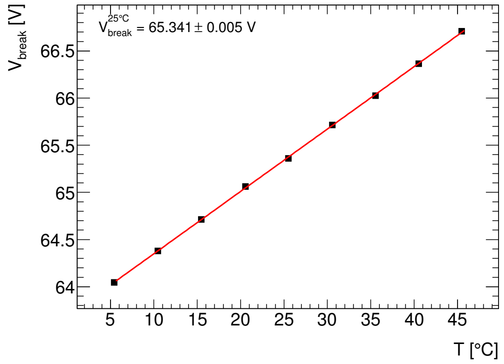

(g) Plot shows the determined breakdown voltage at different temperatures.

Figure A.9: All measurements are taken with the Hamamatsu detector S12571 010C serial number 271 with channel 1 preamplifier.

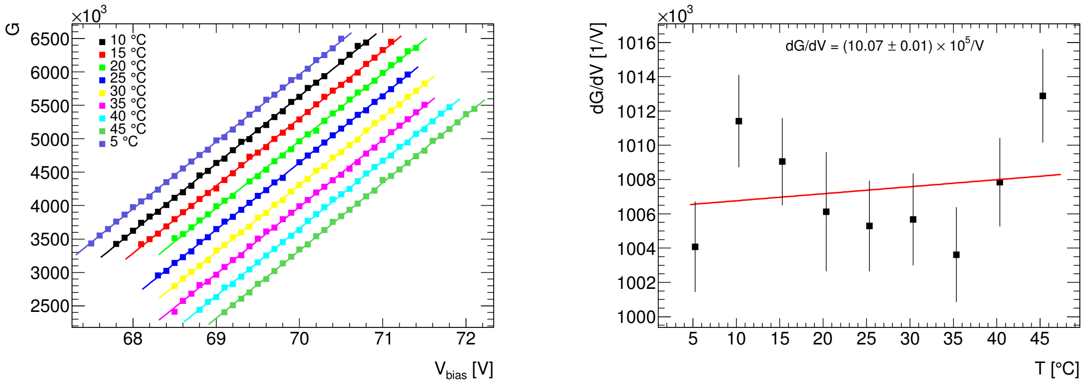

(a) Measurements of gain-versus-bias voltage (dG/dV) for fixed temperatures.

(b) Plot shows the obtained values of the dG/dV versus fixed temperature.

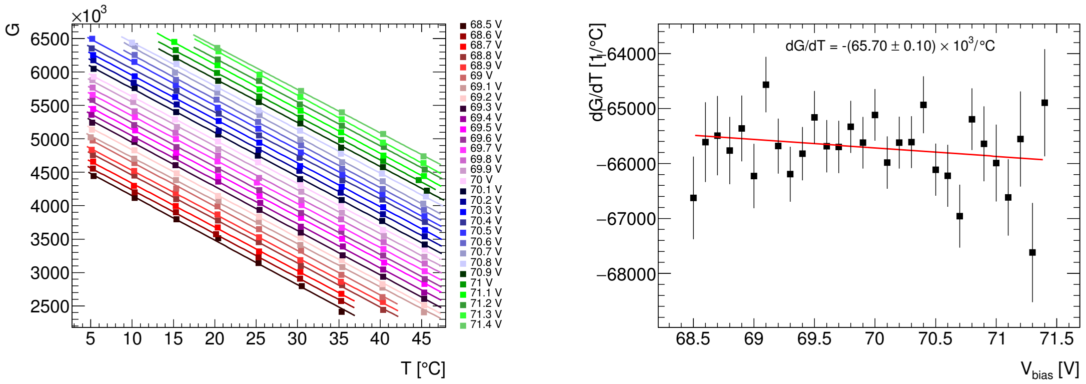

(c) Measurements of gain-versus-temperature (dG/dT) for fixed bias.

(d) Plot shows the obtained values of the dG/dT versus fixed bias voltage.

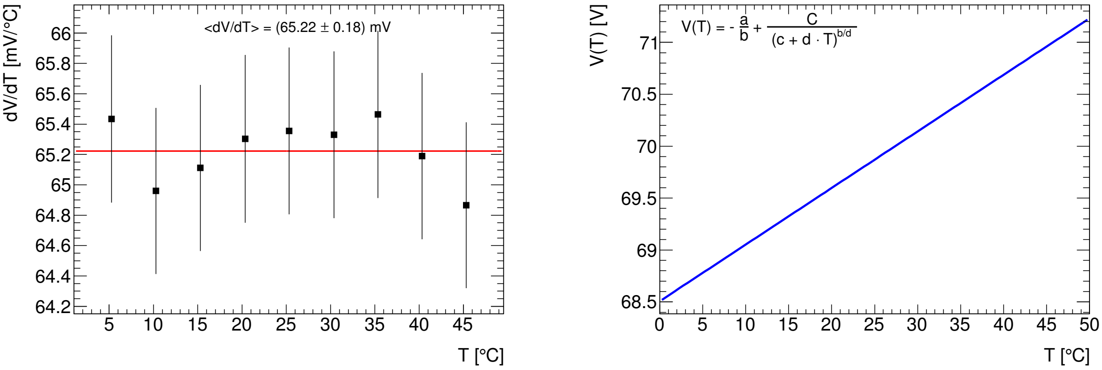

(e) Weighted average distribution of dV/dT as a function of temperature.

(f) Plot illustrates the bias voltage as a function of temperature.

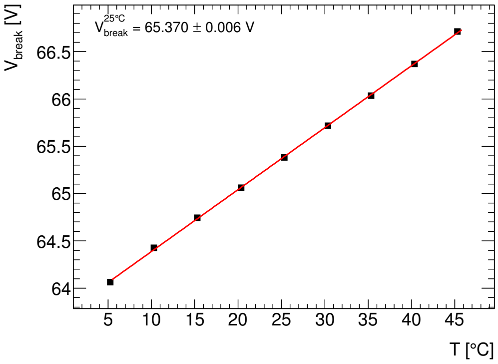

(g) Plot shows the determined breakdown voltage at different temperatures.

Figure A.10: All measurements are taken with the Hamamatsu detector S12571 010C serial number 272 with channel 2 preamplifier.

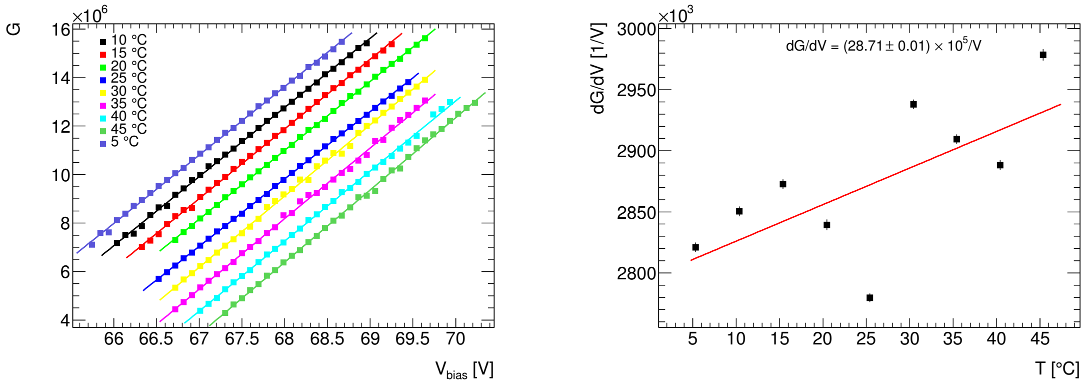

(a) Measurements of gain-versus-bias voltage (dG/dV) for fixed temperatures.

(b) Plot shows the obtained values of the dG/dV versus fixed temperature.

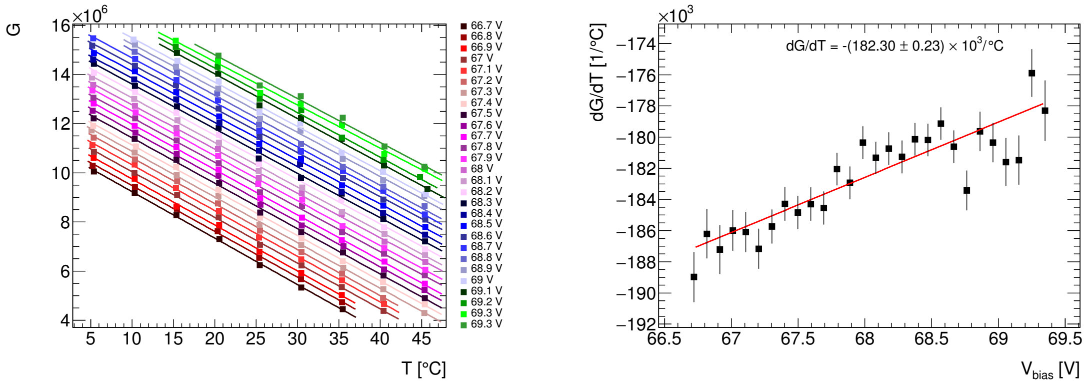

(c) Measurements of gain-versus-temperature (dG/dT) for fixed bias.

(d) Plot shows the obtained values of the dG/dT versus fixed bias voltage.

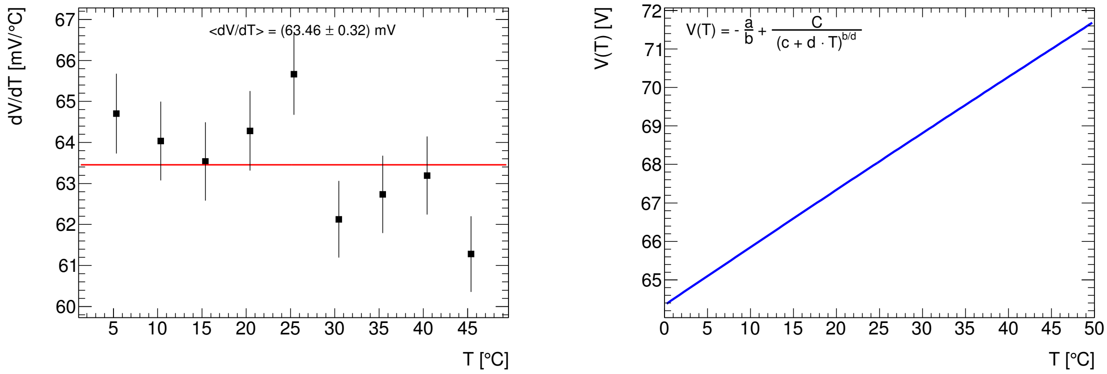

(e) Weighted average distribution of dV/dT as a function of temperature.

(f) Plot illustrates the bias voltage as a function of temperature.

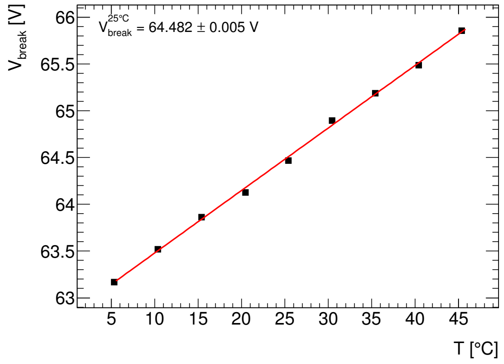

(g) Plot shows the determined breakdown voltage at different temperatures.

Figure A.11: All measurements are taken with the Hamamatsu detector S12571 015C serial number 136 with channel 3 preamplifier.

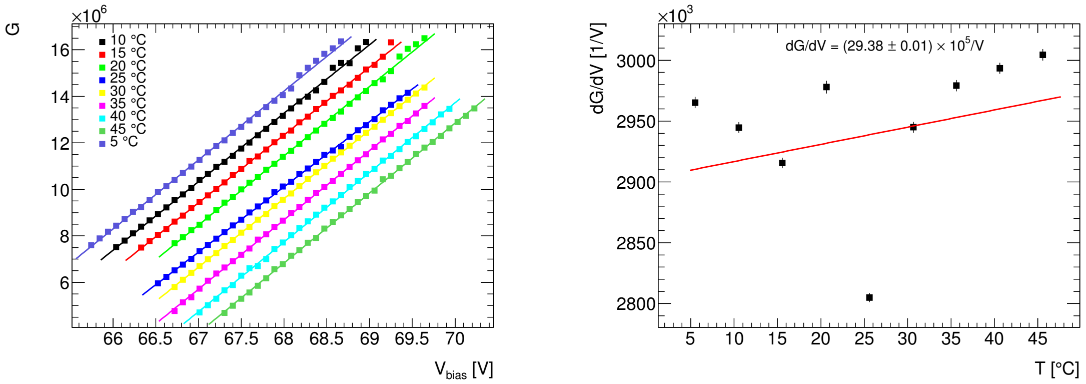

(a) Measurements of gain-versus-bias voltage (dG/dV) for fixed temperatures.

(b) Plot shows the obtained values of the dG/dV versus fixed temperature.

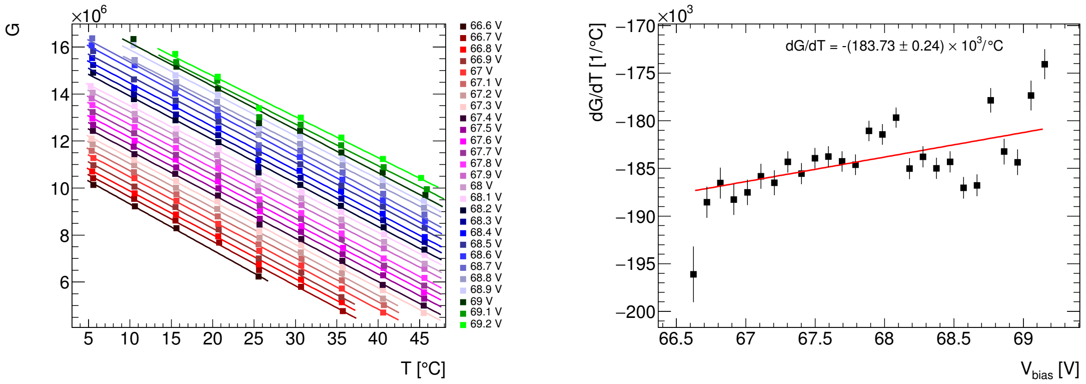

(c) Measurements of gain-versus-temperature (dG/dT) for fixed bias.

(d) Plot shows the obtained values of the dG/dT versus fixed bias voltage.

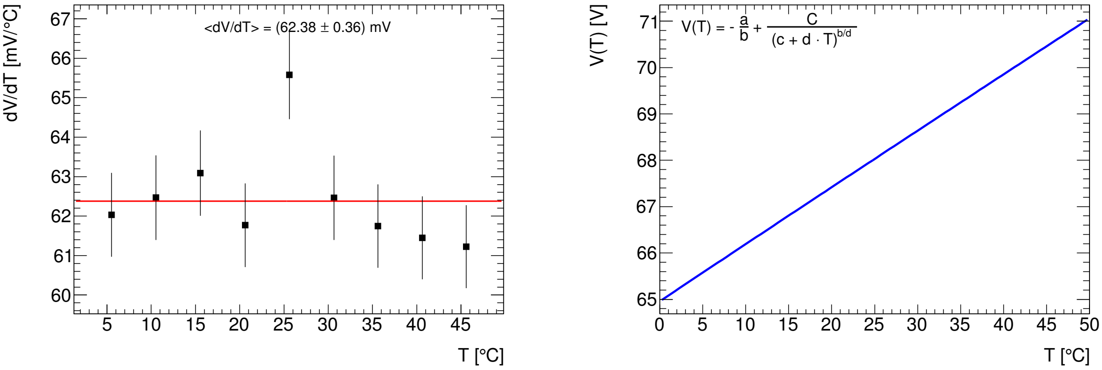

(e) Weighted average distribution of dV/dT as a function of temperature.

(f) Plot illustrates the bias voltage as a function of temperature.

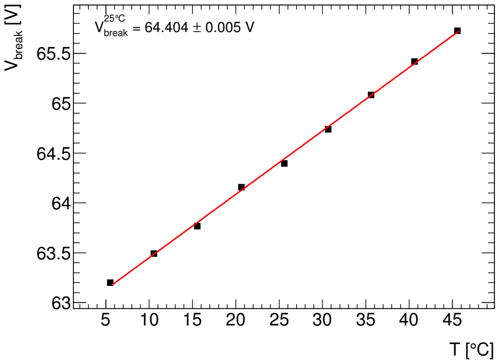

(g) Plot shows the determined breakdown voltage at different temperatures.

Figure A.12: All measurements are taken with the Hamamatsu detector S12571 015C serial number 137 with channel 4 preamplifier.

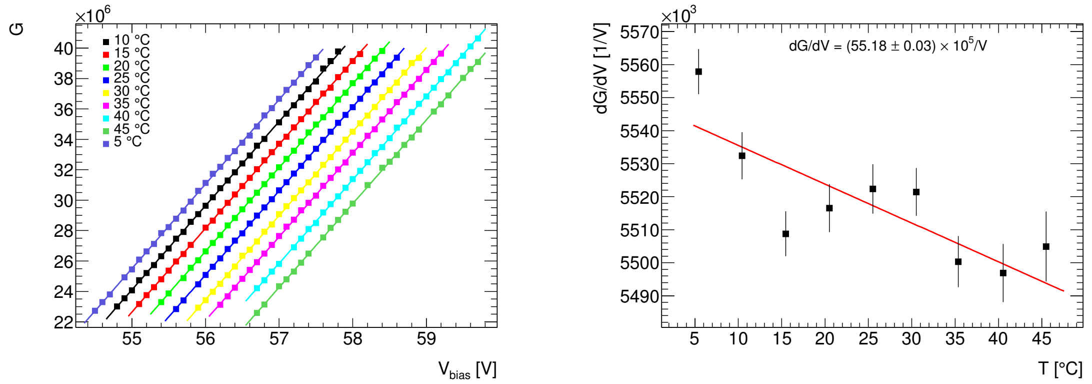

(a) Measurements of gain-versus-bias voltage (dG/dV) for fixed temperatures.

(b) Plot shows the obtained values of the dG/dV versus fixed temperature.

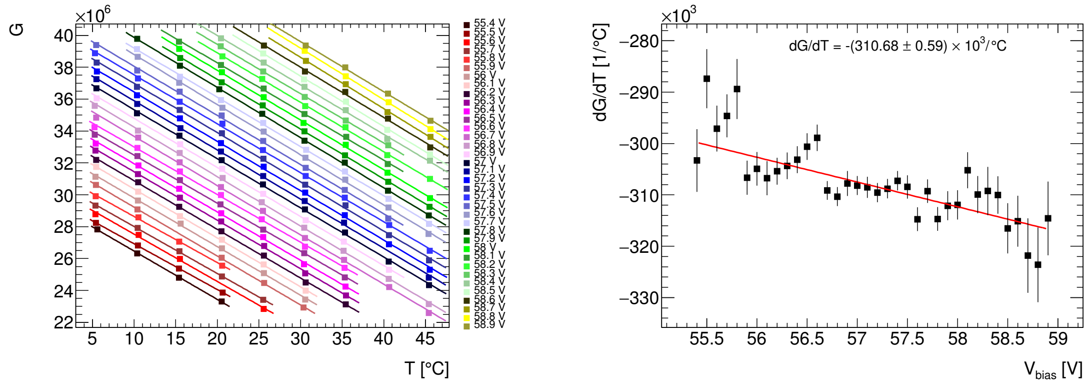

(c) Measurements of gain-versus-temperature (dG/dT) for fixed bias.

(d) Plot shows the obtained values of the dG/dT versus fixed bias voltage.

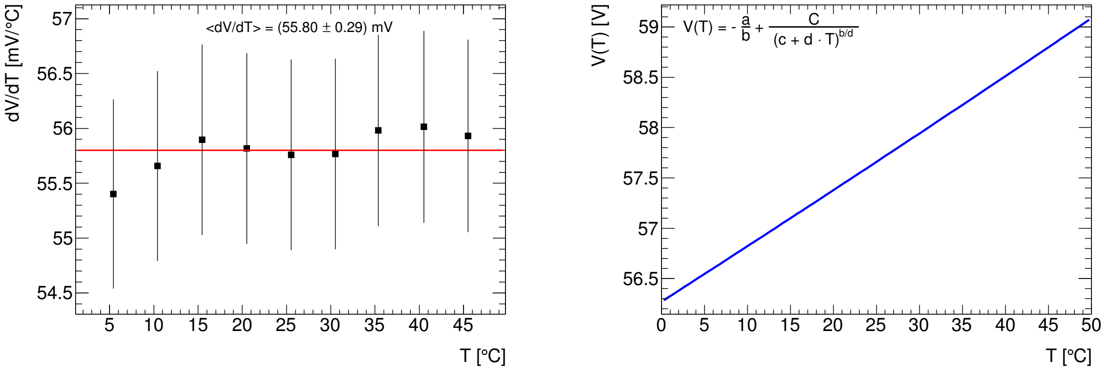

(e) Weighted average distribution of dV/dT as a function of temperature.

(f) Plot illustrates the bias voltage as a function of temperature.

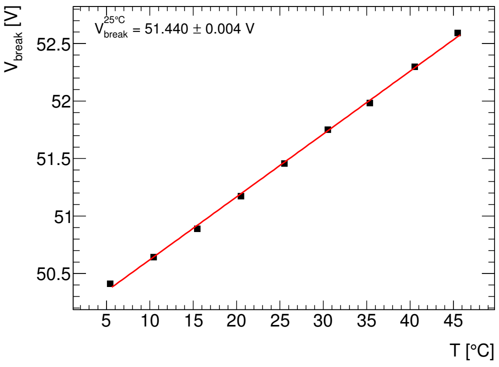

(g) Plot shows the determined breakdown voltage at different temperatures.

Figure A.13: All measurements are taken with the Hamamatsu detector S13360 1325CS 10143 with channel 1 preamplifier.

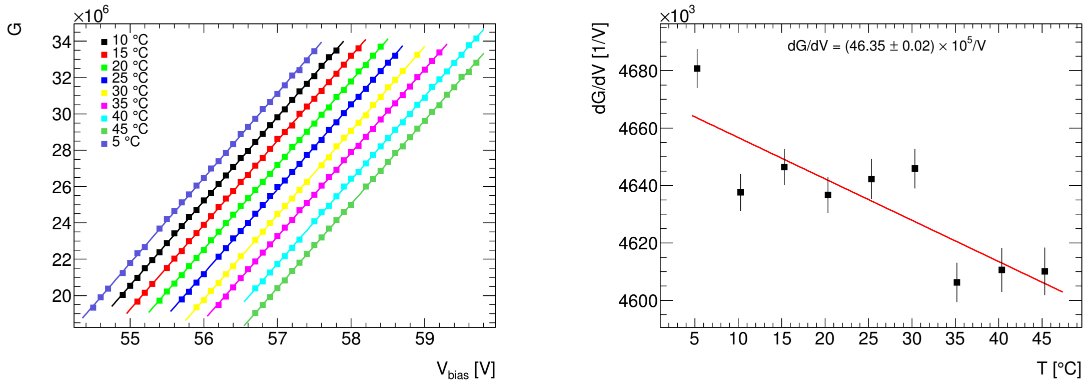

(a) Measurements of gain-versus-bias voltage (dG/dV) for fixed temperatures.

(b) Plot shows the obtained values of the dG/dV versus fixed temperature.

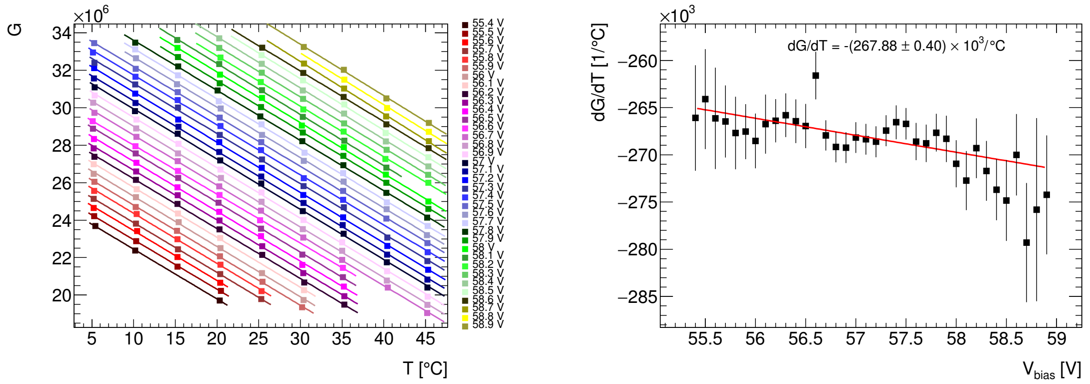

(c) Measurements of gain-versus-temperature (dG/dT) for fixed bias.

(d) Plot shows the obtained values of the dG/dT versus fixed bias voltage.

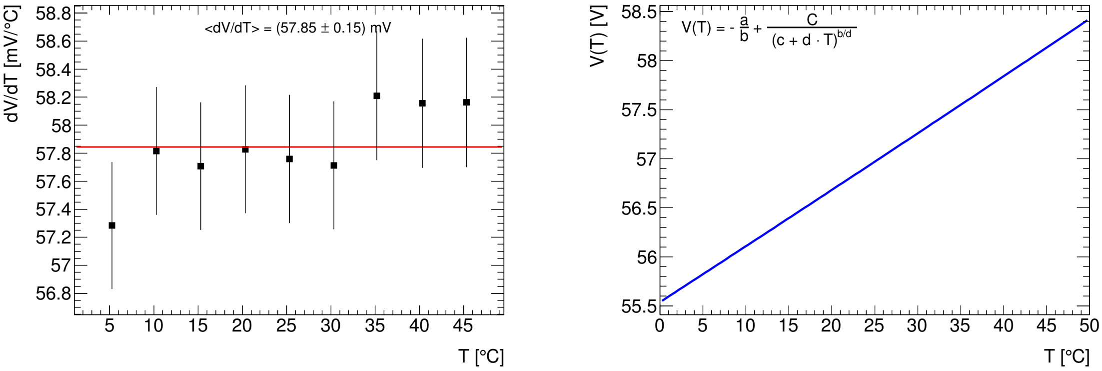

(e) Weighted average distribution of dV/dT as a function of temperature.

(f) Plot illustrates the bias voltage as a function of temperature.

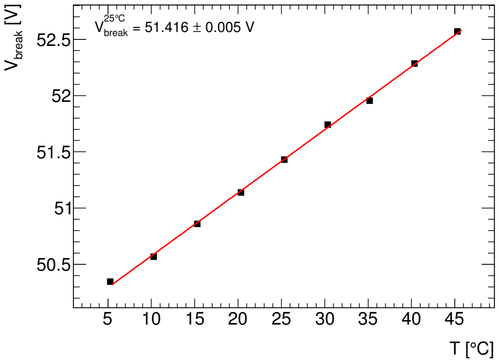

(g) Plot shows the determined breakdown voltage at different temperatures.

Figure A.14: All measurements are taken with the Hamamatsu detector S13360 1325CS 10144 with channel 2 preamplifier.

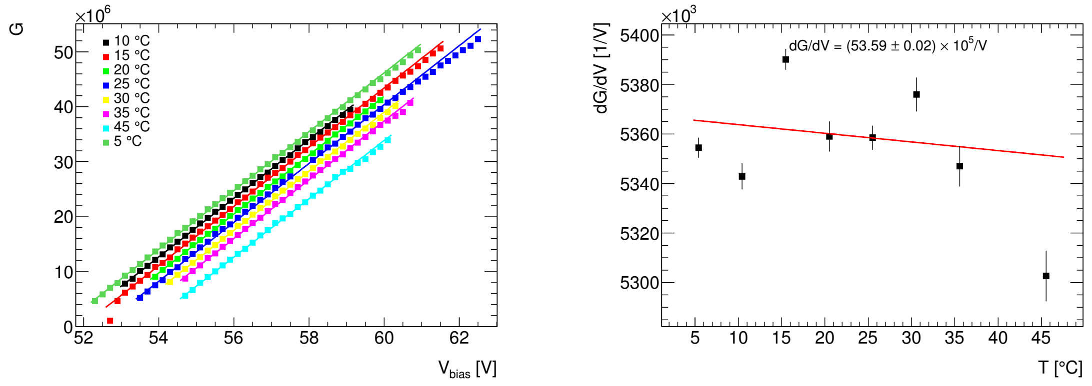

(a) Measurements of gain-versus-bias voltage (dG/dV) for fixed temperatures.

(b) Plot shows the obtained values of the dG/dV versus fixed temperature.

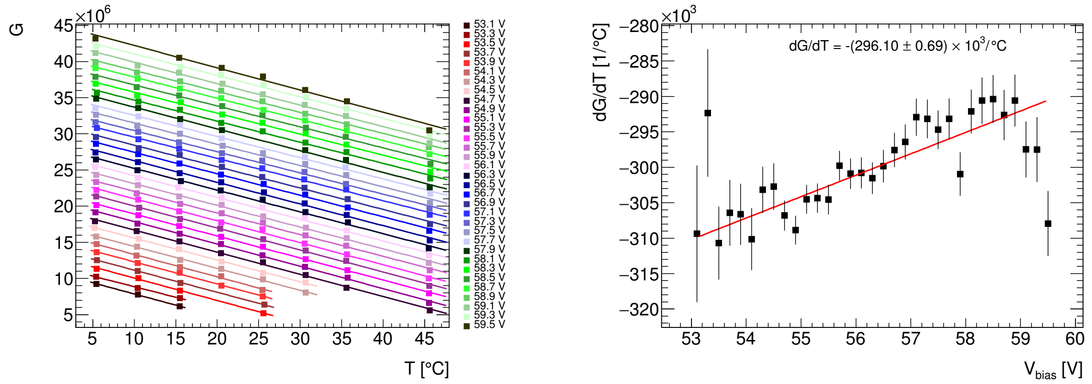

(c) Measurements of gain-versus-temperature (dG/dT) for fixed bias.

(d) Plot shows the obtained values of the dG/dT versus fixed bias voltage.

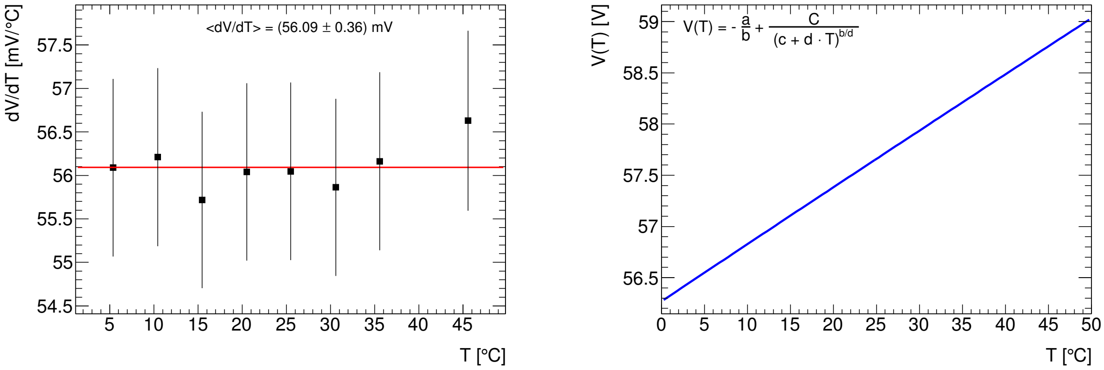

(e) Weighted average distribution of dV/dT as a function of temperature.

(f) Plot illustrates the bias voltage as a function of temperature.

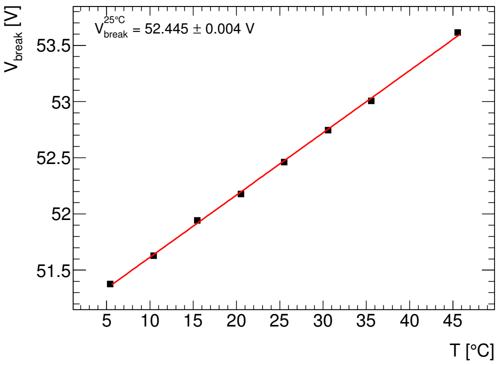

(g) Plot shows the determined breakdown voltage at different temperatures.

Figure A.15: All measurements are taken with the Hamamatsu detector S13360 3025CS 10103 with channel 1 preamplifier.

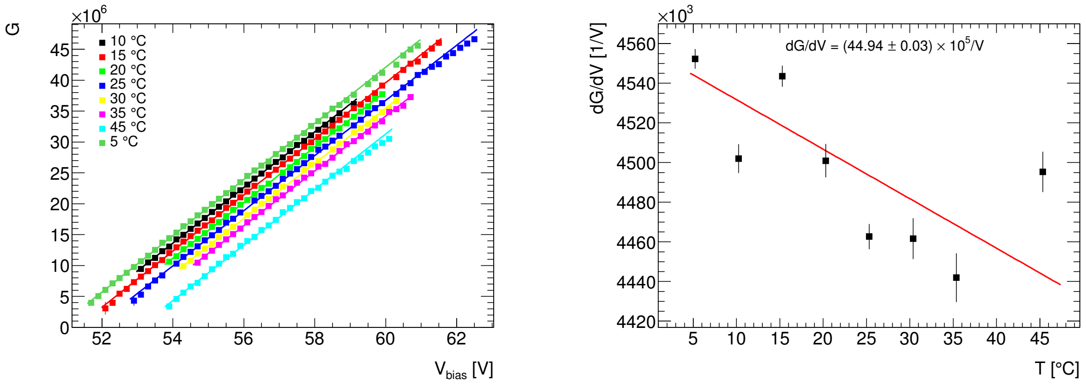

(a) Measurements of gain-versus-bias voltage (dG/dV) for fixed temperatures.

(b) Plot shows the obtained values of the dG/dV versus fixed temperature.

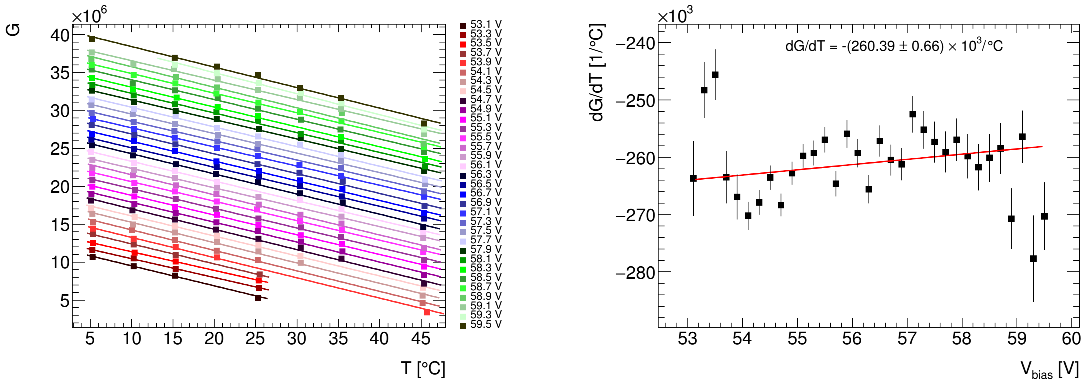

(c) Measurements of gain-versus-temperature (dG/dT) for fixed bias.

(d) Plot shows the obtained values of the dG/dT versus fixed bias voltage.

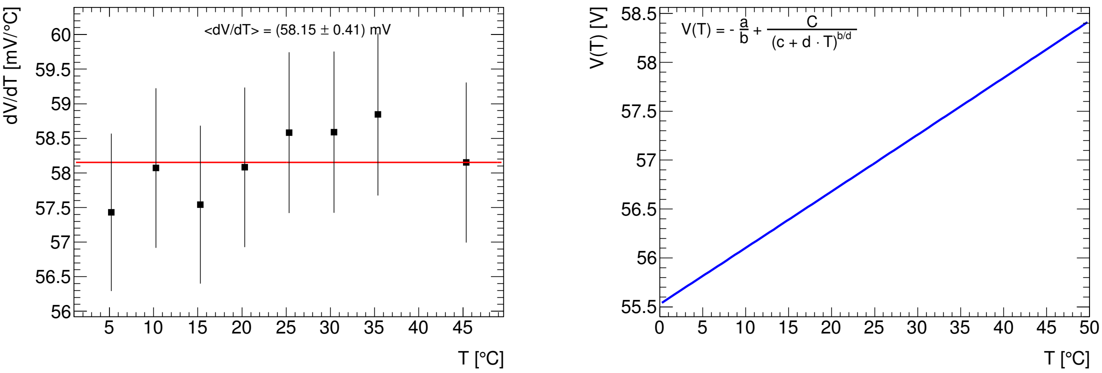

(e) Weighted average distribution of dV/dT as a function of temperature.

(f) Plot illustrates the bias voltage as a function of temperature.

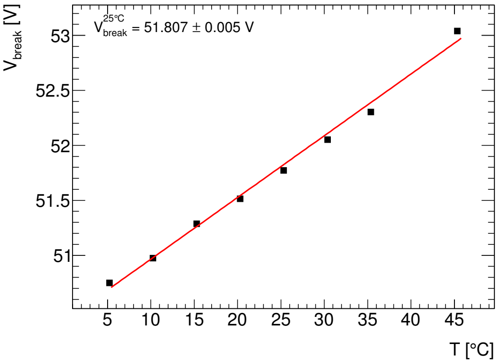

(g) Plot shows the determined breakdown voltage at different temperatures.

Figure A.16: All measurements are taken with the Hamamatsu detector S13360 3025CS 10104 with channel 2 preamplifier.

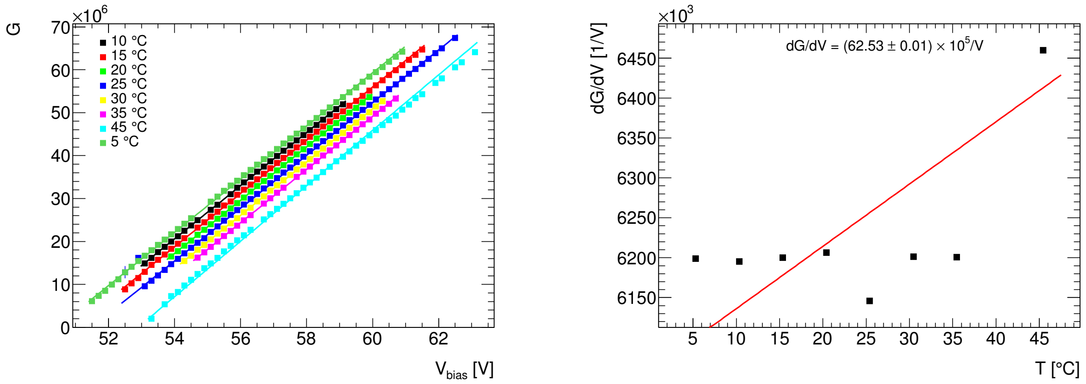

(a) Measurements of gain-versus-bias voltage (dG/dV) for fixed temperatures.

(b) Plot shows the obtained values of the dG/dV versus fixed temperature.

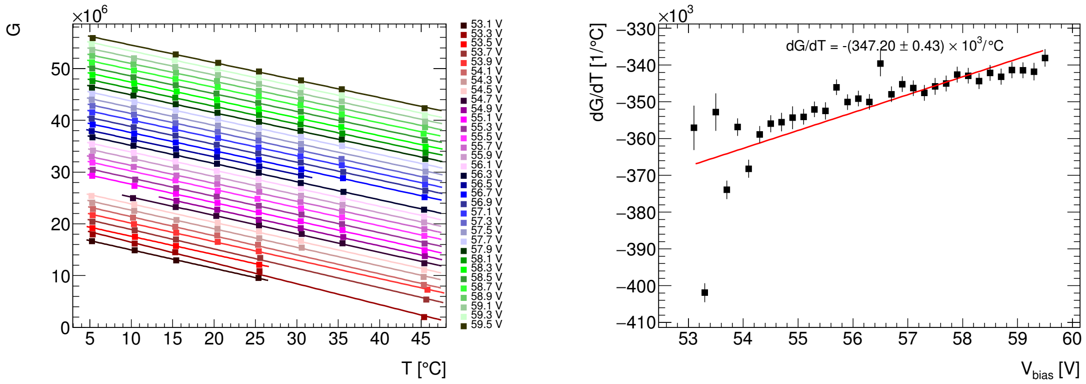

(c) Measurements of gain-versus-temperature (dG/dT) for fixed bias.

(d) Plot shows the obtained values of the dG/dT versus fixed bias voltage.

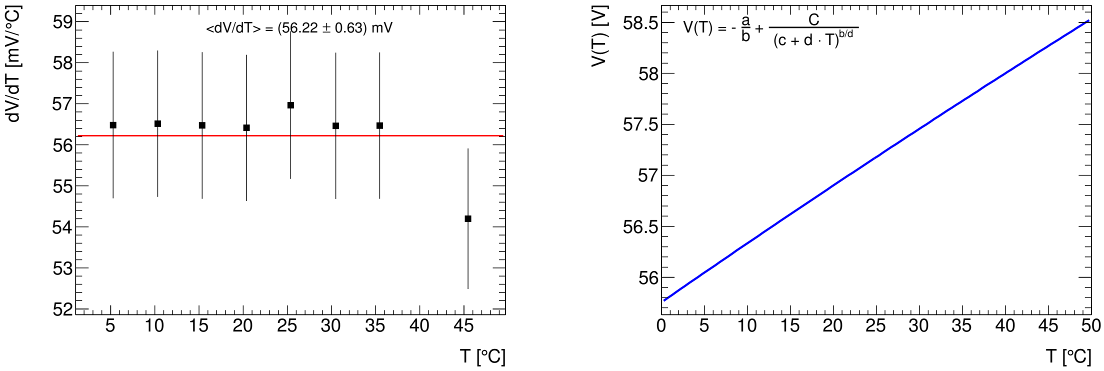

(e) Weighted average distribution of dV/dT as a function of temperature.

(f) Plot illustrates the bias voltage as a function of temperature.

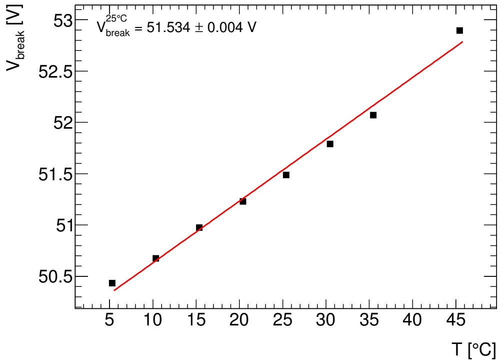

(g) Plot shows the determined breakdown voltage at different temperatures.

Figure A.17: All measurements are taken with the Hamamatsu detector S13360 1325CS 10143 with channel 3 preamplifier.

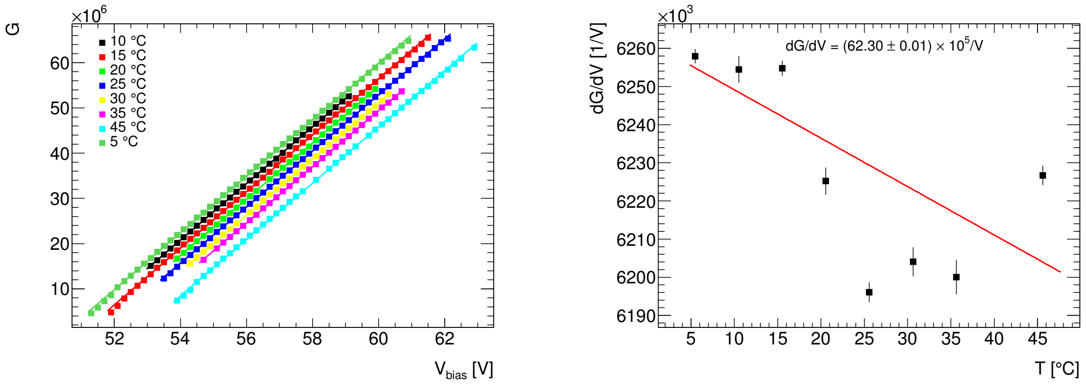

(a) Measurements of gain-versus-bias voltage (dG/dV) for fixed temperatures.

(b) Plot shows the obtained values of the dG/dV versus fixed temperature.

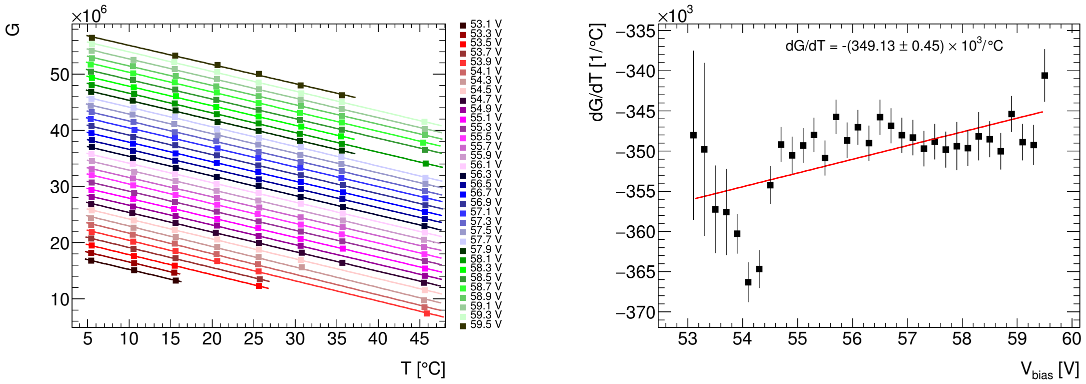

(c) Measurements of gain-versus-temperature (dG/dT) for fixed bias.

(d) Plot shows the obtained values of the dG/dT versus fixed bias voltage.

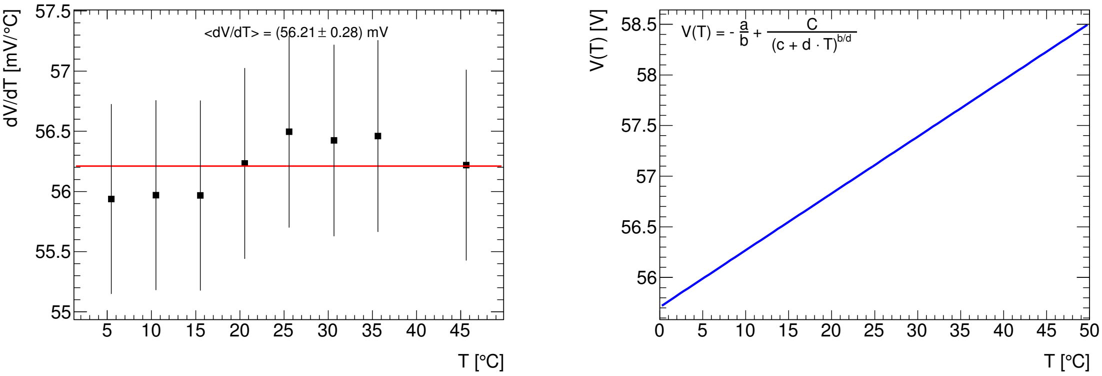

(e) Weighted average distribution of dV/dT as a function of temperature.

(f) Plot illustrates the bias voltage as a function of temperature.

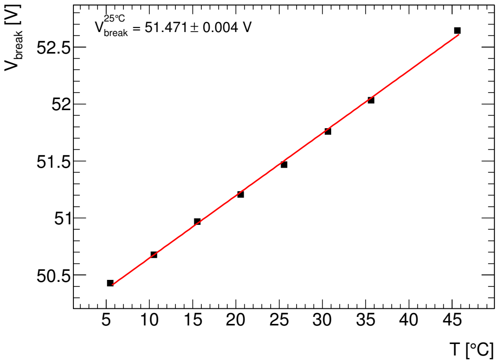

(g) Plot shows the determined breakdown voltage at different temperatures.

Figure A.18: All measurements are taken with the Hamamatsu detector S13360 1325CS 10144 with channel 4 preamplifier.

Appendix B

Bias scan measurements for KETEK

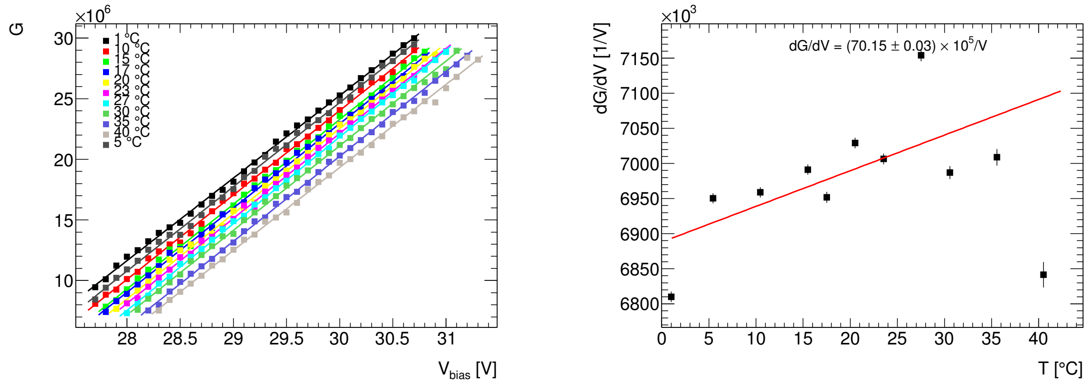

(a) Measurements of gain-versus-bias voltage (dG/dV) for fixed temperatures.

(b) Plot shows the obtained values of the dG/dV versus fixed temperature.

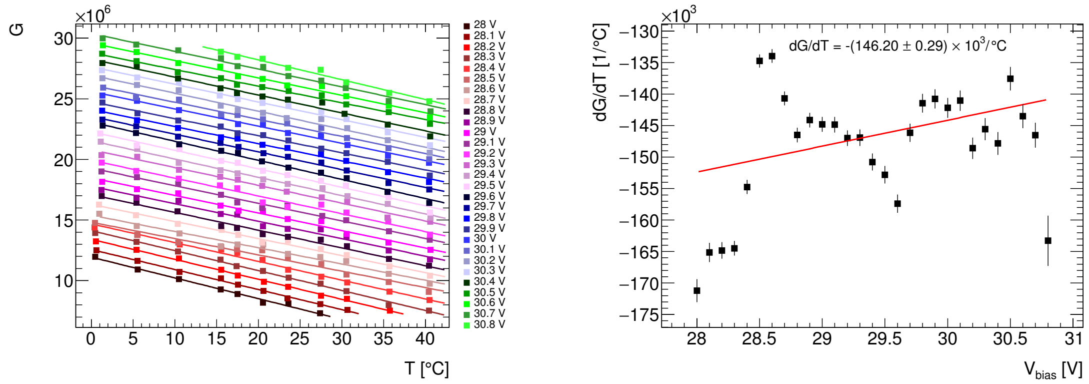

(c) Measurements of gain-versus-temperature (dG/dT) for fixed bias.

(d) Plot shows the obtained values of the dG/dT versus fixed bias voltage.

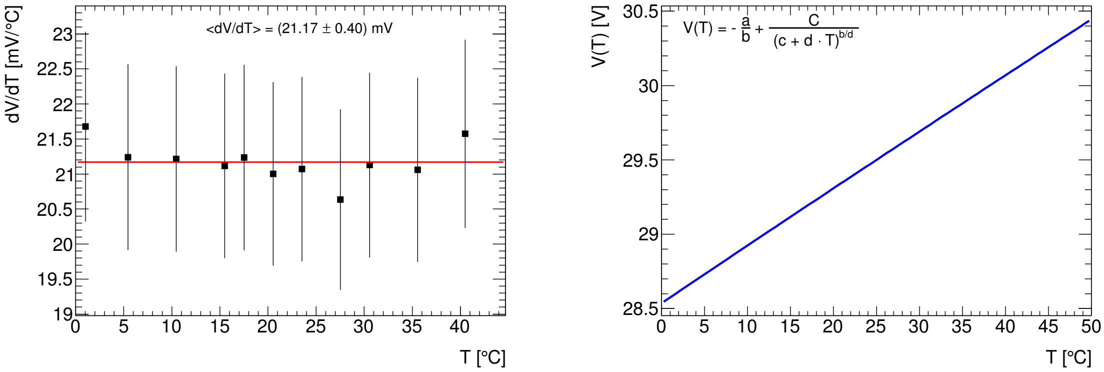

(e) Weighted average distribution of dV/dT as a function of temperature.

(f) Plot illustrates the bias voltage as a function of temperature.

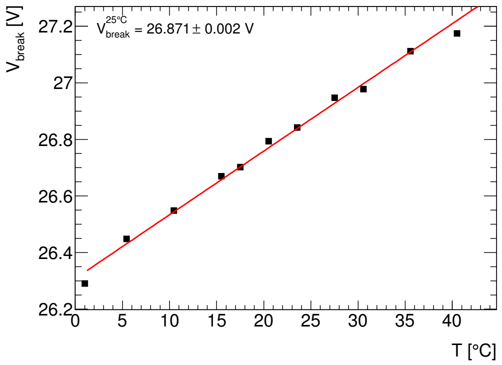

(g) Plot shows the determined breakdown voltage at different temperatures.

Figure B.1: All measurements are taken with the KETEK detector W12 A with channel 1 preamplifier.

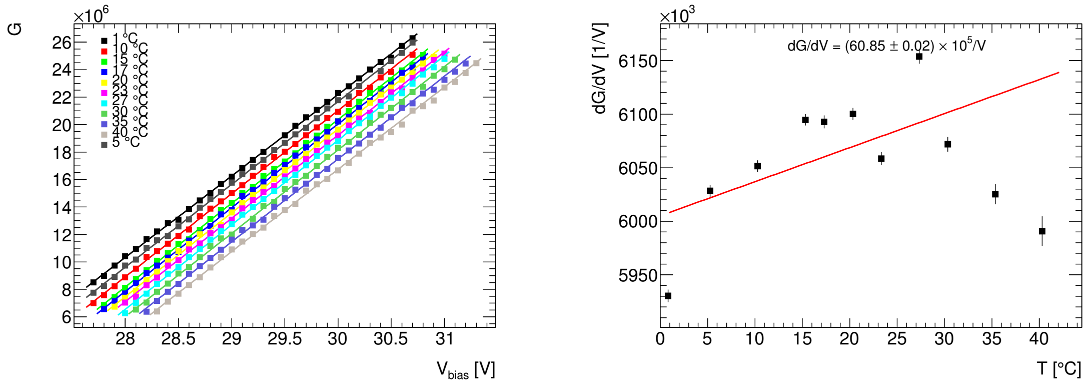

(a) Measurements of gain-versus-bias voltage (dG/dV) for fixed temperatures.

(b) Plot shows the obtained values of the dG/dV versus fixed temperature.

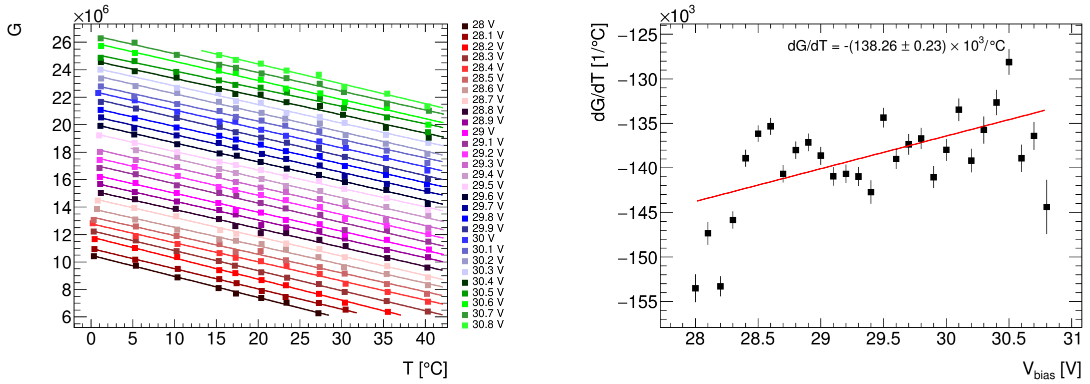

(c) Measurements of gain-versus-temperature (dG/dT) for fixed bias.

(d) Plot shows the obtained values of the dG/dT versus fixed bias voltage.

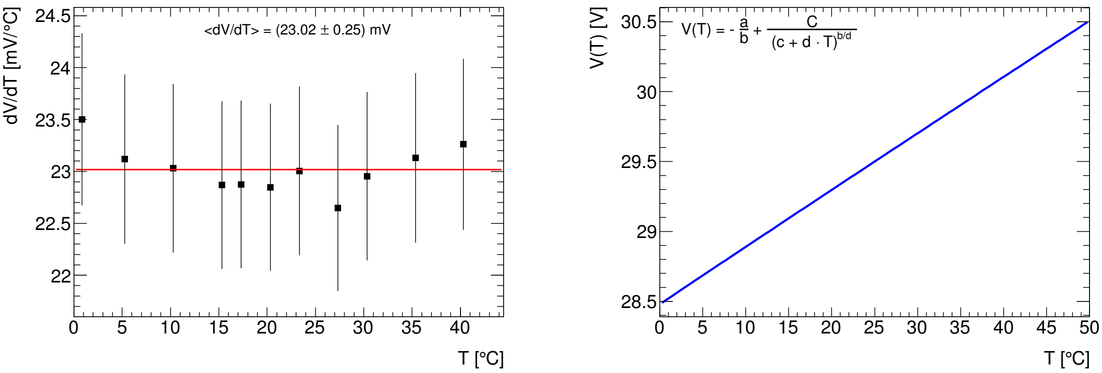

(e) Weighted average distribution of dV/dT as a function of temperature.

(f) Plot illustrates the bias voltage as a function of temperature.

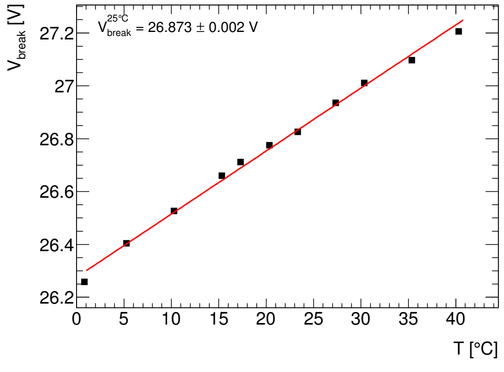

(g) Plot shows the determined breakdown voltage at different temperatures.

Figure B.2: All measurements are taken with the KETEK detector W12 B with channel 2 preamplifier.

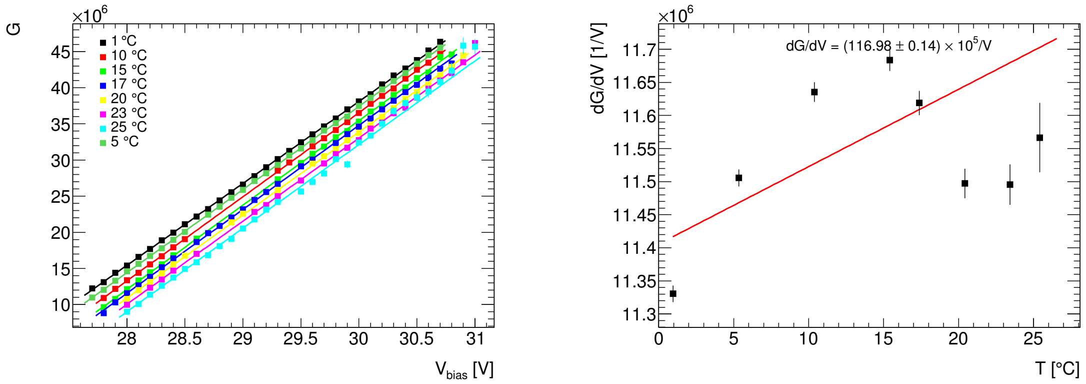

(a) Measurements of gain-versus-bias voltage (dG/dV) for fixed temperatures.

(b) Plot shows the obtained values of the dG/dV versus fixed temperature.

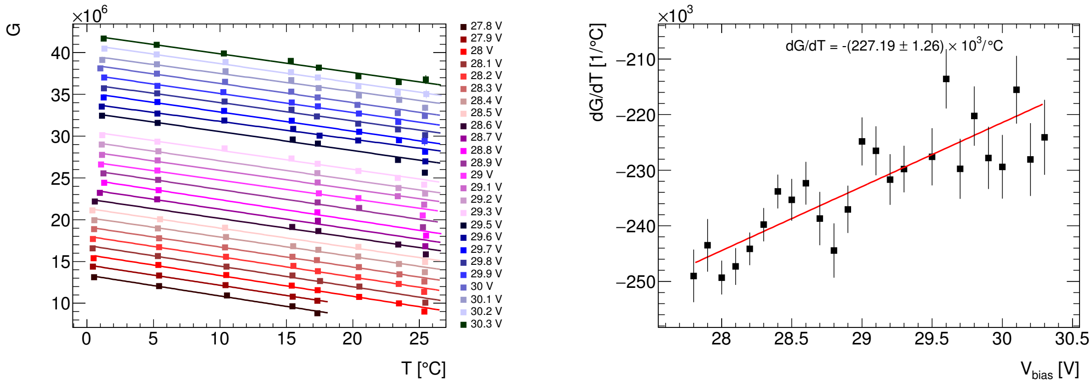

(c) Measurements of gain-versus-temperature (dG/dT) for fixed bias.

(d) Plot shows the obtained values of the dG/dT versus fixed bias voltage.

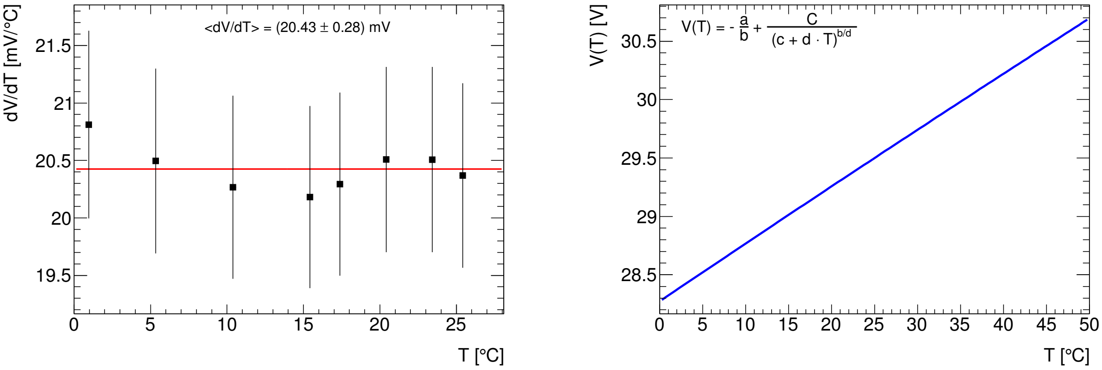

(e) Weighted average distribution of dV/dT as a function of temperature.

(f) Plot illustrates the bias voltage as a function of temperature.

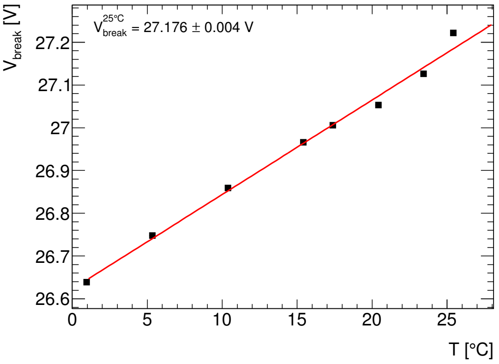

(g) Plot shows the determined breakdown voltage at different temperatures.

Figure B.3: All measurements are taken with the KETEK detector PM3350 serial number 1 with channel 3 preamplifier.

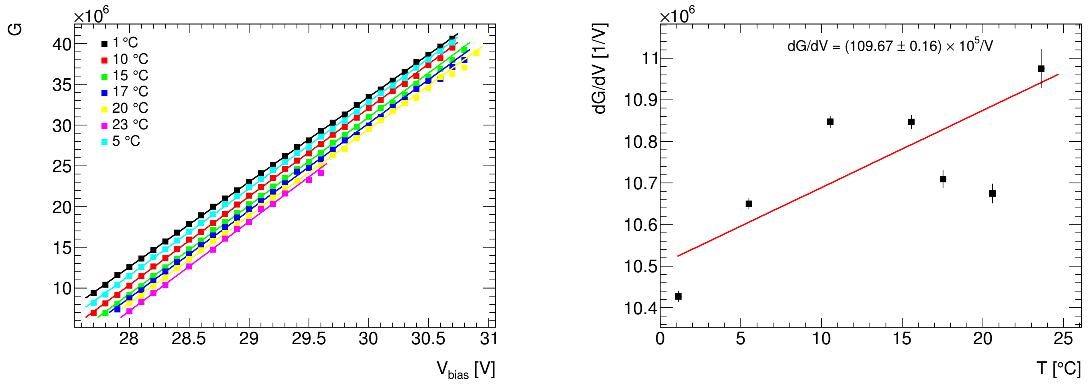

(a) Measurements of gain-versus-bias voltage (dG/dV) for fixed temperatures.

(b) Plot shows the obtained values of the dG/dV versus fixed temperature.

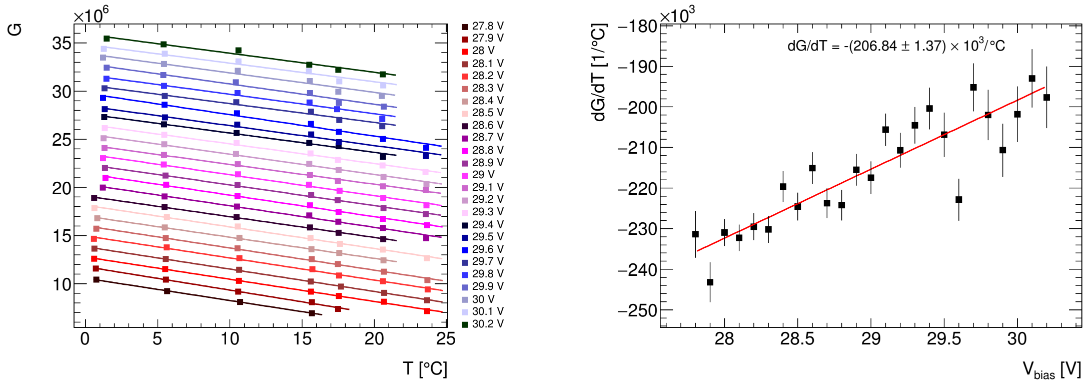

(c) Measurements of gain-versus-temperature (dG/dT) for fixed bias.

(d) Plot shows the obtained values of the dG/dT versus fixed bias voltage.

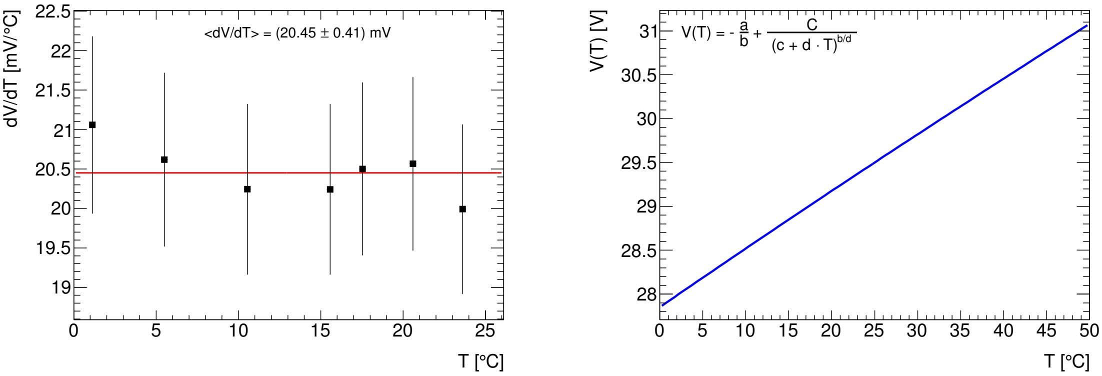

(e) Weighted average distribution of dV/dT as a function of temperature.

(f) Plot illustrates the bias voltage as a function of temperature.

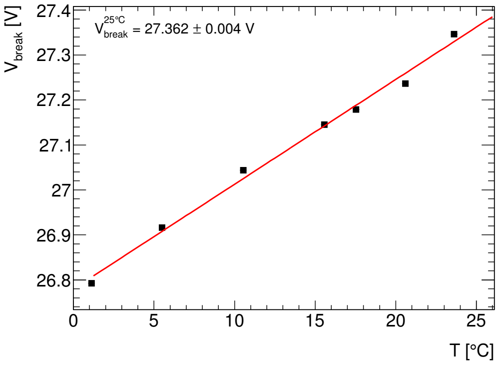

(g) Plot shows the determined breakdown voltage at different temperatures.

Figure B.4: All measurements are taken with the KETEK detector PM3350 serial number 2 with channel 4 preamplifier.

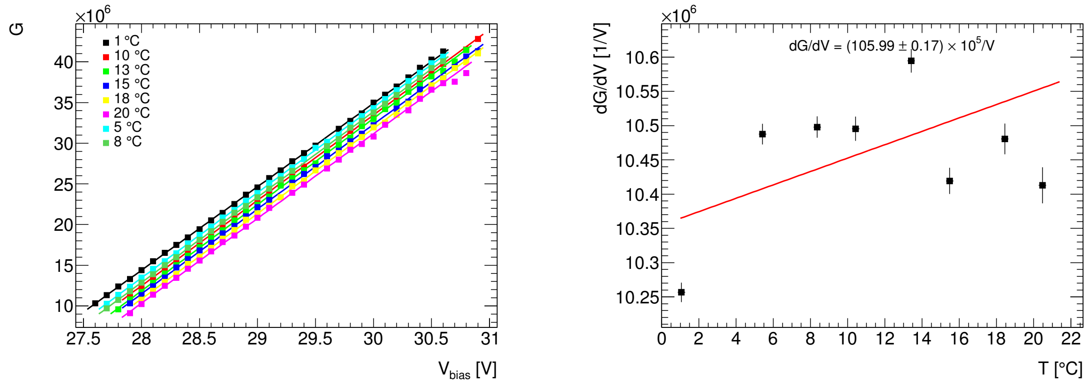

(a) Measurements of gain-versus-bias voltage (dG/dV) for fixed temperatures.

(b) Plot shows the obtained values of the dG/dV versus fixed temperature.

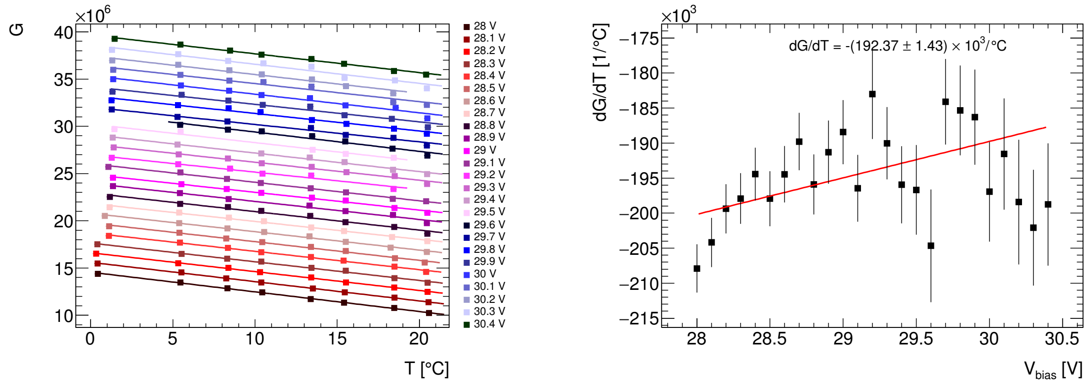

(c) Measurements of gain-versus-temperature (dG/dT) for fixed bias.

(d) Plot shows the obtained values of the dG/dT versus fixed bias voltage.

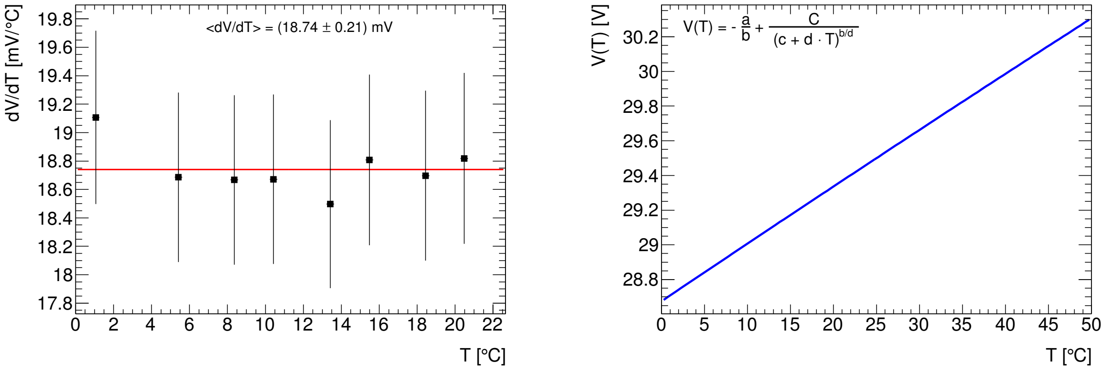

(e) Weighted average distribution of dV/dT as a function of temperature.

(f) Plot illustrates the bias voltage as a function of temperature.

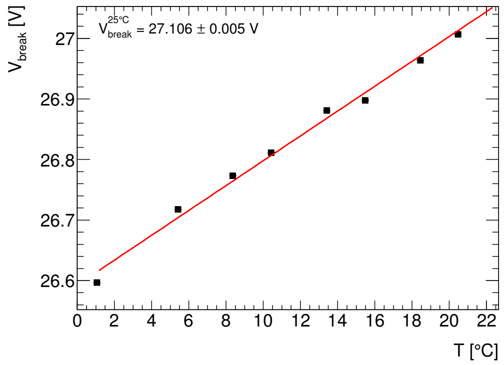

(g) Plot shows the determined breakdown voltage at different temperatures.

Figure B.5: All measurements are taken with the KETEK detector PM3350 serial number 5 with channel 1 preamplifier.

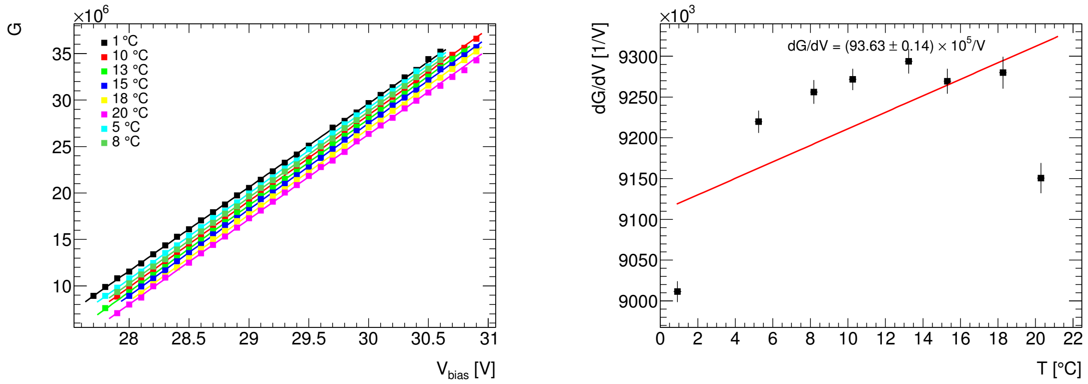

(a) Measurements of gain-versus-bias voltage (dG/dV) for fixed temperatures.

(b) Plot shows the obtained values of the dG/dV versus fixed temperature.

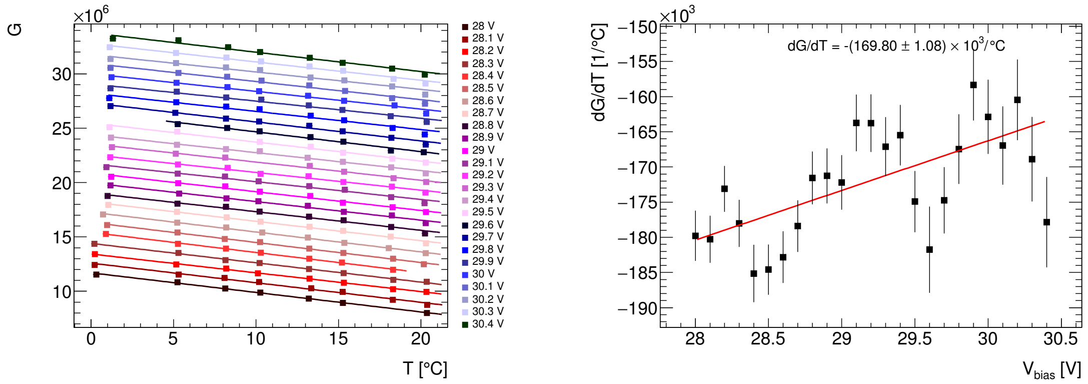

(c) Measurements of gain-versus-temperature (dG/dT) for fixed bias.

(d) Plot shows the obtained values of the dG/dT versus fixed bias voltage.

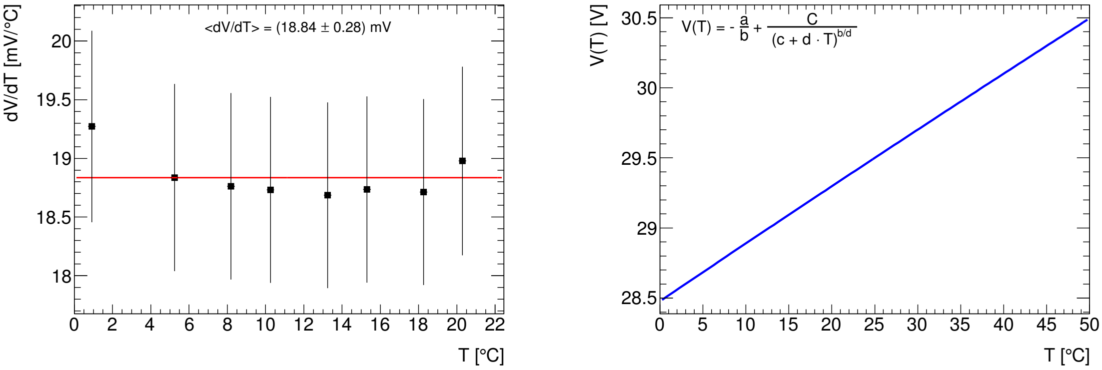

(e) Weighted average distribution of dV/dT as a function of temperature.

(f) Plot illustrates the bias voltage as a function of temperature.

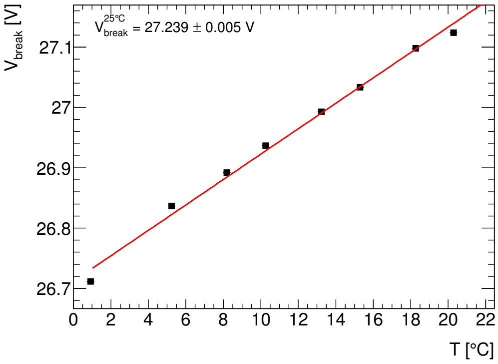

(g) Plot shows the determined breakdown voltage at different temperatures.

Figure B.6: All measurements are taken with the KETEK detector PM3350 serial number 6 with channel 2 preamplifier.

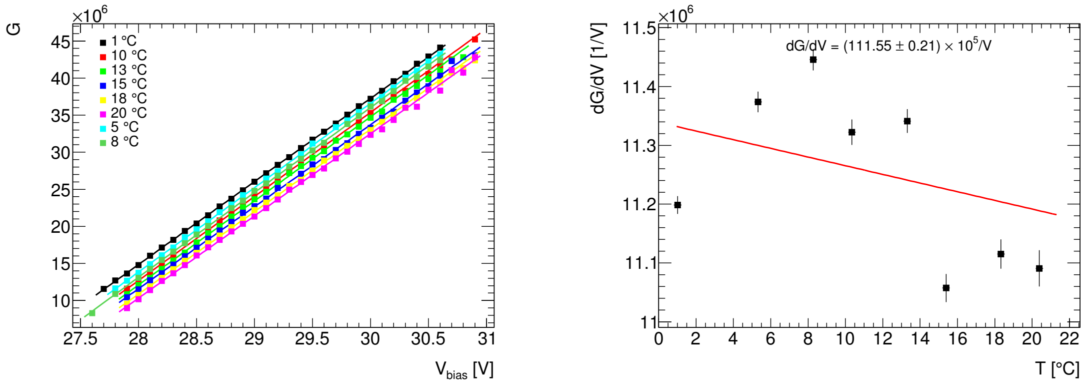

(a) Measurements of gain-versus-bias voltage (dG/dV) for fixed temperatures.

(b) Plot shows the obtained values of the dG/dV versus fixed temperature.

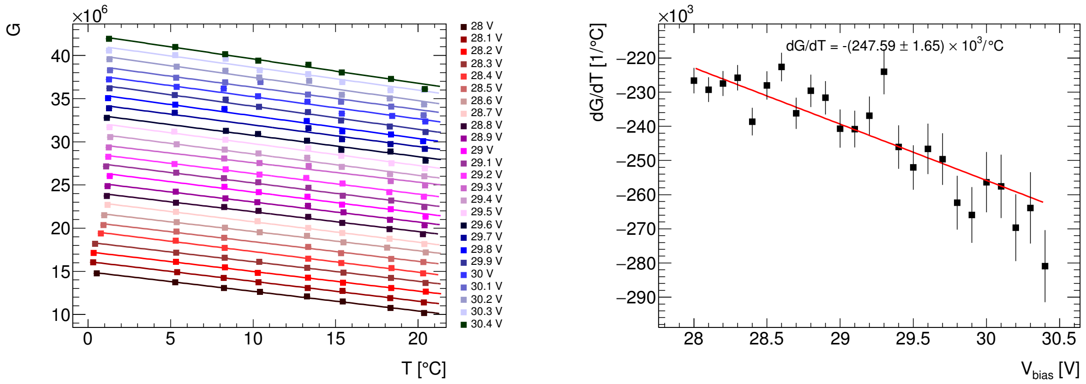

(c) Measurements of gain-versus-temperature (dG/dT) for fixed bias.

(d) Plot shows the obtained values of the dG/dT versus fixed bias voltage.

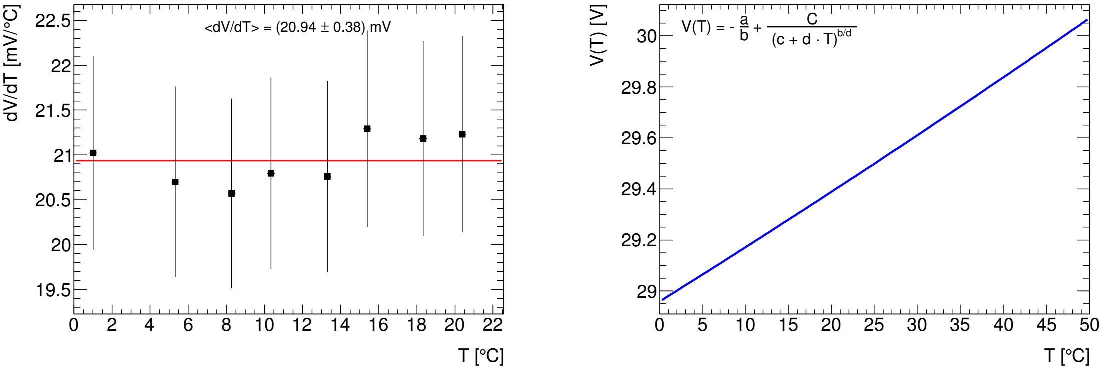

(e) Weighted average distribution of dV/dT as a function of temperature.

(f) Plot illustrates the bias voltage as a function of temperature.

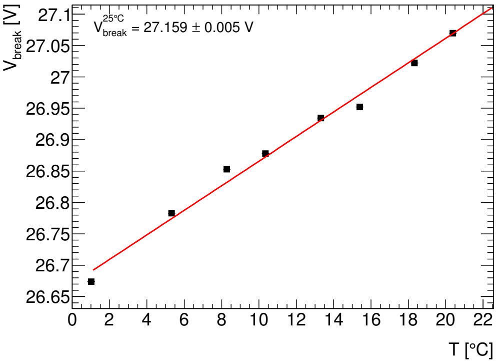

(g) Plot shows the determined breakdown voltage at different temperatures.

Figure B.7: All measurements are taken with the KETEK detector PM3350 serial number 7 with channel 3 preamplifier.

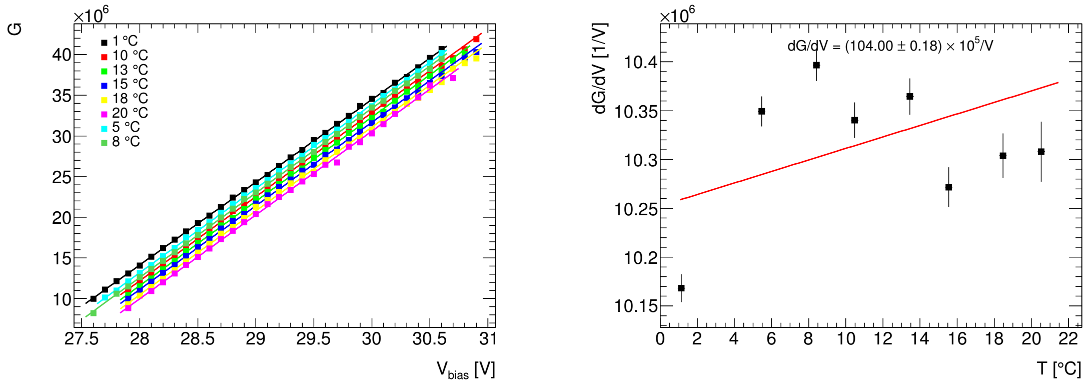

(a) Measurements of gain-versus-bias voltage (dG/dV) for fixed temperatures.

(b) Plot shows the obtained values of the dG/dV versus fixed temperature.

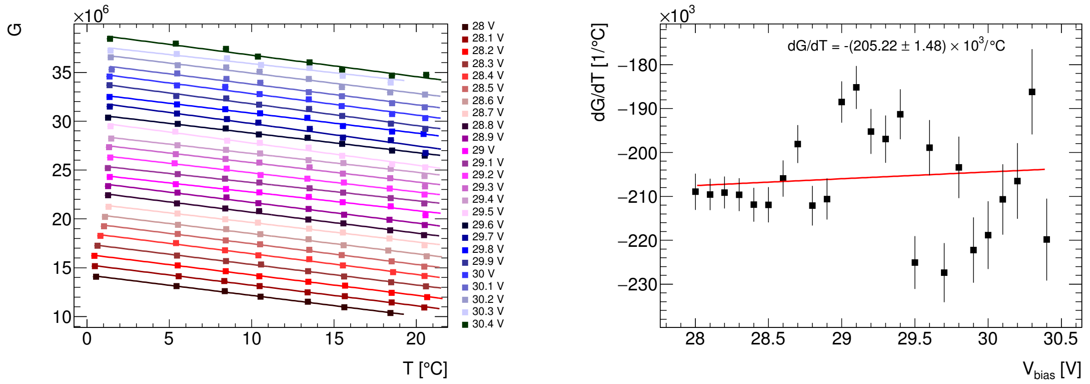

(c) Measurements of gain-versus-temperature (dG/dT) for fixed bias.

(d) Plot shows the obtained values of the dG/dT versus fixed bias voltage.

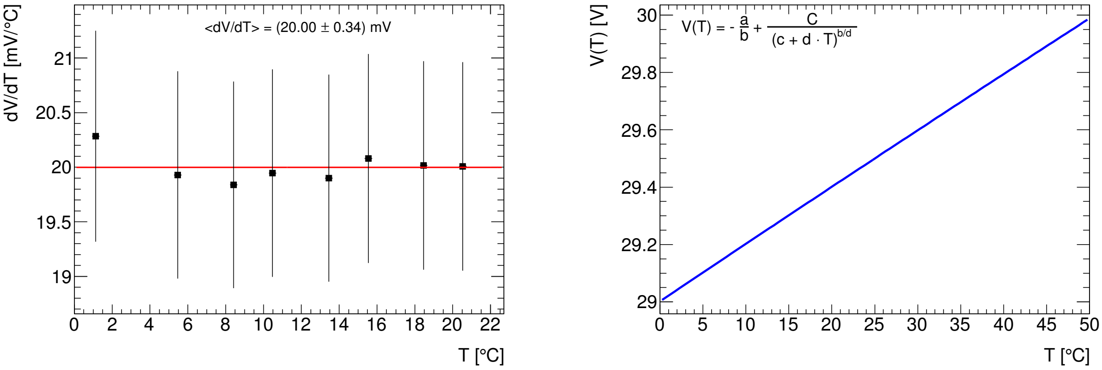

(e) Weighted average distribution of dV/dT as a function of temperature.

(f) Plot illustrates the bias voltage as a function of temperature.

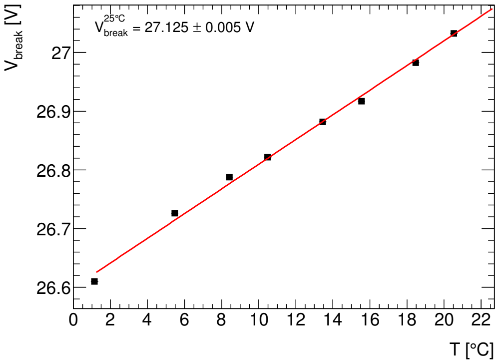

(g) Plot shows the determined breakdown voltage at different temperatures.

Figure B.8: All measurements are taken with the KETEK detector PM3350 serial number 8 with channel 4 preamplifier.

Appendix C

Bias scan measurements for CPTA

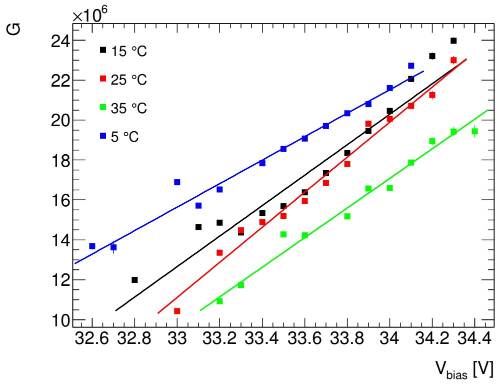

(a) Measurements of gain-versus-bias voltage (dG/dV) for fixed temperatures.

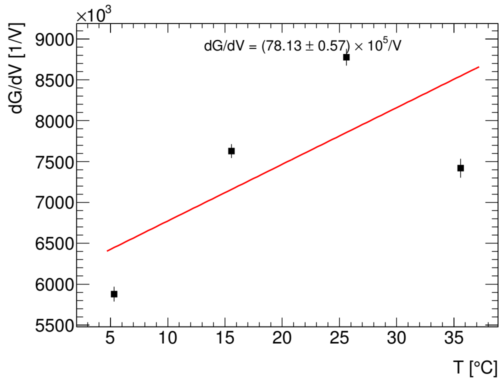

(b) Plot shows the obtained values of the dG/dV versus fixed temperature.

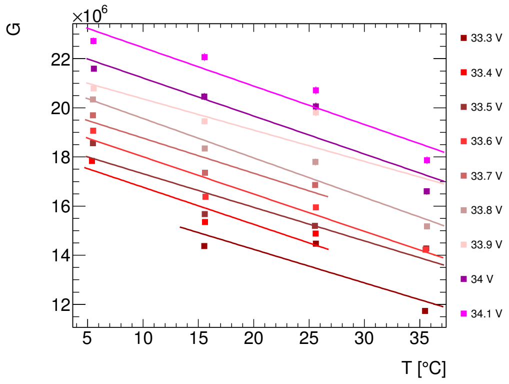

(c) Measurements of gain-versus-temperature (dG/dT) for fixed bias.

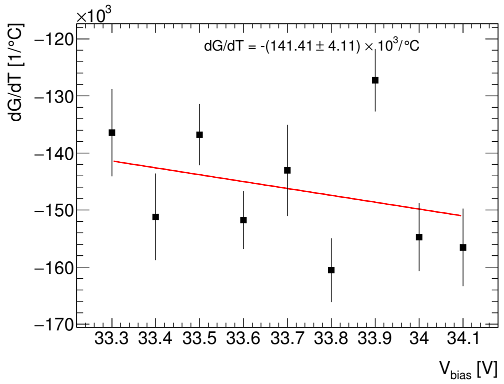

(d) Plot shows the obtained values of the dG/dT versus fixed bias voltage.

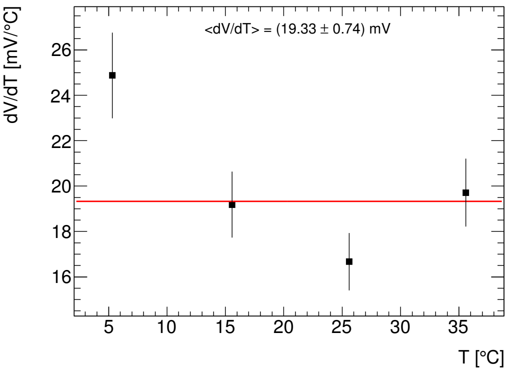

(e) Weighted average distribution of dV/dT as a function of temperature.

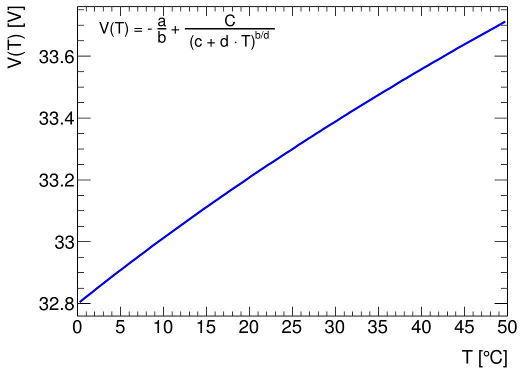

(f) Plot illustrates the bias voltage as a function of temperature.

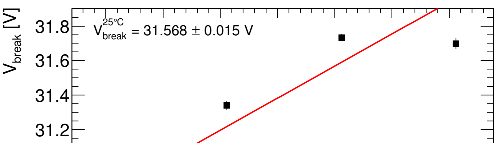

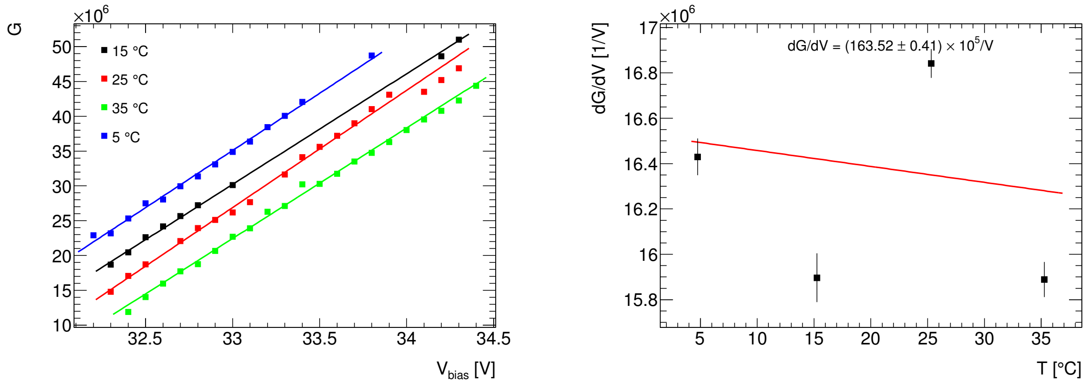

(a) Measurements of gain-versus-bias voltage (dG/dV) for fixed temperatures.

(b) Plot shows the obtained values of the dG/dV versus fixed temperature.

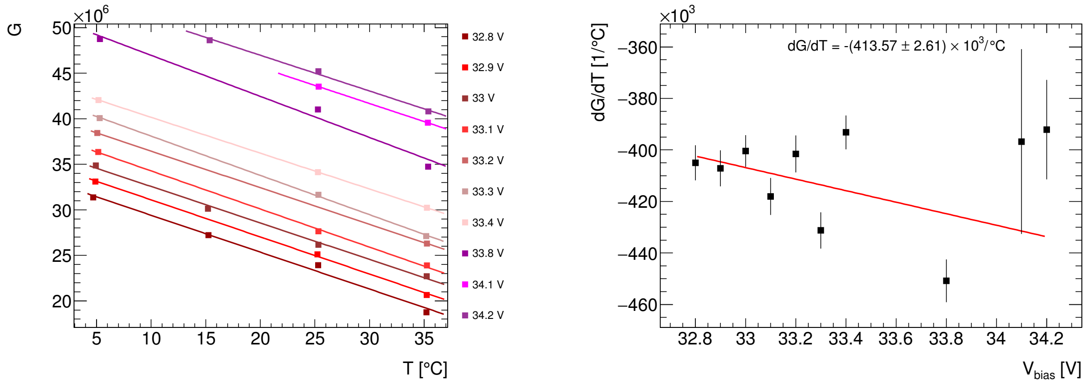

(c) Measurements of gain-versus-temperature (dG/dT) for fixed bias.

(d) Plot shows the obtained values of the dG/dT versus fixed bias voltage.

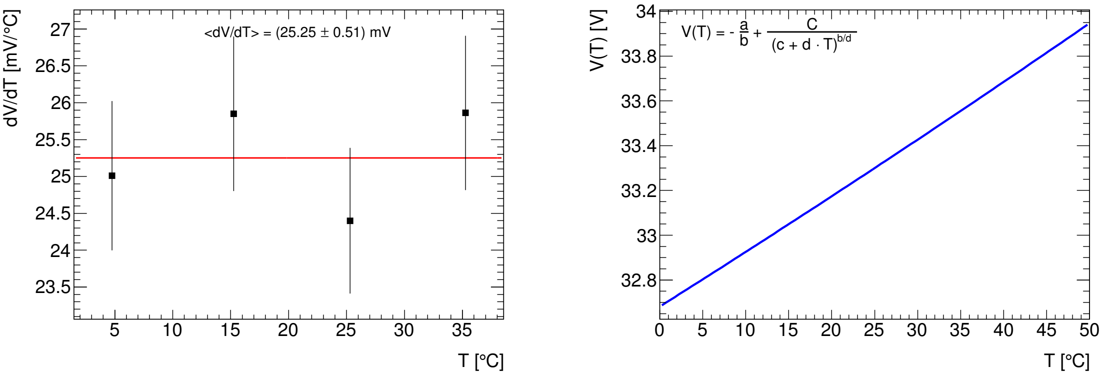

(e) Weighted average distribution of dV/dT as a function of temperature.

(f) Plot illustrates the bias voltage as a function of temperature.

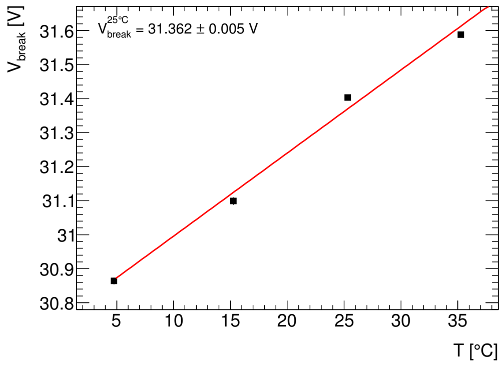

(g) Plot shows the determined breakdown voltage at different temperatures.

Figure C.2: All measurements are taken with the CPTA detector 922 with channel 2 preamplifier.

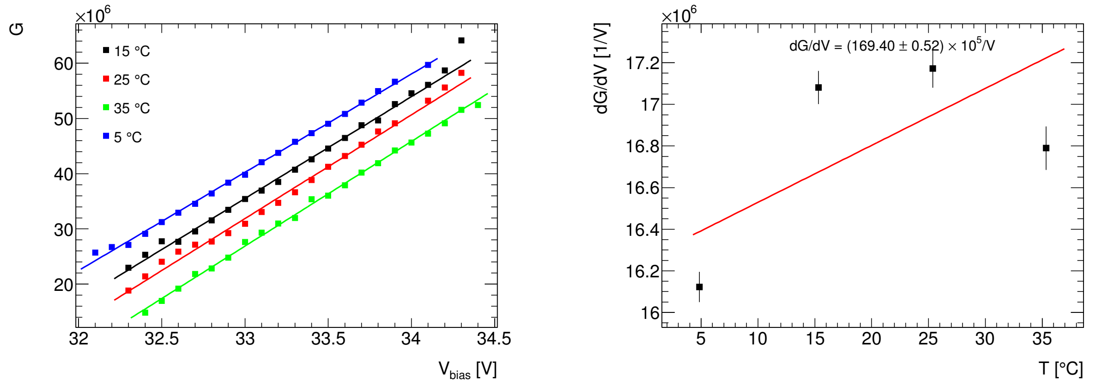

(a) Measurements of gain-versus-bias voltage (dG/dV) for fixed temperatures.

(b) Plot shows the obtained values of the dG/dV versus fixed temperature.

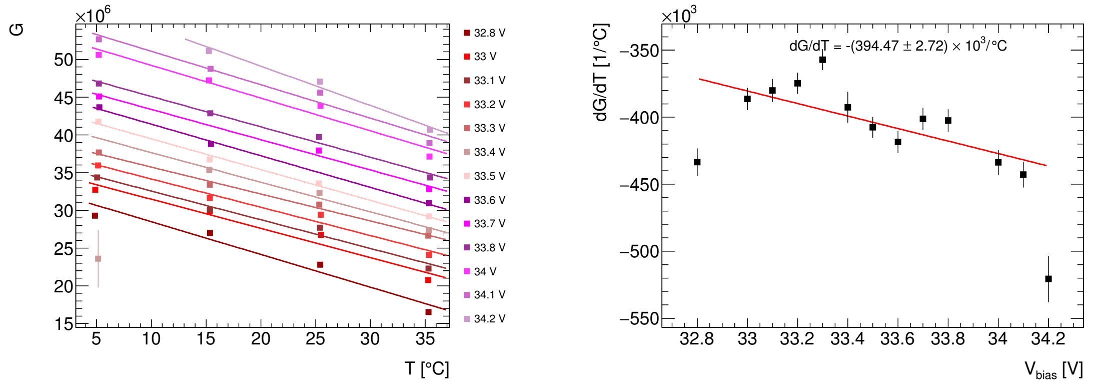

(c) Measurements of gain-versus-temperature (dG/dT) for fixed bias.

(d) Plot shows the obtained values of the dG/dT versus fixed bias voltage.

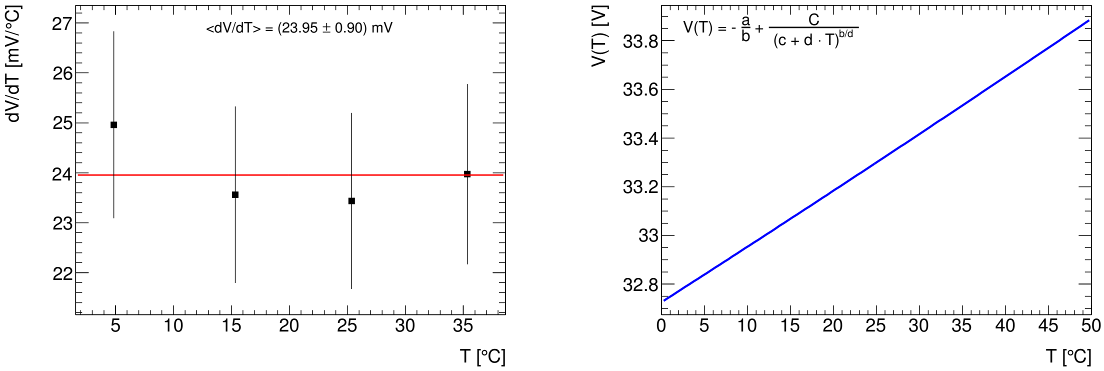

(e) Weighted average distribution of dV/dT as a function of temperature.

(f) Plot illustrates the bias voltage as a function of temperature.

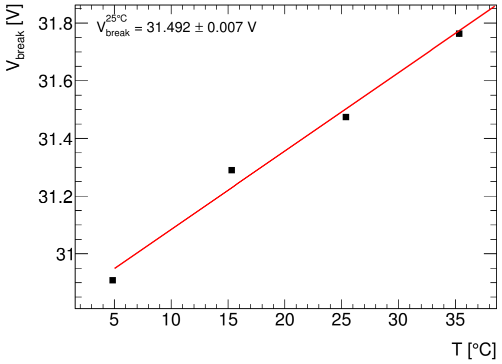

(g) Plot shows the determined breakdown voltage at different temperatures.

Figure C.3: All measurements are taken with the CPTA detector 975 with channel 3 preamplifier.

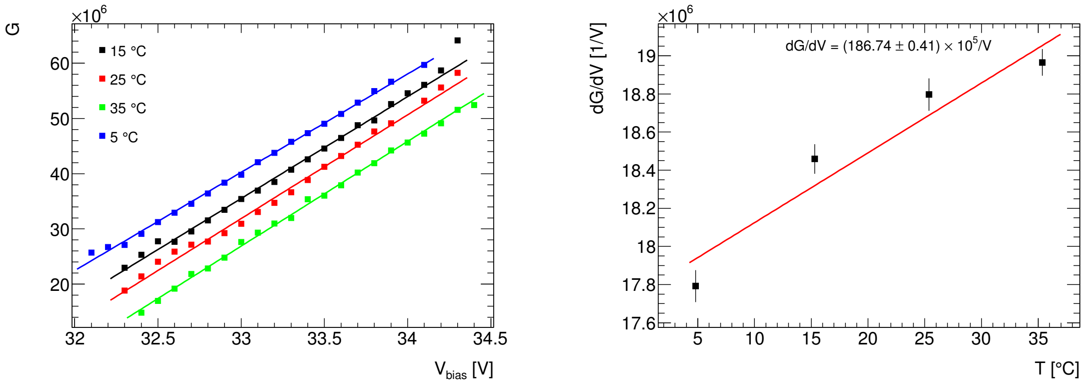

(a) Measurements of gain-versus-bias voltage (dG/dV) for fixed temperatures.

(b) Plot shows the obtained values of the dG/dV versus fixed temperature.

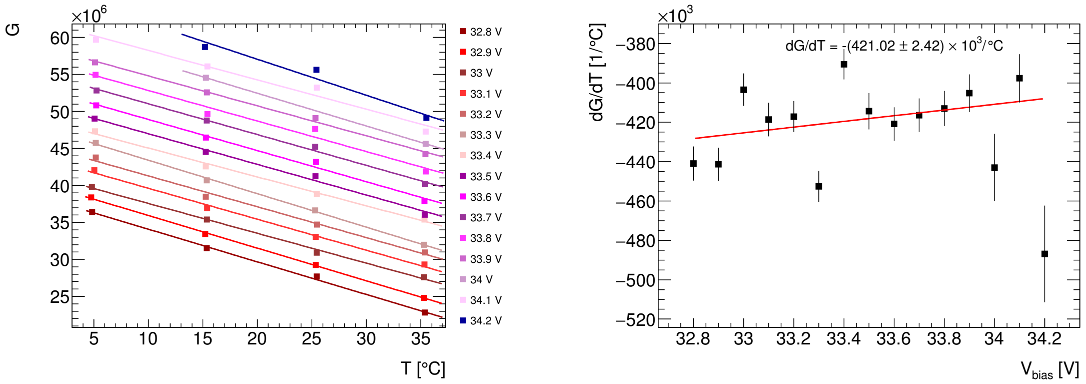

(c) Measurements of gain-versus-temperature (dG/dT) for fixed bias.

(d) Plot shows the obtained values of the dG/dT versus fixed bias voltage.

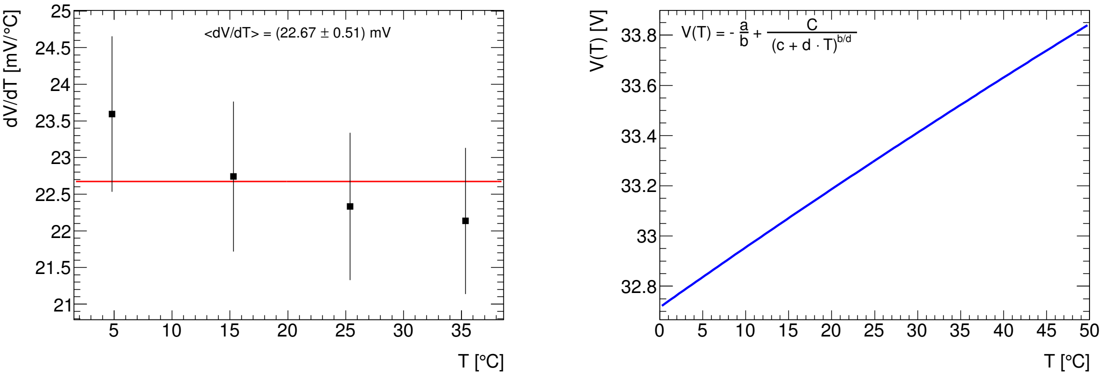

(e) Weighted average distribution of dV/dT as a function of temperature.

(f) Plot illustrates the bias voltage as a function of temperature.

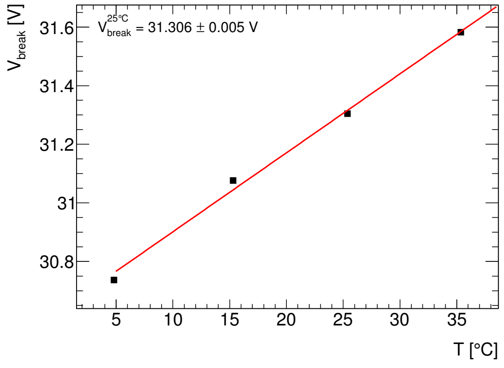

(g) Plot shows the determined breakdown voltage at different temperatures.

Figure C.4: All measurements are taken with the CPTA detector 1065 with channel 4 preamplifier.

Appendix D

Stabilization measurements for Hamamatsu

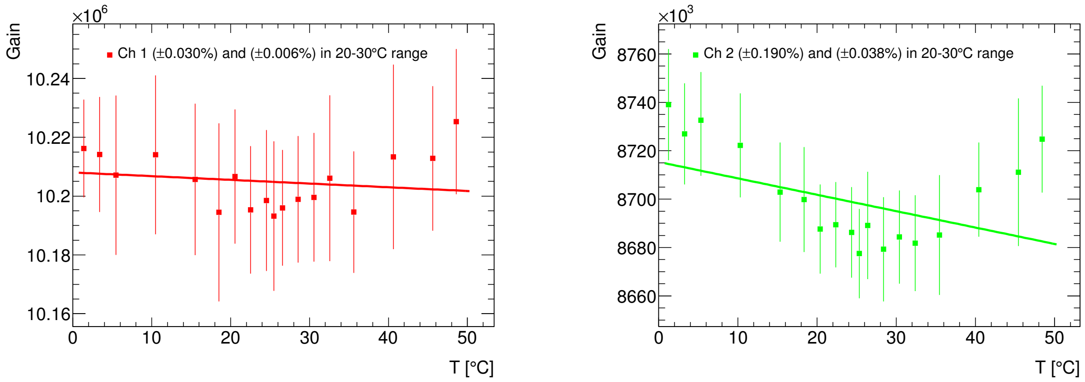

(a) Channel 1 Hamamatsu A1 20 µm.

(b) Channel 2 Hamamatsu A2 20 µm.

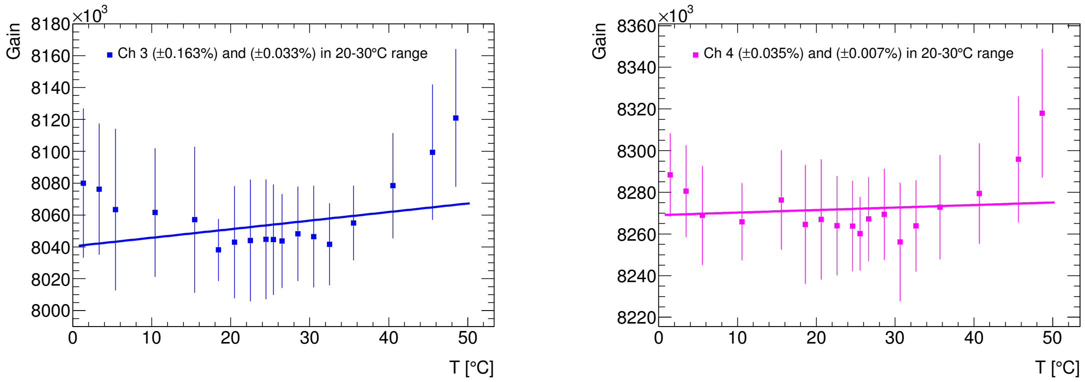

(c) Channel 3 Hamamatsu A1 15 µm.

(d) Channel 4 Hamamatsu A2 15 µm.

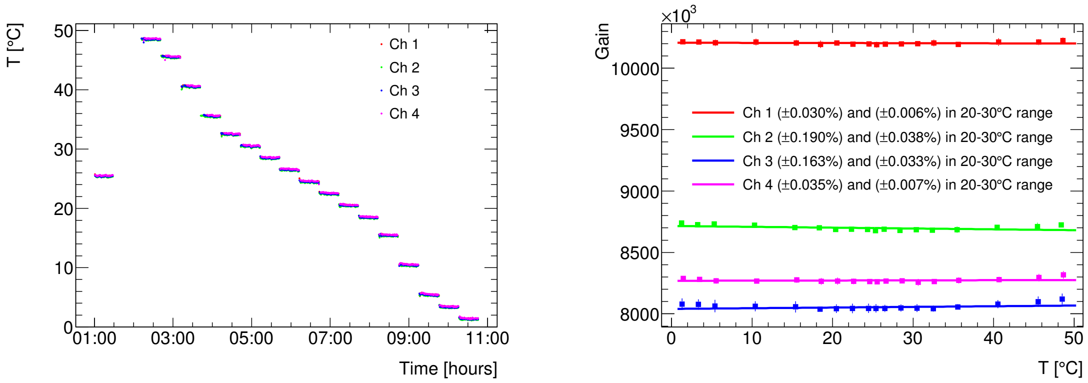

(e) Temperature profile showcasing which data files are used for the different channels.

(f) Illustrates the gain stability for the four detectors.

Figure D.1: All measurements are taken with the Hamamatsu A detectors.

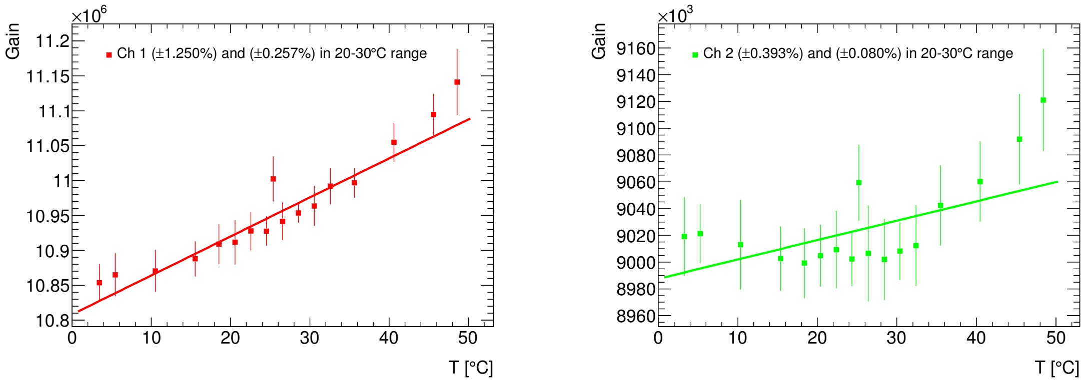

(a) Channel 1 Hamamatsu B1 20 µm.

(b) Channel 2 Hamamatsu B2 20 µm.

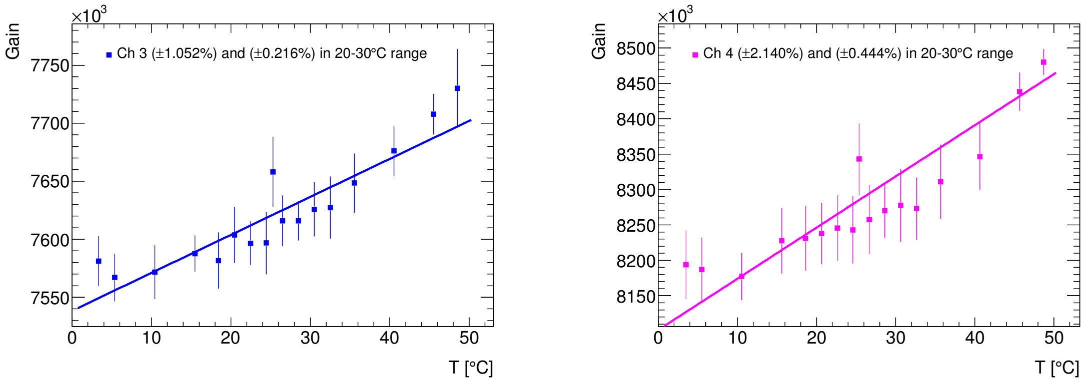

(c) Channel 3 Hamamatsu B1 15 µm.

(d) Channel 4 Hamamatsu B2 15 µm.

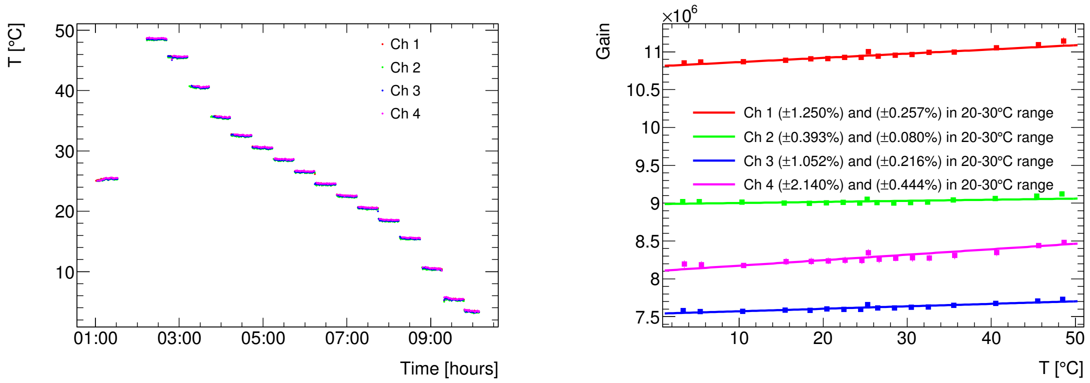

(e) Temperature profile showcasing which data files are used for the different channels.

(f) Illustrates the gain stability for the four detectors.

Figure D.2: All measurements are taken with the Hamamatsu B detectors.

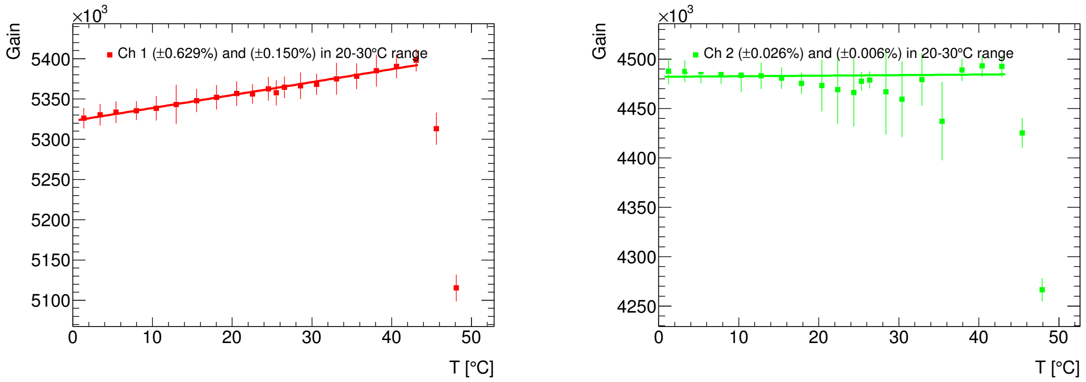

(a) Channel 1 Hamamatsu S12571 010C serial number 271.

(b) Channel 2 Hamamatsu S12571 010C serial number 272.

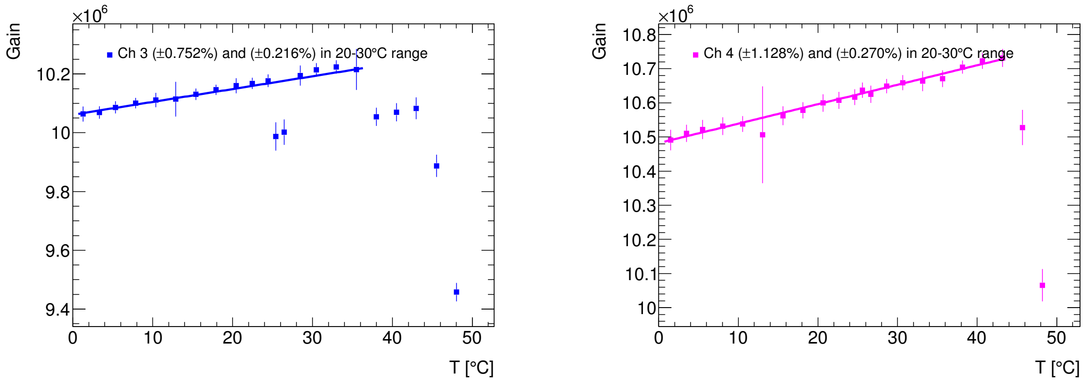

(c) Channel 3 Hamamatsu S12571 015C serial number 136.

(d) Channel 4 Hamamatsu S12571 015C serial number 137.

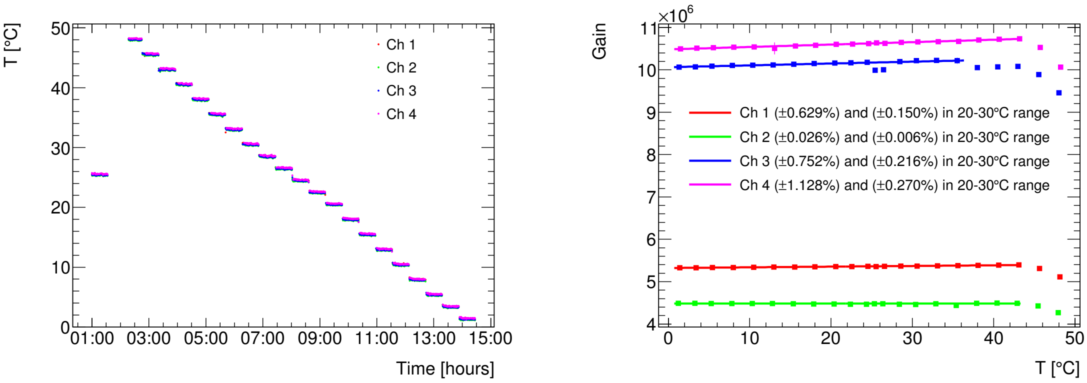

(e) Temperature profile showcasing which data files are used for the different channels.

(f) Illustrates the gain stability for the four detectors.

Figure D.3: All measurements are taken with the Hamamatsu S12571 detectors.

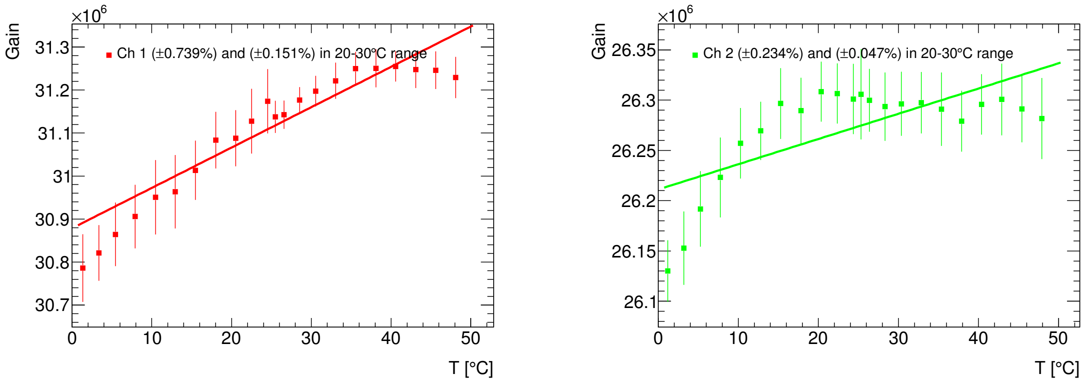

(a) Channel 1 Hamamatsu S13360 1325CS serial number 10143.

(b) Channel 2 Hamamatsu S13360 1325CS serial number 10144.

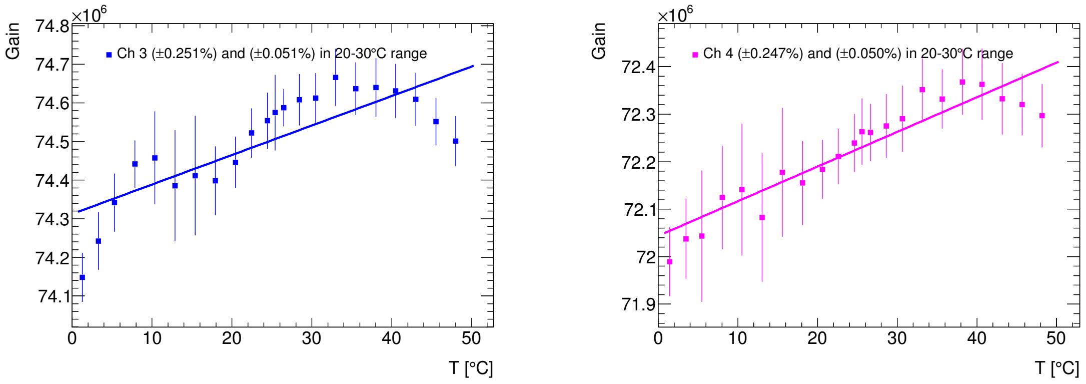

(c) Channel 3 Hamamatsu LCT4 serial number 6.

(d) Channel 4 Hamamatsu LCT4 serial number 9.

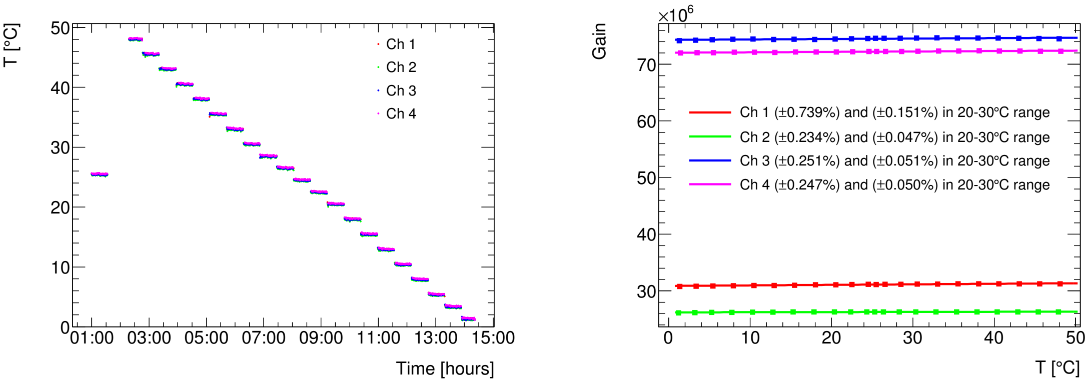

(e) Temperature profile showcasing which data files are used for the different channels.

(f) Illustrates the gain stability for the four detectors.

Figure D.4: All measurements are taken with the Hamamatsu S13360 1325CS and LCT4 detectors.

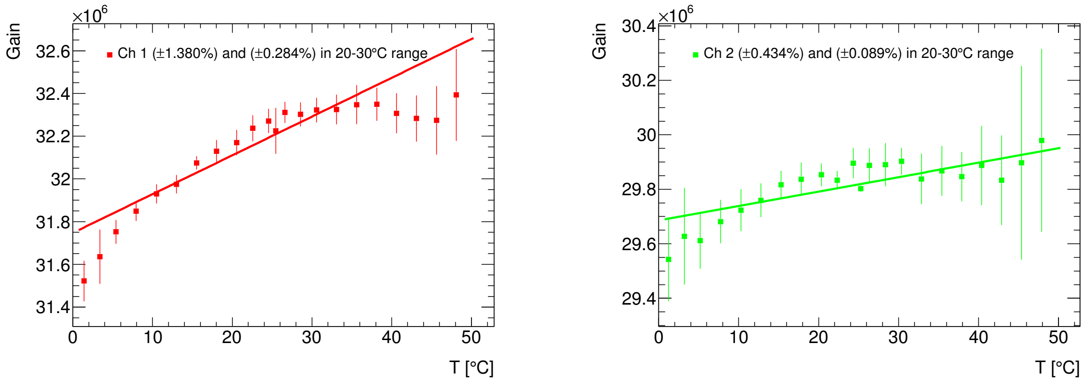

(a) Channel 1 Hamamatsu S13360 3025CS serial number 10103.

(b) Channel 2 Hamamatsu S13360 3025CS serial number 10104.

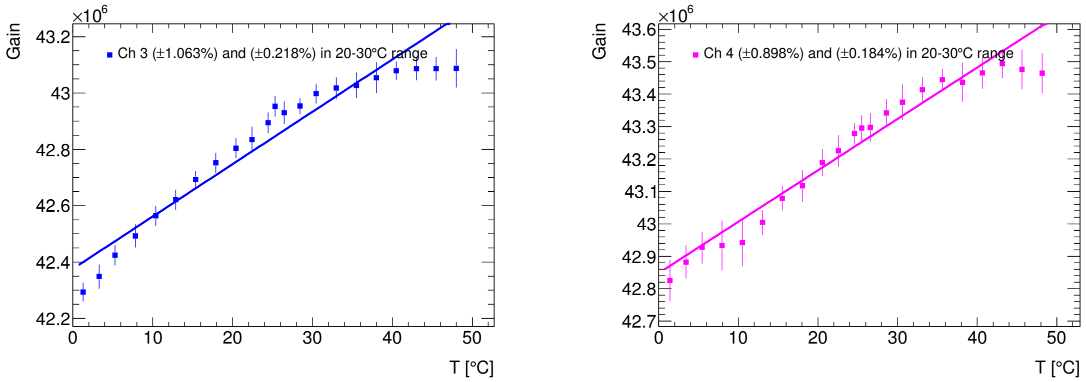

(c) Channel 3 Hamamatsu S13360 1325CS serial number 10143.

(d) Channel 4 Hamamatsu S13360 1325CS serial number 10144.

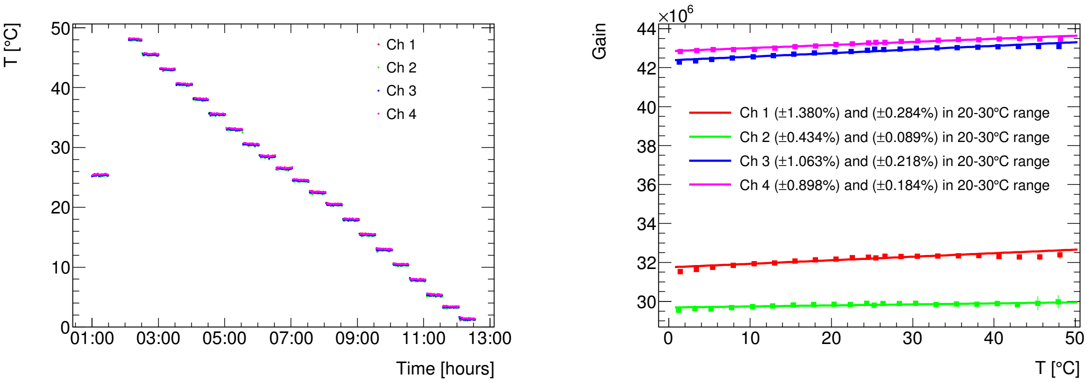

(e) Temperature profile showcasing which data files are used for the different channels.

(f) Illustrates the gain stability for the four detectors.

Figure D.5: All measurements are taken with the Hamamatsu S13360 detectors.

Appendix E

Stabilization measurements for KETEK

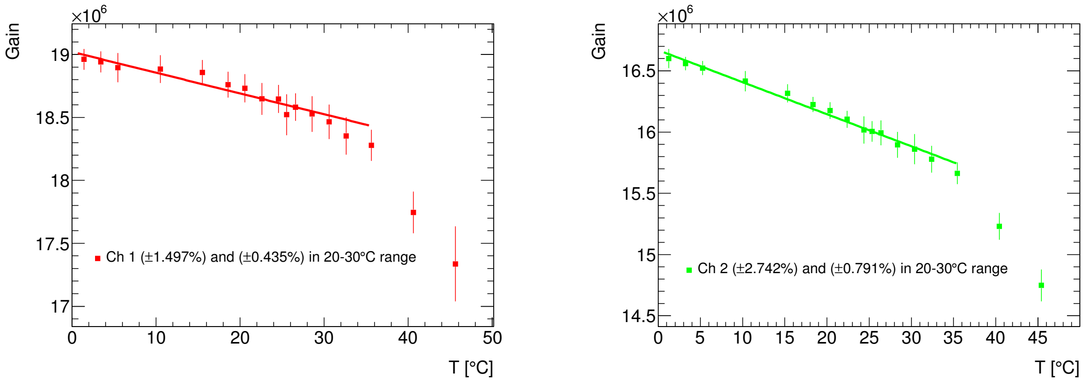

(a) Channel 1 Ketek W12 A.

(b) Channel 2 Ketek W12 A.

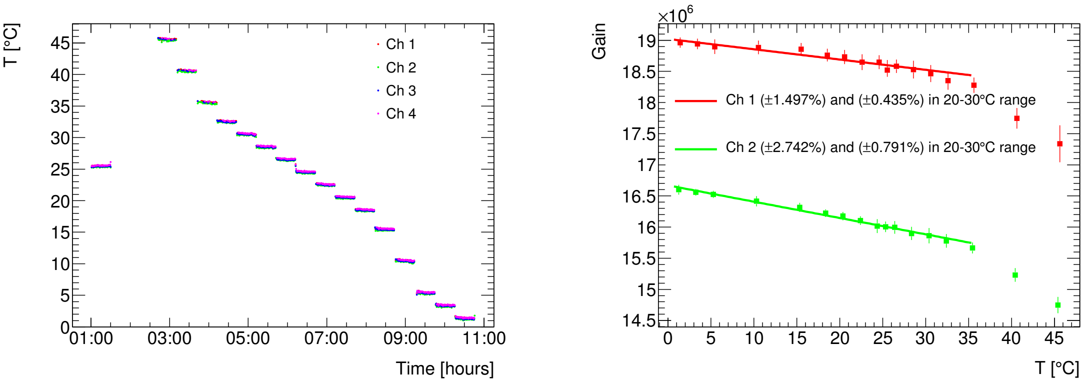

(c) Temperature profile showcasing which data files are used for the different channels.

(d) Illustrates the gain stability for the two detectors with the method.

Figure E.1: All measurements are taken with the Ketek W12 detectors using the method.

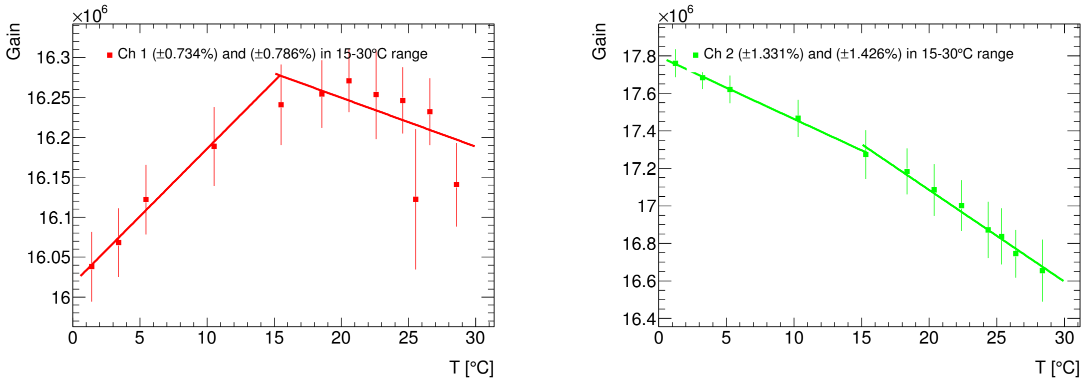

(a) Channel 1 W12 A.

(b) Channel 2 Ketek W12 B.

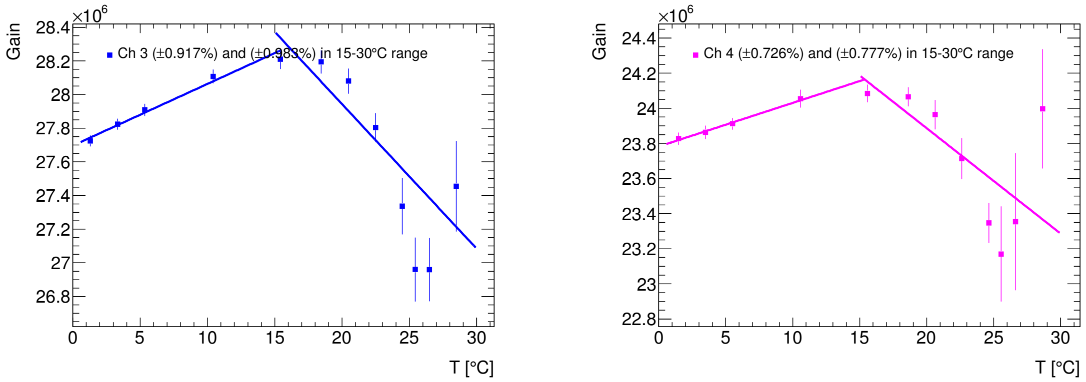

(c) Channel 3 Ketek PM3350 serial number 1.

(d) Channel 4 Ketek PM3350 serial number 2.

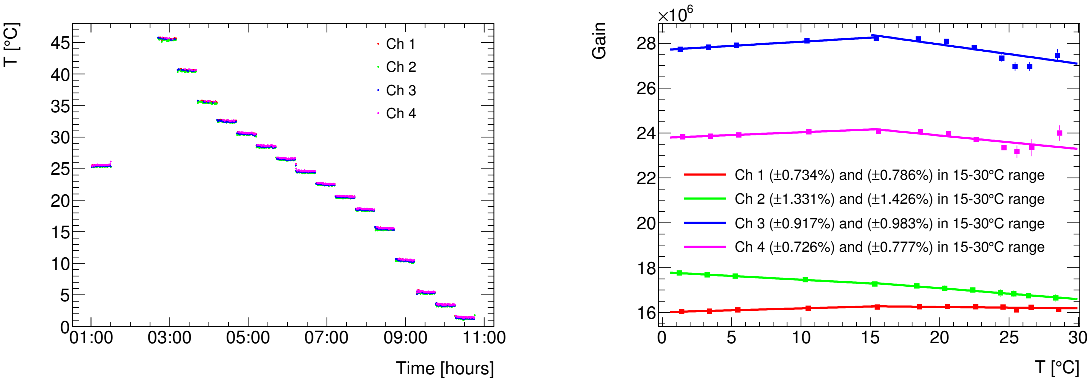

(e) Temperature profile showcasing which data files are used for the different channels.

(f) Illustrates the gain stability for the four detectors.

Figure E.2: All measurements are taken with the Ketek W12 and PM3350 serial number 1 and 2 detectors with the Maximum Amplitude method.

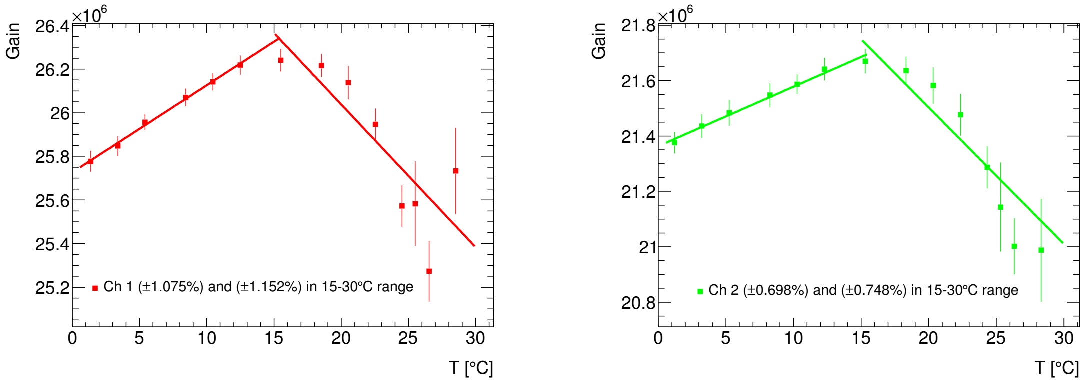

(a) Channel 1 Ketek PM3350 serial number 5.

(b) Channel 2 Ketek PM3350 serial number 6.

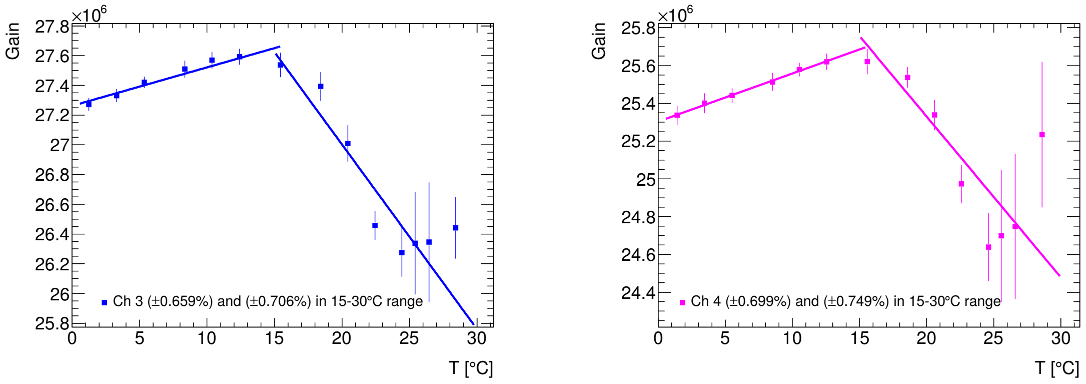

(c) Channel 3 Ketek PM3350 serial number 7.

(d) Channel 4 Ketek PM3350 serial number 8.

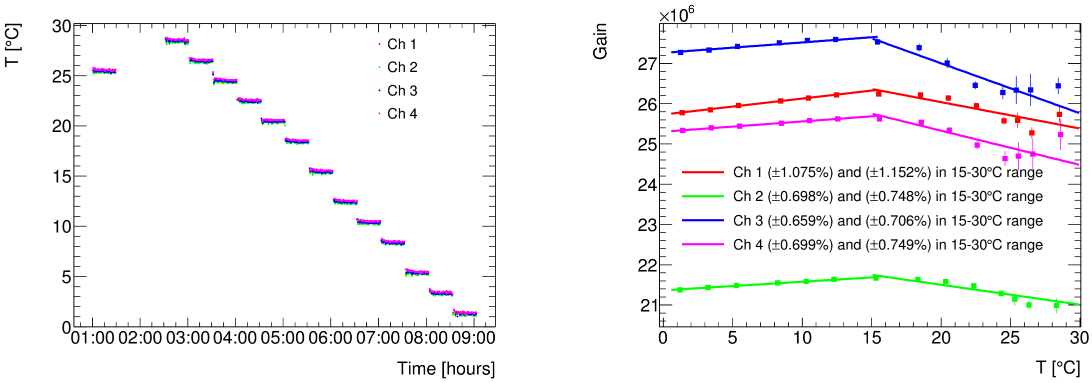

(e) Temperature profile showcasing which data files are used for the different channels.

(f) Illustrates the gain stability for the four detectors.

Figure E.3: All measurements are taken with the Ketek PM3350 serial number 5 through 8 detectors with the Maximum Amplitude method.

Appendix F

Stabilization measurements for CPTA

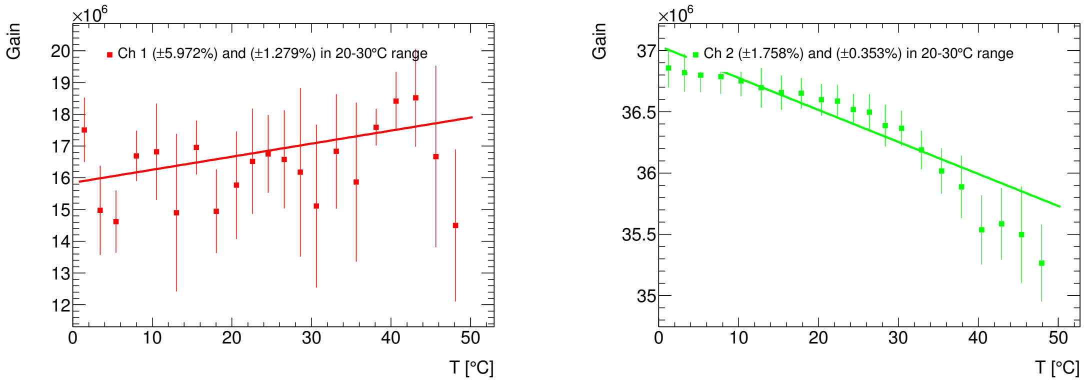

(a) Channel 1 CPTA 857.

(b) Channel 2 CPTA 922.

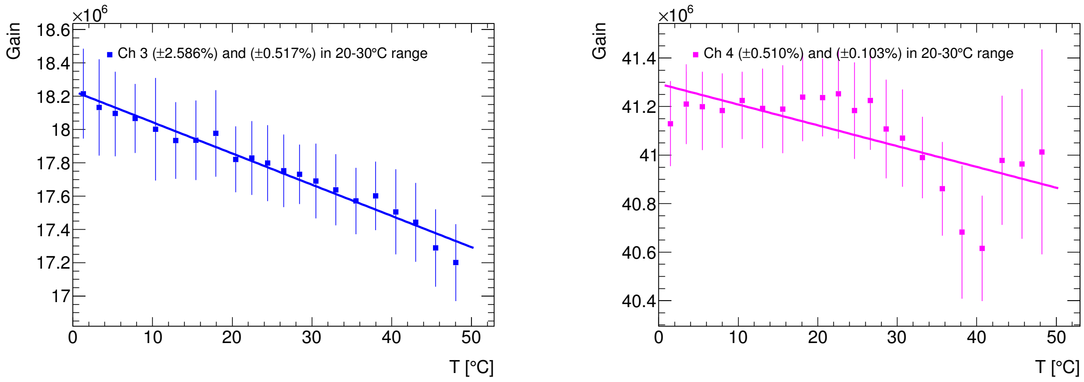

(c) Channel 3 CPTA 975.

(d) Channel 4 CPTA 1065.

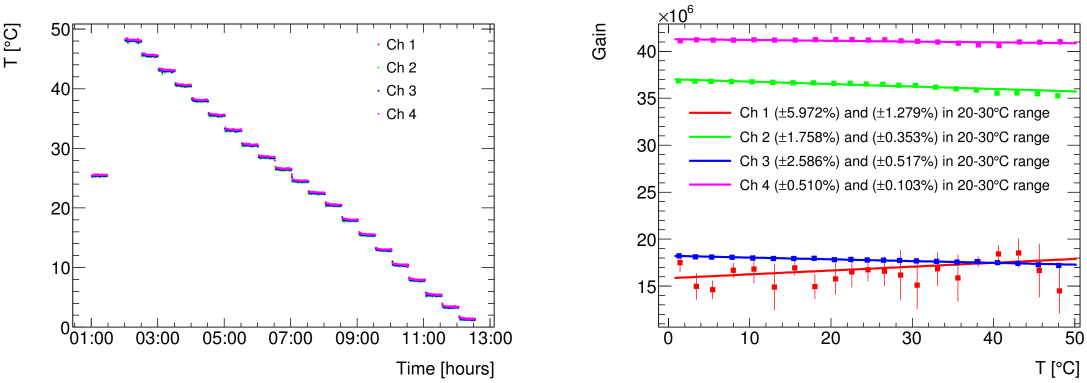

(e) Temperature profile showcasing which data files are used for the different channels.

(f) Illustrates the gain stability for the four detectors.

Figure F.1: All measurements are taken with the CPTA detectors with the Maximum Amplitude method.